Strap on your Boötes: Unveiling AGN Feedback through High Resolution Morphological Studies with LOFAR-VLBI

EMILY LOUISE ESCOTT

Strap on your Boötes: Unveiling AGN Feedback through High Resolution Morphological Studies with LOFAR-VLBI

Emmy L. Escott

A Thesis presented for the degree of
Doctor of Philosophy

Centre for Extragalactic Astronomy
Department of Physics
Durham University
United Kingdom
September 2025

Abstract

Through both observational and theoretical studies we know that Active Galactic Nuclei (AGN) play a key role in regulating galaxy evolution through a process known as AGN feedback. Although we know that this process is occurring in our Universe, it remains unclear how this feedback operates. One promising avenue of research for advancing our understanding of AGN feedback is the study of multi-phase outflows.

In this thesis, I focus on a single phase of these multi-phase outflows: warm ionised gas. By investigating the kinematics of the forbidden [O III] λ5007 Å emission line, it is possible to trace ionised outflows to understand their impact on the host galaxy. Previous works have investigated the impact of these ionised outflows on galaxies, however it is uncertain what mechanism is causing these outflows. Interestingly, this phase of outflow has been found to show a strong connection with radio emission. The relationship between the [O III] emission line and, in particular, low-frequency radio emission forms the primary focus of this doctoral work.

Following a discussion of the relevant scientific background (Chapter 1) as well as an overview of the fundamentals of radio astronomy (Chapter 2), Chapter 3 presents an analysis based on the first Low Frequency Array Two Metre Sky Survey Deep (LoTSS Deep) release. Here, I investigate the low-frequency, deep radio emission of AGN and link this to the kinematics of the [O III] emission line via spectral decomposition of Sloan Digital Sky Survey (SDSS) spectra. In this published work, we demonstrate that AGN detected in LoTSS Deep are more likely to host an [O III] outflow compared to AGN without a detection, hence confirming the link between radio emission and [O III] outflows.

To explore the physical mechanism behind this enhancement, we first examine the radio excess of our AGN sample and find that the majority of sources are non-radio excess, and therefore classified as radio-quiet AGN. This allows us to rule out powerful radio jets as the origin of their emission. To further investigate the nature of the radio emission, we turn to morphological studies. However, ∼90% of our radio detected population are unresolved in LoTSS Deep, limiting our ability to determine the origin of their radio

emission. High-resolution imaging is therefore essential to resolve these sources and advance our understanding of the radio emission in both radio-quiet AGN and the physical mechanism driving the link between [O III] outflows and radio emission.

In Chapter 4, we focus on obtaining sub-arcsecond, kiloparsec-scale radio morphologies of the AGN sample introduced in Chapter 3. To achieve this, we exploit the full capabilities of the International LOFAR Telescope (ILT) and present the first, wide-field, sub-arcsecond resolution image of the Boötes Deep Field at 144 MHz. This represents only the third wide-field image produced using the international ILT stations with Very Long Baseline Interferometry (VLBI) techniques. The scarcity of such images highlights the significant challenges posed during the data reduction process. In this chapter, I discuss the primary obstacles encountered when reducing a $> 6\text{deg}^2$ field of view at low frequencies, and I outline the data reduction steps performed to generate the Boötes image, along with two intermediate resolution images at $0.6''$ and $1.2''$. Thanks to this image, I now have access to sub-arcsecond resolution imaging across all three LoTSS Deep DR1 field.

In Chapter 5, I build on the connection between low-frequency radio emission and [O III] outflows by locating the radio detected AGN population from Chapter 3 within the wide-field, sub-arcsecond resolution images of Boötes (Chapter 4), Lockman Hole, and ELAIS-N1. I utilise the spectral decomposition of SDSS spectroscopy performed in Chapter 3 to now link [O III] outflows with kiloparsec-scale radio emission.

Due to the high-resolution nature of these images, radio emission that was unresolved in LoTSS Deep DR1 ($6''$ resolution) can now be resolved. This enables a deeper understanding of the origin of radio emission in radio-quiet AGN and allows us to investigate the physical mechanism driving the connection between [O III] and low-frequency radio emission. Using a combination of sub-arcsecond morphological studies and brightness temperature measurements, I extend this investigation to a novel regime.

I find that AGN detected on both small ($0.3''$) and large ($6''$) scales are more likely to host [O III] outflows than AGN detected only on large scales. Considering that kiloparsec-scale radio emission is likely associated with the AGN, whereas diffuse large-scale emission is likely due to star formation, we conclude that the enhanced [O III] emission observed in these sources is predominantly AGN-driven.

I conclude this thesis in Chapter 6 by summarising the key outcomes of my doctoral work and by looking ahead to the promising future of statistically significant spectroscopic samples of radio detected sources, as well as forthcoming revolutionary radio surveys and instruments. These developments are expected to enable substantial scientific progress in the near future.

Declaration

The work in this thesis is based on research carried out at the Centre for Extra-galactic Astronomy, Department of Physics, Durham University, United Kingdom between October 2021 and September 2025. The work was supervised by Prof. Leah K. Morabito of the same institute. No part of this thesis has been submitted elsewhere for any other degree or qualification and it is all my own work unless referenced to the contrary in the text.

The research presented in Chapter 3 has been published in Monthly Notices of the Royal Astronomical Society (MNRAS). The material in Chapter 4 and Chapter 5 has been submitted as a single manuscript to MNRAS. These chapters have been adapted so to stand alone within the context of this thesis.

Publications

- *Chapter 3:* **"Unveiling AGN Outflows: [O III] outflow detection rates and correlation with low-frequency radio emission"**
  Emmy L. Escott, Leah K. Morabito, Jan Scholtz, Ryan C. Hickox, Chris M. Harrison, David M. Alexander, Marina I. Arnaudova, Daniel J. B. Smith, Kenneth J. Duncan, James Petley, Rohit Kondapally, Gabriela Calistro Rivera, and Sthabile Kolwa **MNRAS, 536, 2, (2025)**

- *Chapters 4 and 5*: **"Strap on your Boötes: A link between low-frequency kilo-parsec radio morphology and AGN driven ionised outflows"**
  Emmy L. Escott, Leah K. Morabito, Frits Sweijen, Chris M. Harrison, Jame Petley, Jurjen M. G. H. J. deJong, Reinout J. van Weeren, Thomas S. Higginson, Isabella Prandoni, George Miley, and Huub J. A. Röttgering **Submitted to MNRAS, (2025)**

Alongside work included in this thesis, the author has contributed to several other works during the period of the PhD under the following publications:

- **"A decade of sub-arcsecond imaging with the International LOFAR Telescope"**
  Leah K. Morabito, Neal Jackson, Jurjen de Jong, Emmy Escott, Christian Groeneveld, Vijay Mahatma, James Petley, Frits Sweijen, Roland Timmerman, Reinout J. van Weeren **Spinger Nature, 370, 2, (2025)**

- **"Into the depths: Unveiling ELAIS-N1 with LOFAR's deepest sub-arcsecond wide-field images"**
  J. M. G. H. J. de Jong, R. J. van Weeren, F. Sweijen, J. B. R. Oonk, T. W. Shimwell, A. R. Offringa, L. K. Morabito, H. J. A. Röttgering, R. Kondapally, E. L. Escott, P. N. Best, M. Bondi, H. Ye, and J. W. Petley **A&A, 689, A80, 2024**

- **"Ubiquitous radio emission in quasars: Predominant AGN origin and a connection to jets, dust, and winds"**
  G. Calistro Rivera, D. M. Alexander, C. M. Harrison, V. A. Fawcett, P. N. Best, W. L. Williams, M. J. Hardcastle, D. J. Rosario, D. J. B. Smith, M. I. Arnaudova, E. L. Escott, G. Gürkan, R. Kondapally, G. Miley, L. K. Morabito, J. Petley, I. Prandoni, H. J. A. Röttgering, and B-H Yue **A&A, 691, A191, (2024)**

- **"WEAVE First Light Observations: Origin and Dynamics of the Shock Front in Stephan's Quintet"**
  M. I. Arnaudova, Soumyadeep Das, D. J. B. Smith and 62 others **MNRAS, 535, 3, (2024)**

published without the author's prior written consent and information derived from it should be acknowledged".

Acknowledgements

The last four years have been a whirlwind, and throughout my PhD, there have been so many people for whom I am grateful. My experience would not have been the same without them. Here, I would like to highlight those whose contributions to this period of my life I will never forget:

- To the best supervisor anyone could ask for: Leah. Thank you for leading me through this journey with your endless knowledge and enthusiasm, even when times were tough. I truly hope we can continue to work together throughout my career.
- To Dave and Ryan, whose contributions to my PhD has been invaluable thanks to their enthusiasm for AGN research. Thank you for helping me build my knowledge in this inspiring field.
- To James, whose absence left a void so large it had to be filled by two Dutch men, thank you for showing me the ropes of Durham and of the PhD. My experience would not have been the same without you.
- Of course, to the two Dutch men, Frits and Roland. Frits, thank you for being such a pillar throughout my PhD, not only with your technical expertise but also through the friendship you have given over the past couple of years. Roland, you are the ideal travel companion any Aperol Spritz loving girlie could ask for; here's to many more conference adventures. I will think of you both every time I see the colour orange or Nijntje. Dank je wel.
- To other unforgettable members of the LOFAR Durham group: Matthijs, Nicole, and Rohit.
- To the most incredible LOFAR-VLBI working group, in particular Christian, Henrik, Hrishi, Jonny, Jurjen, and Vijay. It was thanks to you all that I always looked forward to our busy weeks.

- To my Astro Barbies: Ciera, Sarah, and Zoe. I will miss getting dressed up with you and taking Durham by storm. Thank you for everything.

- To the close friends I've made along the way: Sam, I will miss our cocktail nights but can't wait to visit you in Hong Kong; Duncan, the legend who came up with "*Strap on your Boötes*", you never fail to make me laughl; Makun, the Bob to my Teddy; and Sutti, thank you for being such an integral part of my life in Durham.

- To my office mates who have had to put up with my shenanigans, especially Scott, for the three years we shared an office and for being a pillar of support for me in the department; Marcus, for being the main driver of my mood swings over the past year, it has been both an honour and a nightmare; and, of course, Nency, for being the moderator during our time in Rochester.

- Thank you to the Durham Astronomy group: Bjarki, Carolina, Jack, Joaquin, Mac, Margarita, Martina, Martyna, Thomas, Vicky, Victor, and especially to Zane for supporting me over the past couple of months. I would also like to thank Shufei for keeping the department running seamlessly.

- My life at Durham would not have been the same without the people I met through college. Thank you to Caitlin, Carys, Chris, Georgie, Josh, Lucie, Nina, Peggy, and a massive shout-out to Izzy for being the best housemate a girl could ask for.

- To my high school Physics teacher, Mr Lambert. Without his influence, I doubt I would have followed the path I have today.

- To Jenny and Clem, thank you for staying by my side throughout my life, kiss kiss fall in love.

- Finally, thank you to my loving Mum and Dad, who have cared for and supported me throughout. I couldn't have done this without you.

Contents

List of Figures

List of Tables

Dedication

To my amazing Grandmas, thank you for everything and always believing in me. Love you both lots.

CHAPTER 1

Scientific Background

1.1 Galaxy Evolution

Charli XCX once said: "*Everything is romantic*" and it is difficult to imagine there is a more romantic job than gazing to the sky in the pursuit of understanding our Universe. I have spent the last four years researching one of the most powerful objects in our Universe: the supermassive black hole (SMBH; Kormendy & Richstone, 1992, 1995; Magorrian et al., 1998). If you are reading this, you are reading my small contribution to our understanding of our Universe. It may only be a small grain of sand upon the beaches of human knowledge. Nevertheless, I hope you enjoy it.

Our Universe is composed of atoms, which form bonds between each other to create molecules. These molecules are the building blocks of planets, which orbit around burning balls of gas, that themselves revolve around the centres of galaxies. The galaxy in which

we live, the Milky Way, contains over 100 billion stars (e.g., Binney & Tremaine, 2011). This average-sized galaxy is part of the Local Group, which hosts more than 50 additional galaxies (e.g., NASA, 2023). The Local Group lies at the centre of the Virgo Supercluster, a region spanning nearly 100 million light years in diameter and contains an estimated 100,000 galaxies (e.g., Scoles, 2019). Hopefully, you are beginning to appreciate the sheer expanse of our Universe. To nudge this realisation further, it is estimated to contain two trillion galaxies. To put this in perspective, Google estimates (as of 2010) that there are roughly 130 million published books in the world (Google, 2011). If each galaxy published its own book telling its own story and each of these were displayed in a cosmic library, our entire planet's literacy output would scarcely fill a single shelf. At the centre of most massive galaxies, there lies a SMBH, either dormant or actively accreting matter from its host galaxy.

No two galaxies are the same. The number of stars, the rotational dynamics, and the mass of the SMBH at their centres are just a few of the many properties that vary from galaxy to galaxy. Given the sheer number of galaxies and each one being unique, understanding these systems presents a significant challenge to astronomers.

Across cosmic time, galaxy properties vary, notably their star formation histories, which evolve significantly from Cosmic Dawn, when the first stars ignited and galaxies began to form, to the present day (e.g., Madau & Dickinson, 2014; Whitaker et al., 2014; Leslie et al., 2020). In observational astronomy, cosmic time is commonly parametrised by redshift, z, which traces shifts of spectral lines to longer wavelengths which occurs due to the expansion of the Universe. Hence, a higher redshift corresponds to earlier cosmic epochs. At low redshift, where present-day galaxies reside, the star formation rates are low. However, as we move to higher redshift and look back further in time, to around $z = 2$ (10 Gyr lookback time), the star formations peaks (e.g., Dickinson et al., 2003; Daddi et al., 2007; Santini et al., 2009; Feldmann et al., 2016; Benton et al., 2024). It is during that time that the Universe was most efficient at forming stars, a key epoch known as Cosmic Noon (see, Förster Schreiber & Wuyts, 2020, for a review). Following this epoch, star formation began to decline towards the modern day (e.g., Hughes et al., 1998; González et al., 2010; Magnelli et al., 2024). This trend implies that galaxies increase in size over time by forming stars, reaching a peak rate of star formation during Cosmic Noon. Despite

the subsequent decrease in star formation rate, galaxies continue to evolve though over processes, raising important questions: What other properties influence galaxy evolution? What factors contribute most significant to this evolution? How does the evolutionary path vary from one galaxy to another?

1.1.1 AGN Feedback

An SMBH resides in the central regions of almost every galaxy. When these SMBHs are accreting, we call these objects Active Galactic Nuclei (AGN). These are some of the most powerful objects in our Universe. To put the sheer power of these elusive objects into perspective, consider the city of Norwich, England, which consumed 477.1 GWh of energy in 2023 [1] to power a population of roughly 140,000 people (2022). In comparison, Centaurus A, one of the brightest AGN in the radio sky, emits a luminosity on the order of 10^{43} erg/s (Terrell, 1986) corresponding to $\sim 10^{31}$ GWh per year. Harnessing the energy output of just that single AGN (of which millions have been discovered) for only one nanosecond we could power the city of Norwich for 6000 Gyr.

Both observational and simulated studies indicate that AGN play a crucial role in the evolution of their host galaxies, due to the immense power they can generate. The influence of an AGN on its host galaxy is known as AGN feedback. Observationally, we see a tight trend between the mass of the SMBH at the galaxy's centre and the velocity dispersion of the galaxy (e.g., Gebhardt et al., 2000; Merritt & Ferrarese, 2001; Gültekin et al., 2009), which quantifies the range in stellar velocities within the galaxy. This trend is commonly known as the M-σ relation. We also observe a similar trend between the mass of the SMBH and the luminosity of the bulge of the host galaxy (e.g., Magorrian et al., 1998; Marconi & Hunt, 2003; Gültekin et al., 2009).

On the theoretical side, AGN feedback is a critical component in cosmological simulations. For example, these AGN can provide essential heating mechanisms that enable simulations to reproduce the observable Universe (Croton et al., 2006; Bower et al., 2006). This effect is nicely summarised in Figure 1.1 from Mutch et al. (2013). Here, we compare the observed galactic stellar mass function (Bell et al., 2003), fitted with a Schechter func-

[1] Sub-national electricity consumption data

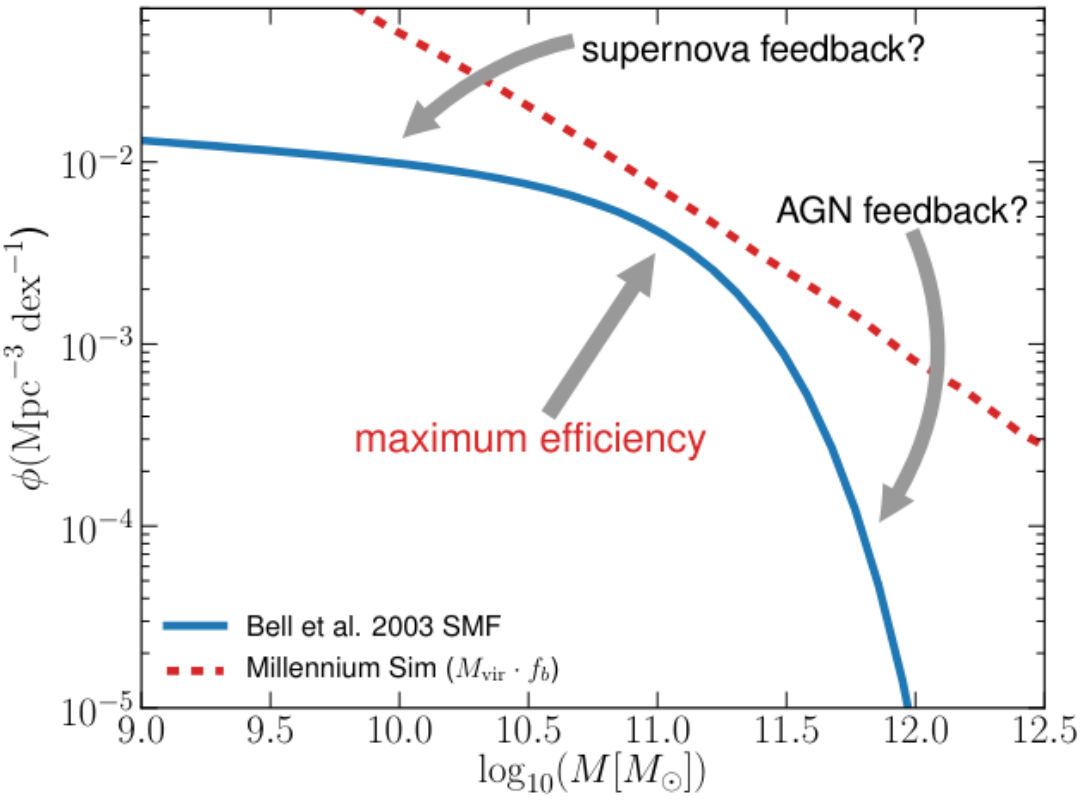

Figure 1.1: Comparison of the simulated halo mass function (red dashed line) with the observed galactic stellar mass function fitted by a Schechter function (blue solid line). The discrepancy between the simulated and observed data at lower masses, is attributed to supernova feedback, while the suppression at higher masses is explained by AGN feedback. Credit: Mutch et al. (2013).

tion (blue solid line), to the halo mass function from the Millennium simulation (Springel et al., 2005) (red dashed line), assuming a ΛCDM cosmology. It is evident that the simulations fail to replicate the observable Universe at both high and low masses, demonstrating that star formation is not occurring efficiently across the mass spectrum.

The discrepancies at low masses are often attributed to supernova feedback, where these immense galactic explosions expel large amounts of gas from galaxies, thereby reducing the fuel available for star formation (Dekel & Silk, 1986; Yepes et al., 1997). At the high mass end, AGN feedback has been attributed to suppressing star formation, as this mechanism has been observed to quench star formation in some systems (e.g., Croton et al., 2006; Schawinski et al., 2007; Beckmann et al., 2017).

We know, therefore, that AGN feedback is occurring in our Universe; however, it remains unclear how this feedback operates, and we can ask: What is driving this feedback?

1.1.2 Active Galactic Nuclei

An important subset of AGN, both historically and in terms of their characteristics are quasars. These are the most luminous type of AGN, and consequently the first to be observed and studied in detail. 3C 273 was initially detected at 159 MHz and catalogued at the University of Cambridge as part of the renowned 3C catalogue (Edge et al., 1959). This object was later re-observed by Hazard et al. (1963) using the Parkes Radio Telescope at 136 MHz, 410 MHz and 1,420 MHz, allowing the authors to determine a precise position for the object via lunar occultations. Due to its point-like appearance, astronomers initially believed this object to be a ordinary star.

The true significance of 3C 273, however, was recognized by Maarten Schmidt in 1963. Schmidt observed this "star" with the Palomar Observatory's 200-inch Hale Telescope to obtain the object's spectroscopy. In the resulting spectroscopic measurements, Schmidt noted the unusually broad nature of several key emission lines, including [O III]. Schmidt proposed two possible explanations for the phenomena he had observed:

" (1) The stellar object is a star with a large gravitational red-shift. Its radius would then be of the order of 10 km. Preliminary considerations show that it would be extremely difficult, if not impossible, to account for the occurrence of permitted lines and a forbidden line with the same red-shift, and with widths of only 1 or 2 per cent of the wavelength."

or

" (2) The stellar object is the nuclear region of a galaxy with a cosmological red-shift of 0-158, corresponding to an apparent velocity of 47,400 km/sec. The distance would be around 500 megaparsecs, and the diameter of the nuclear region would have to be less than 1 kiloparsec. This nuclear region would be about 100 times brighter optically than the luminous galaxies which have been identified with radio sources thus far.".

We now know that Schmidt's second hypothesis correctly explained the nature of 3C 273, which would soon be recognised as a quasi-stellar object, more commonly known today as a quasar.

The structure of AGN varies from object to object, but the scientific community generally describes them using a unified model (Urry & Padovani, 1995), as illustrated in Figure 1.2. At the centre of this model lies the SMBH which is the primary source of an AGN's energy. Surrounding this SMBH is a thin accretion disk, typically assumed to be

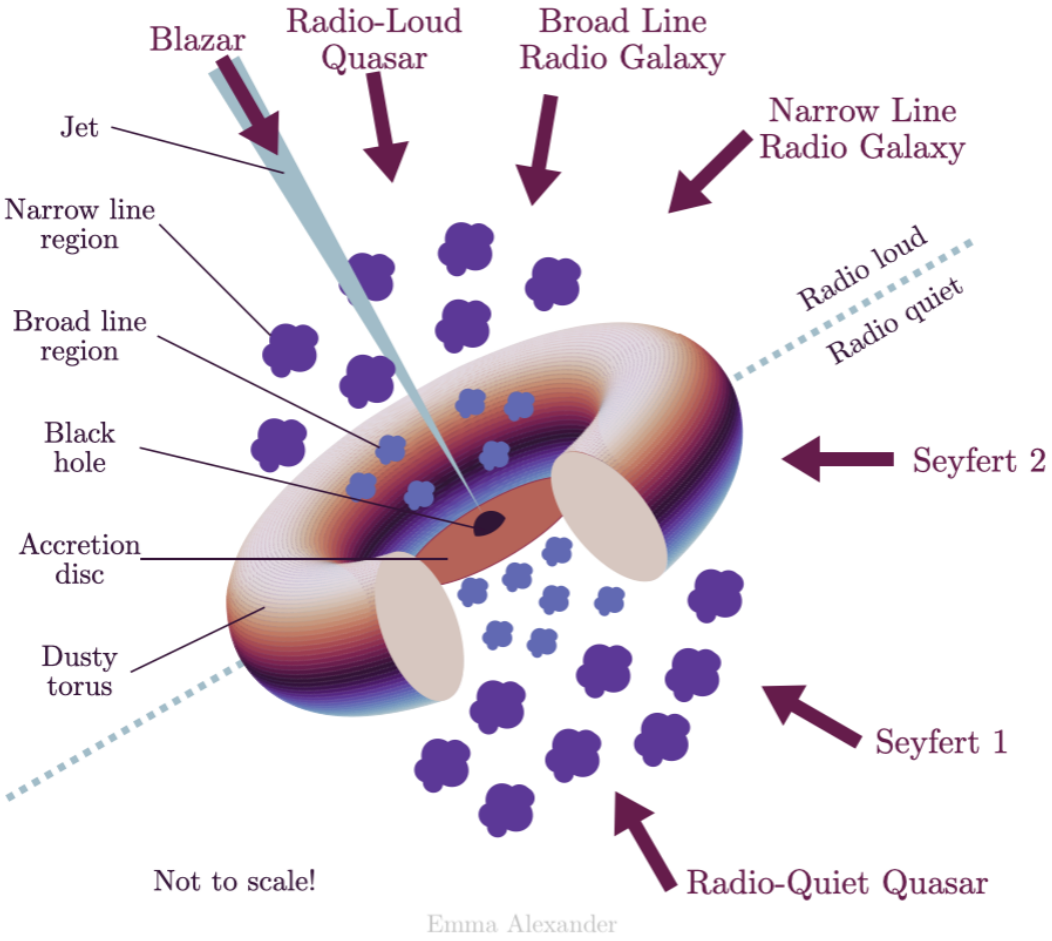

Figure 1.2: Schematic of the AGN unification model, illustrating the key components of an AGN. The central region contains the SMBH, accretion disk, and broad-line region, all surrounded by a dusty torus. Further from the centre are the narrow-line region and a radio jet originating from the central SMBH. The diagram also highlights that the observed type of AGN depends on the observer's viewing angle, e.g., Seyfert 1, Seyfert 2, and blazar. Credit: Emma Alexander.

optically thick but geometrically thin. Encompassing the entire central region is a thick doughnut-shaped dusty torus. Within the torus, an AGN may host a broad-line region (BLR), depending on its current accretion state. The BLR produces broad spectroscopic emission lines due to its proximity to the ionising SMBH, which drives the gas to high velocities and causes these lines to broaden. Beyond the central regions lie the narrow-line region (NLR), where weaker spectroscopic emission lines originate. Additionally, some AGN may host a radio jet depending on the nature of the AGN's radio emission mechanism.

The orientation of an AGN relative the our line of view strongly influences which components we can observe. For instance, when we look directly down the radio jet, the objects is classified as a blazar, exhibiting extremely strong emission at radio wavelengths. If the dusty torus partially or completely obstructs our view of the central regions, the AGN is classified as a Type 2 AGN (or Seyfert 2 in Figure 1.2). In these cases emission from the SMBH, accretion disk, and BLR is largely obscured, while the NLR remains visible. Conversely, if the torus does not obstruct our line of sight, we observe a Type 1 AGN (or Seyfert 1), where both the BLR and NLR are visible. radio-quiet and radio loud AGN, which are both highlighted in Figure 1.2, are discussed in later in this section.

Each component of an AGN emits electromagnetic (EM) radiation at various wavelengths. Figure 1.3 from Harrison (2014) illustrates a typical spectral energy distribution (SED) of an AGN. The black solid line shows the total SED, while the various coloured SEDs represent the contributes from individual components of AGN to the total SED. For the purpose of this discussion, I will only focus on the most relevant components, for full details on the schematic see Harrison (2014).

The dusty torus (red dashed SED) absorbs radiation from the central regions and thermally re-emits at infrared wavelengths primarily in the mid infrared (MIR) and near infrared (NIR). The accretion disk (dashed and dotted blue SED) produces multi-temperature blackbody emission mainly in the optical and ultraviolet (UV), with a substantial contribution in the NIR. The hot corona, consisting of high energy electrons above the accretion disk, energises photons from the disk via inverse Compton scattering producing X-rays, gamma rays, alongside some emission extending into the optical and UV.

Emission from multiple AGN components overlaps extensively across most wave-

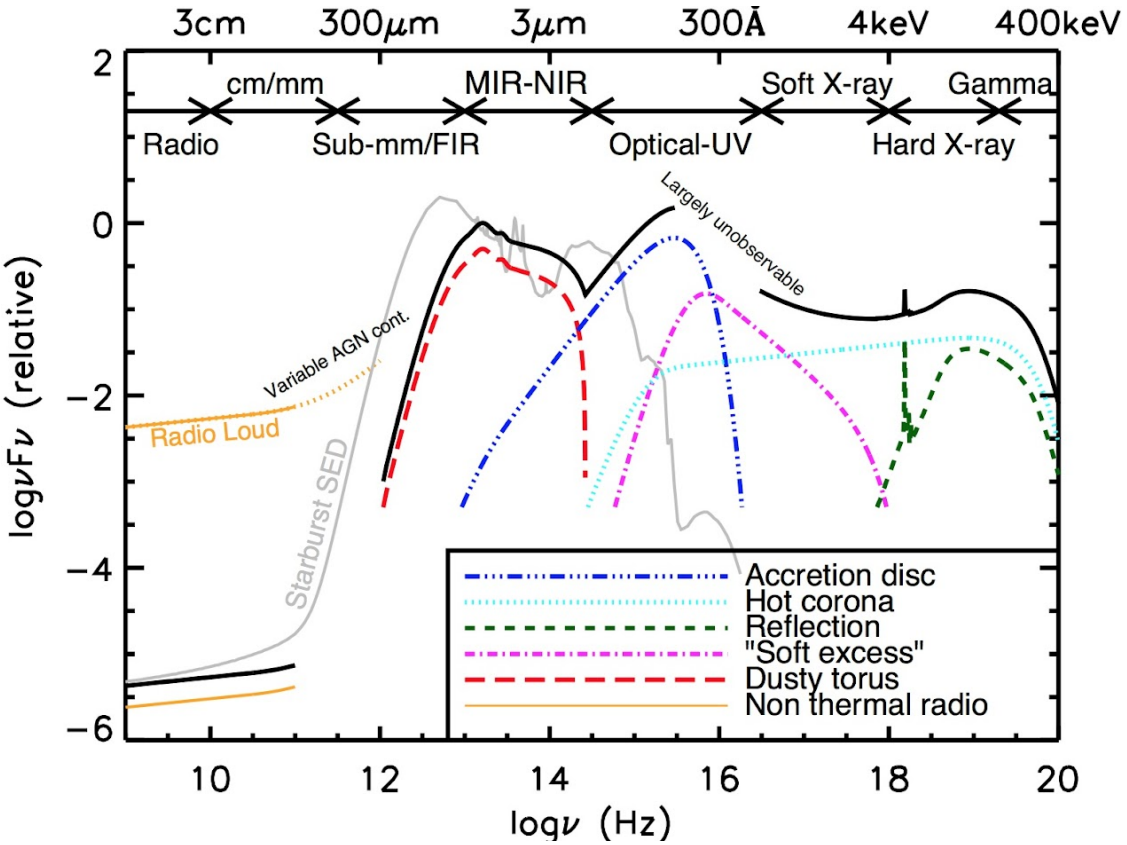

Figure 1.3: Schematic SED of a typical unobscured AGN. The black solid line represents the overall SED, while the coloured line with different styles shows the contributions of individual AGN components, such as the accretion disk and dusty torus, to the total emission. Credit: Harrison (2014).

lengths, making it challenging to individually study components without contamination from others. Interestingly, at the longest wavelengths, in the radio regime, there is no significant contamination from other components. The radio emission arises solely from non-thermal radio processes (yellow solid SED). This makes radio observations a powerful tool for probing the central region of an AGN.

Radio Loud vs radio-quiet

As statistical samples of radio AGN became more common in the late 20th century, it was soon discovered that radio AGN generally fall into two categories: radio-loud and radio-quiet. In early studies, the distribution of the ratio between radio and optical luminosities of sources appeared to be bimodal. One of the first studies to classify this divide was Kellermann et al. (1989), who investigated the radio emission from 91 quasars and 22 AGN using the Very Large Array (VLA) at 5 GHz. Figure 1.4 (Figure 4 from Kellermann et al., 1989) demonstrates this divide in the quasar sample (top) and the smaller AGN sample (bottom) in terms of the radio-loudness parameter, R, defined as the ratio of the radio flux density at 5 GHz to the optical flux density at 4400 Å. In this data, we clearly see a bimodal distribution, with the radio-quiet population lying between $0.1 < R < 10$, while the radio-loud population ranges from $R \simeq 10$ to 100. This led to the traditional cutoff for classifying a source as radio-loud being set to $R = 10$ (Kellermann et al., 1989, 1994).

Over the years, the definition of radio-loudness has became blurred, with multiple criteria used to classify AGN as radio-loud. Some researchers define a radio-loud AGN based on the presence of a radio jet (e.g., Padovani, 2016; Padovani et al., 2017), while others continue to use the definition of radio-loud AGN to be when the ratio of radio to optical emission exceeds a certain threshold, (e.g., Cirasuolo et al., 2003; Liu et al., 2021; Keller et al., 2024). In addition, some studies adopt ratios using other bands, or even [O III] luminosity, instead of optical (e.g., Xu et al., 1999; Zakamska & Greene, 2014; Klindt et al., 2019; Gupta et al., 2020), further highlighting the diversity of definitions in the literature.

However, as radio instrumentation has improved, the apparent bimodality in radio-loudness has become less pronounced (e.g., Cirasuolo et al., 2003; Baloković et al.,

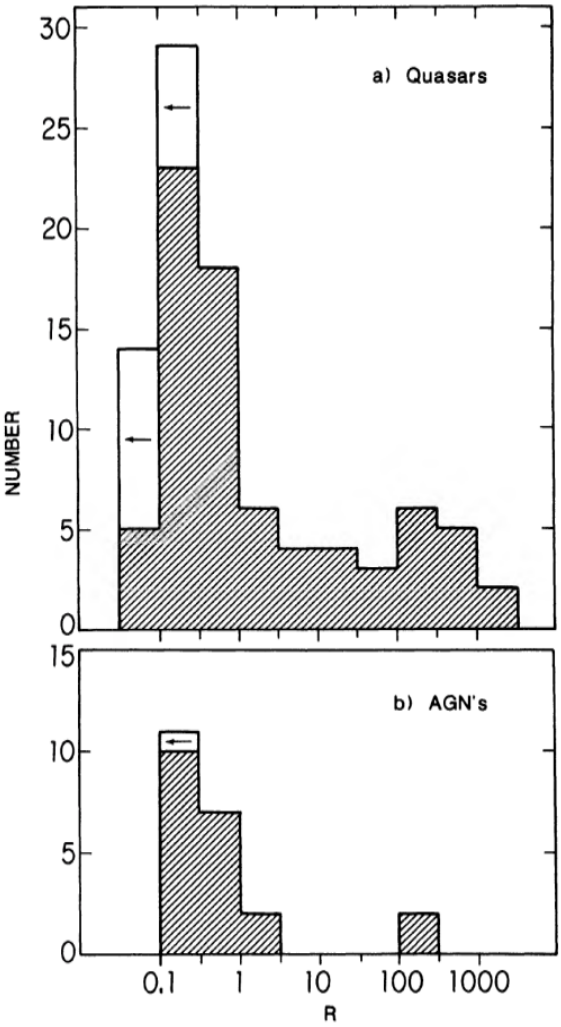

Figure 1.4: Distribution of the radio-loudness parameter, R, for quasars (top) and AGN (bottom). These distributions demonstrate a bimodality in R, with radio-loud AGN lying above $R = 10$. Credit: Kellermann et al. (1989)

2012; Gürkan et al., 2019). Macfarlane et al. (2021) modelled the radio luminosity distribution of around 42,000 Sloan Digital Sky Survey (SDSS) quasars using the highly sensitive LOFAR (LOw Frequency ARay) Two-Meter Sky Survey (LoTSS; Shimwell et al., 2017, 2019, 2022). A key result from this study is shown in Figure 1.5, which plots radio-loudness ($\log(L_{5GHz}/L_{4400})$) as a function of jet dominance ($\log(L_{AGN}/L_{SF})$) for a modelled distribution. In this figure we see the traditional $R = 10$ boundary, as well as a dividing line where AGN-driven emission equals that from star formation, above which sources are considered jet dominated. Under the classical framework, radio-loud AGN are expected to be both jet dominated and have a high radio-to-optical flux density ratio. Interestingly, Macfarlane et al. (2021) identified a population of sources that are jet dominated but have a low radio-to-optical ratio, i.e., they appear radio-quiet by traditional standards. This highlights that as radio sensitivity improves, the dichotomy between radio-loud and radio-quiet AGN becomes increasingly blurred. With current facilities, the radio community should reconsider the traditional binary classification and move toward a new definition. A straightforward method to move beyond this binary definition is to introduce additional thresholds, allowing for more discrete populations, such as a radio-intermediate class, however this still relies on the radio-loudness definition to some extent (e.g., Yue et al., 2025).

Radio excess has become a common method for separating AGN with powerful radio emission from those with weaker radio emission (e.g., Delvecchio et al., 2017; Best et al., 2023). This approach typically involves comparing the star formation rate (SFR) to the observed radio luminosity and estimating the maximum level of radio emission that can be produced by star formation alone, often allowing for some intrinsic scatter in the correlation. Sources that lie above this threshold are classified as radio excess AGN, where the radio emission cannot be attributed solely to star formation and is instead interpreted as being powered by a powerful radio jet. However, the origin of radio emission for sources below this threshold remains less clear, as their radio emission may still be partly or entirely driven by star formation or other AGN-driven mechanism.

We can also disentangle the AGN contribution from star formation in radio detected AGN to better understand where sources lie within the overall population. For instance, Yue et al. (2024) developed a parametric Bayesian model that decomposes the radio flux

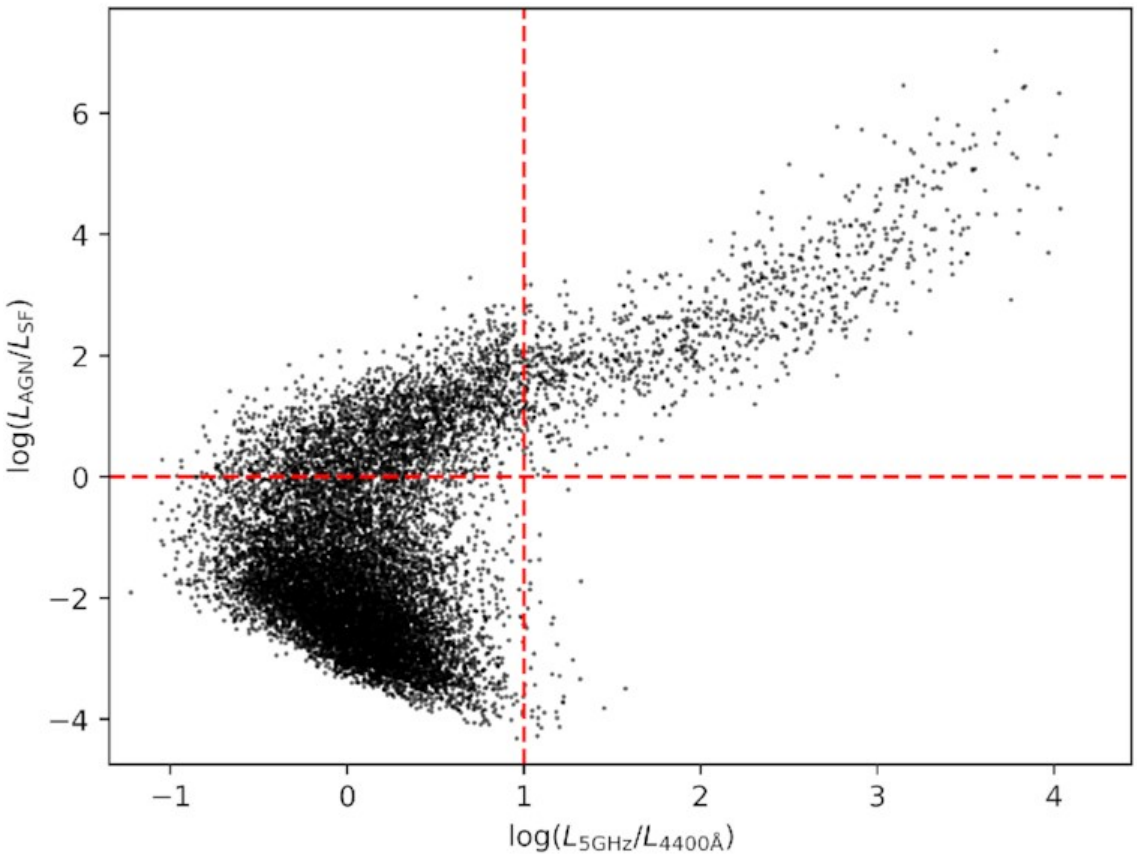

Figure 1.5: The logarithmic relationship between radio-loudness ($L_{5\,\mathrm{GHz}}/L_{4400\,\text{Å}}$) and jet dominance ($L_{\mathrm{AGN}}/L_{\mathrm{SF}}$). The traditional radio-loudness divide is marked at log R = 1, while the horizontal divide at $\log(L_{\mathrm{AGN}}/L_{\mathrm{SF}}) = 0$ indicates the transition to AGN-dominated jets. This illustrates that, for this population of modelled data points, radio-quiet AGN can, in fact, be jet dominated. Credit: Macfarlane et al. (2021).

density into AGN and star forming components using redshift and bolometric luminosity constraints for the entire population at once, thereby providing insight into the relative contributions of AGN and star formation to the radio emission, rather than focusing on individual galaxies. Another approach relies on brightness temperature measurements to diagnose the AGN emission from star formation (Morabito et al., 2022a, 2025b). Brightness temperature, T_b, is a non-physical temperature and represents the temperature a black body would require to replicate the observed surface brightness of a source. Since star formation can only generate a maximum brightness temperature, any measured T_b above this value must be AGN-driven. This provides a robust diagnostic to separate star formation from AGN emission. Therefore, moving forward, the community should shift away from the simplistic binary classification of radio-loud verse radio-quiet AGN and instead focus on disentangling the physical origin of radio emission. Approaches such as parametric modelling of AGN and star formation contributions, or diagnostics based on brightness temperature measurements, provide more physically motivated pathways to classify and understand the populations of radio AGN.

Radio Mechanisms

Only around 10% of radio AGN in our Universe are classified as radio loud, meaning the majority of AGN are radio-quiet. The origin of radio emission from radio-loud AGN is universally attributed to radio jets. Perhaps the most famous examples of radio-loud AGN are the so-called "A-Team" sources, which are among the brightest radio sources in the sky. One such example is Hercules A, the brightest radio source in the Hercules constellation. The powerful radio jet hosted by this AGN is presented in Figure 1.6 at 144 MHz with a resolution of 0.547×0.234 arcseconds (Timmerman et al., 2022).

In the past, radio AGN studies were limited to powerful radio-loud AGN and local radio-quiet AGN due to sensitivity limitations. This is no longer the case thanks to advancements in radio instrumentation, allowing much deeper radio surveys. One key instrument enabling this progress is the International LOFAR Telescope (ILT). Best et al. (2023) demonstrates that LOFAR's high sensitivity allows us to probe radio-quiet AGN out to redshifts beyond 5, expanding the observable population of radio AGN.

With the growing number of radio-quiet sources which are observable, understanding

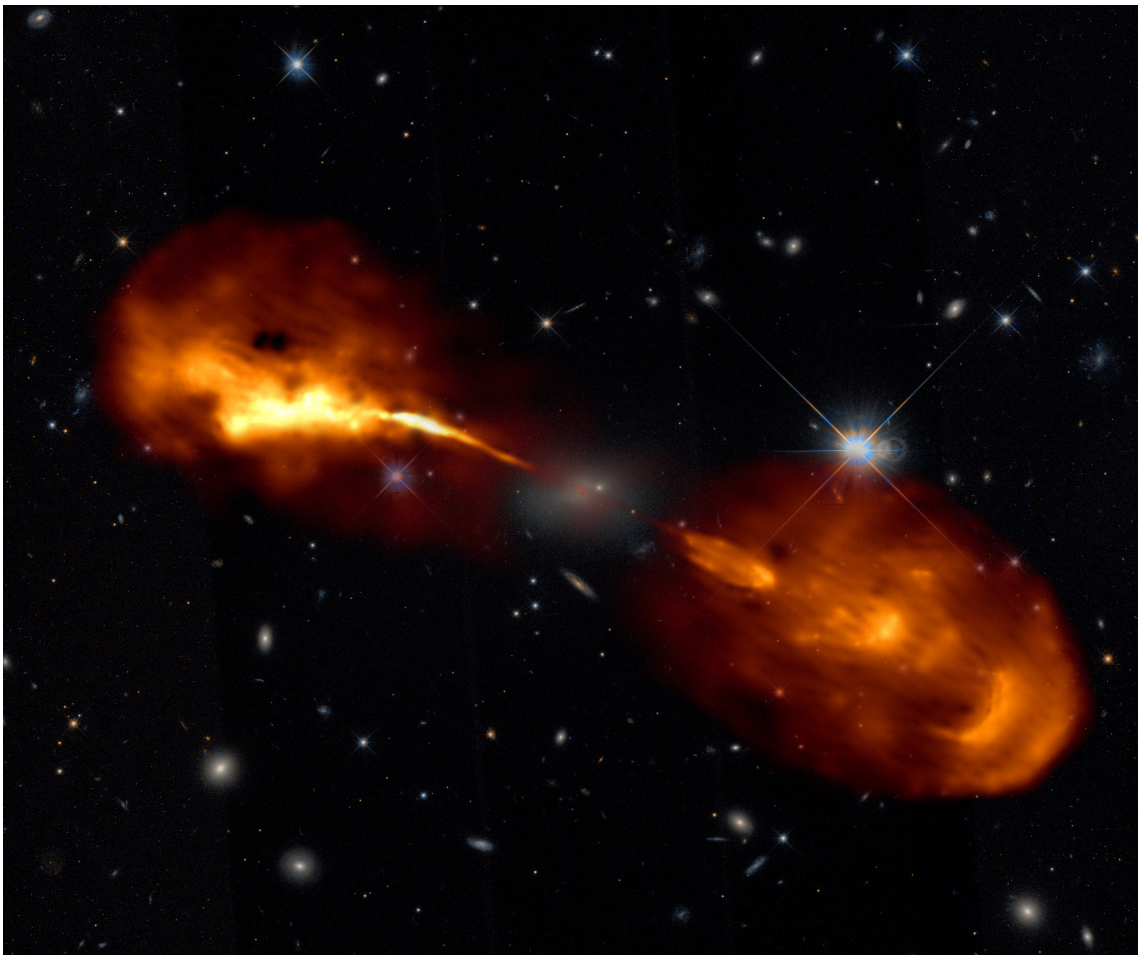

Figure 1.6: Sub-arcsecond resolution radio image of Hercules A at 144 MHz obtained with the ILT, overlaid on optical counterparts from the Hubble Telescope. This radio galaxy hosts one of the most powerful radio jets in the sky and is a poster child of radio-loud AGN. Credit: R. Timmerman.

the origin of radio emission from radio-quiet AGN has become a key focus in AGN studies. In the radio-quiet regime, there is currently no consensus on the relative contribution of radio mechanisms producing the radio emission in radio-quiet AGN. As summarised in Panessa et al. (2019), potential contributors include high or low powered jets, AGN driven winds, star formation or coronal emission. Coronal regions are relatively low luminosity (e.g., Padovani et al., 2017), and thus are not generally considered a significant contributor to the the radio emission from radio-quiet AGN. Diffuse emission from star formation (e.g., Bonzini et al., 2015; Delvecchio et al., 2017; Padovani, 2016), shocks produced by AGN-driven winds (e.g., Zakamska & Greene, 2014; Petley et al., 2022), and radio jets (e.g., Jarvis et al., 2021; Njeri et al., 2025) remain viable candidates, and some studies suggest that AGN-driven processes dominate the radio emission of these radio-quiet sources (e.g., White et al., 2015; Ruiz et al., 2016).

To better understand the origin of radio emission in radio-quiet AGN, spatially resolved radio morphologies are essential to link observed morphologies to physical mechanisms. At relatively low resolution, we can identify whether large-scale radio jets dominate the radio emission. However, detecting low-powered jets requires high resolution imaging to resolve their structure. Star formation occurs on larger, kpc, scales, allowing it to be studied at low resolution, but it is challenging to disentangle star formation from AGN emission at these scales. It is currently not fully understood how uncollimated, diffuse winds manifest at radio wavelengths, and therefore it is unclear how to detect them. This highlights the need for simulations and models (e.g., Nims et al., 2015; Xia et al., 2025) to investigate the spatial extent of this emission across different frequencies and resolutions.

We can further our understanding of the origin of radio emission by utilising brightness temperature measurements which allows us to disentangle star formation emission from AGN-driven emission. To fully exploit brightness temperature, we require high-resolution images that reveal compact morphologies, particularly in cases where morphological information alone is insufficient to determine the emission mechanism.

Therefore, to determine the origin of radio emission, we require high resolution imaging capabilities to obtain resolved radio morphologies for large numbers of galaxies, as well as informative brightness temperature measurements. With this information, we can begin to question: is there a physical mechanism driving AGN outflows? What are the

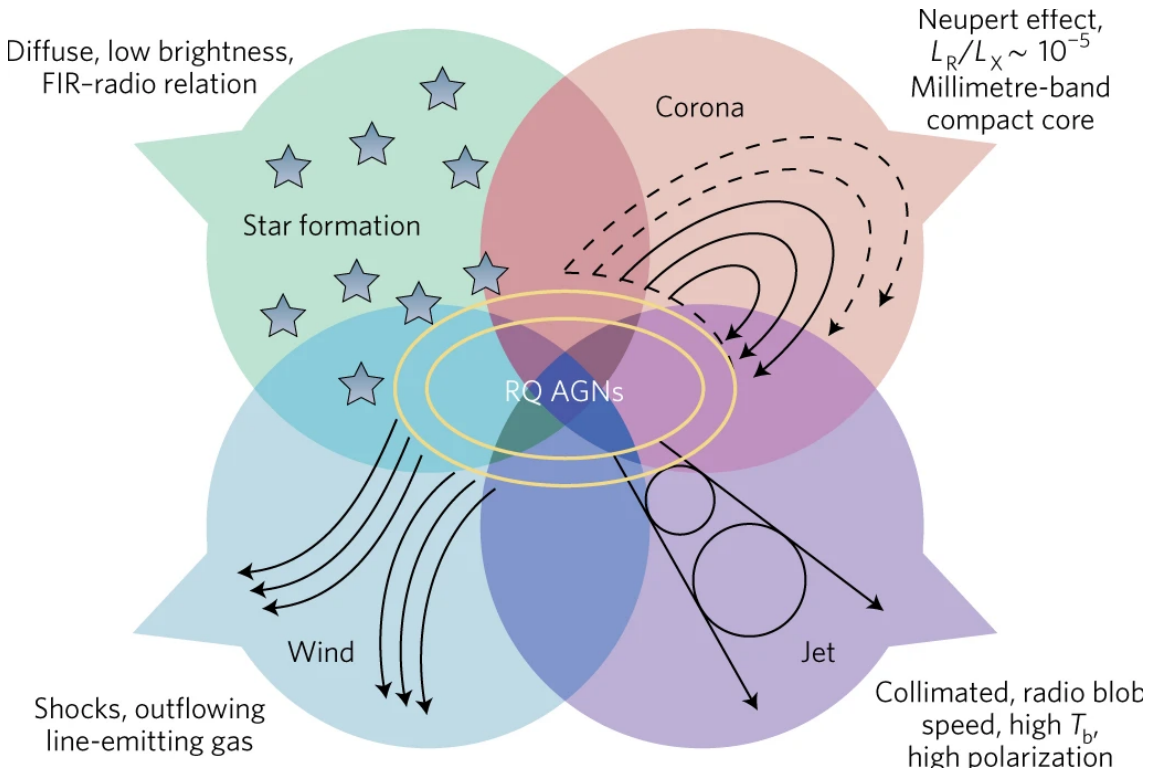

Figure 1.7: Schematic demonstrating the possible main physical mechanisms driving the radio emission from radio-quiet AGN. Credit: Panessa et al. (2019).

contributions of different radio emission mechanisms to the radio emission in radio-quiet AGN?

1.1.3 Multi-phase Outflows

AGN outflows are a key mechanism for driving AGN feedback. These outflows can extend into the host galaxy on kpc scales (Harrison et al., 2014), injecting energy into the surrounding medium and altering the galaxy's evolution. Outflows are multi-phase in nature with four main types identified: hot ionised outflows, warm ionised outflows, neutral atomic outflows, and cold molecular outflows (see, Harrison & Almeida, 2024, for a review).

Hot ionised outflows can reach temperatures between 10^5 K and 10^8 K, making these outflows accessible in the X-ray regime, and have high densities between 10^6 cm^{-3} and 10^8 cm^{-3}. UFOs (ultrafast outflows; Tombesi et al., 2010) are a type of hot ionised outflow, which appear as extremely fast winds reaching velocities up 0.1 c (Gofford et al., 2015). These outflows can be analysed through strongly blueshifted Fe K absorption

lines and are launched from regions of the AGN accretion disk as close as 0.1 pc to the central black hole (Tombesi et al., 2010). A somewhat weaker form of outflowing hot gas is produced by warm absorbers (WAs) which are present in roughly 60% of Seyfert galaxies (Tombesi et al., 2013). WAs can been observed in the soft-X-ray and UV bands. Hot ionised outflows show higher ionisation and outflow velocities the closer they are to the central SMBH (Tombesi et al., 2013). UFOs have also been found to coexist with narrow absorption lines in the UV, suggesting that this phase of outflow occurs on micro-scales (Chartas et al., 2021). Studying these hot ionised outflows in large samples can be challenging, particularly because AGN variability in the X-ray regime (e.g., Gibson & Brandt, 2012; Lanzuisi et al., 2014) introduces additional complexities. Furthermore, due to instrumentation limitations, observations of these hard-X-ray outflows are largely confined to the nuclear regions, despite models predicting that hot gas can be produced on kpc scales (Nims et al., 2015) through shocks.

Warm ionised outflows exhibit temperatures in the range 10^3 K $< T_k < 10^5$ K, where T_k is the temperature of the gas, and densities of 10^2 cm^{-3} $< n_{gas} < 10^5$ cm^{-3}, where n_{gas} is the gas density. This phase of outflowing gas can be detected through emission line profiling in the UV, optical, and NIR, with the specific rest-frame wavelengths depending on an object's redshift. A widely used tracer of warm ionised outflows is the [O III] emission line. The study of this emission line, and therefore the warm ionised phase of outflows, is the main topic of this thesis. Thanks to large spectroscopic surveys such as SDSS, warm ionised outflows have been studied in thousands of low redshift AGN (e.g., Mullaney et al., 2013; Molyneux et al., 2019). Even larger, statistically significant studies are now possible thanks to the Dark Energy Spectroscopic Instrument (DESI; DESI Collaboration et al., 2025), which provides spectroscopic information for over a million quasars. One challenge in studying this outflow phase is understanding its energetics. Many of the emission lines we utilise as tracers can be contaminated by metallicity, extinction, or star formation (see, Harrison et al., 2018, for a review), complicating their interpretation. As a result, many studies have focused primarily on the kinematics of these tracers to infer AGN outflow properties (e.g., Mullaney et al., 2013; Karouzos et al., 2016; Wylezalek et al., 2020), while energetic measurements have often been reported with large uncertainties (e.g., Smethurst et al., 2019; Gofford et al., 2015).

Broad absorption line quasars (BALQSOs) can also trace gas outflows through the broad absorption lines (BALs) observed in their spectra. These BALs arise from high velocity, disk-driven winds, producing complex absorption structures. These absorption lines are primarily associated with highly ionised emission lines, most commonly C IV, and these are referred to as HiBALs. However, lower ionisation lines, such as Mg II, can also exhibit absorption. If such low-ionisation features are present, these are commonly known as LoBALs, which account for only around 10% of the BALQSO population. BALQSOs are linked to enhanced radio emission, showing a higher radio detection fraction compared to non-BALQSOs (Morabito et al., 2020; Petley et al., 2022), independent of optical colour or C IV distance (Petley et al., 2024). Additionally, BALQSOs are weaker in the X-ray regime relative to non-BALQSOs (e.g., Clavel et al., 2006; Morabito et al., 2014), suggesting that the observed differences between BALQSOs and non-BALQSOs are intrinsic rather than solely due to orientation effects.

Atomic outflows are neutral in nature, with relatively lower temperatures of 10^2 K $< T_k <$ 10^3 K, and densities of 10^1 cm^{-3} $< n_{gas} <$ 10^2 cm^{-3} (see Harrison & Almeida, 2024, for a review). These outflows can probe emission ranging from pc to $\sim$ Mpc scales. Common tracers of this neutral gas include neutral hydrogen (HI), the sodium doublet absorption line (Na I D), and [C II]. The fastest atomic outflows are typically observed via HI absorption lines. For instance, Morganti et al. (2005) reports HI outflows reaching velocities of $\sim$1000 km s^{-1} on kpc scales. In a sample of 101 radio-selected sources at 1.4 GHz, Geréb et al. (2015) find an HI outflow detection rate of 5%, with an overall HI detection rate of 30%. These HI outflows can reach mass outflow rates of up to 30 M$_\odot$ yr^{-1}. In a larger sample of 691 radio galaxies, Lehnert et al. (2011) find that a third show a significant excess of Na D absorption, indicating the presence of neutral atomic outflows. Studies of neutral atomic gas have also provided insights into the behaviour of individual bright objects; for example, Rupke & Veilleux (2011) discover an atomic outflow with a velocity of $\sim$1100 kms^{-1} in Mrk 231, traced with Na I D using integral field spectroscopy (IFU) data obtained with Gemini. The examples demonstrate that the atomic phase of outflows is important for building a complete picture of multi-phase outflow properties and their contribution to AGN feedback.

Finally we come to the coldest phase of outflows: molecular outflows, with tem-

peratures 10^1 K $< T_k <$ 10^3 K and densities exceeding 10^3 cm^{-3}. The hotter end of molecular outflows can be traced in the NIR by H_2 lines, while warm molecular gas can be studied in the MIR. Far-infrared (FIR) observations of OH (hydroxyl) transitions also probe these molecular outflows, but the most commonly used tracers are the transitions of carbon monoxide (CO). Starburst galaxies, with their high H_2 fraction, are often targeted to detect CO and/or OH emission lines in order to study molecular outflows. However, long exposure times are required to detect the faint, diffuse emission that may contain the bulk of the outflowing mass (Cicone et al., 2018). The CO(1-0) transition is the most commonly used tracer of molecular outflows, as it represents the lowest energy transition of CO, making it relatively easy to excite and well-suited for probing diffuse, cold, and extended gas. Higher-order transitions (e.g., CO(2-1) and CO(3-2)) can also trace molecular outflows but typically correspond to denser or warmer gas phases. CO emission is generally observed in the millimetre and sub-millimetre regimes, with Atacama Large Millimeter/submillimeter Array (ALMA) being a leading facility for such studies (e.g., Holden et al., 2024; Sun et al., 2014; Baug et al., 2021). Molecular outflows can have a substantial impact on their host galaxy, with mass-loss rates often comparable to those of ionised outflows (Fiore et al., 2017).

We can probe gas emission across multiple outflow phases that occur on a wide range of spatial scales, from sub-pc regions near the SMBH to galactic scales. For example, connecting the energetics of hot ionised winds that arise on nuclear scales with the larger-scale outflows traced by warm ionised or molecular gas is essential for understanding how energy is transferred throughout a galaxy. Outflows therefore provide a powerful tool for investigating AGN feedback. While each phase of outflow has been extensively studied in the literature, most studies focus on a single gas phase or restricting these multi-phase outflows to a single source (e.g., the "Teacup" galaxy; Harrison et al., 2015; Lansbury et al., 2018; Venturi et al., 2023; Audibert et al., 2023). Consequently, it remains unclear how the different phases are physically connected, for instance, whether they represent distinct evolutionary stages that AGN cycle through, or whether they co-exist and interact simultaneously. Thus, we have an incomplete understanding of how these outflow phases are interconnected. Only a handful of AGN, often through detailed single object analysis, have been studied across multi-phase (e.g., Tadhunter et al., 2014; Fiore et al., 2017;

Husemann et al., 2019; Fluetsch et al., 2021; García-Bernete et al., 2021). However, to determine whether the observed phases represent distinct evolutionary stages of AGN outflows, or instead are coexisting phenomena, large statistical samples are required. Achieving such analysis has so far proven difficult. Even for a single target, multiple telescope proposals are needed to probe all the phases of outflows, and the data reduction and consequent analysis demand substantial observation times and human effort. As a result, comprehensive multi-phase studies remain rare, leaving the broader picture unclear.

[O III] Outflows

In the following section, we narrow our focus to a detailed discussion of one specific phase of these multi-phase outflows: the warm ionised outflows. A widely used tracer for warm ionised gas outflows is the [O III] λ5007 Å emission line. William Huggins was the first to identify what we now know as [O III]. In 1864, Huggins became the first person to obtain a spectroscopic measurement of a planetary nebula. On August 29 of that year, he targeted the planetary nebula then referred to as "Draco". He described its appearance as *"very bright; pretty small; suddenly brighter in the middle, very small nucleus"*. This nebula is now known as the Cat's Eye. In its spectrum, Huggins noted the presence of *"three bright lines"* which he attributed to *"the presence of nitrogen, hydrogen and a substance unknown"* (Huggins & Miller, 1864). Many years later, in 1918, W. H. Wright at Lick Observatory identified the "unknown" spectral feature as a doublet with wavelengths λ4959 and λ5007 Å (Wright, 1918). After many scientists attempted and failed to reproduce these lines in laboratory conditions, it was initially hypothesised that they originated from a new element, dubbed "Nebulium". This theory was short lived, as Bowen (1927) resolved the mystery by demonstrating that the doublet arises from doubly ionised oxygen. Specifically, the λ5007 Å transition corresponds to ^{3}P2 → ^{1}D2, while λ4959 Å arises from the ^{3}P1 → ^{1}D2.

The [O III] emission line remained a mystery for many years because it is what we now recognise as a forbidden emission line. Such lines require low-density environments, where excited ions can undergo spontaneous radiative decay rather than being collisionally de-excited. In lab conditions on Earth, densities are too high, so de-excitation occurs almost exclusively through atomic collisions, rendering these transitions as "forbidden",

thus explaining why scientists could not reproduce this emission line in lab experiments. By contrast, astronomical environments provide the opportunity for these forbidden lines to manifest. Forbidden transitions are conventionally denoted by square brackets, with other common examples including [N II] λ6583 Å and [S II] λ6716 Å λ6731 Å.

As previously mentioned, [O III] can trace warm ionised outflows, however, its mere presence is not necessarily indicative of an outflow, as most AGN exhibit [O III] in their spectra. The presence of a broad, blueshifted shoulder attached to the [O III] emission line is the primary diagnostic used to determine whether an AGN is undergoing an outflow (Greene & Ho, 2005). The [O III] line is influenced by both gravitational and non-gravitational components. The gravitational component depends on the host galaxy, specifically the virial motion of the gas within it. This is why a narrow [O III] λ5007 line is present in the majority of galaxy spectra, unless significantly obscured or said galaxy is red and dead where there is no star formation or AGN activity. The non-gravitational component, on the other hand, produced the broad, blue-shifted shoulder that signifies an outflow, as this gas has exceeded the escape velocity of the host galaxy and is no longer gravitationally bound.

Both components can be modelled using Gaussian profiles, and if two Gaussians are required to fit [O III] λ5007, it indicates that the AGN is hosting an outflow. Occasionally, the broad component of [O III] can dominate over the narrow component due to the strength of the non-gravitational component. In such cases, fitting two Gaussian components does not provide the best fit, however an outflow may still be present, but would not be detected. Consequently, alternative metrics are required to confirm the presence of [O III] outflows. A widely used non-parametric measurement is W_{80}, which quantifies the width of the emission line that contains 80% of the flux. Very broad emission line profile cannot be produced by gas gravitationally bound to the host galaxy, whether in the NLR or star forming regions. Thus, AGN with [O III] $W_{80} > 800$ km s^{-1} are considered to definitely host an outflow (Harrison et al., 2014), while sources with 600 km s^{-1} $< W_{80} <$ 800 km s^{-1} are likely to host an outflow. Together, the W_{80} measurements and the presence of a broad, blue-shifted shoulder provide robust diagnostics of AGN outflows.

Optical Spectroscopy

We have discussed that the study of multi-phase outflows relies on spectroscopic measurements to understand the behaviour of emission lines and, in turn, trace outflows. In particular, optical spectroscopy is often utilised, especially for [O III] studies as the λ5007 Å line can be readily observed at relatively low redshifts. At higher redshifts, this emission line shifts into the infrared. This thesis focuses on AGN with $z < 1$ and therefore, the following discussion of instrumentation will concentrate on optical spectroscopy.

The Sloan Digital Sky Survey (SDSS; York et al., 2000) is based at the Apache Point Observatory in New Mexico, which provides millions of spectroscopic measurements across the northern sky. As this is a multi-phase project, the data quality has evolved across its various data releases due to instrumental upgrades. SDSS spectroscopic measurements have been conducted through three main instruments: the original SDSS spectrometer (utilised in SDSS-I and SDSS-II; York et al., 2000), the Baryon Oscillation Spectroscopic Survey (BOSS; Dawson et al., 2016) instrument (SDSS-III; Majewski et al., 2017), and more recently the extended BOSS (eBOSS; Dawson et al., 2016) spectroscopic survey (SDSS-IV and SDSS-V; Blanton et al., 2017; Kollmeier et al., 2017). The original spectrometer covered a wavelength range of 3800-9200 Å, which was expanded to 3650-10400 Å with BOSS, operating at a resolution of 1500 at 3800 Å and at 2500 at 9000 Å.

Each release of an SDSS program is accompanied by a corresponding quasar catalogue. The most recent of these is DR16Q (Lyke et al., 2020), which contains 750,414 quasars, including 225,082 new detections not present in previous data releases. The spectroscopic measurements performed by BOSS are fitted using three models representing the possible spectral types: star, galaxy, or quasar (QSO). A source is classified as a QSO if three criteria are met: (1) the best fitting model corresponds to a QSO, (2) only one model fits the spectrum as a star, and (3) no SDSS spectral warnings are present (i.e., `ZWARNING=0`). Additionally, some spectra are confirmed as QSOs through visual inspection.

A major milestone in spectroscopy was recently achieved with the publication of the first data release of the Dark Energy Spectroscopic Instrument (DESI; DESI Collaboration et al., 2025). DESI, mounted on the four-meter Telescope at Kitt Peak National Observatory in Arizona, aims to produce a 3D map of the Universe to study dark energy. Beyond this primary goal, DESI is also a powerful resource for quasar science, providing

tens of millions of spectroscopic measurements across the northern sky. The five-year spectroscopic survey began in May 2021, and DR1 presents the first 13 months of observations. Within this small period, the survey includes 18.7 million objects, of which 1.6 million are quasars, making it a valuable resource for quasar studies.

DESI is equipped with 10 spectrographs, each containing three cameras that cover different spectral ranges and resolutions, covering a total spectral range of 3600-9824 Å. Camera B observes between 3600-5800 Å with a resolution of 2000-3500, Camera R spans 5760-7620 Å at a resolution of 3400-4800, and Camera Z covers 7520-9824 Å with a resolution of 3800-5200 resolution. Compared to SDSS, DESI provides greater sky coverage and target density, enabling more statistically robust studies of quasar spectroscopy.

1.1.4 Connection between [O III] and Radio

The [O III] λ5007 Å emission line serves as a powerful probe of ionised gas outflows. Notably, the properties of this emission line have been strongly linked to the radio characteristics of the host galaxy. This correlation between radio and [O III] emission was first presented by Rawlings et al. (1989), who studied a sample of 39 radio galaxies at $\leq$0.5. Using the total radio luminosity at 178 MHz they found a Spearman rank correlation of 0.51 between the radio luminosity and [O III] luminosity, demonstrating that these two properties are intertwined. Another pioneering study linking [O III] emission to radio emission was conducted by Mullaney et al. (2013), who used SDSS spectroscopy to compile a statistically robust sample of 24,264 optically selected AGN. Through spectral stacking analysis, they found that [O III] emission is most strongly influenced with the radio luminosity at 1.4 GHz, more so than with bolometric luminosity, Eddington ratio, optical class, or radio loudness, confirming the connection between radio activity and [O III] emission. Interesting, Mullaney et al. (2013) found that AGN with moderate radio luminosities (10^{23} W Hz^{-1} < $L_{1.4\ \mathrm{GHz}}$ < 10^{25} W Hz^{-1}) exhibit the broadest [O III] profiles. At higher redshifts, Zakamska et al. (2016) studies a sample of four extremely red quasars (objects linked to enhanced radio properties; Klindt et al., 2019), at z ∼2.5 using XSHOOTER, finding very broad and strongly blue-shifted [O III] outflows. Similarly, at $z < 2$, Nesvadba et al. (2017b) demonstrated that the [O III] kinematics of 33 radio galaxies are complex in all cases, highlighting the strong influence of radio activity on ionised gas

dynamics. Furthermore, peaked radio AGN exhibit broader outflowing [O III] components than low-frequency radio AGN without a spectral peak, as revealed by stacking analysis of SDSS spectra in Kukreti et al. (2023), hence linking enhanced [O III] outflows to young radio AGN. Radio emission has also been connected to [O III] through spatially resolved spectroscopy. For example in the "Teacup" galaxy radio emission is seen to be co-spatial with [O III] emission (Harrison et al., 2015). Additionally, both Jarvis et al. (2019) and Girdhar et al. (2022) show that jets appear to drive bi-conical [O III] outflows. Despite the stacking evidence supporting the link between radio and [O III] emission, Woo et al. (2016) argued that the enhancement in [O III] with radio luminosity could instead be driven by host galaxy properties. More recently, however, Ayubinia et al. (2023) demonstrated that radio activity does indeed contribute to the enhanced kinematics after controlling for stellar velocity dispersion. Therefore, in the literature we are seeing substantial evidence that the [O III] λ5007 Å emission line is significantly influenced by the radio properties of its host galaxy.

1.2 Radio Astronomy

The longest wavelengths in the electromagnetic spectrum are radio waves. These are the least energetic waves in the EM spectrum and have much lower frequencies than other regions of the EM spectrum. As a result, radio waves can penetrate Earth's atmosphere and can be observed from the ground, while other higher frequency waves are absorbed or reflected back into space. Observing these higher frequency waves required advanced space-based observational facilities. In contrast, radio waves can be studied using ground-based facilities, making them much more accessible to astronomers. Consequently, following the development of optical astronomy, radio observations became the next frontier for exploring and understanding our Universe.

1.2.1 History of Radio Astronomy

It was Karl Jansky in 1932 who was first to turn his attention to the radio sky. Thanks to his expertise in both physics and engineering, he built the first radio telescope which was located at Bell Laboratory, which soon became known as "Jansky's merry-go-round",

due to its circular rotational movement. The antenna operated in the decimetre regime at 20.5 MHz and was fully rotational thanks to being mounted on four wheels taken from a Ford Model-T (AAS, 2018), the first mass-produced auto-mobile. This historical context highlights the remarkable nature of Jansky's achievement situating it at a pivotal moment in both technological advancements and the history of humanity.

Jansky detected a faint hiss from his merry-go-round, which appeared to fade in and out over the course of a day. Naturally, due to its daily pattern, Jansky initially assumed this signal originated from the Sun. However, after months of observations, he noticed that the location of the hiss changed over time. With the help of fellow astronomer Albert Skellett, the pair determined that the period of the signal's variations matched a sidereal day, not a solar day. Much like modern day astronomy, multiwavelength analysis revealed the source of this mysterious static: it was the Milky Way (Jansky, 1933). The next major milestone in radio astronomy was the construction of the first parabolic dish telescope, built by Grote Reber in his own back garden in Illinois. Using this telescope, Reber conducted and published the first systematic radio survey of the sky, achieving a beamwidth of 16$\circ$ at 150 MHz (Reber, 1944).

Scientific and technical progress came to a standstill during the Second World War. However, unlike many other disciplines, radio astronomy benefited particularly from one technological advancement of the war: radar. This technology, originally developed for detecting and tracking the enemy, could be adapted to study celestial radio objects. Furthermore, the war spurred increased interest and, most importantly, investment in the field, ultimately leading to significant advancements in radio astronomy.

Another consequence of the war that spurred progress in radio astronomy was the introduction of a new workforce: women. With men on the frontlines, women stepped into roles previously unavailable to them, enabling countries to continue functioning while also contributing significantly to the war effort from afar. Women were not only recruited for manual labour in factories producing military supplies, but their intellect was also put to use in research facilities, developing innovative solutions to help end the war.

One of the many notable women whose contributions during the war influenced the progress of humankind was the underappreciated genius Hedy Lamarr. Lamarr co-invented a technique that is now fundamental to modern wireless communication:

frequency hopping, in which the radio wave's frequency rapidly changes between the transistor and receiver while the signal remains synchronised. This technique was designed to prevent enemy interception of critical US radio transmissions. However, this technique was not implemented during the war, but Lamarr's invention did not go to waste. In 1992, a team of scientistic and engineers led by John O'Sullivan at the Commonwealth Scientific and Industrial Research Organisation (CSIRO) in Australia overcame a major problem faced by radio astronomers: how to process distorted signals produced by interferometric systems. By applying Lamarr's frequency hopping technique, the team developed a solution that they later patented and sold to major technology companies. This eventually became what we now know as Wi-Fi. Despite proving her potential as a world class inventor, once the armistice was announced, Lamarr returned to her pre-war career, forcing her to conceal her genius by continuing life as a Hollywood actress. During her acting career, Lamarr was often described as *"the most beautiful woman in the world"*. Yet Lamarr had complex feelings towards her beauty, famously remarking, *"My beauty is my biggest curse"*. Lamarr was an extraordinary inventor with a brilliant mind, yet, like many women, her intellect was overshadowed by her appearance.

Another brilliant mind brought to light by the female war effort was Ruby Payne-Scott. During the war, Payne-Scott specialised in radar technology at the Radiophysics Laboratory at CSIRO. Unlike Lamarr, she was able to continue in a related scientific field transitioning her expertise to solar physics. In 1946, Payne-Scott and her team discovered that radio bursts originate from solar hot spots, a phenomena that could not be observed using traditional radio telescopes. Thanks to the laboratories location at Dover Heights, Sydney, the team set up Second World War Yagi antennas along the coast and aimed them at the Sun. These antennas captured both direct waves from the Sun and secondary signals reflected off the ocean past the cliff face. The direct and secondary reflected signals then constructively interfered, enhancing the signal and providing higher resolution than standard techniques allowed. This marked the first published use of interferometry, a technique that has since revolutionised radio astronomy and is discussed in depth in Section 2.1.

Women's early contributions to radio astronomy were not limited to the post-war era. Moving into the 1960s, radio astronomy continued to deliver groundbreaking discoveries

and, once again, women were at the forefront. In 1967, the British female astronomer Jocelyn Bell Burnell discovered the first Pulsar, which are rapidly rotating neutron stars that emit intense periodic bursts of radio emission. The discovery of pulsars is now regarded as one of the most important astrophysical breakthroughs of the second half of the 20th century. Bell Burnell observed a series of unusual signals while working at the Mullard Radio Astronomy Observatory in Cambridge, UK. At 81.5 MHz, she detected a 40 millisecond pulse repeating around every 1.3 seconds. The origin of this mysterious signal was initially unclear, and one early interpretation was that the signal had an extraterrestrial origin, hence these objects became dubbed "Little Green Men", or "LGM" for short. Despite her central role in this breakthrough, Bell Burnell was not included in the Nobel prize that was later awarded for the discovery, a decision that, more than 50 years on, remains one of the most widely recognised injustices in modern astronomy. Dame Jocelyn Bell Burnell's monumental contribution to astronomy is now well recognised and celebrated. In 2025, she was awarder the prestigious Companion of Honour in the King's Birthday Honours, a distinction held by only 65 people at any given time, highlighting her importance to British science and her lasting legacy in modern astronomy.

I highlight these three stories to provide a space to acknowledge the vast knowledge lost throughout human history by diminishing the female mind, hence restricting scientific progress. For centuries, the brilliance of half of humanity has been overlooked, their potential suppressed, and their genius denied recognition in too many cases. In doing so, we have silenced countless voices that could have reshaped the trajectory of science. To conclude this history of radio astronomy, I leave you with the words of Dame Jocelyn Bell Burnell: *"There are likely to have been many female 'Einsteins' and 'Newtons' who never got to study, publish, or be heard."*.

1.2.2 Synchrotron Radiation

The primary form of radiation relevant to this thesis that produces radio emission is synchrotron radiation. This process occurs when charged particles, most commonly free electrons, spiral along magnetic field lines at ultra-relativistic speeds ($E_k >> m_e c^2$). Synchrotron emission is non-thermal, meaning it does not depend on the physical temperature

of the emitting body. Instead, it provides a powerful probe of high-energy environments where particle acceleration dominates the emission processes. Remarkably, synchrotron radiation is observed not only in extreme astrophysical settings but also within our own Solar System with Jupiter's magnetosphere producing this radiation.

The flux density produced by synchrotron emission, (S_ν), follows a simple power law relation,

$$S_\nu \propto \nu^{-\alpha}, \tag{1.2.1}$$

where ν is the frequency and α is the spectral index. This power law arises from the interaction of relativistic electrons with the magnetic field, which we outline below.

We begin with the ultra-relativistic angular gyrofrequency, ω_G, which describes the angular frequency of an electron of mass m_e spiralling around magnetic field lines of strength B:

$$\omega_G = \frac{eB}{\gamma m_e c}, \tag{1.2.2}$$

where e is the electron charge, m_e is the electron rest mass, and γ the Lorentz factor.

The radiated power from an accelerated charge can be described using Larmor's formula. For a single electron, this takes the form

$$P = \frac{2}{3}\frac{e^2 a_\perp^2}{c^3}, \tag{1.2.3}$$

where a is the electrons acceleration perpendicular to its velocity. We can now use the fact that the acceleration of an electron in a circular orbit is given by

$$a_\perp = \omega_G v \sin\alpha, \tag{1.2.4}$$

where α is the pitch angle, i.e. the angle between the electron's velocity and magnetic field. Substituting Eq. 1.2.2 into this expression, and introducing the Lorentz transformed velocity parameter $\beta = v/c$, we obtain

$$P = \frac{2}{3}\frac{e^4}{m_e^2 c^3}\gamma^2\beta^2\sin^2\alpha B^2. \tag{1.2.5}$$

We can incorporate the Thompson cross section of an electron,

$$\sigma_T = \frac{8\pi}{3}\frac{e^4}{m_e^2 c^2}, \tag{1.2.6}$$

into Eq. 1.2.2 to achieve,

$$P = \frac{\sigma_T c}{4\pi}\gamma^2\beta^2 \sin^2\alpha B^2. \tag{1.2.7}$$

Next, we account for all electrons contributing to this radiation by calculating the time-averaged synchrotron power over all possible pitch angles, which can be obtained by performing the integral,

$$\langle \sin^2\alpha \rangle = \frac{\int \sin^2\alpha \; d\Omega}{\int \; d\Omega}, \tag{1.2.8}$$

and using the definition of the solid angle, $d\Omega = \sin\alpha d\alpha d\phi$, for which the integral over all directions is equal to 4π, we then obtain

$$\langle \sin^2\alpha \rangle = \frac{1}{4\pi}\int_{\phi=0}^{2\pi}\int_{\alpha=0}^{\pi} \sin^2\alpha \sin\alpha \; d\alpha \; d\phi = \frac{2}{3}. \tag{1.2.9}$$

Putting this altogether we reach the average synchrotron power,

$$\langle P \rangle = \frac{\sigma_T c}{6\pi}\gamma^2\beta^2 B^2. \tag{1.2.10}$$

We know that power is the related to energy by, $P = -\frac{dE}{dt}$, and the energy distribution of electron in synchrotron sources follow a power law,

$$n(E)dE \propto E^{-\delta}dE. \tag{1.2.11}$$

We now introduce the emission coefficient which quantifies the energy radiated per unit time and per unit frequency, as:

$$j_\nu d\nu = -\frac{dE}{dt}n(E)dE \propto \langle P \rangle E^{-\delta}dE. \tag{1.2.12}$$

By adopting the relativistic energy of an electron and assuming that each electron radiates predominately at a single frequency, $\nu \approx \gamma^2 \nu_G$, and then differentiating with respect to ν,

we obtain:

$$\frac{dE}{d\nu} \approx \frac{1}{2}\left(\frac{1}{\nu\,\nu_G}\right)^{1/2} m_e c^2, \tag{1.2.13}$$

and therefore we can express j_ν as,

$$j_\nu \propto \left(\frac{\sigma_T c}{6\pi}\gamma^2\beta^2 B^2\right)\left(\left(\frac{\nu}{\nu_G}\right)^{1/2} m_e c^2\right)^{-\delta} \frac{1}{2}\left(\frac{1}{\nu\,\nu_G}\right)^{1/2} m_e c^2. \tag{1.2.14}$$

Grouping all constants into a single factor, which can be absorbed into the proportionality, and using the relation between the magnetic field and the gyrofrequency (Eq. 1.2.2) along with $\nu \approx \gamma^2 \nu_G$, we achieve,

$$j_\nu \propto (\nu B)\left(\frac{\nu}{B}\right)^{-\delta/2} (\nu B)^{-1/2}. \tag{1.2.15}$$

Simplifying this further by collecting like terms, we obtain,

$$j_\nu \propto B^{(\delta+1)/2}\nu^{(1-\delta)/2}. \tag{1.2.16}$$

Therefore as $S_\nu \propto \nu^{-\alpha}$ and $S_\nu \propto j_\nu$ then we can relate δ and α by,

$$\alpha = \frac{\delta - 1}{2}, \tag{1.2.17}$$

and hence we have derived the synchrotron spectral index, α.

1.2.3 Resolved vs. Unresolved Radio Observations for [O III]

Radio observations vary not only in frequency but also in resolution, depending on the telescope and the survey for which the data is taken. As a result, a source may appear resolved at one frequency and resolution, yet unresolved at another. This can occur due to intrinsic properties of the source, such as its radio spectrum. For instance, a source detectable at high frequency but not at lower frequency exhibits an inverse spectral slope. However, differences in resolution between instruments can also play a major role. In such cases, a source may be resolved at higher angular resolution but unresolved, i.e., compact in morphology, at lower resolution.

We discussed in Section 1.1.4 that the literature shows a significant connection between radio emission and [O III] emission. However, the physical mechanism driving this link remains unclear. One way to investigate the origin of the radio emission, and therefore better understand the underlying physical processes, is through morphological studies. But, due to instrumentation limitations, such studies have largely been restricted to unresolved radio observation.

Mullaney et al. (2013), uses the Faint Images of the Radio Sky at Twenty-centimeters (FIRST) survey at 1.4 GHz with 5″ resolution to investigate the morphology of optically selected AGN and examine the form of radio emission associated with the most disturbed gas kinematics traced by [O III]. As all sources in this statistically large sample are detected in FIRST, the study is limited to radio emission detectable at this resolution and frequency, and the authors divide their sample into compact and extended morphologies. They define unresolved (i.e., compact) AGN to have a deconvolved extend less than 2″, and AGN with a deconvolved size greater than 2″ are classed as extended. They take the population of AGN with $\mathrm{FWHM_{avg}}$>1500 km $\mathrm{s^{-1}}$ and find extended radio sources do not have broader [O III]. Therefore, the most disturbed gas is predominately found in compact, unresolved AGN, leading the authors to suggest that the radio emission associated with the most disturbed [O III] kinematics originates from radio cores, rather than powerful radio jets. Zakamska & Greene (2014) suggest that the enhanced [O III] emission observed in radio detected AGN could be driven by winds propagating into the ISM (interstellar medium). As these winds move through the ISM, they compress the gas, potentially producing shock fronts that accelerate particles and generate radio emission. The authors also acknowledge that relativistic jets could supply the excessive heating required to enhance [O III]. Molyneux et al. (2019) present morphological results of a sample of 2922 low redshift AGN, selected to be jet-dominated, all of which are detected at 5″ resolution at 1.4 GHz using FIRST. To analyse the morphology of this sample, the authors employ both machine learning techniques and size measurements. The authors find that if the radio emission is unresolved within 3″, an AGN is twice as likely to exhibit broad [O III] components exceeding velocities of 1000 km $\mathrm{s^{-1}}$ compared to AGN with more extended radio emission. They also follow-up 42 sources at 0.3″ (1.4 GHz) and 1″ (6 GHz) resolution, with logarithmic $L_{1.4\ \mathrm{GHz}}$ between 23.5 and 24.5 W $\mathrm{Hz^{-1}}$,

revealing that small-scale radio jets at 1.4 GHz are prevalent. This provides evidence that compact jets could be responsible for driving the stronger outflows observed in their sample. Using radio information from LoTSS, the VLA Sky Survey (VLASS; Lacy et al., 2020), and FIRST, Kukreti & Morganti (2024) derive spectral slopes for a sample of 5720 radio AGN and perform stacking analysis to investigate [O III]. They examine the morphological properties of their sample using the deconvolved major axis from FIRST observations, defining compact AGN as having a major axis <3″ and extended AGN as having a major axis >3″. Consistent with the previous studies above, they find that AGN with a compact morphology demonstrate more distributed [O III] gas compared to extended radio emission. Liao et al. (2024) analyse a sample of around 37,000 radio-quiet AGN to further investigate the connection between [O III] and radio emission. Using stacked radio images from VLASS, they find that the observed radio enhancement is likely driven by the central AGN, either through low-powered jets or AGN-driven winds.

In recent years, advances in both hardware and radio reduction software have enabled several studies to explore the connection between resolved radio observations and [O III]. Jarvis et al. (2019) presents ten high-resolution images obtained with both VLA (frequency range: 1.5-6 GHz, resolution: 0.3″-1″) and e-MERLIN (enhanced Multi-Element Radio Linked Interferometer Network, 1.5 GHz, 0.25″), selected for targets exhibiting broad [O III] line profiles and spatially resolved ionised gas kinematics using Gemini-GMOS (Gemini Multi-Object Spectrographs). For nine out of ten of their targets, they find that less than 10% of the radio emission is produced by star formation, with 80-90% showing extended radio emission on scales of 1-25 kpc. These resolved radio morphologies led the authors to suggest that radio jets are the dominant contributor to the radio emission in these strongly outflowing quasars. Jarvis et al. (2021) expands upon this by studying 42 quasars from the Quasar Feedback Survey, selected for their enhanced [O III] emission, using high-resolution VLA data at the same frequency and resolution as Jarvis et al. (2019). With a larger sample size, the authors determine that ~70% of the sample show spatially resolved radio emission on scales of 1-60 kpc. By combining morphological information, brightness temperature, spectral indices, and the radio-to-infrared relation, they attribute around 57% of the radio emission to AGN-driven processes. Another notable study is Njeri et al. (2025), which follows up the same sample of 42 quasars studied by Jarvis

et al. (2021) with high angular resolution e-MERLIN radio imaging. These observations achieve 50 milli-arcsecond resolution, corresponding to sub-kpc scales (tens to hundreds of pc) across the redshift range of the sample. The authors combine morphological analysis with brightness temperature measurements to investigate the origin of radio emission in these [O III] enhanced quasars. Using their e-MERLIN images alongside the VLA images from Jarvis et al. (2021), they find that over 86% of their quasars are radio AGN, and therefore, suggesting that the emission is predominantly driven by AGN processes such as jets and shocks from outflows.

These resolved studies, enabled by new high-resolution radio capability, are shedding light on the connection between radio emission and the [O III] emission line. However, as demonstrated above, these high-resolution studies have so far been limited to powerful quasars at GHz frequencies. This leaves an open question: is the driving mechanism connecting radio emission and [O III] also AGN-driven at low-frequencies?

1.3 Boötes

Boötes is one of the largest constellations in the northern hemisphere, spanning a declination of $\sim 7^\circ$ to $\sim 55^\circ$ and a right ascension from $13^h\ 36.1^m$ to $15^h\ 49.3^m$, covering over 900 deg^2 of the sky. I show this constellation in Figure 1.8 which shows illustrations of this area of the sky from both the 1930s and 1920s. This constellation was first described in the 2nd century by Claudius Ptolemy, a man of many professions, as was typical for wealthy ancient Greeks with ample time, one of which was astronomy. The official boundaries of Boötes were formalised in 1930 by Eugene Delporte. Its name derives from the Ancient Greek for "ox-driver" and it is now commonly referred to as the "herdsman", owing to its human-torso-like shape. Boötes is even mentioned in Homer's *Odyssey*: the god of the sea, Poseidon, abandoned two of his children on Mount Pelion, who were later rescued by a lone herdsman. This herdsman raised the children and named one Boeotus, a name derived from the Ancient Greek word for "cattle".

Within this large constellation, there is a tiny patch of sky that has been intensely targeted by many multiwavelength surveys, known as the Boötes Deep Field. This field is ideal for deep observations and is sometimes referred to by the nickname: the Boötes Void.

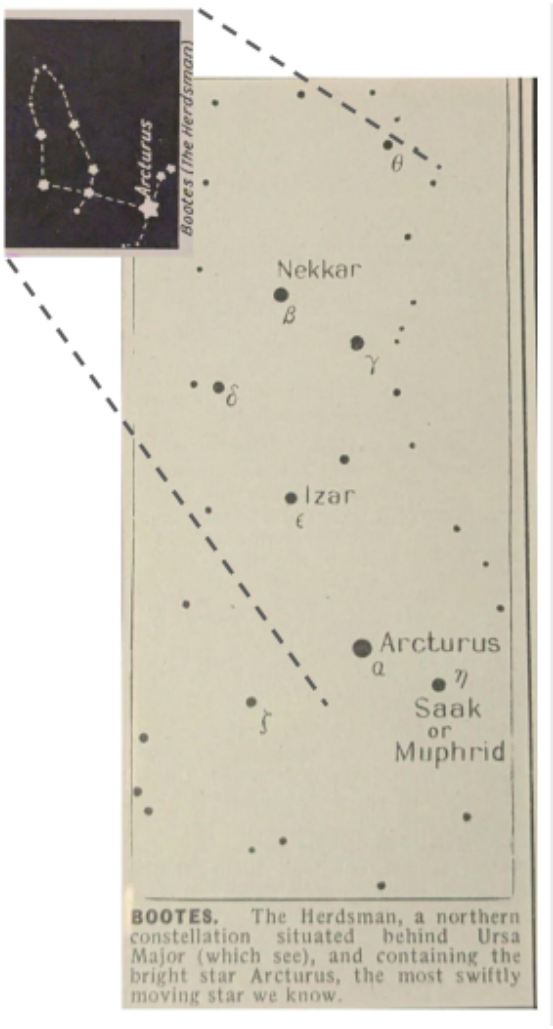

Figure 1.8: The Boötes constellation is illustrated in an original 1938 print, accompanied by a smaller, zoomed-out version from 1928 shown in the top left corner. Both prints highlight the constellation's brightest star, Arcturus. Courtesy of the Beverley Escott Prints.

In 1981, Robert Kirshner at the University of Michigan undertook the task of measuring redshifts for large numbers of galaxies across the sky, but he soon noticed something peculiar. This 10^8 pc section of the sky should contain hundreds, even thousands, more galaxies than were actually observed. This void is now recognised as one of the largest discovered to date. Over the years, it has hence been called various names, such as the "supervoid", "The Great Nothing", and the Boötes Void, but among modern astronomers it is most commonly referred to as the Boötes Deep Fields.

This relatively empty section of the sky is ideal for astronomers to probe some of the faintest objects in the Universe, as we can observe these voids for long periods, collecting photons from the faintest galaxies across all wavelengths due to the lack of bright sources dominating the field of view. Deep images of this field have been released across the electromagnetic spectrum, from X-ray with Chandra (Murray et al., 2005; Kenter et al., 2005; Masini et al., 2020) to radio wavelengths using telescopes such as LOFAR (Sabater et al., 2021; Williams et al., 2021) and Westerbork Synthesis Radio Telescope (WSRT) (De Vries et al., 2002; Kutkin et al., 2023) along with optical observations such as the National Optical Astronomy Observatory (NOAO) Deep Wide Field Survey (NDWFS; Jannuzi & Dey, 1999) and extending through the UV band (e.g., Ashby et al., 2009; Gonzalez et al., 2010).

Deep fields, such as Boötes, provide astronomers with access to a new regime of emission to analyse. For example, three deep, low-frequency fields have been released in the LoTSS Deep DR1: Boötes (Tasse et al., 2021), Lockman Hole (Tasse et al., 2021), and European Large Area Infrared Space Observatory Survey North 1 (ELAIS-N1, Sabater et al., 2021). With the ELAIS-N1 field now fully processed for over 505 hours (Shimwell et al., 2025), a sensitivity of 10.7 μJy beam^{-1} has been achieved, representing the deepest low-frequency radio image ever produced. By comparison, the key wide-field LOFAR survey, LoTSS, reaches a central sensitivity of ∼70 μJy beam^{-1}. Therefore, these fields increase our sensitivity by more than a factor of six, allowing us to probe the faintest radio emission currently detectable. They also benefit from extensive multi-wavelength coverage (Kondapally et al., 2021), providing a statistically significant sample of low-frequency AGN, as these three fields combined cover ∼26 deg^2 with 7.2 million 144 MHz detected sources with ancillary data. To emphasise the relative depth of this dataset, the

ELAIS-N1 field at its full depth corresponds to 2.2 μJy beam^{-1} at 1.4 GHz, assuming a synchrotron spectral index of -0.7. To put this in perspective, the VLA-COSMOS Deep Survey (Schinnerer et al., 2004, 2007) reaches sensitives of 7-15 μJy beam^{-1}, covering ∼2 deg^2. This demonstrates that the LoTSS Deep Fields allow us to probe a new regime of radio emission, unlocking significant scientific potential, including advancing our understanding of the radio-quiet AGN population.

1.4 Thesis Structure

This thesis advances our understanding of the connection between radio emission and the properties of the [O III] λ5007 Å emission line. By exploiting the full capabilities of the ILT, this work investigates this connection in a previously unexplored regime, enabling the study of radio emission across multiple spatial scales.

The primary questions that this thesis addresses are:

1. **How do [O III] kinematics vary with deep, low-frequency radio emission?**
I address this question in Chapter 3 using the LoTSS Deep Fields, and begin a short discussion in Appendix C.2 on how [O III] kinematics vary with sub-arcsecond resolution morphologies.

2. **What are the contributions of different emission mechanisms to the origin of radio emission in radio-quiet AGN?**
I begin this discussion in Chapter 3 with 6″ resolution radio data, and extend it in Chapter 5 to sub-arcsecond, kiloparsec-scale radio emission.

3. **Are [O III] outflows more prevalent in sources detected on small, kiloparsec scales than in AGN detected only on large scales?**
I investigate this using high-resolution radio morphologies in Chapter 5.

4. **What is the physical mechanism driving the enhancement of [O III] associated with radio emission?**
I present this discussion in both Chapter 3 and 5.

The answers to the questions above ultimately contribute to our overall understanding of galaxy evolution, as they shed light on the processes of AGN feedback. To address these

questions, it is essential to characterise the origin of radio emission from AGN in order to link it to the physical mechanisms driving the emission. Morphological studies provide one approach, but they require high-resolution, resolved radio imaging at low-frequencies. Consequently, a comprehensive analysis demands not only a deep understanding of spectral decomposition to exploit [O III] kinematics but also expertise in radio interferometry and data reduction techniques to produce the high-resolution images necessary to resolve radio emission.

The thesis has the following structure:

- **Chapter 2 - Fundamentals of Interferometry**

  I present an overview of the fundamentals of radio interferometry, along with a summary of VLBI. I then focus on the revolutionary low-frequency interferometer, the ILT, and go on to discuss both LOFAR-VLBI and the ILT's wide-field imaging capabilities.

- **Chapter 3 - Unveiling AGN Outflows: [O III] Outflow Detection Rates and Correlation with Low-Frequency Radio Emission**

  In this chapter, I present a sample of 198 optically selected AGN within the LoTSS Deep Fields, performing spectral decomposition on SDSS spectroscopy to investigate [O III] kinematics. I show that AGN detected in LoTSS Deep are more likely to host an [O III] outflow compared to those without a low-frequency, deep radio detection.

- **Chapter 4 - Strap on your Boötes: The Journey to Achieve Wide-field Subarcsecond Resolution with LOFAR**

  Here, I present the first, wide-field, sub-arcsecond resolution image of the Boötes Deep field at 144 MHz, alongside intermediate resolution images at $0.6''$ and $1.2''$. The highest resolution image at $0.3''$, contains 4091 sources, has a restoring beam of $0.50'' \times 0.34''$, and reaches a central sensitivity of 37.0 μJy beam^{-1}. Images of this nature have only been published twice before in the literature, highlighting the complexity of the procedures required to obtain this Boötes image. This chapter describes the challenges that must be overcome to produce such images and outlines the data reduction steps and techniques employed to create an image of this calibre.

- **Chapter 5 - A link between low-frequency kiloparsec radio morphology and AGN driven ionised outflows**

  Using the three sub-arcsecond, wide-field images of the LoTSS Deep Fields, I extend the analysis conducted in Chapter 3 at 6″ resolution by examining 0.3″ morphologies. This allows a deeper investigation into the origin of radio emission in the radio detected population and its connection to the enhancement of [O III] emission associated with a 144 MHz radio detection. I find that sources detected on both small (0.3″) and large (6″) scales are more likely to host an [O III] outflow compared to AGN detected only on large scales, implying that the radio emission driving the enhanced [O III] is predominantly AGN-driven.

- **Chapter 6 - Conclusions** In this final chapter, I highlight the main conclusions of this thesis and I also look towards the future of both radio astronomy and spectroscopy, which are expected to further advance our understanding of the connection between ionised outflows and radio emission.

CHAPTER 2

Fundamentals of Interferometry

2.1 Interferometry

As demonstrated in Section 1.2.1, historically, radio astronomy relied on either single dish parabolic telescopes or individual dipoles antennas. However, as this scientific field became saturated, the limitations of single telescope observations became increasingly apparent. One major constraint is the collecting area of these telescopes. Even one of the largest fully steerable radio telescope, the Green Bank Telescope, built in 2000 with a diameter of 100 metres, can only achieve a resolution around 6″ at 116 GHz. It was theorised that one could combine the radio signals from multiple telescopes spread over a large area, effectively increasing the baseline, or "diameter", to create a much larger telescope. This concept, known as interferometry, was first successfully implemented by Ruby Payne-Scott.

A telescope's primary limiting factor is its angular resolution, θ. This limitation is set by the Rayleigh criterion, which defines the smallest angular resolution a telescope can resolve, given its diameter, D, and the observed wavelength, λ,

$$\theta = 1.22\frac{\lambda}{D}. \tag{2.1.1}$$

Therefore, as we select the observing wavelength based on our science goals, we can improve angular resolution by increasing the telescope's diameter. However, both engineering and financial limitations restrict this approach. Currently, the world's largest single dish radio telescope has a diameter of 500 m, and is the aptly named, Five-hundred-meter Aperture Spherical Telescope (FAST) in China. Constructing a dish of this calibre requires embedding it into a natural depression in the landscape, which limits the number of appropriate sites. Before FAST's completion in 2016, the record holder was the Arecibo telescope in Puerto Rico, built in the 1960s with a 305 m diameter dish. Unfortunately, after decades of service, it unexpectedly collapsed in 2020. Another notable incident highlighting the engineering challenges of large single disk telescopes was the 300-foot (around 92 m) Green Bank Telescope, which collapsed unexpectedly in 1988, and the aftermath is shown in Figure 2.1. These examples illustrate the need for alternative techniques to achieve high angular resolution without solely relying on physically large single dishes.

Interferometry is the technique that overcomes the limitation of oversized single dish telescopes. The principle of radio interferometry is to synthesise multiple voltages captured by different telescopes or dipoles into a single coherent radio signal. This adapts the Rayleigh criterion by replacing D to B, where B is the baseline, i.e., the distance between the telescopes included in the interferometer.

When the signal arrives at each antenna, the voltages are multiplied together to obtain the interfered signal. Figure 2.2 demonstrates the simplest interferometric model, which is a two-element system. Each telescope observes a voltage (V_1 for telescope 1 and V_2 for telescope 2) from the same source, however the signal is received by each dish at slightly different times due to their positions on Earth. This resulting geometric time delay, (τ_g), is given by,

Figure 2.1: Photograph taken in 1988 of the collapsed 300-foot Green Bank Telescope in West Virginia. This incident highlights the engineering limitations of constructing large single dish telescopes to achieve higher angular resolution. Credit:NRAO/AUI/NSF.

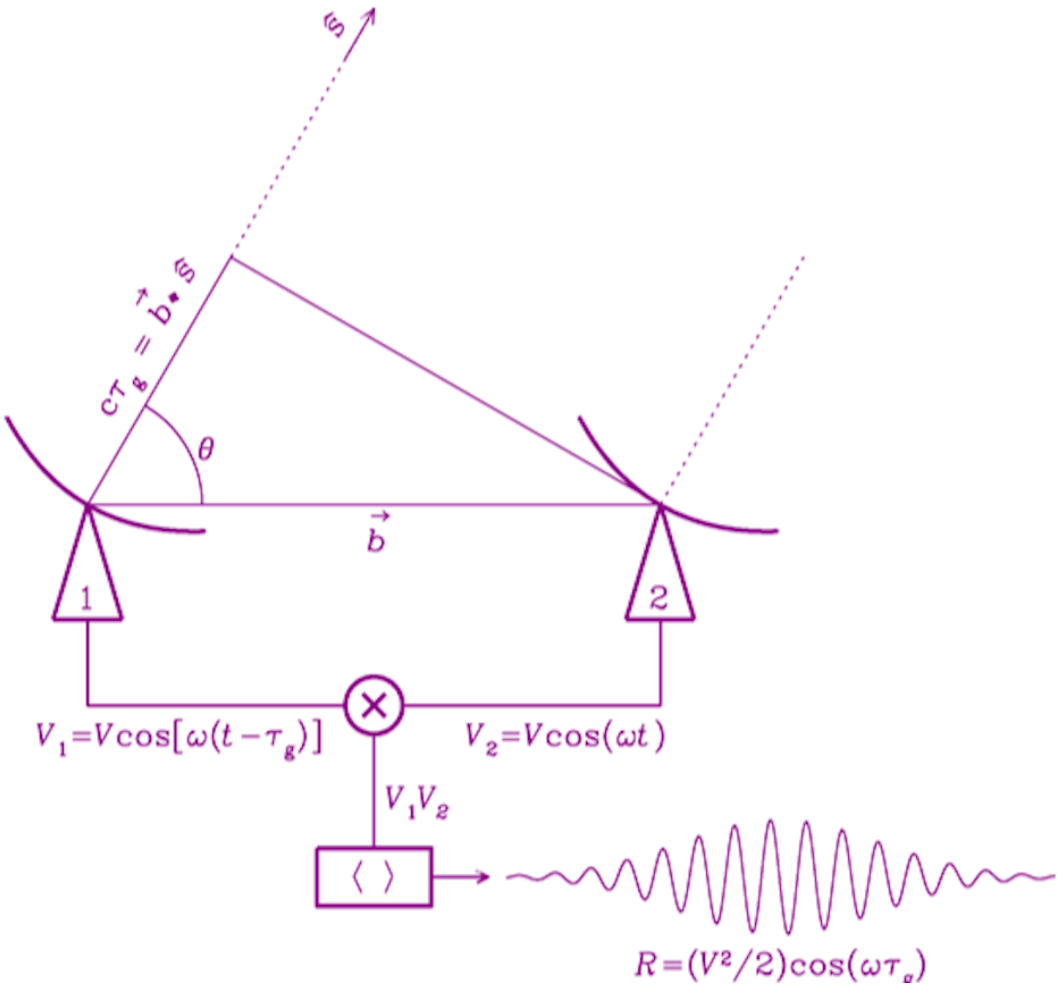

Figure 2.2: Diagram demonstrating the components of a two telescope interferometer, with baseline b. Credit: Adapted from NRAO.

$$\tau_g = \frac{\vec{b} \cdot \hat{s}}{c} \tag{2.1.2}$$

where $\vec{b}$ is the baseline vector between the antennas, $\hat{s}$ is the unit vector along the direction of the source. These signals are then correlated in a correlator by taking the cross-products of each frequency channel, resulting in,

$$V_1 V_2 = (\frac{V^2}{2})[\cos(2wt - w\tau_g) + \cos(w\tau_g)], \tag{2.1.3}$$

with w representing the angular frequency. In the correlator, a time average is also computed, which removes the high-frequency term, leaving the output voltage, R, as:

$$R = \langle V_1 V_2 \rangle = (\frac{V^2}{2})\cos(w\tau_g). \tag{2.1.4}$$

From this expression, we can begin to understand the response of interferometers to spatially resolved sources, not just point-like objects. Since these voltages measured are equivalent to the power received from the source, the voltage term is proportional to the effective area alongside the source flux. By replacing the angular frequency term, w, with the frequency, $v = w/(2\pi)$, and substituting our earlier expression of τ_g in terms of the baseline vector, we can rewrite this as,

$$R = A(\hat{s})S\cos(2\pi v\vec{b} \cdot \hat{s}/c). \tag{2.1.5}$$

Furthermore, we can use the fact that the measured flux, S, is proportional to the integrated sky brightness, $I(\hat{s})$, over the collection of solid angles, Ω. This gives,

$$R = \int I(\hat{s})\cos(2\pi v\vec{b} \cdot \hat{s}/c)\, d\Omega. \tag{2.1.6}$$

The expression above is known as the "cosine" correlator response, which is sensitive only to the even (symmetric) part of the source brightness distribution. To capture the odd (antisymmetric) component, we use the "sine" correlator, which incorporates a phase delay of $\pi/2 = 90°$. By replacing the cosine term with a sine term, we obtain the sine correlator response,

$$R_s = \int I(\hat{s})\sin(2\pi v\vec{b}\cdot\hat{s}/c)\, d\Omega. \tag{2.1.7}$$

By combining these two correlators, we form a complex correlator. This allows us to fully capture the sky brightness distribution, as both the amplitude and phase of the signal are preserved. We define the complex visibility as:

$$\mathcal{V} = R_c - iR_s, \tag{2.1.8}$$

and using Euler's formula we obtain,

$$\mathcal{V} = Ae^{-i\phi}, \tag{2.1.9}$$

where A is the amplitude of the visibility and ϕ is the phase. Incorporating this expression into 2.1.7 and converting frequency to wavelength, we obtain,

$$\mathcal{V} = \int I(\hat{s})\exp(-i2\pi\vec{b}\cdot\hat{s}/\lambda)\, d\Omega. \tag{2.1.10}$$

Due to the rotation of the Earth, over time interferometric observations sample a three-dimensional space. To describe this, we replace the baseline vector, $\vec{b}$, with a right-handed rectilinear coordinate system (u, v, w), where w points towards the source ("up"), u points due east, and v points due north. The plane perpendicular to the source direction is commonly referred to as the $u - v$ plane. The unit vector towards the source, $\hat{s}$, can be expressed in terms of its direction cosine (l, m, n) along the u, v, and w axes, respectively. We adopt a spherical model of the celestial plane, where θ is the angle from the zenith and ϕ is the azimuthal angle. Here ϕ is defined as the angle between l and the projection of $\hat{s}$ onto the $u - v$ plane. The following expressions describing our 3D plane,

$$l = \sin\theta\cos\phi, \quad m = \sin\theta\sin\phi, \quad n = \cos\theta. \tag{2.1.11}$$

Since $\hat{s}$ is unit vector, it satisifes $l^2 + m^2 + n^2 = 1$, which can be rearranged to give

$$n = \cos\theta = \sqrt{1 - l^2 - m^2}. \tag{2.1.12}$$

Now we use the solid angle on a unit sphere alongside the Jacobian determinant for the coordinate transformation. We can now obtain the expression for the differential solid angle,

$$d\Omega = \frac{dl\ dm}{\sqrt{1 - l^2 - m^2}}. \tag{2.1.13}$$

By substituting Eq. 2.1.13 and taking the dot product of $\vec{b}$ with $\hat{s}$, we can express the complex visibility as,

$$\mathcal{V}(u, v, w) = \int \int \frac{I_v(l, m)}{\sqrt{1 - l^2 - m^2}} \exp[-i2\pi(ul + vm + wn)]\ dl\ dm. \tag{2.1.14}$$

We can simply this further by setting $w = 0$, as all antennas lie in the same plane. This reduces the problem to a 2D Fourier transfer, allowing us to compute the sky brightness distribution from the measured visibilities,

$$\mathcal{V}(u, v, 0) = \int \int \frac{I_v(l, m)}{\sqrt{1 - l^2 - m^2}} \exp[-i2\pi(ul + vm)]\ dl\ dm. \tag{2.1.15}$$

However a single visibility measurement only represents one Fourier component and we require observations that fill the $u - v$ plane in order to reconstruct the full brightness distribution. Aperture synthesis (Ryle & Hewish, 1960) achieves this by combining multiple baselines within an array, increasing the sampling space with $N_{base} = N_{ant}(N_{ant} - 1)/2$, where N_{base} is the number of baselines and N_{ant} is the number of antennas, and by incorporating multiple frequencies into our observations. Additionally, Earth-rotation synthesis exploits the rotation of the Earth to subsequently fill the $u - v$ plane, hence obtaining more Fourier components and ultimately enabling a detailed reconstruction of the true sky brightness distribution.

2.1.1 Calibration

The interferometric strategies described above are ideally applied to visibilities where the only abnormality arises from the point spread function (PSF) of the beam. In practice, however, observed visibilities are contaminated by a range of systematic effects. These

include, Radio Frequency Interference (RFI), distortions caused by the ionosphere (a thin layer of charged particles in the Earth's atmosphere extending from about 60 km to 1,000 km), and the polarisation offsets between data streams (producing polarisation leakage). Failure to account for these effects when producing radio images can introduce artifacts, and therefore result in an inaccurate representation of the true brightness distribution. To properly account for this, we perform calibration directly on the raw visibilities before converting them to brightness measurements. Calibrating at this stage is crucial because once an inverse Fourier transform is applied to generate a dirty image, these systematics become embedded in the data, and therefore we must remove these effects in the early stages of data reduction.

The radio interferometer measurement equation (RIME; Hamaker et al., 1996; Smirnov, 2011) has become an invaluable tool for calibration in radio astronomy, as it enables the correction of both directional independent effect (DIEs) and directional dependent effects (DDEs). The simplest form of the RIME, describing a single point source observed by two spatially separated antennas, p and q, is presented below:

$$\mathrm{V_pq} = \boldsymbol{J}_p \mathrm{B} \boldsymbol{J}_q^{\dagger}, \tag{2.1.16}$$

where $\mathrm{V_pq}$ presents the visibility matrix, while $\boldsymbol{J}_q$ and $\boldsymbol{J}_p$ are Jones matrices, which are 2×2 complex matrices. Each Jones matrix can be expressed as a chain of successive Jones terms, with each term corresponding to a specific systematic effect present in the measured visibilities. The composition of this Jones chain depends on calibration strategy and the nature of the data, additionally for each Jones matrix we perform a minimisation, commonly using least squared fitting, between the observed data and the model visibilities. Importantly, not all Jones matrices commute, meaning that the order in which these matrices appear in the chain is critical. Consequently, the Jones matrices must be applied in the same sequence that the systematic effects impact the signal path.

Systematic effects that require calibrating vary from instrument to instrument, but they are broadly divided into two main categories: directional independent effects (DIEs) and directional dependent effects (DDEs). DIEs affect all sources in the same way, independent of the target's position in the sky, and are therefore comparatively straightforward to calibrate. A common example is the polarisation offset. Most instruments record two

orthogonal polarisations, which may be linearly polarised (X and Y) or circularly polarised (R and L). These polarisation streams can drift relative to each other during the course of an observation, but this can be corrected by introducing an appropriate phase offset. A further example is the bandpass response of the instrument. Since raw visibilities are recorded in non-physical units, we are required to convert them into physical flux density units, typically expressed in Janskys (Jy). In radio interferometry it is essential to ensure that the clocks of each antenna remain synchronised to a strict tolerance. Clock drift introduces offsets that must be corrected during calibration, and these effects are also independent of direction. In contrast, the DDEs are generally more complex to calibrate because they vary across the sky and evolve with time as the Earth rotates. Layers of the Earth's atmosphere pose as one of the most significant obstacles to overcome in radio observations. The specific atmospheric layer responsible for these distortions, as well as the extent of these distortions, scale significantly with frequency. At low radio frequencies, the ionosphere is the dominant source of distortion, introducing dispersive delays and phase variations (see Section 2.1.4). At higher frequencies, the lowest layer of the atmosphere, the troposphere (0-15 km), becomes the primary challenge. Fluctuations in temperature, pressure, and water vapour content introduce path length variations that distort the observed radio signals.

These effects can largely be accounted for by obtaining calibration solutions from a set of calibrators. The number of calibrators required depends on the instruments and size of the field of view (FoV). Most instruments require a flux calibrator, which must have an accurately known flux density and remain stable over time. Commonly, one of the 3C sources (Edge et al., 1959) is used, as these are among the brightness radio sources in the sky. In addition, an in-field calibrator may be required, and it should lie within the pointing's FoV. An ideal in-field calibrator should be close to the centre of the pointing, possess high surface brightness, compact flux, and also progress well through self-calibration cycles (see Section 2.1.1 for further details on this calibration strategy). For large FoVs, further calibrator sources may be necessary, since DDEs vary across the sky. In such cases, multiple calibrators are needed to fully characterise and correct for the systematics effects across the entire FoV. This is discussed in depth in Chapter 4.

Self-calibration

Further calibration is likely to be required, even after applying the flux calibrator solutions to the measurement set, because of residual amplitude and phase errors which still reside in the data. A widely used method to further improve the image quality is self-calibration, in which the source itself is used as the calibrator. This technique requires a source with sufficient signal-to-noise so that an initial source model can be constructed, allowing calibration solutions to be derived that provide a better approximation to the true visibilities. This allows us to find the complex gains, for both the amplitude and phase, which we can use to reproduce the sky intensity model. An initial model is created and the corrected visibilities are obtained by solving for the complex gain. From this a new improved model is then generated, and the process is repeated iteratively until the reconstructed model closely matches the true sky brightness distribution visibilities.

2.1.2 Imaging

Now that we have constructed the brightness distribution of a source, the next step is to convert these visibilities into an image. This is done by performing a two-dimensional inverse Fourier transform, which recovers the sky brightness distribution from the sampled visibilities,

$$I_v(l,m) = \int\int \mathcal{V}(u,v)\,\exp[i2\pi(ul+vm)]\;du\;dv. \tag{2.1.17}$$

Alongside this inverse Fourier transform, we must also compute the inverse Fourier transform of the sampling function, which describes the sampling of the $u-v$ plane. This produces the instrument's PSF, which represents the response of the array to a point source. The observed (or "dirty") image is obtained by taking the inverse Fourier transform of the measured visibilities. Due to incomplete sampling in the uv-plane, this dirty image corresponds to the true sky brightness distribution convolved with the PSF. The dirty image is of limited scientific value due to the contamination of the PSF. To recover the true sky brightness distribution, we "clean" our dirty image by performing a non-linear deconvolution of the PSF. The most widely used algorithm which performs deconvolution is `CLEAN` (Högbom, 1974). The `CLEAN` algorithm find the brightest pixel in the dirty

image and subtracts a scaled version of the PSF centred at that location. The subtracted component produces a new clean component, which is then stored in a separate model domain. This process is repeated many times with each subtraction becoming a new CLEAN component. Gradually the PSF is removed from the dirty image and then the accumulated clean components build a clean image which is then convolved with an idealised PSF, typically a Gaussian, resulting in a restored clean model. Finally, this model is then added back to the residual dirty image, producing the final cleaned image. Interestingly, this means that many radio images are not a direct representation of raw observations but rather reconstructions based on models built iteratively from the dirty image.

These imaging methods rely on the use of Fast Fourier Transforms (FFTs; Cooley & Tukey, 1965) as Fourier transforms are too computationally expensive. In order to perform FFTs, the data is sampled on a regular grid in the $u - v$ plane, whereas the raw visibilities are observed at random, irregular intervals. To address this, the visibilities must first undergo a process known as "gridding", where these FFTs are uniformly sampled. The visibilities are assigned weights either during or before the gridding step, which determines the extent of the contribution of each sampled $u-v$ point to the final image. There are three commonly used weighting schemes: natural weighting, uniform weighting, and Briggs (or robust) weighting.

Natural weighting is applied during the gridding process and assigns an equal weight to each element. This weighting scheme favours scales which have higher density of baselines and therefore, as most interferometers have a dense core, this scheme will likely favour the shorter baselines. As a result, natural weighting will produce a larger synthesised beam, i.e., lower angular resolution but best point source sensitivity.

In contrast, uniform weighting assigns equal weight to each cell in the gridded $u - v$ plane. However if multiple visibilities occupy the same cell, they are down-weighted so that no region dominates the image, therefore this scheme does not favour more compact visibilities, unlike natural weighting. So, on long baselines, where visibility density is low, these baselines will get the same weight as sources where the density is higher (i.e. short baselines). Consequently, uniform weighting will likely result in the best angular resolution by giving longer baselines greater relative influence, but at the cost of sensitivity as the down-weighting means fewer visibilities are available at longer baselines.

Finally, Briggs weighting, also referred to as robust weighting, provides a compromise between natural and uniform weighting by taking into account the signal-to-noise ratio (SNR) of each cell. Cells with high SNR are uniformly weighted, giving them more influence regardless of the visibility density, while cells with low SNR are naturally weighted, favouring regions with denser sampling. Therefore, Briggs weighting allows a balance of angular resolution and sensitivity, with a robustness parameter determining the SNR threshold so that either higher resolution or lower noise can be emphasised in the final image.

2.1.3 Very Long Baseline Interferometry

Interferometry is not restricted to multiple receivers being local to each other; in fact, the receivers can have baselines spanning thousands of kilometres. When signals are correlated across geographically large distances, this technique is known as Very Long Baseline Interferometry (VLBI). Producing radio images using these extended baselines is technically complex and requires a sophisticated network of hardware systems. The intricacies of VLBI are rewarding to overcome as we can replace Eq. 2.1.18 with,

$$\theta = 1.22\frac{\lambda}{B}, \tag{2.1.18}$$

where the size of the interferometer which was previously limited to the diameter of a single dish, is now defined by the baseline (B) between antennas which can span thousands of kilometres. This results in a dramatic improvement in the angular resolution of radio observations. VLBI allows us to sample the $u - v$ plane more extensively due to these long baselines, hence improving the quality of the resulting radio images.

VLBI networks can consist of either multiple single dish telescopes, such as e-MERLIN, or multiple stations, each containing large quantities of dipoles, as in LOFAR. Each station or telescope observes independently, meaning that a clock is required at each site. These oscillators are synthesised to each other using a highly stable frequency reference, produced by an astronomical source such as a hydrogen maser, to minimise time drift. The received signals are then sent to a correlator to determine the observed visibilities, as described in Eq. 2.1.15. Precise clock synchronisation between VLBI stations is

critical, since each incoming signal is divided into time-tagged blocks. Even a nanosecond discrepancy between clocks can reduce the signal coherence. During correlation, these time-tagged blocks must be accurately aligned to maintain the correct time tags and ensure coherent signal combination.

2.1.4 Low Frequencies

The first pioneering work in radio astronomy was conducted at low frequencies, for example, Jansky's merry-go round discussed in Section 1.2.1. This is primarily due to the low expenditure required to build a single dipole. However, progress in this area stalled for several decades due to technological and engineering limitations, including the difficulty of achieving the high angular resolution necessary to obtain new scientific results.

In recent years, thanks to advances in interferometry, data processing, storage, and array configurations, low-frequency radio astronomy has experienced a resurgence. Despite these improvements, one main challenge remains: the ionosphere. This thin layer of charged particles in the Earth's atmosphere distorts radio wave propagation as signals pass through it and is the culprit for the most problematic DDEs to calibrate. These distortions cause the radio waves polarisation plane to rotate as it propagates through a magnetised ionised medium. The magnitude of this effect is dependent on both the magnetic field strength and the Total Electron Content (TEC), defined as the integrated free electron count along the line of propagation. These distortions also exhibit a strong frequency dependence, scaling as ν^{-2}, making them particularly severe at low radio frequencies.

This regime of radio astronomy enables unique scientific discoveries, and in recent years one ground-breaking instrument has revolutionised the field: the Low Frequency Array (LOFAR).

2.1.5 LOFAR

The International LOw Frequency ARray Telescope (ILT) has revolutionised low-frequency radio astronomy. The ILT is an international interferometric array that is composed of two separate telescopes: the Low Band Antennas (LBA) and the High Band Antennas (HBA). The LBA feature the iconic design with a central pole supporting two long wires, each

end connected to a mesh grid on the ground. The telescope operates at lower frequency, ranging from 10 MHz to 90 MHz. The HBA, which is the focus of this thesis, also used dipoles antennas but with a different tile-like layout. Each tile contains a dipole protected by a waterproof casing and the tiles themselves are covered with an additional waterproof fabric layer. Thanks to this design, it is possible to safely walk across a HBA station. These antenna operate between 110-240 MHz, with a central frequency of 144 MHz.

The ILT is composed of 52 stations across Europe, with the majority located in the Netherlands, where 24 core stations and 14 remote stations are situated. The core stations are near Exloo in the Netherlands, arranged in an island-like structure colloquially known as the "Superterp". There are an additional 14 international stations with the largest baseline being 1980 km, spanning between the stations in Ireland and Poland. Other international station locations include five in Germany, three in Poland, one each in France, UK, Ireland, Luxemburg, and Sweden.

The station layout varies depending on the type of station, but here I focus on the HBA layout. Core stations consist of two "ears", each with 24 antennas. Remote stations are larger, containing 48 antenna, while the largest stations are the international stations with 96 antennas. Due to the larger physical size of the international stations, they have the smallest station beams, which limit the final FoV.

It is notable to mention that LOFAR is currently offline. Due to the low-frequency nature of this array, the quality of observations is highly dependent on the ionosphere, as discussed in Section 2.1.4. Ionospheric conditions are influenced by solar activity, so when the Sun is more active, the ionosphere becomes more turbulent, which adversely affects radio observations. The solar cycle follows an average period of 11 years and in 2025 we are at a solar maximum. While this has thrilled aurora enthusiasts, enabling the Aurora Borealis to be visible across parts of the UK, it poses significant challenges for low-frequency radio astronomers. During such periods, ionospheric disturbances can render large amounts of telescope observing time useless.

The solar maximum will last for several years, and during this time LOFAR has paused its operations to enable an upgrade: LOFAR 2.0. This upgrade will add two new international stations to the array, one in Italy and another in Bulgaria. The primary improvement for LOFAR 2.0 will be to the LBA. Currently, only half of the LBA antennas

can be used during an observation. However, after the upgrade, all LBA antennas will be utilised, significantly increasing the array's sensitivity. Furthermore, observations with the LBA and HBA will now be conducted simultaneously. Due to the lower frequency of the LBA, deriving calibration solutions is considerably more challenging than for the HBA. However, with simultaneous observations, calibration solutions from the HBA can be transferred to the LBA, aiding in its calibration process.

The main survey conducted with the HBA is the LOFAR Two-metre Sky Survey (LoTSS Shimwell et al., 2017, 2019, 2022), which operates at 144 MHz and aims to map the entire northern sky. The third data release (DR3) is internally released and contains 13.7 million radio detections, many of which have never before been detected in the radio, or at all. The second data release reaches a sensitivity of 83 μJy beam^{-1} with a resolution of 6″. This level of sensitivity at this frequency was unprecedented. As shown in Figure 2.3 (Morabito et al., 2022b), LoTSS occupies a previously unexplored regime in radio astronomy. Alongside LoTSS DR1, three Deep Fields were also published: ELAIS-N1, Lockman Hole, and Boötes (discussed in Section 1.3). Like the main LoTSS survey, these images have a 6″ resolution but cover a much smaller sky area. Despite the smaller coverage, these fields are significant given the unprecedented depth of these images.

It is important to note that for this survey, only the core and remote stations of the ILT were utilised, meaning that the international stations were not included, even though these stations were also collecting data during these observations. This exclusion is due to the complex technical strategies required to incorporate the international stations into the data reduction process. However, their inclusion is possible through VLBI, which is introduced in Section 2.1.3.

LOFAR-VLBI

LOFAR truly becomes a unique and powerful radio interferometer when the international stations of the array are included. These stations, located across Europe, can be incorporated into the data reduction process using VLBI techniques. By utilising the full potential of the ILT, we improve the angular resolution of our observations by a factor of 20, allowing us to achieve sub-arcsecond resolution at 144 MHz, down to 0.3″. LoTSS-HR (LoTSS High Resolution) is also illustrated in Figure 2.3, demonstrating that including the interna-

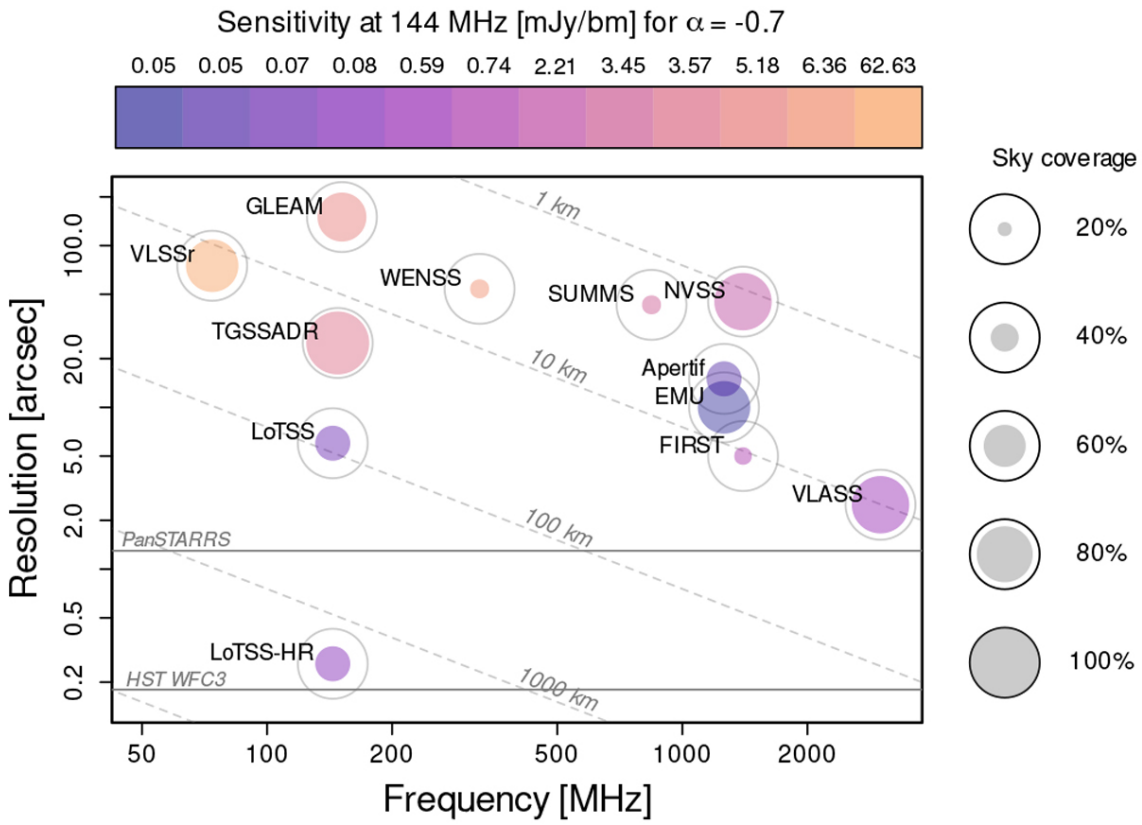

Figure 2.3: Figure demonstrating the parameter space occupied by various radio telescopes. We can clearly see both LOFAR lie in a new regime with high sensitivity at such low frequencies. Credit: Morabito et al. (2022b).

tional stations produced unprecedented resolution at this frequency. It is also important to note that, using these VLBI techniques, the resolution we achieve is comparable to optical telescopes such as the Hubble Space Telescope (HST).

As performing VLBI at such low frequencies is a complex procedure (see Chapter 4), the vast majority of publications using the ILT rely on 6″ data available from LoTSS. Thanks to a publicly available pipeline (Morabito et al., 2022b), high-resolution processing is becoming standard practice (Morabito et al., 2025a), and it will become even more accessible with the upcoming automated version of the pipeline (van der Wild in prep.).

Incorporating the international stations into the data reduction process to obtain sub-arcsecond resolution is vital for understanding the origin of radio emission from these sources. At 6″ resolution, i.e., using only the Dutch stations, around 90% of the sources detected in LoTSS (Shimwell et al., 2019) are unresolved. This implies that the emission originates on spatial scales smaller than our instruments beam produced with only the Dutch stations, meaning we can only measure the emission integrated over this resolution element. Consequently, we cannot decipher the origin of radio emission from these sources from the radio morphologies alone, because improving the resolution, hence reducing the beam size, may reveal extended structure that is not compact on this same scale. This is why employing VLBI techniques, alongside brightness temperature measurements, is essential for disentangling the radio emission at sub-arcsecond scale.

LOFAR-VLBI Wide-field

While the most common application of LOFAR-VLBI is producing images centred on an individual sources, the capabilities of the ILT extend far beyond this. Using this method, we can only study the sub-arcsecond radio emission from a single source at a time, and since each pointing can take months to reduce, we are limited by sample statistics, hence restricting our ability to address the open questions outlined in Section 1.1.2. However the ILT, provides a solution to this limitation.

Thanks to the ILT's impressive FoV, this instrument is also ideal for performing wide-field, high-resolution surveys. Building on the VLBI techniques required to produced single source images, we can produce images on a wide-field scale of ∼6 deg^2, containing thousands of sub-arcsecond sources per image. Of course, producing such extensive im-

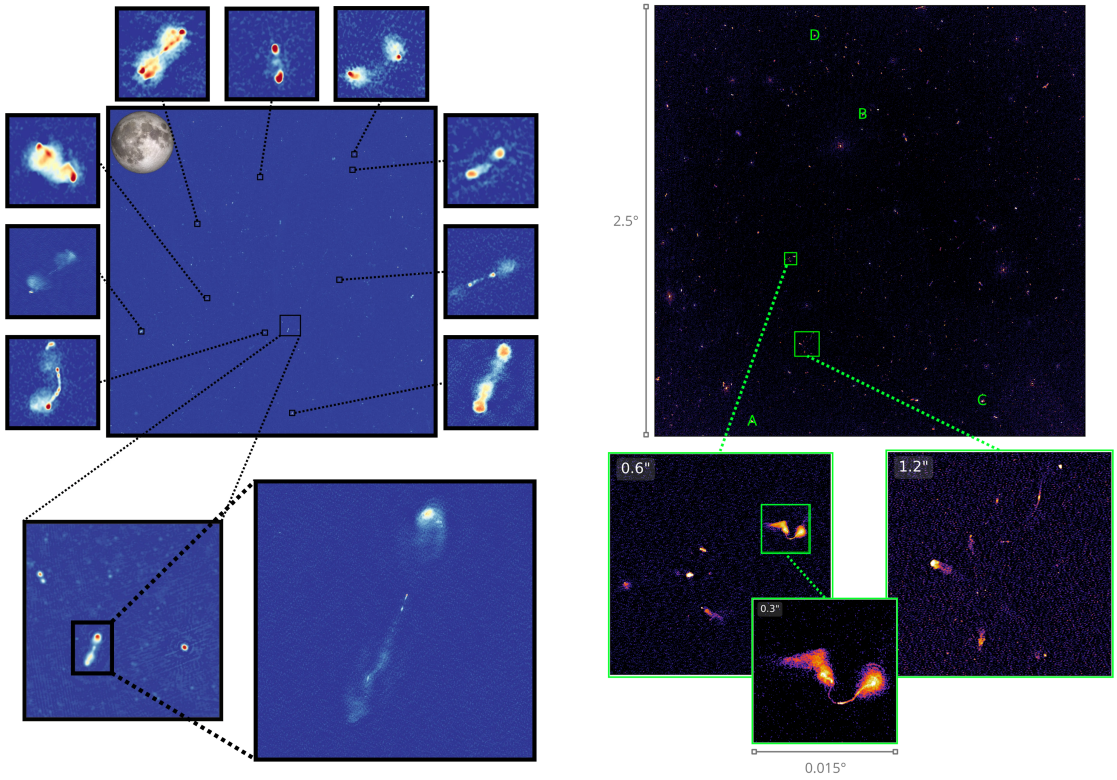

Figure 2.4: The two previously published wide-field 144 MHz sub-arcsecond resolution images of Lockman Hole (left credit: Sweijen et al., 2022) and ELAIS-N1 (right credit: de Jong et al., 2024).

ages is not straightforward, as there are further complications introduced in the calibration process. As described in Section 2.1.4, the ionosphere presents a significant hurdle at low-frequencies, and this challenge is amplified in the wide-field domain. Ionospheric conditions can vary on arcminute scales, causing sources in the FoV to shift and vary in amplitude with each source experiencing these effects differently. For instance, some sources may appear brighter, while others dimmer due to local ionospheric variations. Furthermore, with VLBI observations incorporating stations separated by over a thousand kilometres, the ionospheric conditions vary above each station. Therefore, calibrating and correcting these effects to produce wide-field, low-frequency images is a strenuous task, which is why such images using the ILT remain exceptionally rare.

Thus far, only two wide-field, sub-arcsecond resolution images have been published using the ILT, and these are two of the LoTSS Deep Fields discussed in Section 1.3 and shown in Figure 2.4: Lockman Hole, and ELAIS-N1. The sub-arcsecond resolution image of the Lockman Hole field (Sweijen et al., 2022) was the first wide-field, sub-arcsecond image produced with the ILT. The observation had an 8-hour integration time and achieved a central sensitivity of 25 μJy beam^{-1}, detecting 2483 sources detected across the ~ 6 deg^2 FoV. The ELAIS-N1 image (de Jong et al., 2024) combines four ILT observations to achieve a total integration time of 32-hours, resulting in a substantially deeper image. At $0.3''$, this image achieves a central sensitivity of 14μJy beam^{-1}, detecting 9203 source.

These images consist of billions of pixels in order to achieve the highest possible resolution, making them highly computationally expensive. The Lockman Hole image required around 250,000 CPU hours, while improvements in calibration and imaging reduced the computational cost for ELAIS-N1 to 139 CPU hours per pointing. A sub-arcsecond image of the Euclid Deep Field North (EDFN; Bondi et al., 2024) will soon be publicly available (Bondi et al. in prep.). In Chapter 4 of this thesis, I present the third sub-arcsecond 144 MHz image of one the LoTSS Deep fields: the Boötes Deep Field.

Thanks to the thousands of sub-arcsecond resolution 144 MHz sources detected in these deep, wide-field images, we can now construct statistically significant samples of radio-quiet AGN. This enables us to probe kpc-scale radio emission, and with optical spectroscopic measurements we can study the kinematics of the [O III] emission line.

Together, these tools allow us to address key open questions: What physical mechanism is driving the connection between radio emission and [O III]? What are the relative contributions of the different radio emission mechanisms in radio-quiet AGN? Which [O III] kinematic components are most enhanced by radio activity? This thesis begins to shed light on these questions.

CHAPTER 3

Unveiling AGN Outflows: [O III] Outflow Detection Rates and Correlation with Low-Frequency Radio Emission

In this chapter I present a chapter published in Monthly Notices of the Royal Astronomical Society on connecting [O III] outflows to low-frequency radio emission (Escott et al., 2025). In this chapter I use the LOFAR Two Metre Sky Survey Deep Fields Data Release 1 (LoTSS Deep DR1) and perform spectral fitting on optical Sloan Digital Sky Survey (SDSS) spectra to compare [O III] properties and kinematics between populations of AGN with a radio detection and those without.

3.1 Introduction

A significant number of observational studies show that at the centre of almost every galaxy, there is a super-massive black hole (SMBH; Kormendy & Richstone, 1992, 1995; Magorrian et al., 1998) and when a SMBH shows signs of accretion, it is known as an Active Galactic Nucleus (AGN). Some of the most powerful objects in our Universe and the most powerful subclass of AGN, which are termed quasars, have the potential to emit a bolometric luminosity of 10^{48} erg s^{-1} (see Alexander & Hickox, 2012, for a review). The gravitational potential of an accreting SMBH can power intense phenomena (Antonucci, 1993; Urry & Padovani, 1995) which can expel vast amounts of gas out of the host galaxy.

The activity from the SMBH is believed to have a profound effect on the evolution of the galaxy, a process called AGN feedback, although our only evidence for this is indirect (Fabian, 2012). I see in observational data that there is a correlation between the mass of the SMBH and global properties such as the velocity dispersion of the galaxy (Gebhardt et al., 2000; Merritt & Ferrarese, 2001), which suggests the two are linked. Furthermore, cosmological simulations are unable to reproduce the observed Universe without including AGN feedback providing heating effects from AGN in their models (Bower et al., 2006; Croton et al., 2006). AGN feedback can be enacted by powerful phenomena such as shocks induced by winds, ionised and molecular outflows, and jets. However, despite indications that AGN impact how galaxies form and evolve, AGN feedback is still a major open area of research, with many questions waiting to be answered, such as which physical processes are the major cause of turbulent outflows in the interstellar medium (ISM) and how these outflows differ with galactic properties.

Processes that generate radio emission are often associated with AGN feedback. One channel is through the most powerful radio jets that commonly originate from AGN which have a much higher radio to optical flux density ratio (radio-loud AGN; Kellermann et al., 1989). Powerful radio jets are clearly seen to interact with their environments and host galaxies, for example by driving bulk outflows of ionised gas (e.g., Tadhunter & Tsvetanov, 1989; Villar-Martín et al., 1999; Birzan et al., 2004). I see evidence for AGN feedback from these radio jets on large scale (~100 kpc), e.g from galaxy clusters (e.g., McNamara & Nulsen, 2012; Gitti et al., 2012; Timmerman et al., 2022) where jets inflate radio lobes into the ISM producing X-ray cavities. On galactic scales, jets are associated with, for

example, disturbed emission line kinematics (e.g., Zakamska & Greene, 2014; Speranza et al., 2023) or radio lobe expansion (Webster et al., 2021).

The radio emission from radio-loud AGN is likely due to a radio jet being present (Urry & Padovani, 1995), on the other hand the origin of the radio emission in radio-quiet AGN remains unclear. The emission could be produced by low-powered jets, the corona, stellar winds or star formation (see Panessa et al., 2019, and references therein). Bonzini et al. (2015); Padovani et al. (2011); Delvecchio et al. (2017) suggest the emission is due to star formation however, other studies (e.g., White et al., 2015; Macfarlane et al., 2021; Calistro Rivera et al., 2023; Yue et al., 2024) propose that the radio emission from radio-quiet AGN is due to accretion activity rather than star formation. Moreover, Petley et al. (2022) connects the radio emission in broad absorption line quasars to the outflow properties, suggesting the radio emission may originate from AGN induced winds.

The [O III] λ5007 emission line is commonly used as a tracer for warm, ionised gas outflows. These outflows are firmly linked to radio properties, which makes studies of the connection between radio and [O III] a promising avenue for investigating AGN feedback. Rawlings et al. (1989) shows that the [O III] and radio luminosities are correlated in a sample of radio galaxies at $z \sim 0.5$. Mullaney et al. (2013) characterises the [O III] λ5007 profiles of 24,264 optically selected AGN at $z \sim 0.4$ and links the most disturbed [O III] to being induced by compact radio cores rather than powerful radio jets. Using a sample of 129 uniformly selected radio AGN with $z < 0.23$, Kukreti et al. (2023) uses stacking analysis with SDSS spectra to discover that radio AGN with a peak in their radio spectra drives a broader outflowing component in [O III] than radio AGN without a peak in their spectrum. In the more distant Universe, Nesvadba et al. (2017a) presents the [O III] λ5007 maps and kinematics for 33 $z > 2$ radio galaxies using VLT/SINFONI imaging spectroscopy, finding complex gas kinematics in all sources and Zakamska et al. (2016) studies the [O III] kinematics of red quasars at $z \sim 2.5$ using `XSHOOTER` on the VLT, discovering very broad and blueshifted [O III] emission lines. Extending to a sample of radio-quiet AGN, Jarvis et al. (2019) and Girdhar et al. (2022) show that jets drive bi-conical [O III] outflows with the jets strongly interacting at their termini with the ISM. Due to these links between radio emission and [O III] outflows, after identifying outflows, I can then compare the extracted kinematics to radio data and start to understand how the

radio emission is linked to these outflows.

The [O III] λ5007 emission line is driven by both a gravitational and non-gravitational component. The gravitational component is dependent on the virial motion of the gas of the host galaxy, whereas if an outflow is present, this will produce a non-gravitational component which is commonly seen as the blueshifted shoulder (Greene & Ho, 2005). Woo et al. (2016) suggests that the enhanced [O III] velocity dispersion seen with increasing radio luminosity is due to host galaxy properties. They report that the positive relation between [O III] velocity dispersion and $L_{1.4\mathrm{GHz}}$ becomes insignificant once normalised by the stellar velocity dispersion. However, more recently Ayubinia et al. (2023) shows that radio activity does play a role in the enhancement of ionised gas kinematics after normalising in stellar velocity dispersion, suggesting that radio activity yields an additional boost to these outflows. It is still unclear how and to what extent radio emission is linked to the ionised outflows observed in the [O III] emission line.

The LOw Frequency ARray (LOFAR; Haarlem et al., 2013) has the potential to provide the answer. The LOFAR Two-metre Sky Survey (LoTSS; Shimwell et al., 2017, 2019, 2022) is an ongoing survey, which aims to cover the entire northern hemisphere at a frequency of 144 MHz. With this data, 6″ resolution imaging is possible with an average sensitivity of ∼70 μJy beam^{-1}. Due to LOFAR's wide field of view and high level of sensitivity, it is a powerful instrument to conduct deep field surveys. Alongside LoTSS there is also a data release for three deep fields: Lockman Hole, European Large Area Infrared Space Observatory Survey-North 1 (ELAIS-N1) and Boötes (Sabater et al., 2021; Tasse et al., 2021). The first deep fields data release reached sensitivities of 22, 20, and 30 μJy beam^{-1}, respectively, which before LoTSS was unprecedented at such low frequencies. To emphasise how deep this survey is, if LOFAR operated at the same $L_{1.4\mathrm{GHz}}$ frequency as the VLA (Very Large Array), then Boötes and Lockman would have sensitivities (assuming a typical synchrotron spectral index of -0.7) of 6 μJy beam^{-1}and 5 μJy beam^{-1}, respectively. Comparatively the VLA-COSMOS Deep Survey (Schinnerer et al., 2004, 2007) reaches sensitives between 7-15 μJy beam^{-1} at this frequency, but only covers ∼ 2 deg^2 of the sky, whereas the LoTSS Deep Fields combined cover a much larger field of view of ∼ 27 deg^2, providing bigger samples for statistical studies. With such deep data at low frequencies I can probe significantly faint radio emission produced

predominately by synchrotron emission, without susceptibility to free-free contamination, to further our understanding of the radio sky and large samples of low radio luminosity AGN can be obtained and studied.

This is the first of two chapters to help us further understand the link between [O III] and low frequency radio emission. Within this chapter, I fit the [O III] emission line to investigate [O III] kinematics of AGN within the LoTSS Deep Fields to investigate the link between radio emission and [O III] kinematics for a well-defined sample of AGN. This allows us to compare the [O III] properties between AGN detected within the LoTSS Deep Fields and AGN that are not detected. In chapter 5, I will fully utilise the capabilities of LOFAR by studying the radio morphologies of these AGN at sub-arcsecond resolution using images from Sweijen et al. (2022); de Jong et al. (2024), and chapter 5. This will allow us to understand the radio emission of these AGN down to sub-galactic scales and link these morphologies to [O III] kinematics and outflows.

In this chapter, I first summarise the data and sample selection in Section 3.2. In Section 3.3 I outline the spectral fitting procedure and treatment of [O III] outflows. I present the results of this chapter in Section 3.4 and then the discussion and conclusions are in Section 3.5 and 3.6 respectively. In this work I assume a WMAP9 cosmology (Hinshaw et al., 2013) with $H_0 = 69.32$ km s^{-1} Mpc^{-1}, $\Omega_m = 0.287$, and $\Omega_\Lambda = 0.713$.

3.2 Data

3.2.1 LoTSS Deep Fields

I focus on all three LoTSS Deep Fields: ELAIS-N1, Lockman Hole, and Boötes (Sabater et al., 2021; Tasse et al., 2021) (~7.15 deg^2, ~10.7 deg^2, and ~9.5 deg^2 respectively). I use the Deep Fields in LoTSS due to Lockman Hole and ELAIS-N1 benefiting from high-resolution images presented in (Sweijen et al., 2022) and (de Jong et al., 2024). A similar image will soon be available for the Boötes field (Escott et al. in prep). In chapter 5, I use these high resolution images to further understand the link between [O III] and radio emission. Furthermore, I use these Deep Fields because the low-frequency radio emission is ~4 times deeper than the standard DR2 LoTSS images meaning I can probe a new parameter space, down to fainter radio luminosities. These fields also provide

excellent ancillary data. The observations are at a central frequency of 144 MHz for both Boötes and Lockman Hole, and 146 MHz for ELAIS-N1, with a total integration time of 80 hours for Boötes, 112 hours for Lockman Hole and 164 for ELAIS-N1. Boötes has a central sensitivity of 32 μJy beam^{-1}, for Lockman Hole the central sensitivity is 22 μJy beam^{-1}, and 20 μJy beam^{-1} for ELAIS-N1, with the noise increasing towards the edge of the images and bright sources.

Multi-Wavelength Data

The multi-wavelength catalogue for the LoTSS Deep Fields is described in Kondapally et al. (2021) but I summarise the data here. The LoTSS Boötes Deep Field catalogue is cross-matched with the NOAO Deep Wide Field Survey (NDWFS; Jannuzi & Dey, 1999) which are detected in the I and IRAC 4.5 μm bands (Brown et al., 2007, 2008) where Brown et al. (2007) combines 15 multi-wavelength bands between 0.14 μm and 24 μm from various surveys with PSF matched aperture photometry. The catalogue also contains: Ultra Violet (UV) from GALEX surveys, Near Infrared (NIR) from Gonzalez et al. (2010), as well as Mid Infrared (MIR) from the *Spitzer* Deep Wide Field Survey (SDWFS; Ashby et al., 2009), and Far Infrared (FIR) data from HerMES and MIPS.

The multi-wavelength catalogue for Lockman Hole has the largest area of the Deep Fields covered in Kondapally et al. (2021) and has wavelength coverage between 0.15 μm and 500 μm. The MIR data uses the IRAC instrument on the *Spitzer* Space Telescope (Werner et al., 2004), more specifically, SWIRE (Lonsdale et al., 2003) and the *Spitzer* Extragalactic Representative Volume Survey (SERVS; Mauduit et al., 2012). For more details on both fields consult Kondapally et al. (2021).

ELAIS-N1 has the same wavelength coverage as Lockman Hole, 0.15-500 μm, and the MIR data also uses SWIRE AND SERVS. The UV data is from the Deep Imaging Survey (DIS) using GALEX (Martin et al., 2005; Morrissey et al., 2007), the NIR data is from the UK Infrared Deep Sky Survey (UKIDISS) Deep Extragalactic Survey (DXS) DR10 (Lawrence et al., 2007), and FIR from HerMES and MIPS. The optical data comes from the Pan-STARRS-1 (Kaiser et al., 2010) and HSC-SSP (Aihara et al., 2018).

I use derived properties for the radio detected AGN such as star formation rates (SFR) and stellar masses from the catalogue described in Best et al. (2023). The authors use

Spectral Energy Distribution (SED) fitting to calculate these derived properties. These SEDs span from the UV to FIR and from these the authors obtain a consensus SFR and consensus stellar mass. When an AGN component is present, this is accounted for within the SED fitting code.

3.2.2 Optical SDSS Spectra

In this work, I use optical spectra from the Sloan Digital Sky Survey (SDSS). To identify these spectra, I use two catalouges: the SDSS DR16 Quasar catalogue (Lyke et al., 2020) and a broad-line AGN catalogue from (Liu et al., 2019). The DR16 Quasar catalogue (Lyke et al., 2020) consists of 750,414 spectroscopically confirmed quasars across 9,376 square degrees. The broad-line AGN catalogue, Liu et al. (2019), is composed of 14,584 AGN at $z < 0.35$, identified by the width of Balmer emission lines, particularly Hα. Lyke et al. (2020) includes all quasar sources classified by SDSS I,II and III, while the catalogue from Liu et al. (2019) identifies broad-line AGN among SDSS DR7 sources. The SDSS spectra associated with these catalogues are from the original SDSS spectrograph or the newer BOSS instrument. The wavelength coverage for the original spectrograph is 3800-9200 Å, compared with the improved BOSS coverage of 3650-10400 Å with a spectroscopic resolution of 1500 at 3800 Å, and 2500 at 9000 Å . These catalogues together fill the redshift-luminosity space with AGN at lower redshifts (Liu et al., 2019) and quasars at higher redshifts (Lyke et al., 2020). I use these two catalogues as the basis to select our sample as described in Section 3.2.3.

3.2.3 Sample Selection

To construct our sample, I first remove any sources in Liu et al. (2019) that are duplicated within Lyke et al. (2020) and then apply Multi-Order Coverage Maps (MOCs) of the respective Deep Fields (Kondapally et al., 2021) so that radio data from the LoTSS Deep Fields (see Section 3.2.1) is available. Bright sources may also affect the data quality of some areas of the sky. I therefore apply starmasks [1] to each field to remove this unreliable data.

[1]The MOCs and starmasks are available at `https://lofar-surveys.org/deepfields.html`

The next step is to ensure [O III] spectral information is accessible so I can analyse the emission line's kinematics. I remove AGN from our sample with $z > 0.83$, to ensure I can analyse [O III] equally across the AGN. This leaves 332 AGN remaining.

The spectra for seven sources could not be downloaded from the SDSS spectral search and upon manually searching their plate details it appeared these spectra had no spectral lines which indicates potential incorrect classification, hence I remove these from our sample. I remove an additional two AGN in Boötes. One is removed because upon visual inspection I find that [O III] and Hβ are double peaked emission lines, which can be characteristic of dual AGN (Zhou et al., 2004). Very Long Baseline Interferometry (VLBI) imaging at 1.7 GHz and 5 GHz from Frey et al. (2012) further supports that this object is a dual AGN. For the other source, I choose to discard this due to a lack of emission lines in the optical spectrum, including [O III]. It is possible that this is a mis-identification or this AGN could be an optically quiescent quasar (Greenwell et al., 2021), which maybe obscured due to a "cocooned" phase of the NLR (Narrow Line Region). To confirm this, I would require the infrared (IR) spectrum to see if there is strong [O III] emission present and an X-ray observation to see if the emission can be identified as an AGN. In the Lockman Hole field, I remove three AGN after attempting to fit the spectra. It became clear there is not enough information in the spectral window to provide robust fits and therefore I remove the sources from the sample. This leaves a sample of 320 AGN: 100 in Boötes, 137 in Lockman Hole and 83 in ELAIS-N1.

The results of this chapter rely on extracting information from spectra, so I implement a Signal-to-Noise (SNR) cut of 5, where the signal is taken from the continuum subtracted [O III] λ5007, while the noise is measured from two line-free spectral windows at 5040-5060 Å and 4760-4840 Å . I also test SNR cuts of 3 and 10 and find the results remain consistent, therefore I use a cut of 5 as a balance between high SNR and sample size. The mean SNR of the 320 AGN is 15.32 and using a cut of 5 I reduce the sample from 320 AGN to 217 AGN with a similar percentage of sources removed in each field. The SNR cut is necessary because, as discussed in Section 3.3.1, distinguishing between broad, weak outflows and noise can be difficult for low SNR sources.

To further ensure that any [O III] emission is real and not noise, I incorporate a cut which removes AGN which have a very broad narrow component fitted to [O III], where

the peak of this narrow component is not significantly higher than the RMS (root mean squared) noise. If an AGN has a single component with a FWHM (Full Width Half Max) greater than 850 km s^{-1} and the peak of the fitted component is less than 5 times the RMS of [O III], I remove these sources. This leaves 208 AGN.

I cross-match all 208 AGN with the optical and IR catalogue from Kondapally et al. (2021) using a search radius of 2″ . I then ensure that MIR data are available for all of these sources which I can use as a proxy for AGN luminosity as described in Section 3.2.4. I discover that two sources (105057.30+593214.4 and 105902.18+584008.2) do not contain channel 3 and/or channel 4 *Spitzer* information and therefore I are unable to conduct the matching process described in Section 3.2.4 and hence I remove these two sources from our sample. This leaves 206 AGN.

As part of the SDSS targeting procedure, in DR16Q many AGN are targeted because they are detected within 1″ of a FIRST radio source, which could provide a radio-biased sample. I therefore remove 8 sources with either a `QSO_EBOSS_FIRST`, `QSO1_EBOSS_FIRST` or `QSO_FIRST_BOSS` flag, all of which are located in Boötes.

This leaves us with a final sample of 198 AGN. 90 reside in Lockman, 55 in Boötes, and 53 in ELAIS-N1.

Radio Properties of the Sample

The multi-wavelength catalogue from Kondapally et al. (2021) has already been cross-matched with the LoTSS data, providing radio information. As mentioned previously, the flux limits for the three Deep Fields are different. There is only one 5σ source in Lockman Hole and another in ELAIS-N1 which is below the flux limit in the Boötes field. I therefore move these sources (ILTJ104811.63+591047.6 and ILTJ160946.89+550533.3) from the radio detected to radio non-detected population to provide an effectively consistent flux limit for the sample, but note that this does not change the results. I find that 115 of the 198 sources have a LoTSS detection: 33 in Boötes, 55 in Lockman Hole, and 27 in ELAIS-N1. This leaves 83 AGN without a detection; 22 in Boötes, 26 in ELAIS-N1, and 35 in Lockman Hole.

I calculate the 144 MHz k-corrected luminosity using the spectral index, α (where $S_\nu \propto \nu^{-\alpha}$), assuming a typical synchrotron spectral index of $\alpha = 0.7$ (Klein et al., 2018)

and use the spectroscopic redshift from SDSS. For the radio non-detected AGN, I present upper limits calculated using the median value of an aperture with radius 3″ from the RMS map of the relevant field [2] to ensure any possible emission is captured.

The final catalogue of the 198 AGN will be available on CDS upon publication, containing both optical and radio data, the fitting results described in Section 3.3.1 will be available upon request.

3.2.4 $L_{6\mu m}$-z Matching

Differences seen in [O III] between our radio detected and non-detected AGN could be driven by a luminosity bias. The MIR luminosity at 6µm, $L_{6\mu m}$, is a popular tracer for AGN bolometric luminosity (Richards et al., 2006) because UV emission produced by the central AGN is absorbed by dust from the torus or NLR and gets re-emitted at MIR wavelengths, providing an orientation-free proxy for the AGN luminosity. Therefore $L_{6\mu m}$ can be used to remove an intrinsic luminosity bias between populations. I adopt a common method to match the populations in $L_{6\mu m}$ and redshift (e.g., Rosario et al., 2020; Andonie et al., 2022; Fawcett et al., 2023). I calculate $L_{6\mu m}$ for AGN within Boötes using the interpolated aperture and extinction corrected flux densities from channel 3 (5.8 µm) and channel 4 (8 µm) of the SDWFS, and for Lockman Hole, as well as ELAIS-N1, I use the *Spitzer* Wide-Area Infrared Extragalactic Survey (SWIRE; Lonsdale et al., 2003) fluxes, which are both included in Kondapally et al. (2021). To begin the matching process I start with the radio non-detected AGN (as this has the smaller population), and then I randomly select from the radio detected population so that each radio non-detected AGN has an equivalent radio detected AGN. I set the tolerance to be $\Delta\, z = 0.06$ and $\Delta \log L_{6\mu m} = 0.3$.

In Figure 3.1 I see both the total sample without any matching alongside the closest matched population, where starting from the radio non-detected AGN, the closest radio detected AGN has been matched to said radio non-detected AGN. This closest matched population contains 118 AGN in total, 59 radio detected and 59 radio non-detected and are indicated by coloured markers in Figure 3.1. When considering all 198 AGN, I can see that the average $L_{6\mu m}$ is higher in the radio detected AGN. However, after matching, the

[2] RMS maps are available at `https://lofar-surveys.org/deepfields.html`

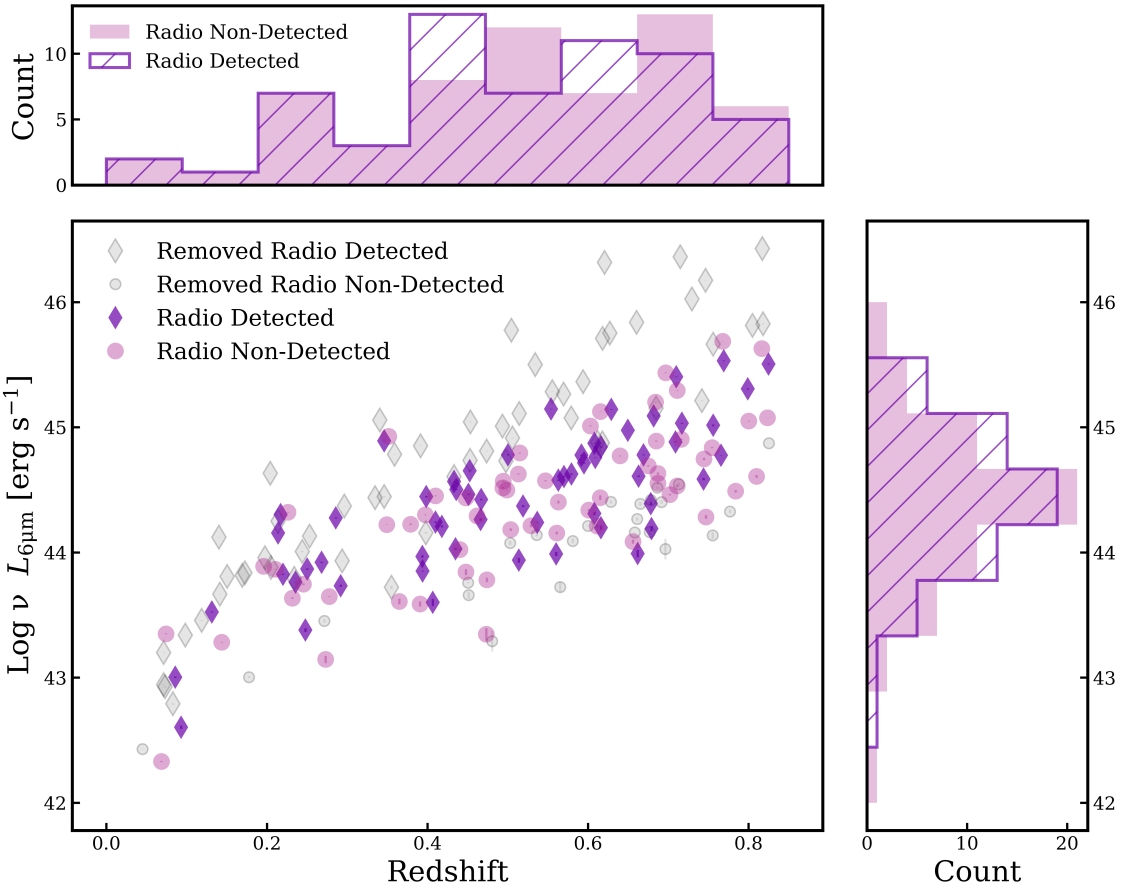

Figure 3.1: The $L_{6\mu m}$ and redshift relation of our radio and radio non-detected populations. The coloured markers show one iteration from the 1000 trials to match a radio detected AGN (purple diamonds) in $L_{6\mu m}$ and redshift to a radio non-detected AGN (pink circles). The grey points represent the AGN which, in this iteration, are removed as these are unmatched, with diamonds portraying the radio detected AGN, and circles for the radio non-detected AGN. The top histogram conveys the redshift distribution and the right histogram is the distribution of $L_{6\mu m}$. The hashed purple histogram is the radio detected AGN and the pink solid histogram are the radio non-detected AGN, showing they present similar distributions.

distribution of $L_{6\mu m}$ and redshift is now similar for the two populations. To statistically quantify the differences between the populations from the closest matched population portrayed in Figure 3.1, I perform a 2D Kolmogorov-Smirnov (KS) test after the populations are matched between the $L_{6\mu m}$ and redshift of the two populations using the public code `ndtest`[3] and obtain a p-value of 0.61, confirming that the two populations are statistically indistinguishable.

3.3 [O III] emission line profiles and outflow identification

3.3.1 Spectral Fitting

To model the emission line profile of the [O III] emission line and identify outflows, I use the fitting module of `QubeSpec` IFU analysis code [4] (Scholtz et al., 2021). I simultaneously fit the [O III] λλ4959, 5007 and Hβ λ4861 emission lines and their neighbouring continuum between λ4800 Å and λ5100 Å . To describe emission line profiles, each line is modelled with one or two Gaussian components, with the line centroids, FWHM and fluxes (normalisation) as free parameters. In each case the continuum is well characterised by a power-law with slope and normalisation as free parameters. For the [O III] λλ4959, 5007 Å emission line doublet I simultaneously fit [O III] λ4959 Å and [O III] λ5007 Å, using the respective vacuum rest-frame wavelengths of 4960.3 Å and 5008.24 Å. For both the narrow component and broad component (where present), I tie the line widths and central velocities of the two lines and fix the [O III] λ5007/[O III] λ4959 flux ratio to be 2.99 (Dimitrijević et al., 2007). I initially fit the continuum, [O III], and Hβ models.

As some of our targets are luminous Type-1 AGN, I need to take into consideration the Fe II emission, originating from close to the accretion disk (see Scholtz et al., 2020, 2021). This emission originates from a series of blended faint Fe II transitions that can appear as subtle features in the continuum that can mimic faint [O III] broad components. If I detect a broad Hβ component indicating a BLR (Broad Line Region), I refit the spectra with all the models including the Fe II templates. I follow the approach of Kakkad et al.

[3] Written by Zhaozhou Li, `https://github.com/syrte/ndtest`
[4] Available at `https://github.com/honzascholtz/Qubespec`

(2020) and use different templates: no Fe II template, Veron, BG92, and Tsuzuki. I take the Veron template from the works of Véron-Cetty et al. (2004), which takes the spectrum of I Zw 1 and uses the intensities of the broad and narrow Fe II lines to create a Fe II template. BG92, Boroson & Green (1992), removes all emission lines from I Zw 1 that are not Fe II and creates a template from this information. Finally, Tsuzuki from Tsuzuki et al. (2006) obtains further spectral information for I Zw 1 and separates Fe II emission from Mg II λ2798 in order to create this template. In each case, these templates are fitted after convolving with a Gaussian profile with a width of 2000-6000 km s^{-1} (Park et al., 2022). The free parameters for each template are Gaussian convolution width and flux normalisation of the template.

I do not couple the width and redshifts of Hβ to the [O III] as these emission lines can have different line profiles in luminous AGN such as the ones I are investigating in this work (Scholtz et al., 2020, 2021). Furthermore, our observations are not sensitive enough to detect the faint outflow component in Hβ. Instead, two Gaussian profiles describe the emission from the NLR and BLR regions (if present). The Hβ and [O III] velocity offset range from -180 km s^{-1} to 193 km s^{-1} for our matched AGN.

I use the Bayesian Information Criterion (BIC) to assess the quality of the fit and select the model with the lowest BIC score as best representing the data. I find the best-fit parameters using a Markov Chain Monte Carlo (MCMC; Goodman & Weare, 2010) method, implemented using the `emcee` python library (Foreman-Mackey et al., 2013). I set uniform priors in log space for the normalisations of the continuum, Gaussian profiles and Fe II templates, for example the FWHM of the broad component of [O III] was set to 2000 km s^{-1} and allowed to deviate between 500 km s^{-1} above and below this value. The final parameters quoted in this chapter are the 50^{th} percentile of the posterior distribution with errors describing the 68% confidence interval.

After visual inspection of the spectral fits which are deemed to have the best fit by their BIC values, I find that for several spectra, the model with the lowest BIC value did not have the best fit to [O III]. This is because I calculate the BIC value by considering the whole spectral window, i.e including Hβ. I therefore visually inspect all spectra to ensure that I prioritise the fit to the [O III] emission line, rather than other emission lines such as Hβ that are within the spectral window. Figure 3.2 and Figure 3.3 show some example

spectra.

To calculate the [O III] luminosity, I integrate the continuum-subtracted region between 4975 Å and 5030 Å . I then convert this to luminosity by using the distance modulus, using spectroscopic redshifts from SDSS. To calculate the error in the [O III] luminosity I take the inverse square root of the inverse variance from the SDSS spectral information. I then sum the errors in quadrature.

3.3.2 Identifying outflows

I identify an outflow if there is a second, blueshifted Gaussian fitted to [O III] λ5007. However, even if an outflow is present, it might not always appear as a second component, due to observational limitations. Therefore, I further make use of the non-parametric W_{80} measurement of [O III] to identify outflows. W_{80} is the velocity width containing 80% of the flux, calculated using the 10^{th} and 90^{th} percentiles of the velocities (v_{10} and v_{90} respectively) of [O III] λ5007 with $W_{80} = v_{90} - v_{10}$. I define two sub-categories of outflows following the definitions stipulated in Harrison et al. (2014). When one component is fitted to [O III], AGN with $W_{80} > 800$ km s^{-1} definitely host an outflow, and AGN with 600 km s^{-1} < W_{80} < 800 km s^{-1} are likely to be undergoing an outflow because the majority of the [O III] total flux would be due to the outflowing component which is common especially in high luminosity AGN (e.g., Carniani et al., 2015; Kakkad et al., 2020). Applying these limits is necessary to ensure that the kinematics seen are due to outflowing gas rather than gas bounded by the NLR or produced by star formation. Therefore, I separate our sample into two categories of [O III] outflows with sub-categories within them:

- Outflow Present
  - [O III] Fitted Outflow - Second, blueshifted Gaussian present
  - W_{80} Outflow - One Gaussian fitted with $W_{80} > 800$ km s^{-1}
  - W_{80} Likely Outflow - One Gaussian fitted with 600 km s^{-1} < W_{80} < 800 km s^{-1}

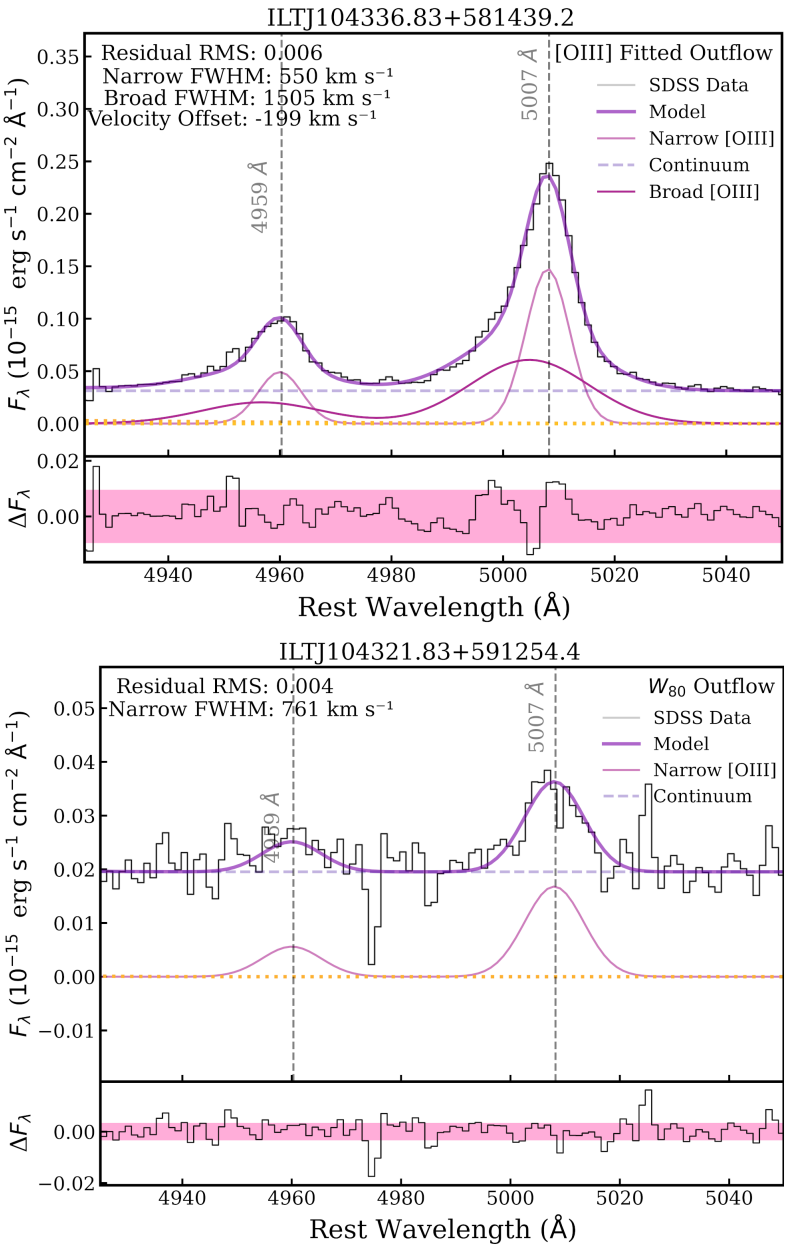

Figure 3.2: Example spectra for two categories of the [O III] SDSS spectral fitting results. The top panel of each subplot represents the SDSS spectral data in black, alongside the MCMC fitting results. The dark purple solid lines shows the final MCMC fitting result. The pink Gaussians represent the narrow component to [O III] and the Gaussians in magenta, if plotted, is the broad component of [O III] which implies an outflow is occurring. The light pink dashed lines, where present, shows the Fe II template used when modelling the data and finally the grey or yellow dashed lines shows the continuum. The lower panel of each subplot shows the residuals of the fit of the model to the SDSS data. The pink shaded region corresponds to rms 1σ region, calculated over the full spectral range of the model. This figure contains AGN from the radio detected population so the titles are the LoTSS source names. The top spectra shows an example of an AGN within the [O III] fitted outflow population and the bottom spectra shows an AGN undergoing a W_{80} outflow.

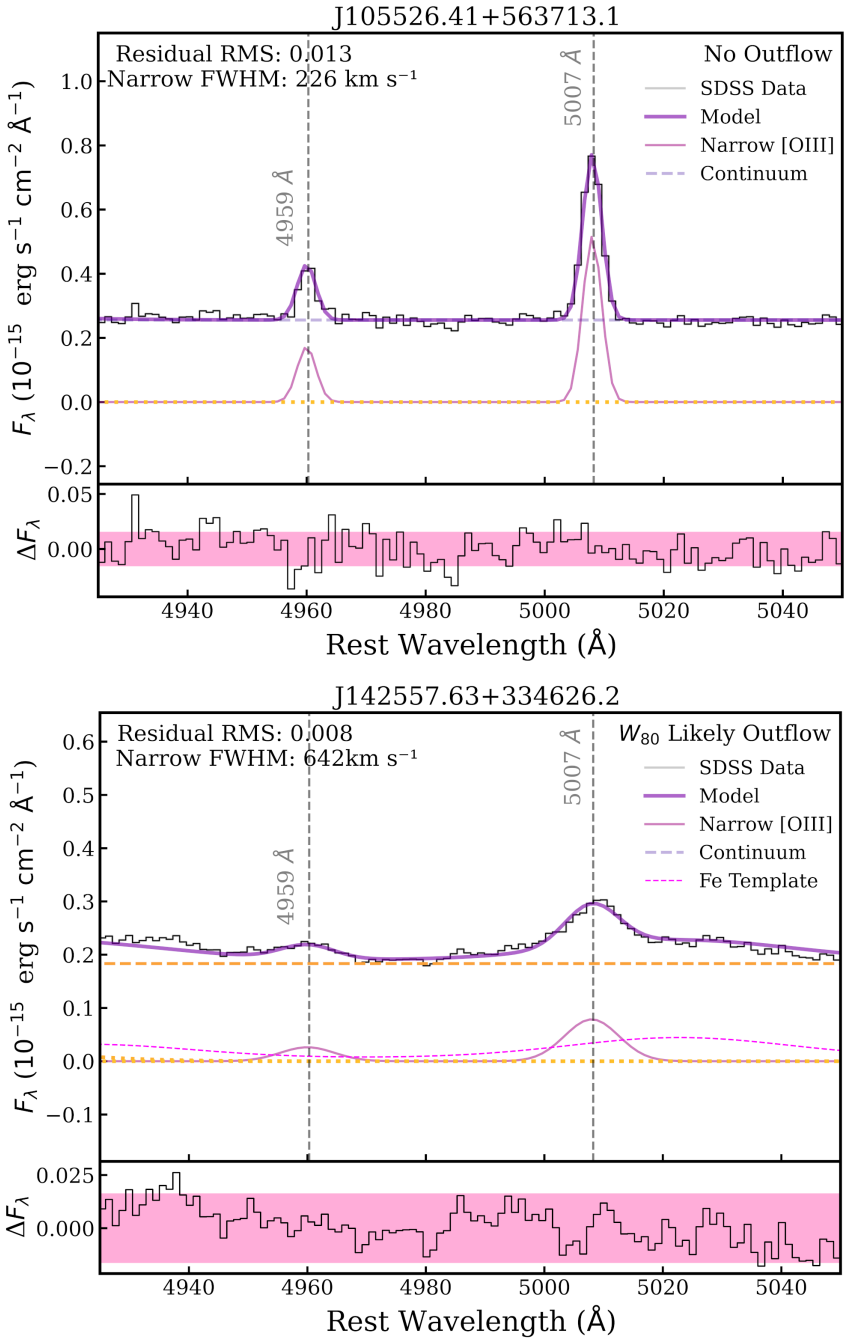

Figure 3.3: Example spectra for the other two categories of the [O III] SDSS spectral fitting results. See the caption for Figure 3.2 for details. The AGN in this figure are from the radio non-detected population so the titles are the SDSS names. The top spectra shows the spectra of an AGN within our no outflow category and the bottom spectra shows an example of an AGN which hosts a W_{80} likely outflow.

- No Outflow - One Gaussian fitted with $W_{80} < 600$ km s^{-1}

An example of spectra showing each of these categories can be seen in Figure 3.2 and Figure 3.3, where in Figure 3.2, the top panel shows an [O III] fitted outflow, and the bottom panel presents a W_{80} outflow. In Figure 3.3 the top panels shows an AGN with no outflow, and the bottom panel presents a W_{80} likely outflow.

3.3.3 Stacking

To help visualise the average proportions of the [O III] emission line profile, I stack the radio detected population and radio non-detected populations separately within our matched sub-sample. As I are most interested in comparing the outflow properties of radio detected AGN to radio non-detected AGN, I first normalise each individual spectra by both their continuum as well as the peak of the narrow component of [O III] and then stack these normalised spectra. By normalising the narrow component, I can directly compare the relative broad component in each stack. I use the stacking code presented in Arnaudova et al. (2024). In the observed frame, I first correct the spectra for Galactic extinction by using the re-calibrated reddening data from Schlegel et al. (1998), along with the Milky Way reddening curve from Fitzpatrick (1999). Then, all spectra are shifted to the rest-frame by using the spectroscopic redshifts as measured from [O III] and are resampled onto a common wavelength grid, with a channel width of 1 Å using the `SpectRes`: Simple Spectral Resampling tool (Carnall, 2017). In order to perform the stacking procedure, I take the median of each of the spectra and normalise them by subtracting the median and then dividing by the peak of [O III], where the median is computed at the reddest possible end of the area where all spectra populate the grid. A median stack is then performed where the associated uncertainties are bootstrapped. To ensure that the uncertainties are not underestimated, and that spectral features have not impacted the normalisation, an additional simulation is performed (see Arnaudova et al., 2024, for details).

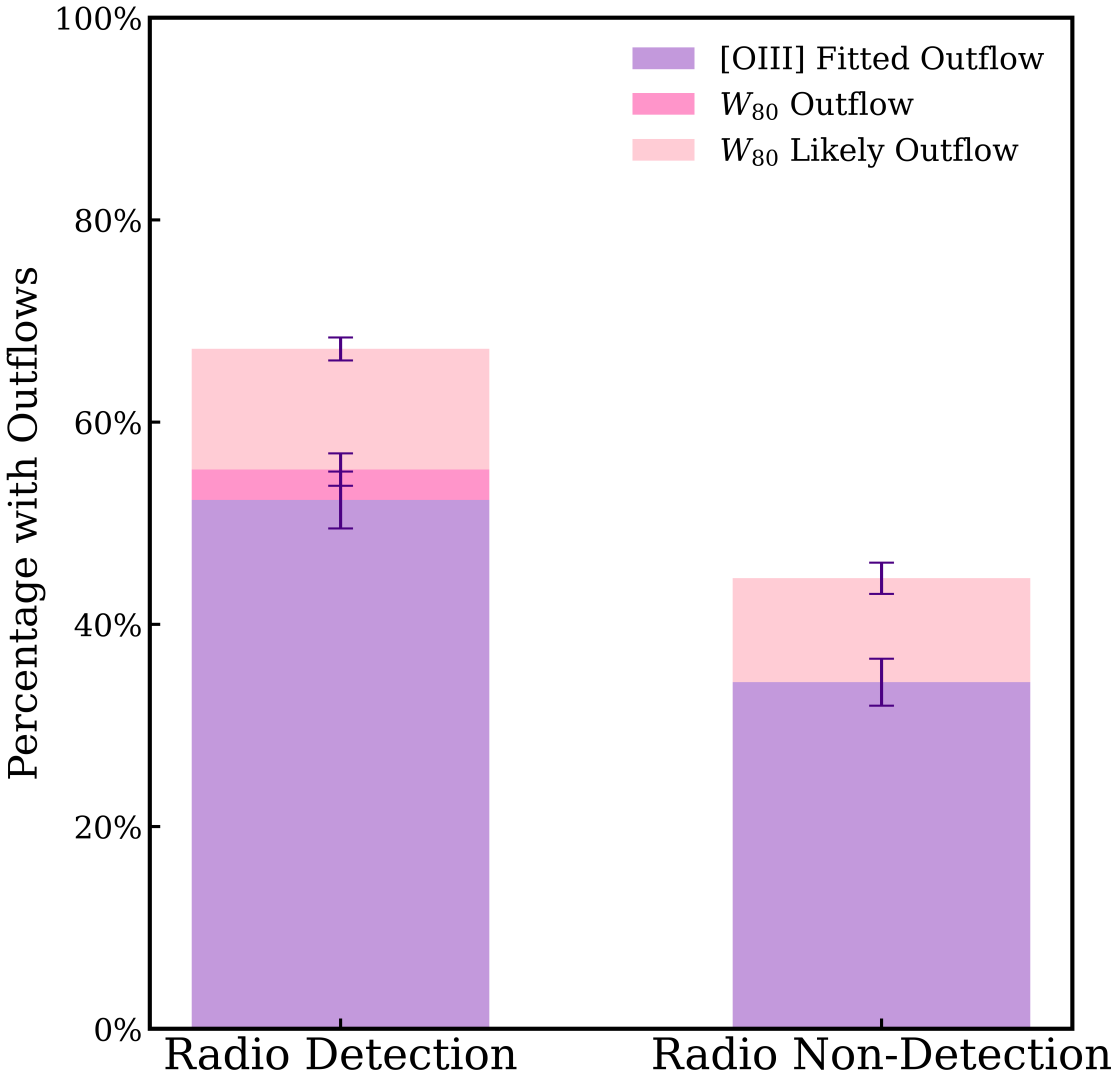

Figure 3.4: The stacked bar chart represents the average outflow detection rates from all 1000 iterations of randomly matching the radio detected AGN to the radio non-detected AGN. The light pink bar showing the W_{80} likely outflows, the darker pink is the W_{80} outflows, and the purple is the [O III] fitted outflows. For the radio detected AGN, 52.3 ± 2.8% have an [O III] fitted outflow, 3.0 ± 1.6% have W_{80} outflows, 11.9 ± 1.1% W_{80} likely outflow, and 32.8 ± 2.5% showing no signs of an outflow. In the same order the results for the radio non-detected AGN is, 34.3 ± 2.3%, 0.0 ± 0.0%, 10.3 ± 1.5% and 55.4 ± 2.4%.

	Radio Detected	radio non-detected
[O III] Fitted Outflow	52.3 ± 2.8	34.3 ± 2.3
W_{80} Outflow	3.0 ± 1.6	0.0 ± 0.0
W_{80} Likely Outflow	11.9 ± 1.1	10.3 ± 1.5
All Outflow Categories	67.2 ± 3.4	44.6 ± 2.7
Definite Outflows	55.3 ± 3.2	34.3 ± 2.3
No Outflow	32.8 ± 2.5	55.4 ± 2.4

Table 3.1: Outflow detection rates of the radio detected and radio non-detected populations, where [O III] fitted outflows have two components fitted to [O III], W_{80} outflows have a single component and $W_{80} > 800$ km s^{-1}, W_{80} likely outflows have a single component and 600 km s^{-1} < W_{80} < 800 km s^{-1}, and no outflows where a single component is fitted to [O III] with $W_{80} < 600$ km s^{-1}. AGN within the Definite outflow category have an outflow classed as either a [O III] fitted outflow, or a W_{80} outflow. AGN classed with a [O III] fitted outflow, W_{80} outflow or W_{80} likely outflow are consider in the all outflow category.

3.4 Results

3.4.1 Outflow Detection Rates

To obtain the [O III] outflow detection rate, which is the fraction of AGN that host an outflow out of each population, I calculate the number of AGN which showed signs of each category of outflow, [O III] fitted outflow, W_{80} outflow, and W_{80} likely outflow. As the matching process has inherent randomness, I calculate these fractions and bootstrap the uncertainties at the same time by re-performing the random $L_{6\mu m}$-z matching 1000 times. This provides a more representative sampling of the data and its uncertainties. From the summation of these samplings, I calculate the mean value and its 1σ (16th and 84th percentiles) uncertainties for each of these fractions. These errors are displayed in Figure 3.4.

Figure 3.4 clearly shows that I see a higher outflow detection rate in radio detected AGN than radio non-detected AGN, with > 3σ significance for AGN with a fitted [O III] outflow. Considering all outflow categories, 67.2 ± 3.4% of radio detected AGN indicate signs of an outflow compared to just 44.6 ± 2.7% of the radio non-detected AGN. If I consider only definite outflows within the [O III] fitted and $W_{80} > 800$ km s^{-1} categories, the outflow detection rates are 55.3 ± 3.2% for the radio detected AGN but 34.3 ± 2.3% for the radio non-detected AGN.

3.4.2 [O III] Properties

To further understand the differences between [O III] from radio detected AGN and radio non-detected AGN, I plot the cumulative distribution functions (CDFs) of average emission line properties in Figures 3.5, 3.6, and 3.7. As for the outflow detection rates, I use the 1000 matching runs to bootstrap the uncertainties. These CDFs encompass all 1000 matching runs. For the uncertainties, I bootstrap over all these 1000 matching runs to obtain a distribution of AGN for each bin. From these distributions I fit a Gaussian and take the standard deviation as the presented uncertainty of each bin.

Figure 3.5 shows how the populations differ in W_{80} and the FWHM of the narrow, or single Gaussian component fitted to [O III]. These CDFs contain all matched AGN. The CDF of W_{80} (Figure 3.5 top) shows us that the radio detected population has a significantly larger W_{80} across the majority of the population than in the radio non-detected sample. The results change slightly when considering the AGN within the [O III] fitted outflow category, where radio detected AGN show a significantly larger W_{80} at intermediate bins (See Appendix A.1 for additional CDFs). I do point out however that W_{80} is a non-parametric measurement and is degenerate between the narrow and the broad components.

I check if the W_{80} is dominated by one component by examining if there is a clear relationship between W_{80} and either the broad or narrow components. There is a clear dependency only when a single component is present, as expected. This is consistent with W_{80} being a non-parametric measurement with degeneracies between two components when they are present.

The bottom panel in Figure 3.5 presents the CDFs of the FWHM of the narrow, or single Gaussian component of the [O III] λ5007 emission line. It appears that radio detected AGN significantly dominate in the vast majority of bins when all matched AGN are considered. Radio detected AGN with two components fitted to [O III] still seem to dominate however at a lesser extent. For AGN with a single component fitted to [O III] the radio detected AGN appear to be very dominant within this category at all levels of FWHM (see Appendix A.1).

The top panel of Figure 3.6 presents the CDF of the FWHM of the broad component which shows that radio non-detected AGN have a larger FWHM of the second component compared to the radio detected AGN until the highest FWHM where the distributions

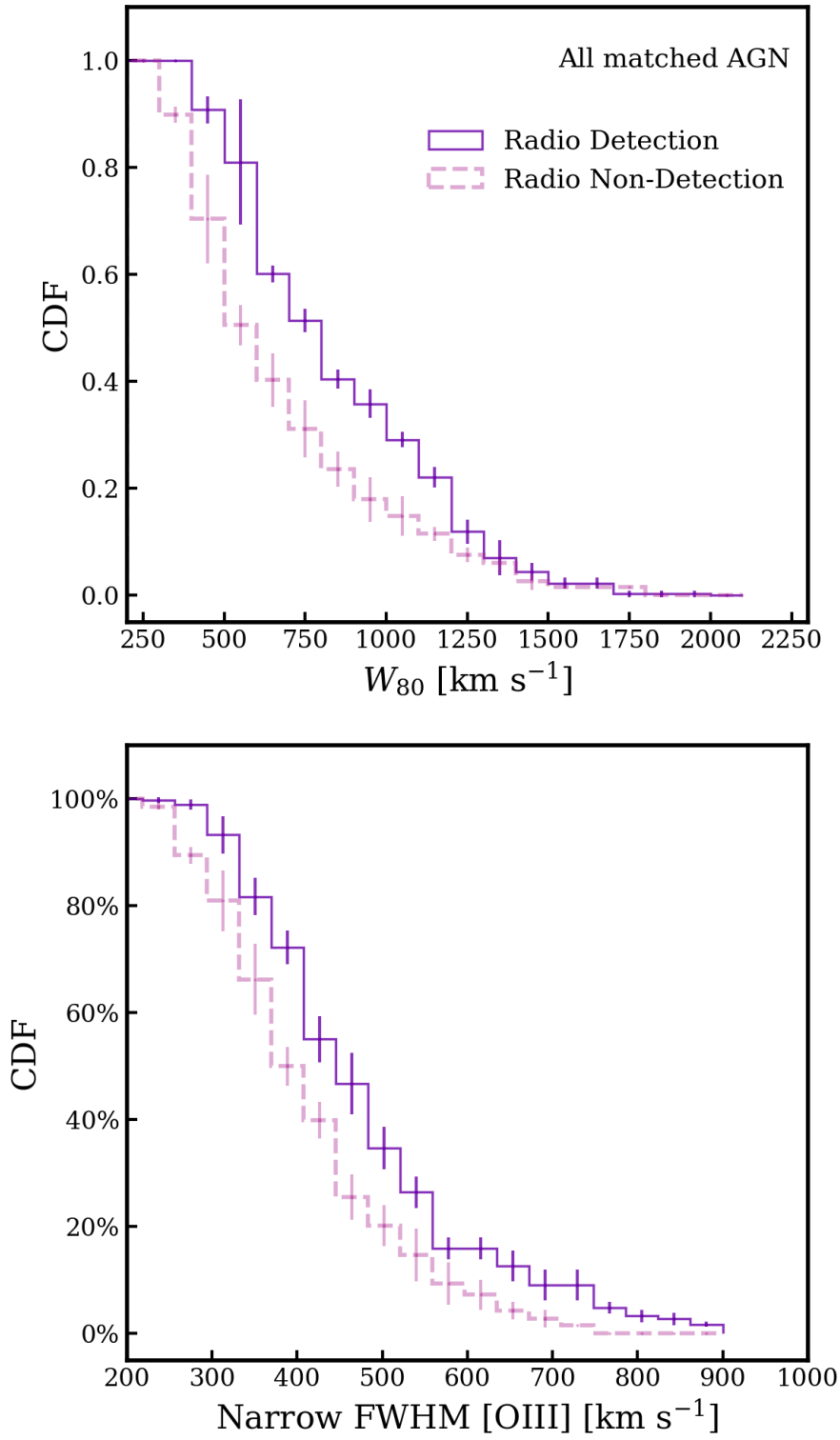

Figure 3.5: Average cumulative distribution functions of [O III] properties. The solid purple step function shows the distribution for the radio detected AGN and the dashed pink line shows the information from the radio non-detected sources. *Top:* Average CDFs of W_{80} [O III] showing the results from all 1000 matching iterations. *Bottom:* Average CDFs of the FWHM of the narrow component of [O III] with the all matching iterations. Uncertainties are constructed using bootstrapping.

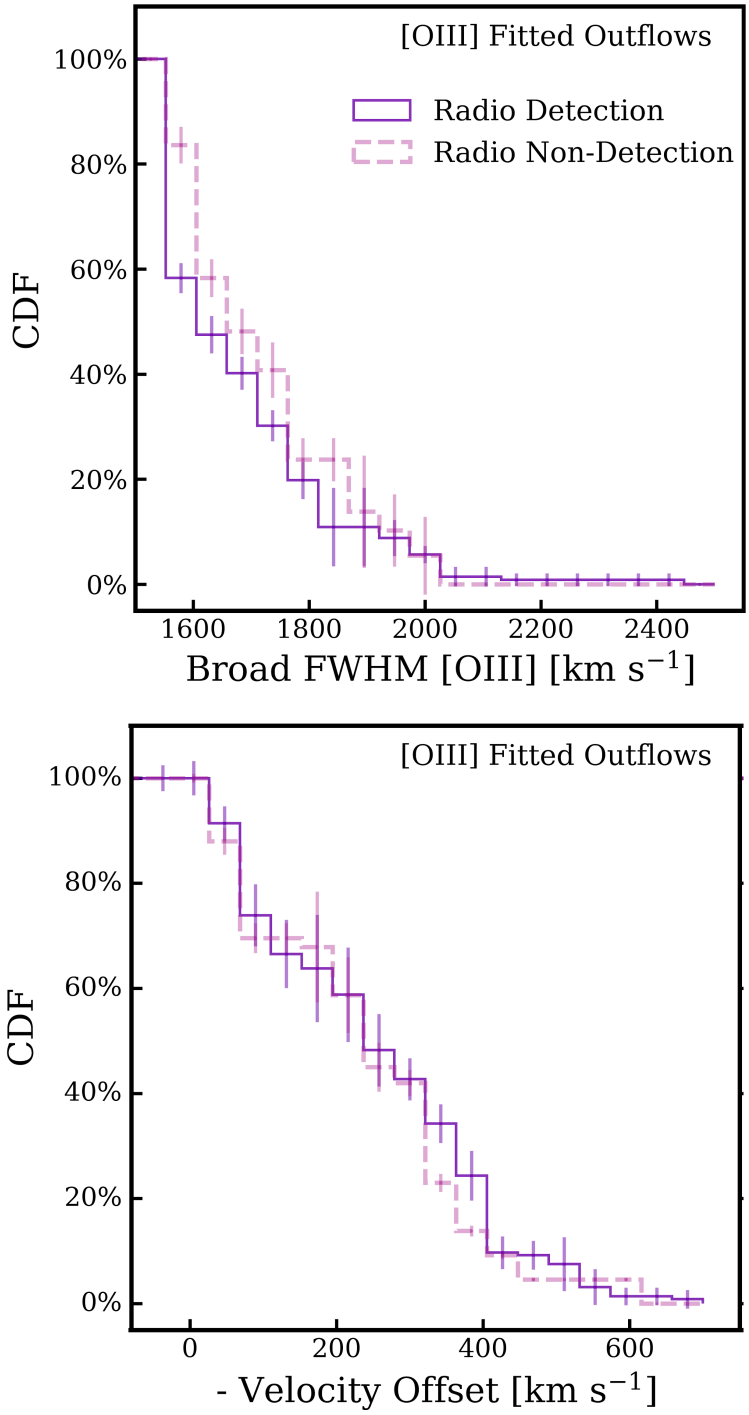

Figure 3.6: Further average cumulative distribution functions of [O III] properties. The solid purple step function shows the distribution for the radio detected AGN and the dashed pink line shows the information from the radio non-detected sources. Both panels have AGN with a second component fitted to [O III] and thus are in the [O III] fitted outflow category. *Top:* CDF of the broad component of [O III] FWHM. *Bottom:* Negative velocity offset of the broad component relative to the narrow component. Uncertainties are constructed using bootstrapping.

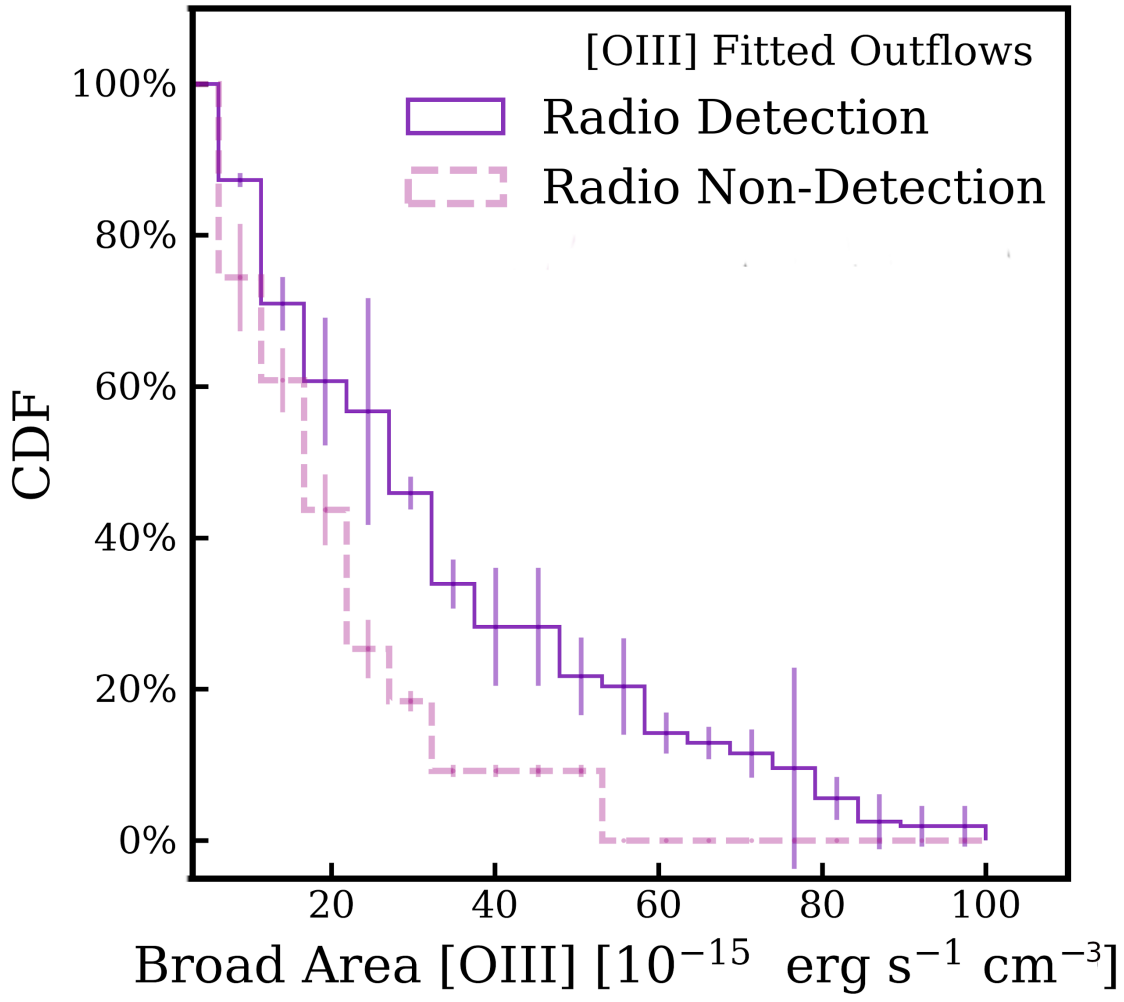

Figure 3.7: Average cumulative distribution function of the area of the broad component fitted to [O III], calculated using the peak and FWHM of the broad component. The solid purple step function shows the distribution for the radio detected AGN and the dashed pink line shows the information from the radio non-detected sources. AGN contributing to this figure have a second component fitted to [O III] and uncertainties are constructed using bootstrapping.

become equal within the uncertainties. This implies that if a second component is fitted to [O III], then this would be broader if the AGN does not have a detection in LoTSS.

The velocity offset CDF (bottom panel in Figure 3.6) shows us that the two populations have similar velocity offsets or blueshifts, aside from a few intermediate bins, where the radio detected AGN significantly dominate. I can therefore imagine that the two components in radio detected AGN would have similar separation as the two components in radio non-detected AGN.

Finally, Figure 3.7 shows the CDF for the area of the broad component of [O III] for both the radio detected and radio non-detected populations. This area is calculated using both the peak and FWHM of the broad component. This CDF informs us that radio detected AGN have a brighter broad, second, component than radio non-detected AGN at a significant level for the majority of the bins.

One of the main differences I see in the CDFs between the two populations is the kinematics of the narrow, [O III] core component with the radio detected AGN having a larger FWHM. As I are most interested in the difference between the [O III] outflowing properties of the two populations, I produce a stack in Figure 3.8 where I show the spectral fitting conducted to the median stacked spectra after I normalised spectra in the stack by the peak of the narrow component. The AGN contributing to these figures are from the closest matched population of the $L_{6\mu m}$ and redshift matching process. The top panel shows the results of the radio detected AGN and on the bottom I see the radio non-detected AGN. I see that both the radio and radio non-detected AGN stacking results show that there appears to be an [O III] fitted outflow in both populations as a broad, second, component is fitted to both. It is interesting to note that from Figure 3.8 I see an enhanced outflowing component in the normalised stack for the radio detected AGN. To quantify this, I calculate the area of just the broad component and find that the radio detected AGN have an outflowing component with an area of $204.74\ ^{+17.97}_{-18.98}$ km^2 s^{-2} compared to the radio non-detected AGN having an outflowing area of $173.91\ ^{+17.74}_{-16.11}$ km^2 s^{-2}. I note that this result is not significant when considering the extremities of these uncertainties by < 5 km^2 s^{-2}. As radio detected AGN show a brighter second component after normalisation of the narrow component, this indicates that this is not a luminosity dependent effect because the ratio of the broad to the narrow component is larger for radio detected AGN than radio non-

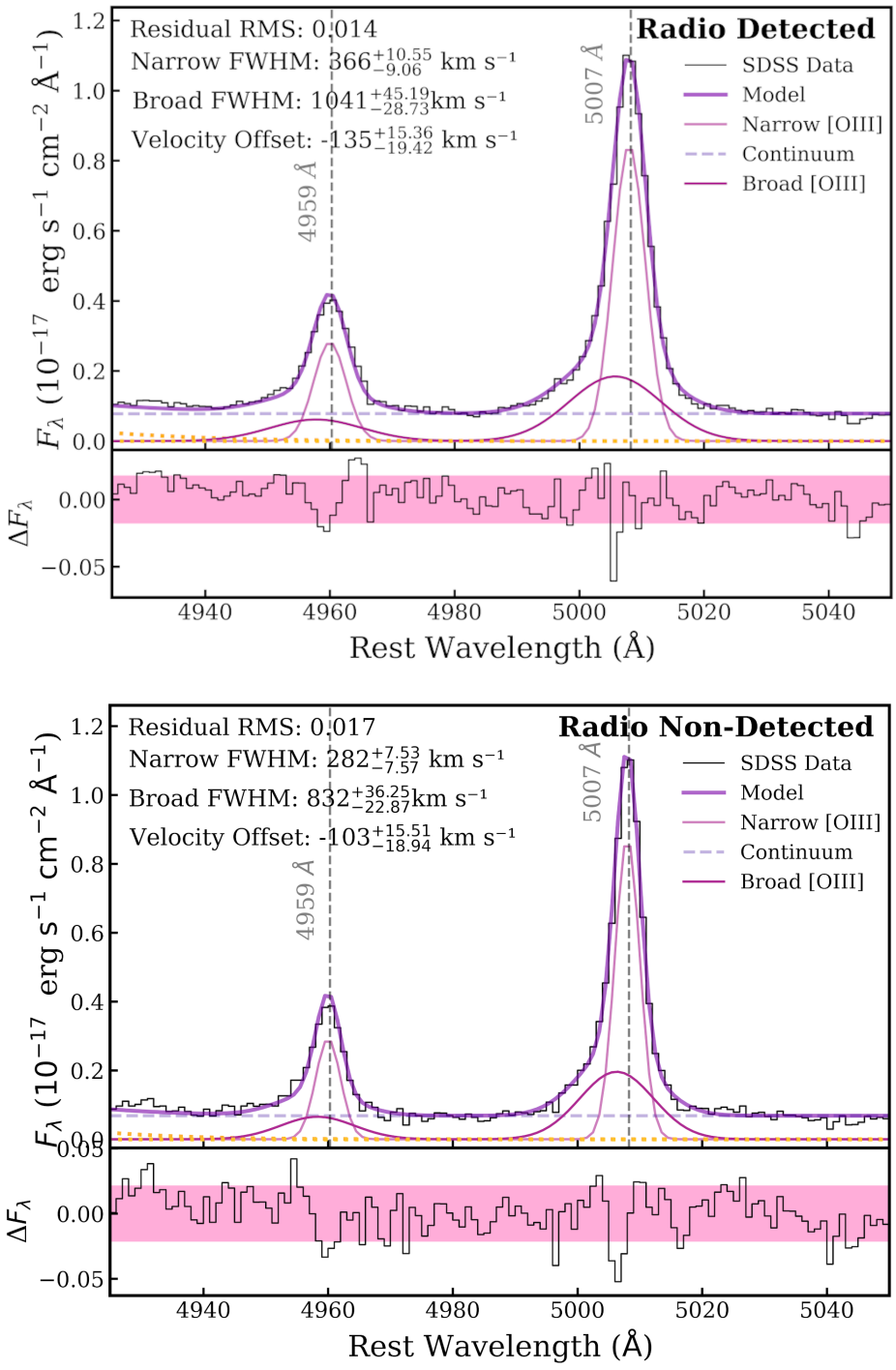

Figure 3.8: Composite spectra which are normalised by the peak of the narrow [O III] component and are produced from the closest matched $L_{6\mu m}$ and z run, containing 59 AGN in each population with the MCMC fitting tool results applied. *Top:* Radio detected AGN. *Bottom:* Radio non-detected AGN. The bottom panel shows the residuals of the fits with 1σ of the residuals highlighted in the pink region. In the upper panel, the purple solid line shows the fit from the MCMC code to the SDSS data which is shown in back. The magenta line shows the broad component of [O III] with the pink Gaussians representing the narrow component of [O III].

detected AGN, regardless of the brightness of the narrow component. From these stacks, I find the velocity offset is larger for the radio detected AGN, however if I consider the extremity of the uncertainties, this difference is not significant by < 3 km s^{-1}.

Combining all the information from the CDFs and the stacked spectra, I can begin to build a picture of [O III] for typical radio and radio non-detected AGN. The [O III] λ5007 of radio detected AGN appear to have a slightly broader, narrow component, but a narrower broad component than radio non-detected AGN, with a brighter broad component of [O III]. The distance between these two components are similar for both populations.

3.4.3 Radio and [O III] Luminosity Relationship

In this section, I explore the relationship between radio and [O III] luminosity. Figure 3.9 shows the [O III] λ5007 luminosity as a function of redshift. I bin our results in six redshift bins and take the median value of z and $L_{[OIII]}$ for the AGN in each bin. Other work conducted with similar redshift ranges are also shown (Harrison et al., 2014; Liu et al., 2013; Rodríguez Zaurín et al., 2013). Our sample has lower [O III] luminosities on average than these previous studies.

Figure 3.10 depicts the relationship between L_{144MHz} and redshift with the W_{80} of [O III] traced with a colour scale, with L_{144MHz} of the radio non-detected AGN being upper limits. I create five redshift bins and the median values of L_{144MHz} for each bin are shown, with the median absolute deviation as the error.

The relationship between [O III] and radio luminosity was first presented in Rawlings et al. (1989). They discovered a positive correlation between the total $L_{[OIII]}$ (both 5007 Å and 4959 Å) and L_{178MHz}. Figure 3.11 shows L_{144MHz} as a function of $L_{[OIII]}$ (5007 Å only) with W_{80} traced with a colour scale. Here I see that as L_{144MHz} increases, so does $L_{[OIII]}$, which is to be expected and is in agreement with Rawlings et al. (1989). I note that our results show a Spearman rank correlation of 0.223, whereas Rawlings et al. (1989) presents a value of 0.51. A value of zero indicates no association, while a value of unity indicated a strong association. I therefore find a weaker correlation than Rawlings et al. (1989). The difference may be due to Rawlings et al. (1989) using the total $L_{[OIII]}$ while I use just λ5007 Å to calculate $L_{[OIII]}$. Our results produce a best fit with a slope of 0.58. Rawlings et al. (1989) does not remove any relation that would be introduced by

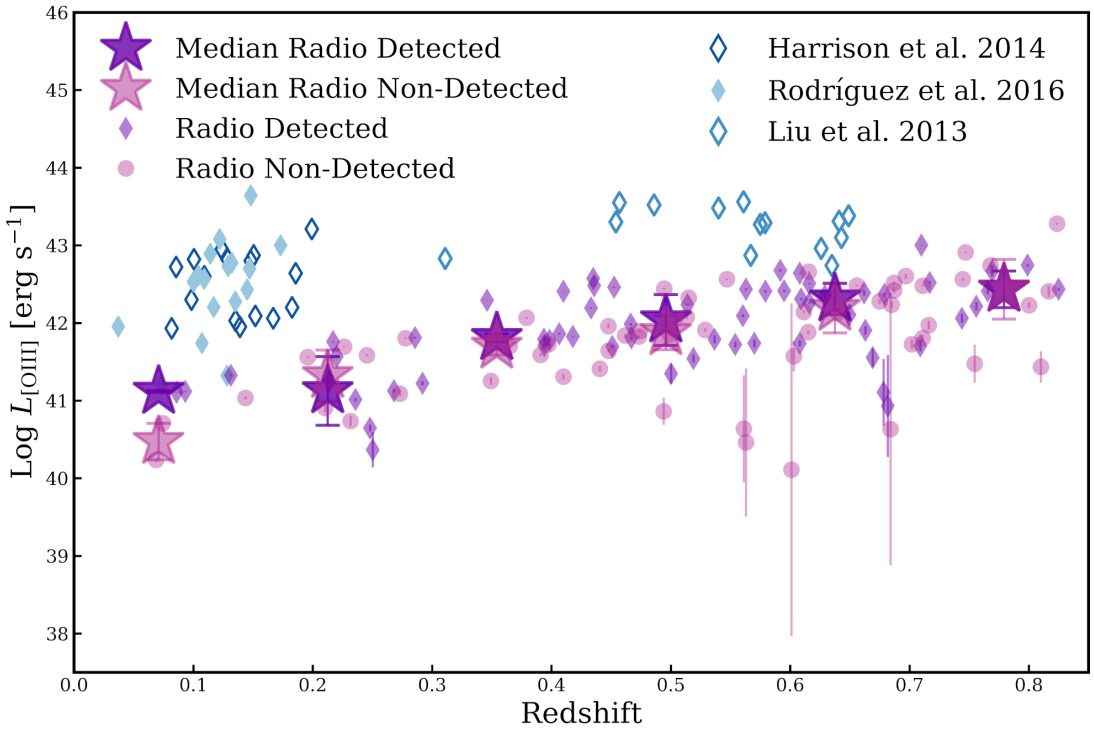

Figure 3.9: Total λ5007 Å $L_{[OIII]}$ as a function of redshift. The star markers show the median values for six redshift bins, with purple indicating the median for the radio detected AGN, and pink for the radio non-detected AGN. The errors are the median absolute deviation. For the background sources, the purple diamonds show the radio detected population and the pink circles show the radio non-detected AGN. Similar studies are presented with various blue diamond markers.

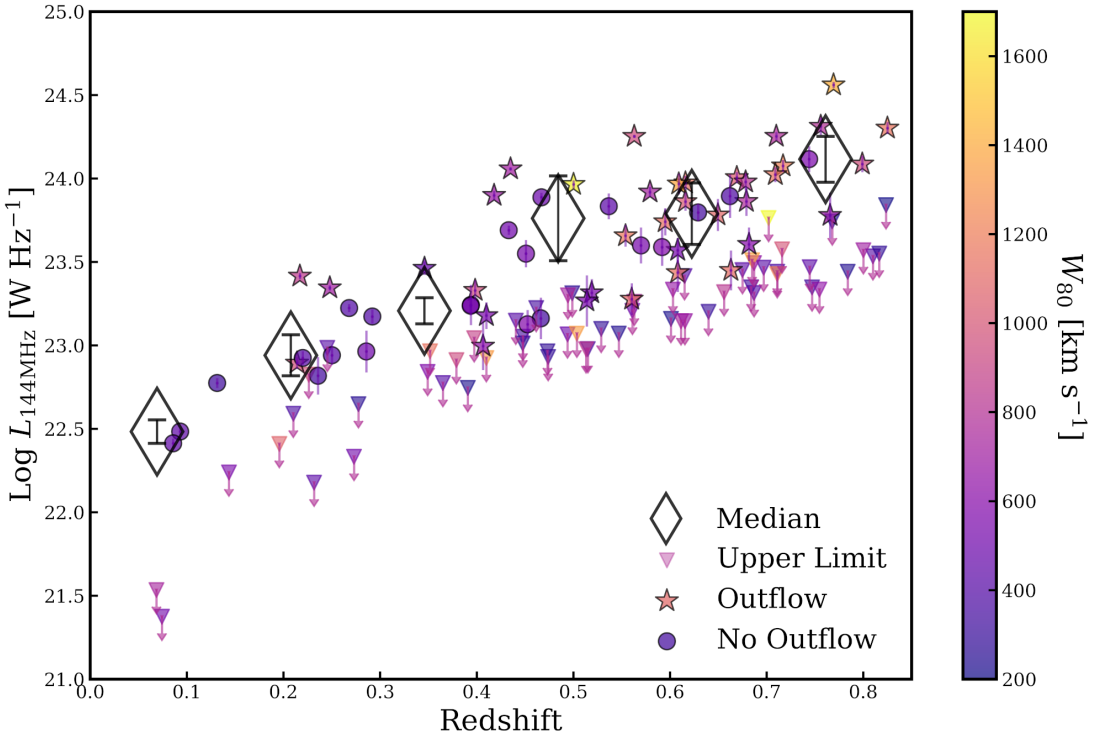

Figure 3.10: Relationship between $L_{144\mathrm{MHz}}$ and redshift with the W_{80} of [O III] traced with a colour map. Radio detected AGN are shown with either an outflow (small stars) or AGN with no outflow (circles). The median for five redshift bins are shown by large black hollow diamonds, with errors as the median absolute deviation. The upper limits for the radio non-detected AGN are shown by downward triangles.

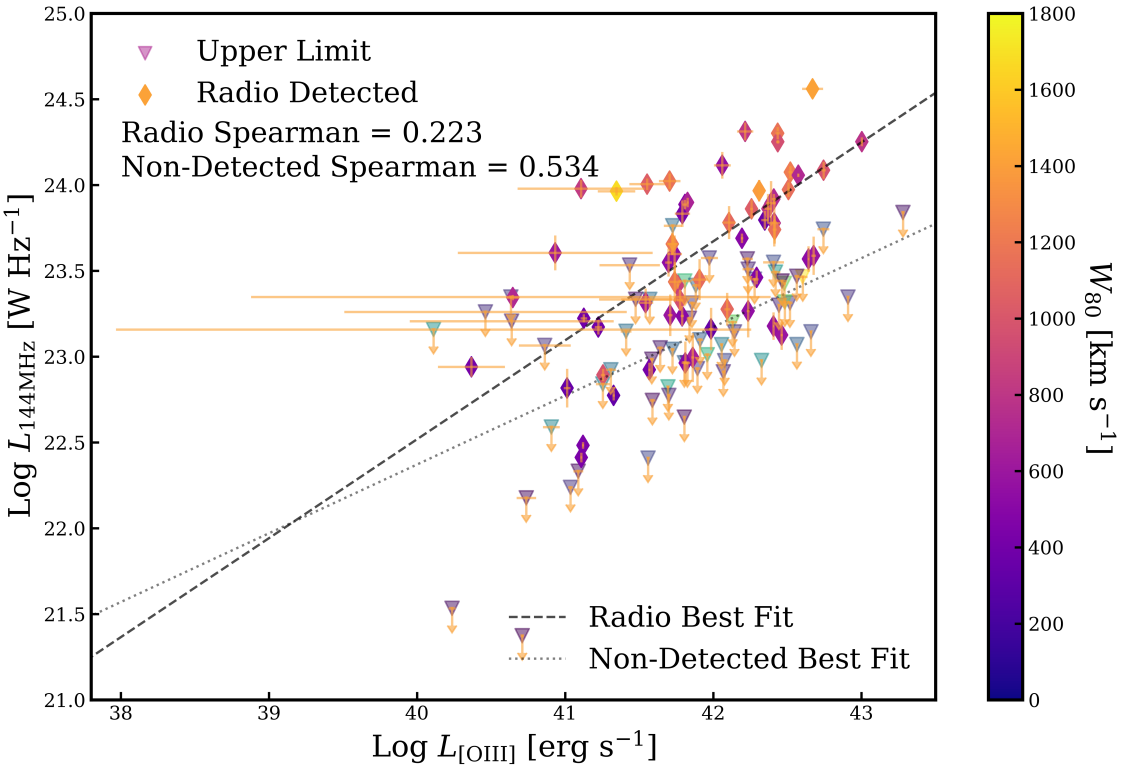

Figure 3.11: $L_{144\mathrm{MHz}}$ as a function of total $L_{[\mathrm{OIII}]}$ with the W_{80} traced by a colour scale. Radio detected AGN are plotted with diamonds and the upper limits for the radio non-detected AGN are shown by the downward triangles. The dashed black line show the best fit relationship for the radio detected AGN and the grey dotted line shows the best fit to the upper limits of the radio non-detected population.

an AGN luminosity bias, however even after matching in $L_{144\mathrm{MHz}}$ and redshift, I still see a correlation between [O III] and radio luminosity. I note that I can not determine if this relationship is real or due to the effect of the limited field of view and flux limits of our sample. To determine this I would require a larger sample.

3.4.4 Radio Emission

Radio Excess

To investigate the origin of the radio emission, I show the relationship between SFR and $L_{144\mathrm{MHz}}$ in Figure 3.12. Only radio detected sources are shown in this figure since Best et al. (2023) only carried out SED fitting to calculate the SFR for radio detected sources (see Section 3.2.1). I use the redshift presented in Best et al. (2023), which can be either spectroscopic or high quality photometric redshifts from Duncan et al. (2021), to calculate the radio luminosities to be consistent with their results. Overlaid I show our $L_{6\mu\mathrm{m}}$-z matched sample.

On the top I see the results for the sources within the Boötes field and on the bottom I see the Lockman Hole and ELAIS-N1 sources. I show these fields separately as the scatter in the Boötes is slightly different, leading to an extra adjustment in this field. I show the SFR and $L_{144\mathrm{MHz}}$ relation found in Best et al. (2023) in both panels as well as the radio excess line which is 0.7 dex above the relation in Lockman Hole and ELAIS-N1. For Boötes an extra redshift dependent correction is necessary so the radio excess line is 0.7+0.1z above the relation, due to increased scatter in the SFR and $L_{144\mathrm{MHz}}$ relation for this field. Above these lines, sources are considered to be radio excess, where their radio emission is dominated by star formation. To guide the eye, I use the maximum redshift of our sample, z = 0.83, for the redshift dependent definition of radio excess in the Boötes field.

Only four sources from our sample appear to be radio excess as they lie above the radio excess divide, one in ELAIS-N1, three in Lockman and none in Boötes. Two of the radio excess AGN have a broad, second component fitted to [O III]. Radio emission in sources above the radio excess line can be attributed to radio jets. The majority of our sample lies below the radio excess line, and I are unable to use this diagnostic to determine the origin

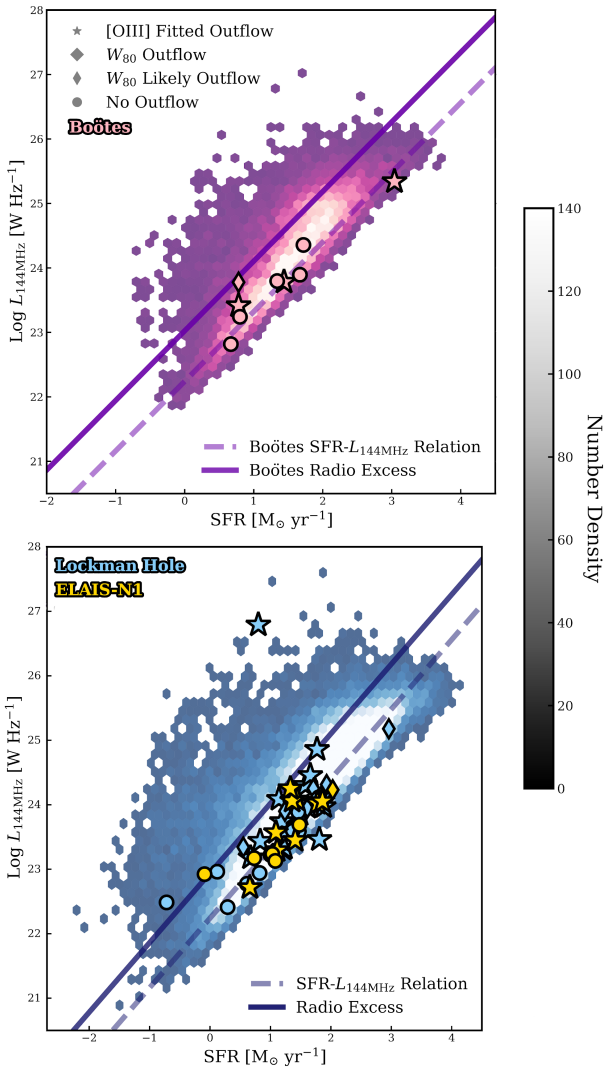

Figure 3.12: The relationship between SFR and L_{144MHz}. The upper subplot shows the result of the Boötes field (pink markers) and on the right Lockman Hole (blue markers) and ELAIS-N1 (yellow markers), the fields have been split because of the need for an extra adjustment to the radio excess in Boötes. Error bars are included but are too minimal to see. No upper limits are shown for the radio non-detected AGN because I do not have access for reliable SFR measurements for these AGN. The background hexagon bins show the distribution of sources with reliable SFR measurements with Boötes in purple and Lockman Hole and ELAIS-N1 combined in blue, where a hexagon is plotted for areas where there is four or more sources. On each panel, the faint dashed line shows the SFR-L_{144MHz} relation, which is the same for both fields. The solid line shows the radio excess divide which is 0.7 dex above the SFR-L_{144MHz} for Lockman Hole and ELAI-N1 with a slight redshift adjustment for Boötes. The over laid points with black edges are the sources within the best matched populations. The stars are sources with an [O III] fitted outflow, thick diamond host an W_{80} outflow and thin diamonds are AGN with a likely outflow. Circles represent sources that show no indication of an outflow. The colour scale traces the number density of each hexagon and is shown as grey as the scale is the same for both subplots, hence it would be pink for Boötes and blue for Lockman Hole and ELAIS-N1.

of their radio emission.

Radio Morphology

Radio morphology can help diagnose the source of radio emission, for example by identifying jets which can only be produced by AGN and not star formation. I study the radio morphology of the radio detected population at 6″ which is available using the LoTSS catalogue. I visually classify the morphology of our sample. In all our 115 radio detected AGN, I find ∼93% of sources (107/115) are unresolved, meaning only eight sources show resolved structure; two of these resolved AGN which lie within Boötes are shown in Figure 3.13, five in Lockman, and one in ELAIS-N1. These unresolved source imply radio sizes less than 4.7 kpc.

For the majority of our sample, I therefore cannot use morphology to determine the source of the radio emission. This emphasises the need for high resolution imaging to securely identify the radio morphology.

3.4.5 Comparison to Other Studies

The [O III] emission line kinematics in radio enhanced vs. radio weak AGN were studied extensively by Mullaney et al. (2013). The authors show that AGN with $L_{1.4\mathrm{GHz}} > 10^{23}$ W Hz^{-1} have a larger average FWHM than AGN with lower radio luminosities. In this large statistical sample, the authors use the flux-weighted average FWHM of the broad and narrow components whereas I study them separately. Although I have a smaller sample size, our study extends to lower radio luminosities (down to $L_{1.4\mathrm{GHz}} \sim 10^{20}$ W Hz^{-1}) and higher redshifts, and I match in $L_{6\mu\mathrm{m}}$ and redshift which may contribute to the seemingly different results I find. However, overall conclusions are still consistent: our sample is not dominated by powerful radio jets (Section 3.4.4), and I find differences in sources with strong vs. weak radio emission (either radio detected vs. not radio detected, this work; or $L_{1.4\mathrm{GHz}} < 10^{23}$ vs. $L_{1.4\mathrm{GHz}} > 10^{23}$ W Hz^{-1}, Mullaney et al., 2013). To check the consistency of our samples I convert our $L_{144\mathrm{MHz}}$ to $L_{1.4\mathrm{GHz}}$ assuming a spectral index of 0.7 and split the radio detected sample into sources with $L_{1.4\mathrm{GHz}} > 10^{23}$ W Hz^{-1} or $L_{1.4\mathrm{GHz}} < 10^{23}$ W Hz^{-1} as well as removing sources that are above a redshift of 0.4 to match their selection. I then calculate the average FWHM as in Equation 2 from Mullaney

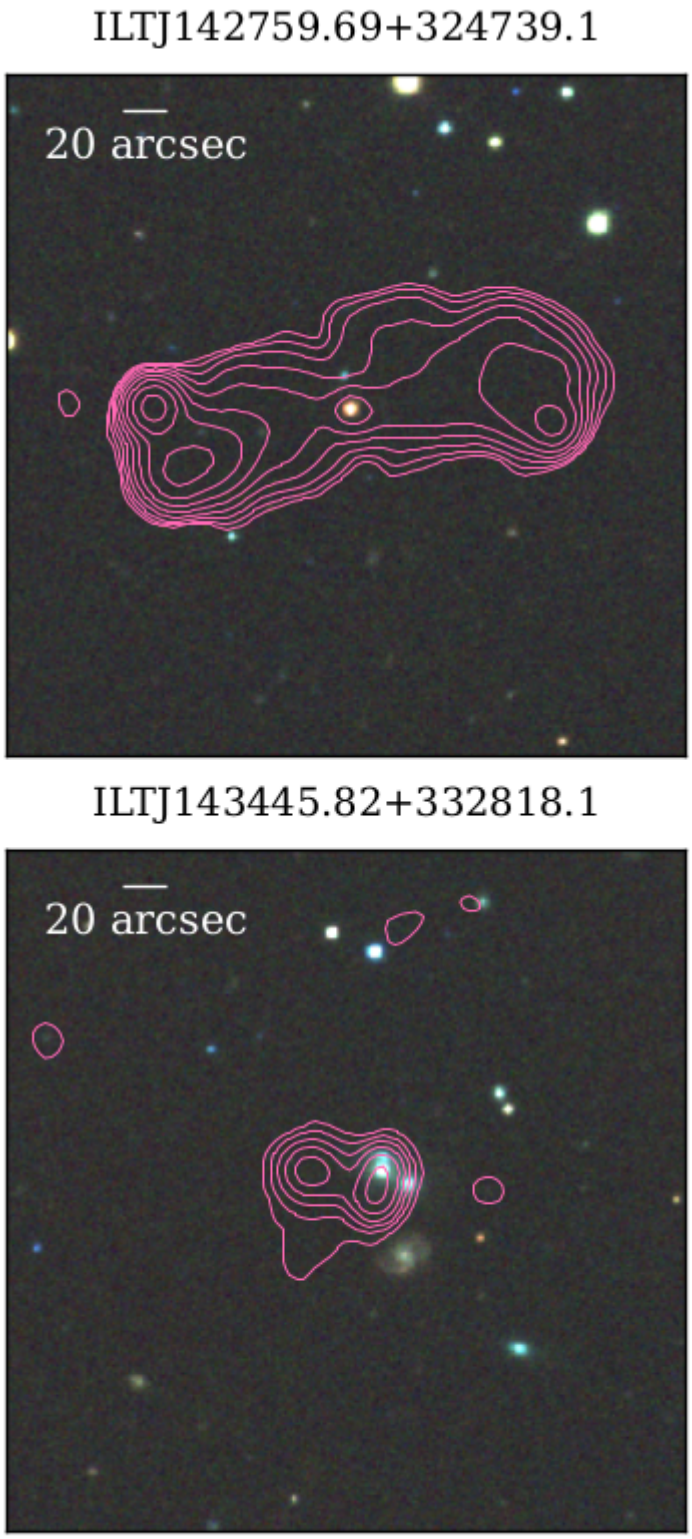

Figure 3.13: Cut outs ($150'' \times 150''$) of the only two resolved Boötes radio sources within our sample. I use the g, r and i bands from SDSS to make a composite rgb optical image. The LoTSS radio contour plots are overlayed and the noise is set to 30μJy beam^{-1} (Tasse et al., 2021). The contour levels are 3σ, 5σ, 10σ, 20σ and 40σ.

et al. (2013), and find the same trend for the average FWHM for low and high luminosity AGN (see Fig. 9 in Mullaney et al., 2013).

Recently Calistro Rivera et al. (2021) and Calistro Rivera et al. (2023) found that red quasars (which are known to be radio enhanced; Klindt et al., 2019) have a larger FWHM of the second component fitted to [O III] than their control quasars. It is difficult to draw a direct comparison between their work and ours because our sample spans the whole range of colours and the majority would not be classed as red quasars.

3.5 Discussion

I see that radio detected AGN have a higher outflow detection rate compared to our radio non-detected population as well as differences in the kinematics of the [O III] emission line between the two populations. After normalising for the narrow [O III] component, in the resulting stacked spectra I see that the radio detected AGN have a larger broad outflowing component than the radio non-detected AGN. This is suggestive of the radio detected AGN hosting outflows with a larger amount of gas than outflows produced by the radio non-detected population.

3.5.1 What is the Origin of Radio Emission?

The SFR-$L_{144\mathrm{MHz}}$ relation has shown us that the majority of sources are not radio excess in both fields. Sources above the radio excess divide have radio emission which is likely to originate from a powerful jet. As only four AGN are above the radio excess divide, this shows that the radio emission is not driven by powerful radio jets. However I can only rule out powerful jets as the dominant cause of the radio emission in this sample. The results of this chapter also indicate that radio emission is produced when a large amount of ionised outflowing gas is present and here I discuss two possible explanations as to why I see this. The possible mechanisms responsible for the radio emission in this sample are star formation, small (weak) radio jets, or shocks associated with AGN winds.

Star formation is unlikely to be the driver of radio emission in our sample. I see that in radio detected AGN, there is a significantly larger amount of outflowing gas. Star formation is a relatively weak and widespread phenomenon in a galaxy, and therefore is

unlikely to be the main driving mechanism for the increase in outflow gas.

Radio emission from low-power or small scale jets would be directional, and have a particular geometric relationship with ionised outflows. If the radio jets are co-spatial with the outflows, then it is possible the correlation between outflow detection rate and radio detection is due to orientation effects. In this scenario, the radio emission could be higher due to beaming in sources where outflows are along our line of sight. However, at the low-frequencies of these observations, I expect beaming effects to be negligible. Small scale jets can also explain the increased gas level as it could lead to more fuel for the AGN, and this fuel can possibly be launched as a radio jet later on in the AGN life cycle.

The alternative explanation is that AGN winds can be the main mechanism in producing radio emission in our sample. If the outflow is in the form of a wind then the higher level of gas would lead to the wind becoming more dense, and this increased density could cause a shock to occur within the wind and hence produce radio emission due to the particle acceleration within the shock front. This could explain the higher level of outflowing gas seen in radio detected AGN. Zakamska & Greene (2014) suggests that the driving mechanism is quasar winds that propagate into the ISM and produce shock fonts where particle acceleration occurs, hence producing radio emission. However, the authors also acknowledge that the radio and [O III] correlation could be driven by the mechanical energy of relativistic jets due to excessive heating releasing an ionised wind. The shocks suggested by Zakamska & Greene (2014) are not expected to produce radio emission causing sources to be radio excess. Nims et al. (2015) calculates that the synchrotron emission generated by shocks are about 5% of the bolometric luminosity and in a later study Zakamska et al. (2016) investigates the kinematics of [O III] of four extremely red quasars and estimates that at least 3% of the bolometric luminosity is powering the kinematic energy of dusty winds. The addition of these to the radio emission from star formation is still well within the scatter of the SFR-$L_{144\mathrm{MHz}}$ relation, and the fact that a source is not radio excess does not rule out that AGN wind shocks are the cause of the radio emission. Therefore, high resolution follow-up will be crucial to determine the origin of this radio emission.

The driving mechanism linking radio emission and [O III] outflows is still up for debate. As already discussed, Zakamska & Greene (2014) suggests that outflows trigger shocks which drive the radio emission. More recently, Liao et al. (2024) studies the

connection between w_{90} (the 90% equivalence of W_{80}) of [O III] and radio emission from median stacked radio images from the Karl G. Jansky Very Large Array (VLA) Sky Survey (VLASS) (Lacy et al., 2020) from ~37,000 radio-quiet AGN. Similar to this work, the authors confirm a significant connection between [O III] and radio emission as well as suggesting the most likely explanation for the radio emission from their radio-quiet AGN is also AGN driven by either low-powered jets or winds.

Jarvis et al. (2019, 2021) follows-up around 40 radio-quiet AGN from Mullaney et al. (2013) with high frequency, high resolution radio images from the VLA and e-MERLIN. These high resolution images proved to be crucial to determining the origin of radio emission from this sample of radio-quiet AGN, where the authors found that the majority of the radio emission originates from radio jets with star formation likely to be responsible for ~10% of the radio emission. This highlights that high resolution imaging of our sample will be key to furthering our understanding of the radio emission from our sample of 198 AGN.

3.6 Conclusions

I form a sample of 198 AGN in the LoTSS Deep Fields, 115 of which are detected in LoTSS at 144MHz, and 83 with no detection. I use SDSS as a base sample and supplement the data with the deep multi-wavelength information from the LoTSS Deep Fields. I match the radio non-detected to the radio detected AGN in $L_{6\mu m}$ and redshift to remove any possible biases from AGN luminosity.

Using an MCMC statistical approach, I fit the [O III] emission line. I place each AGN in one of the four [O III] outflow sub-categories: i) [O III] fitted outflows, where two Gaussians are fitted to [O III]; ii) W_{80} outflow with one component fitted and $W_{80} > 800$ km s^{-1}; iii) W_{80} likely outflows with one component fitted and 600 km s^{-1} < W_{80} < 800 km s^{-1}; iv) and finally no outflow, where one component is fitted to [O III] and $W_{80} < 600$ km s^{-1}.

In the radio detected population I find 67.2 ± 3.4% of these AGN show signs of an outflow occurring compared to just 44.6 ± 2.7% of radio non-detected AGN. Even when I remove the W_{80} outflow based sub-categories, radio detected AGN still show a higher outflow detection rate. This indicates that [O III] outflows are more common in AGN

where there is a detection in LoTSS compared to there being no detection present.

I use both stacked spectra and CDFs of the emission line parameters to understand the average profile of [O III] of the two populations. The CDFs tell us that radio detected AGN have a larger W_{80} than the radio non-detected AGN as well as a broader, [O III] core component, however radio non-detected AGN have a broader, second component. To allow us to just study the differences between the outflowing component [O III], I produce stacks which have been normalised by the peak of the narrow component and find that radio detected AGN have a larger outflowing component with respects to the radio non-detected AGN, implying that more gas is present in [O III] outflows hosted by a radio detected AGN. This suggests radio emission from either low-powered jets or shocks from AGN driven winds.

I find that the majority of our radio detected sources are not radio excess. Therefore this radio emission appears not to originate from high-powered radio jets but is more likely from star formation, winds or low-powered radio jets.

To determine the origin of this radio emission from radio-quiet AGN, I must study the radio morphology. However, I find that ~93% of sources within all three LoTSS Deep Fields are unresolved at 6″ . By incorporating the international stations of LOFAR I can obtain sub-arcsecond resolutions down to 0.3″ which improves the resolution by a factor of 20. Using this sub-arcsecond resolution imaging, which provides access to sub-galactic scales, I can use radio morphology and brightness temperature to determine the nature of AGN emission and separate it from radio emission due to star formation (Morabito et al., 2022b). With this sub-arcsecond resolution I will be able to study the morphology of previously unresolved sources. This will allow us to determine if the radio emission from these AGN is from the AGN activity or star formation.

The Lockman Hole Deep Field is the first widefield image produced at sub-arcsecond resolution with a frequency of $L_{144\mathrm{MHz}}$ (Sweijen et al., 2022). This process is very computationally heavy and took an estimated 250,000 core hours. A deeper image of ELAIS-N1, at the same resolution and frequency, combines four nights of observations, has also been released in de Jong et al. (2024). Using the same techniques, I are processing the Boötes Deep Field which will result in another widefield image at sub-arcsecond resolution at $L_{144\mathrm{MHz}}$. With these three datasets, I will be able to study their radio morphology and

determine whether the radio emission is from AGN activity or star formation. This will lead us closer to understanding the nature of radio emission in radio-quiet AGN.

CHAPTER 4

Strap on your Boötes: The Journey to Achieve Wide-field Sub-arcsecond Resolution with LOFAR

This chapter is based on the technical aspects of the manuscript "*Strap on your Boötes: A link between low-frequency kiloparsec radio morphology and AGN driven ionised outflows*", which has been submitted to *Monthly Notices of the Royal Astronomical Society*. Here, I focus on the data reduction performed of radio interferometric observations. The scientific results, which are made possible by the images released in this chapter, are presented and discussed in Chapter 5. Additional information and figures have been included in this chapter which are not included in the submitted manuscript, in order to offer the reader further insight into the data reduction process.

4.1 Introduction

The International LOw Frequency ARay (LOFAR) Telescope (ILT) is an interferometer that has revolutionised low-frequency radio astronomy. It consists of two arrays: the low-band antenna (LBA), operating between 10 and 80 MHz, and the high-band antenna (HBA), operating between 110-240 MHz. The ILT is an extensive interferometric network comprising 52 stations, with 38 located in the Netherlands and 14 international stations spread across Europe. With baselines extending up to 1980 km, the ILT enables Very Long Baseline Interferometry (VLBI) imaging at low-frequencies. By incorporating the international stations into the data reduction process, I can achieve sub-arcsecond resolution imaging. This improves the resolution of the main wide-area survey conducted with the ILT, the LOFAR Two Metre Sky Survey (LoTSS; Shimwell et al., 2017, 2019, 2022) by a factor of 20, as this survey only uses the Dutch stations.

Furthermore, thanks to the ILT's combination of high-resolution, impressive field of view (FoV), good uv-coverage, and high sensitivity at low frequencies, this telescope is a powerful instrument to perform both wide area and deep high-resolution surveys (Morabito et al., 2025a). Three Deep Fields were released alongside LoTSS at standard, Dutch, $6''$ resolution: Lockman Hole, European Large Area Infrared Space Observatory Survey North 1 (ELAIS-N1), and Boötes, with sensitives of 22, 20, and 32 μJy beam^{-1} respectively (Sabater et al., 2021; Tasse et al., 2021). ELAIS-N1 is now processed at its full depth of 10.7 μJy beam^{-1} using 505 hours of observations and is, to date, the deepest low-frequency radio image produced (Shimwell et al., 2025). Creating sub-arcsecond images of these fields is challenging due to ionospheric effects, which require advanced calibration techniques. To date, only two wide-field images have been published at the highest resolution at 144 MHz. Sweijen et al. (2022) published an initial, sub-arcsecond resolution image of the Lockman Hole Deep field using a 8-h integration time reaching a central sensitivity of 25 μJy beam^{-1} with 2483 sources detected. A deeper, sub-arcsecond resolution image of ELAIS-N1 with an integration time of 32-hours is published in de Jong et al. (2024) with a depth of 14 μJy beam^{-1} and 9203 source detections. This chapter presents the first high-resolution images of the third deep field, Boötes. Therefore, I now have access to a combined area of $\sim$19 deg^2 of sub-arcsecond resolution images. A sub-arcsecond image of Euclid Deep Field North (EDFN; Bondi et al., 2024) will soon be

available (Bondi et al. in prep) alongside a ∼2 deg^2 of Abell 2255 (Rubeis et al., 2025, Rubeis et al. in prep).

This chapter is structured as follows: In Section 4.2, I introduce the LoTSS Deep Field images previously published at sub-arcsecond and present the first high-resolution, wide-field images of the Boötes Deep Field at 144 MHz. Section 4.3 describes the data reduction and imaging techniques used to create the Boötes high-resolution images. In Section 4.4 I compare new Boötes sub-arcsecond image with the sub-arcsecond images of the Lockman Hole and ELAIS-N1. I conclude this chapter in Section 4.5. In this work I adopt a WMAP9 cosmology (Hinshaw et al., 2013) with H_0 = 69.32 km s^{-1} Mpc^{-1}, Ω_m = 0.287, and Ω_Λ = 0.713.

4.2 Data

4.2.1 LoTSS Deep Fields

For this investigation, I use the derived properties from LoTSS Deep Fields DR1 in Kondapally et al. (2021) which is at 6″ resolution. Best et al. (2023) provides us with star formation rates for sources within the Deep Fields derived from Spectral Energy Distribution (SED) fitting.

I take the sub-arcsecond resolution morphologies and flux densities from the 0.3″ resolution images at 144 MHz of Lockman Hole (Sweijen et al., 2022), ELAIS-N1 (de Jong et al., 2024), and Boötes. These sub-arcsecond resolution images allow us to probe low-frequency radio emission down to scales of down to sub-kiloparsec scales which is not possible at 6″. Across all fields, these 0.3″ resolution images combined cover ∼19 deg^2 which contain ∼14,000 sources at sub-arcsecond resolution.

4.2.2 Boötes high-resolution Images

Here, I release the first images of the Boötes Deep Field at 0.3″, 0.6″, and 1.2″at 144 MHz. The 0.6″ and 1.2″ images are important to understand the flux density distribution at different spatial scales. These high-resolution images and catalogues are available on the

Image	Resolution (arcsec^2)	Sensitivity (μJy beam^{-1})	Source Count
0.3″	0.50″ × 0.34″	37.0	4091
0.6″	0.67″ × 0.60″	48.2	4675
1.2″	2.23″ × 1.03″	84.6	2488

Table 4.1: Summary of the three high-resolution Boötes images presented in this work: angular resolution of each image, sensitivity and source counts.

LOFAR surveys website [1].

I present the 0.3″ resolution image of the Boötes Deep Field in Figure 4.1. This image consists of 8.09 billion pixels, has a central sensitivity of 37.0 μJy beam^{-1}, a resolution of 0.50″ × 0.34″, contains 4091 sources with detections ≥ 5σ (where σ is the local RMS noise), and has an 8-h integration time.

Our 0.6″ resolution image consists of 2.02 billion pixels with 4675 sources and has a central sensitivity of 48.2 μJy beam^{-1} with a resolution of 0.67″ × 0.60″. At 1.2″ the pixel number reduces to 0.506 billion with a source count of 2488 and a central sensitivity of 84.6 μJy beam^{-1} with a resolution of 2.23″ × 1.03″.

4.3 Data Reduction

4.3.1 High-resolution Imaging Considerations

This section briefly outlines the method I use to create the Boötes wide-field images using the ILT. For full details about the publicly available pipeline to produce VLBI images using the ILT, consult Morabito et al. (2022b) and for further information on the wide-field aspect of imaging using the ILT at sub-arcsecond, consult Sweijen et al. (2022) and de Jong et al. (2024). I summarise our data reduction here as it differs slightly from the above papers, due the fact that data processing pipelines were still in development at this time.

I retrieve the raw data of a 8-h observation to produce the high-resolution images of Boötes from the Long Term Archive (LTA [2]). The initial flux density calibrator observation

[1]The Boötes high-resolution images and associated catalogues are publicly available at: `https://lofar-surveys.org/hd-bootes.html`

[2]`https://lta.lofar.eu/`

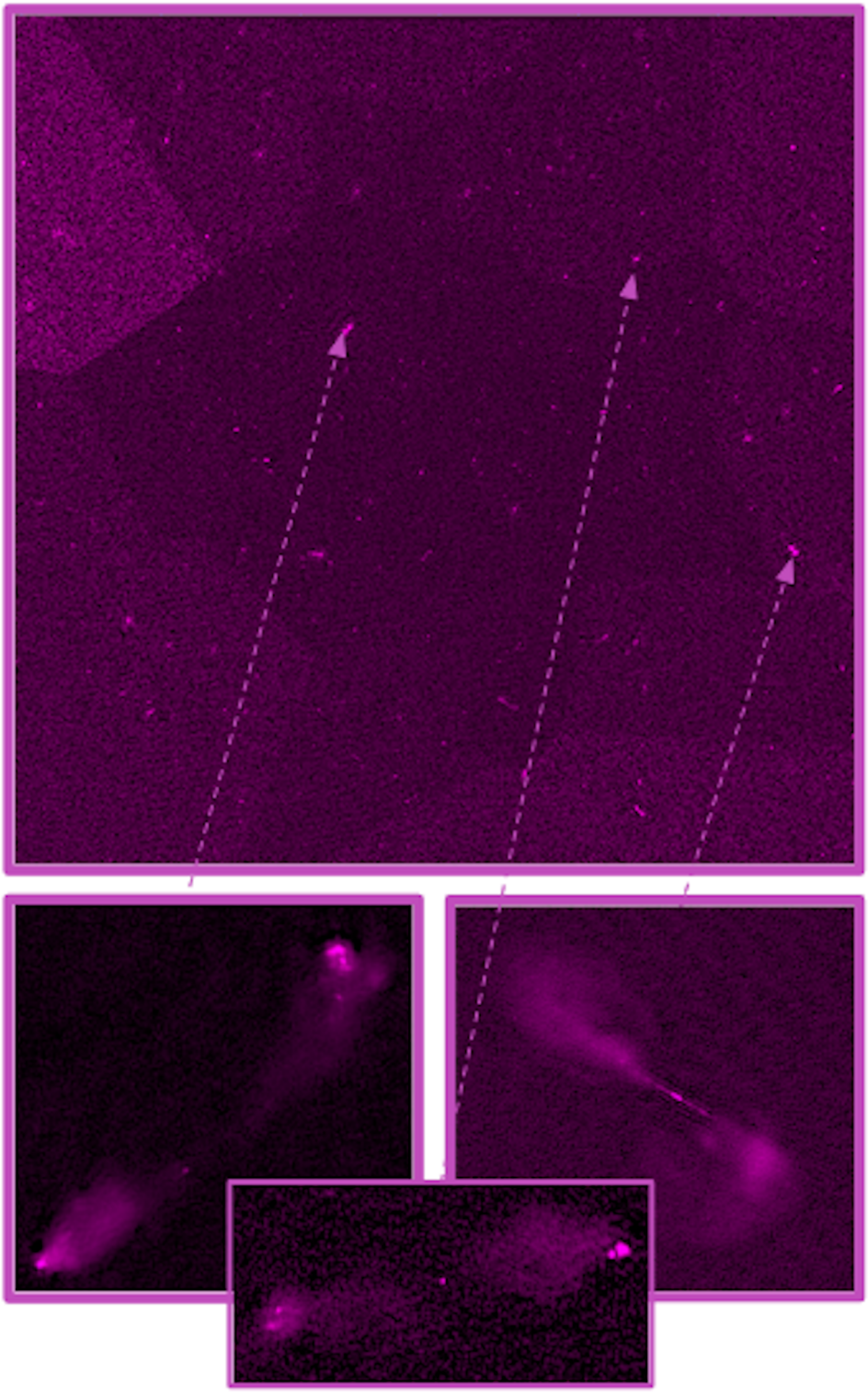

Figure 4.1: The first ∼0.3″ resolution image of the Boötes Deep Field. This image consists of ∼8 billion pixels, contains over 4,000 sources, and has a central sensitivity of 37.0 µJy beam^{-1}. The image is 2.5 × 2.5 deg^2 with a restoring beam of 0.50″ × 0.34″. I overlay interesting extended sources within this field where I can now probe radio emission of these sources to a new level thanks to the sub-arcsecond resolution.

has an observation ID of 726520 and the Boötes target field is 726524 with the project ID of LT10_10. The observation date is 2019-10-20 with a central position of right ascension (RA) 218.0° and declination (Dec) 34.5°. I use a frequency range of 121-166 MHz with 50 stations included in the final images: 24 core stations, 13 remote stations, and 13 international stations without the Swedish station (SE607), which I removed due to poor calibration solution for this station.

All the scripts I discuss in the following sections are integrated into the publicly available pipeline (van der Wild et al. in prep) [3].

Systematic Effects

Radio data reduction relies heavily on calibration techniques that remove systematic effects embedded within the data visibilities. These systematic effects are removed by calibrating against a known in-field source, which I call a delay calibrator. An ideal calibrator source is a bright, compact, object which calibrates well through self-calibration cycles. Obtaining corrections using these calibrators allow us to understand how to calibrate for systematic effects across our FoV. I discuss in-field calibration in full using delay calibrators in Section 4.3.2.

There are two types of systematic effects present in the raw data. These are direction independent effects (DIEs) and direction dependent effects (DDEs). I briefly provide an overview of these effects; consult de Gasperin et al. (2019) for full details.

Direction Independent Effects

For ILT data reduction, the DIEs requiring correction are the polarisation offsets, the bandpass, and the clock offsets. LOFAR has two data streams, one for each of the X and Y polarisations. During observations these polarisations can deviate from each other, and therefore I must align the polarisations by applying a delay offset between the two streams. I calibrate these polarisations independently, allowing us to probe and correct for the offset between them. In this step, I assume that the calibrator sources are unpolarised. This polarisation offset is only present in the phases and is time independent. I therefore

[3] VLBI Github repository: `https://git.astron.nl/RD/VLBI-cwl`

take one station as reference and apply a phase matrix which describes this delay offset causing the XX and YY streams to align.

Another DIE which I must correct for are systematic effects present across the bandpass. When I take observations with interferometers such as the ILT, I measure visibilities, and these visibilities have non-physical units. By correcting for the bandpass, I convert these visibility units to the physical units of Janskys (Jy) as well as correcting for any variation in sensitivity across the frequency band. The bandpass affects both the XX and YY polarisation in the same way, however the corrections I require are different for each polarisation stream. These bandpass effects are time independent.

The final DIE I must correct for is the offset between different station clocks. Each remote and international station has its own independent clock (all core stations use the same clock) and over time these clocks drift from one another. When correcting for the clock offsets for the remote and international stations, I use the clock of the core stations as reference. All these clocks need to be synchronised to enable coherent signal processing across the vast network of stations which make up the ILT.

Direction Dependent Effects

The wide FoV of the ILT provides both advantages and challenges. The primary benefit is the increase in the number of sources that lie within one pointing and hence, in the wide-field mode of LOFAR-VLBI, I can produce wide-field images with thousands of sources within them. However, DDEs pose a significant challenge when reducing ILT data to sub-arcsecond resolution images. The DDEs which must be corrected for while reducing ILT data are the ionospheric effects and the beam. These effects become more prominent at a wide-field scale, as ionospheric conditions exhibit variability on arc-minute scales, and can fluctuate across multiple degrees of the sky. It is therefore essential to correct for these effects when reducing ILT data.

The ILT's dipoles are fixed in place however, because the sources of interest move through the stations beam, any beam corrections I apply during calibration are time variable and the location of the source of interest within the FoV is directional dependent. When the dipole observations are correlated, the time and frequency of the observed phase varies between the stations and therefore this variation needs to be accounted for and thus

a beam correction is applied.

The ionosphere poses the largest obstacle in LOFAR data reduction. The ionosphere is a layer of charged particles within the Earth's atmosphere. These particles interact with waves propagating through the atmosphere and as a result, these incoming waves become distorted in both phase and amplitude. These distortions have a frequency dependency of ν^{-2}, and hence have a larger effect at low-frequency (Intema et al., 2009, 2011). Therefore, in LOFAR observations, the ionosphere is the prevailing cause of DDEs. The effects are dependent on both the magnetic field strength along the line of sight and the Total Electron Content (TEC). The ionosphere poses a greater challenge for wide-field observations, as its conditions vary on degree scales. For VLBI, an even more serious concern is that ionospheric conditions can differ substantially between stations across Europe.

4.3.2 Data Reduction Techniques

Before the observation becomes available on the LTA, some pre-processing is required. Any time periods or frequencies affected by Radio Frequency Interference (RFI) are flagged using `AOFlagger`[4] (Offringa, 2010). The first and last channels were flagged, as their edges contain various imperfections that can degrade data quality. The data was then averaged to 16 channels per subband with a frequency of 12.21 kHz per channel in order to reduce data volume and this averaged data is then uploaded to the LTA.

I note that the data reduction steps below are now being automated in the publicly available pipeline (van der Wild et al. in prep, Jong et al., 2025). I conducted these steps manually as the automated pipeline development was in early stages at the start of data processing for Boötes.

The second stage of reducing our Boötes LTA pointing uses the `PREFACTOR`[5] pipeline which is split into two parts, `Pre-Facet-Calibrator` and `Pre-Facet-Target`. `PREFACTOR` is now deprecated and users should now turn to `LINC`[6], but this was not fully operational at the time of processing.

[4] `AOFlagger`: `https://aoflagger.readthedocs.io/en/latest/`
[5] The `PREFACTOR` pipeline is publicly available at: `https://github.com/lofar-astron/prefactor`
[6] `LINC` is publicly available at: `https://git.astron.nl/RD/LINC`.

Pre-Facet-Calibrator

The first step of running the PREFACTOR pipeline is running `Pre-Facet-Calibrator` which considers all stations, both Dutch and international. Here, I derive corrections for the DIEs, namely polarisation offset, bandpass, and clock offset.

This section of the pipeline uses a bright 3C source that was specifically specified for the particular observation and uses this 3C source as a flux calibrator. These sources have a known radio spectrum, morphology, and are unpolarised at 144 MHz (Scaife & Heald, 2012). For this 8-h observation of Boötes the flux calibrator source was 3C 196.

Pre-Facet-Target

After I run `Pre-Facet-Calibrator`, the solutions from the flux calibrator are applied to the target observation of the Dutch stations only and hence dramatically reduces the data volume. I then apply the calibrator solutions to the target data for the polarisation alignment, bandpass, clock offset, and finally, a beam correction. If required, bright off-axis sources are removed from the target observation during the A-Team clipping step, where the four brightest radio sources in the northern hemisphere (the supernova remnants Cassiopeia A and Taurus A, and the radio galaxies Cygnus A and Virgo A) are flagged if their emission exceeds a certain threshold and they are in close proximity to the centre of the observation. Then, I further average the data to 8 sec and 97.64 KHz. I also apply a coarse rotation measure correction based on Global Position System (GPS) information alongside the flux calibrator solutions. The final step of `Pre-Facet-Target` is to perform a direction independent phase-only calibration, only on the Dutch stations, using a skymodel from TGSS (Tata Institute of Fundamental Research (TIRF) Giant Metrewave Radio Telescope (GMRT) Sky Survey; Intema et al., 2017). This provides an initial direction independent correction for ionospheric effects. Finally, these corrections are applied to the measurement sets, producing DIE corrected data sets.

Subtraction

When incorporating the international stations into the data reduction process, I significantly reduce our FoV. This is because the international stations of the ILT are physically larger

in size than the Dutch core and remote stations, therefore the beams of the international stations are smaller in comparison to the beam of the Dutch stations. I therefore subtract sources from the *uv* data that are outside of the international station FoV.

I run the `DDF` pipeline [7], which provides both DDE and DIE solutions for the Dutch stations. I took the 6″ resolution image which I produce during our run of the `DDF` pipeline and I ran `sub-sources-outside-region.py` [8]. I subtracted sources outside of a 2.5×2.5 deg^2 box region which represents the international FoV. This step is taken to prevent areas of the sky visible only to the Dutch stations, and not to the international ones, from affecting calibration and imaging, especially in the presence of bright sources.

In-field Calibration

The next stage of data processing is using the LOFAR-VLBI pipeline. As a first step it performs a bulk DIE correction for the international stations, using the best in-field delay calibrator within the FoV of the international stations. I apply the solutions I produce using this in-field calibrator to both the Dutch and international stations. This is a critical part of reducing any ILT pointing because once the solutions from the in-field calibrator have been applied, calibration errors introduced at this stage are difficult to correct for, due to the use of small time and frequency solution intervals. Before I select a calibrator, I first apply the DI solutions from both `Pre-Facet-Calibrator` (Section 4.3.2) and `Pre-Facet-Target` (Section 4.3.2). Then I separate the data into 24 manageable measurements sets, each with ∼2 MHz bandwidth. During this process, I produce a list of potential LBCS (LOFAR Long-Baseline Calibrator Survey; Moldón et al., 2015; Jackson et al., 2016, 2022) sources. This catalogue contains potential in-field calibrator sources, taking into account the brightness of these sources at 6″ and the position relative to the pointing centre. The ideal in-field calibrator source is compact and bright at 0.3″ while being within the international station Full Width Half Maximum (FWHM). At this stage of the data reduction process, the source's morphology at 0.3″ is not known. Therefore, the source ranked as the most likely best in-field calibrator in the

[7] The `DDF` pipeline is publicly available at: `https://github.com/mhardcastle/ddf-pipeline`

[8] `sub-sources-outside-region.py` script is publicly available: `https://github.com/rvweeren/lofar_facet_selfcal/blob/main/submods/sub_sources_outside_region.py`

LBCS catalogue may not be the best one, and hence I verify the LBCS selection. The previous pipeline version selected the LBCS calibrator with compact flux and was closest to the pointing centre, however, these two criteria alone are insufficient for identifying a suitable in-field calibrator. Consequently, I process multiple candidate calibrators during data reduction. I then split out these potential in-field calibrators from the field and calibrate them individually to determine which source is the best calibrator within the FoV.

To determine whether the sources which I select using LBCS are suitable in-field calibrators, I conduct self-calibration of these sources. The aim of self-calibration is to find the complex gains which I require to reproduce the sky intensity model given the visibilities observed. To do this, an initial model is created and the complex gains are then solved for and the corrected visibility is calculated. Using this corrected visibility, a new and improved model is formed. I repeat this process until the model created is representative of the observed source. I implement `facetselfcal` (van Weeren et al., 2021) to perform all self-calibration procedures to create these Boötes images. This software uses the default preprocessing pipeline (`DP3`; van Diepen et al. (2018)) to calculate complex gains and `WSClean` (Offringa et al., 2014) for imaging. For our potential calibrator sources I set the number of self-calibration cycles to 10, as this generally leads to convergence (e.g., Sweijen et al., 2022; Ye et al., 2024).

For this Boötes pointing, I reduce two LBCS sources to sub-arcsecond resolution, both of which are double sources at 0.3″. Of the two, I chose ILTJ142905.10+342641.0 as the in-field calibrator because the calibration solutions are cleaner compared to the first source, and this source is closer to the pointing centre of the observation. This highlights the importance of considering multiple sources as potential in-field calibrators.

I utilise the following calibration steps: `scalarphasediff`, `scalarphase`, `complexgain`, `scalarcomplexgain`, and `fulljones`. Before the first step, I convert the polarisation from linear (XX, YY) to circular (RR, LL), since the distortions present are more straightforward to correct for in circular polarisation. I now conduct a `scalarphasediff` calibration where I enforce identical across the Dutch station, as differential effects are minimal on these short baselines. I implement a solution interval of 8 min with a frequency smoothness kernel of 10 MHz.

Next, I perform three rounds of `scalarphase`, each targetting a different class of stations (core, remote, international). `scalarphase` steps solves for phase errors as a function of both time and frequency. I first calibrate the international stations, which, owing to their long baselines exhibit the greatest phase variability. For this case, I adopt the small frequency smoothness of 1.25 MHz and solve for fast phase changes by utilising a solution interval of 8 sec to capture rapid phase fluctuations. The second `scalarphase` address the remote stations, again with a solution interval of 8 sec but with a larger frequency smoothness kernel of 10 MHz. Finally, the third `scalarphase` includes the Dutch core stations, for which I use a solution interval of 1 min and a smoothness kernel of 10 MHz.

I next perform a `scalarcomplexgain` calibration, which solves for both phase and amplitude errors, but with a primary focus on correcting amplitudes, since the bulk of the phase errors are already addressed in the `scalarphase` steps I outline above. For this step, I adopt long solution intervals of 1 h with a frequency smoothness kernel of 1 MHz to provide slow calibration. Following this, I run a `complexgain` step, which performs two separate gain solutions to each polarisation stream, whereas the previous solutions from `scalarcomplexgain` are polarisation independent. Here, I apply a long solution interval of 10 h, since this step only corrects frequency dependent effects. I then conduct an additional `scalarcomplexgain` calibration with a shorter solution interval of 2 min alongside the same 20 MHz smoothness kernel to ensure the stability of the solutions. I finish with a `fulljones` solve to correct for leakage in the cross-hand polarisations (RL and LR), using a frequency smoothness kernel of 5 MHz and a solution interval of 30 min.

I applied the calibrator solutions which I produced from the self-calibration of the in-field calibrator to the subtracted measurement set. For this step, I phase-shift toward our in-field calibrator and form a “super station” (ST001) where I combine all the core stations to reduce the data volume, increase SNR, and suppress signals from other sources due to the reduced FoV.

4.3.3 Direction Dependent Calibrators

The solutions I apply from the in-field calibrator only provide corrections in the direction of the in-field calibrator, leaving residual DDEs that still require correcting. For wide-field

imaging using the ILT, I require multiple calibrator sources across our FoV referred to as DDCs (Directional Dependent Calibrators) to correct for the residual DDEs.

The ideal candidates for these DDCs are the same as our selection of an in-field calibrator where high brightness and compactness are desirable. Unfortunately, at such high-resolution, these sources are rare. Therefore, I must loosen our requirements to obtain the best understanding of ionospheric conditions across our FoV. I do not have to be as strict with our selection of DDCs compared to the selection of our in-field calibrator, as our in-field calibrator has corrected for the bulk of distortions. I consequently include fainter and extended sources within our selection of these DDCs, as long as these objects' calibration solutions converge through the self-calibration cycles.

For this field I select 26 DDCs and hence have 27 directions in total within our field, including the in-field calibrator. To begin this selection, I consider sources identified as potential in-field calibrators, but ultimately do not adopt them as the in-field calibrator. I also consider the next 100 brightest objects in the 6″ image that lie within the international FoV. Therefore, I choose our DDCs from 112 sources. I split each of these sources from the field and then conduct self-calibration on each of them individually to determine if they are a suitable DDC. I then visually inspect the resulting images and solutions to determine their suitability.

Now that I have our DDCs, I split the field into facets using Voronoi tessellation (e.g., Weeren et al., 2016), which sets the dimensions of each facet by assigning every point in the plane to its nearest calibrator source such that each facet contains all points closer to that calibrator than to any other. This results in the non-symmetric facets and from this step forward I consider each facet individually rather than the entire FoV. I demonstrate the facet layout for the sub-arcsecond resolution Boötes images in Figure 4.2, and I note that facet 20 has higher noise in comparison to other directions which is further described in Section 4.3.4.

4.3.4 Imaging

The first image I create of Boötes (using `WSClean`) is at ~1.2″ resolution. I produce this image first to check the quality of the calibration of the image because of its comparatively low computational cost. This 1.2″ image was imaged in one go using `WSClean`'s facet

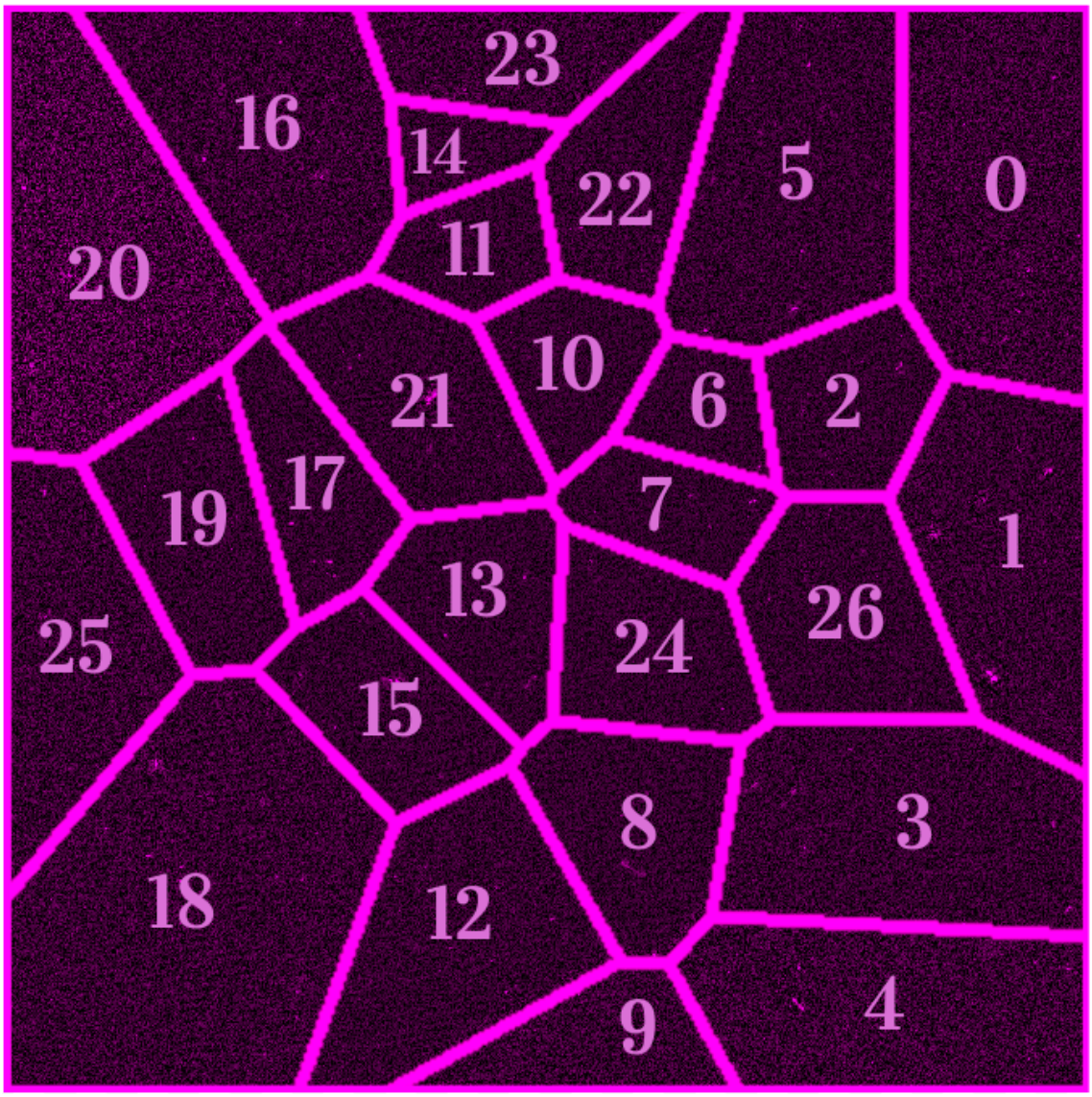

Figure 4.2: The layout of the 27 facets I use to produce the sub-arcsecond resolution, wide-field, images of the Boötes Deep Field. The background is the ∼0.3″ image and facet 20 has a higher level of noise due to an extra flux scale correction required for this facet.

mode, however this is not possible for the 0.6″ and 0.3″ images. Instead, the 1.2″ model images were used to create individual datasets for each facet which could then be imaged independently, allowing for faster and less computationally expensive sub-arcsecond imaging.

To create the individual datasets for each of these facets, I first subtract all sources within the field and using the `-predict` functionality of `WSClean` and the 1.2″ model images. I then add back the sources within the facet using the solutions of the corresponding DDCs, hence giving calibrated datasets for each facet. I complete this for each of the 27 facets, and are left with 27 facet images. I do this independently for the 0.3″ and 0.6″ images.

The final step is to mosaic these facets together using `SWarp`[9] (Bertin et al., 2002) to create the final image at 0.3″ (which I show in Figure 4.1), as well as the final 0.6″image.

Flux Density Scale and Astrometry

The self-calibration which I implement to create these images is agnostic to the position of sources when there is not a reference source, therefore, the resulting images contain both an astrometry and flux density offset. The flux density offsets is introduced by the delay calibrator rather than our DDCs, as during self-calibration of our DDCs I normalise the amplitudes to minimise any drift in the flux scale. A position shift may also be present because for Boötes, I do not have an astrometric reference for the delay calibrator selected. Similarly, although the amplitude scale was tied to archival data, residual offsets from the desired flux density scale may remain, so the source flux densities require scaling to match to known flux density measurements within the literature. To derive these corrections, I locate compact, high SNR, sources using a compactness measurement from the peak intensity and total flux intensity from Kondapally et al. (2021) as well as the respective high-resolution images from `pyBDSF`[10]. For the flux scale correction, I apply a universal correction across all facets, by taking the median flux scale correction of all facets combined (due to the substantial uncertainties in the flux scale correction for the ILT) and I perform the astrometry correction for each facet individually. I apply the

[9] `SWarp` is publicly available at: `https://ascl.net/1010.068`
[10] `https://pybdsf.readthedocs.io/en/latest/`

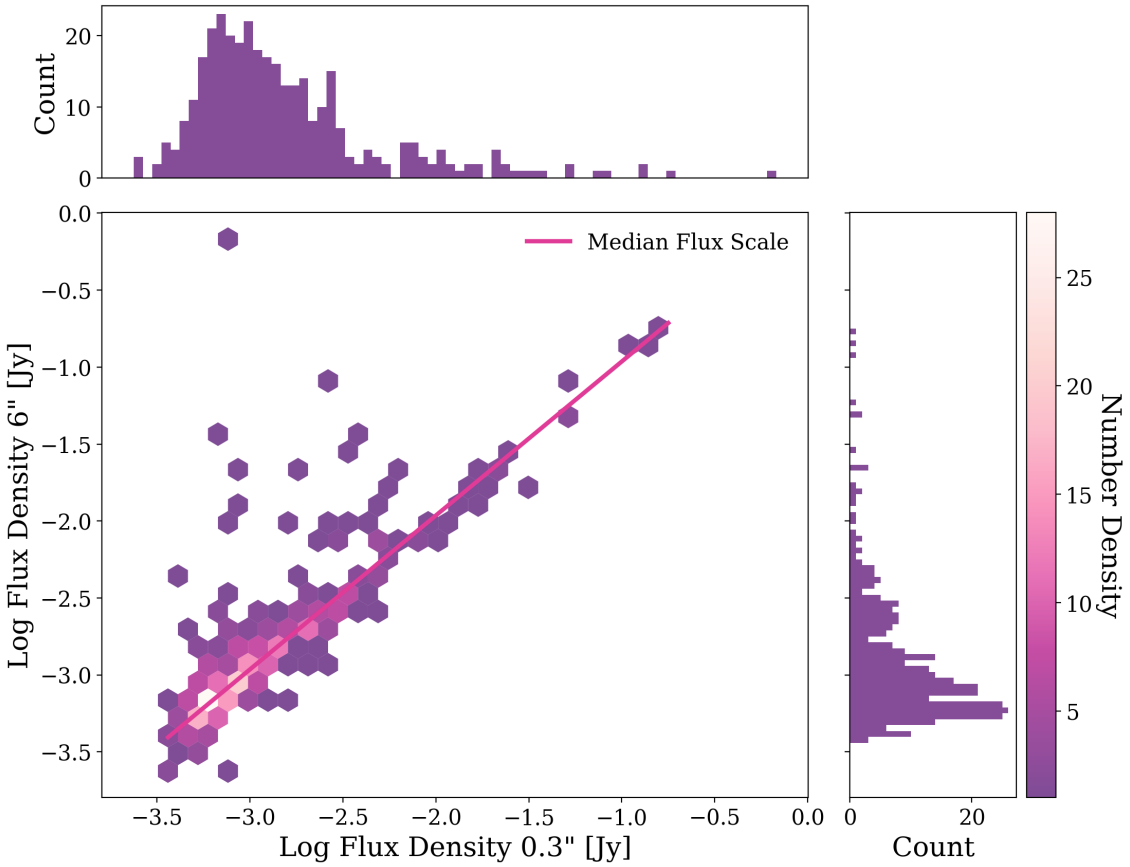

Figure 4.3: The relationship between the log flux density at 0.3″ and 6″ from LoTSS. The 0.3″ flux densities have been scaled by the final correction of 1.02. The sources contributing to this figure are high SNR, compact sources I select to measure the universal flux density scale required for Boötes. The top histogram shows the distribution of log flux densities at 0.3″, while the right histogram shows the distribution at 6″. The pink link indicates the median flux scale between these flux densities. Each hexbin contains at least one source, with the number density represented by the colour scale.

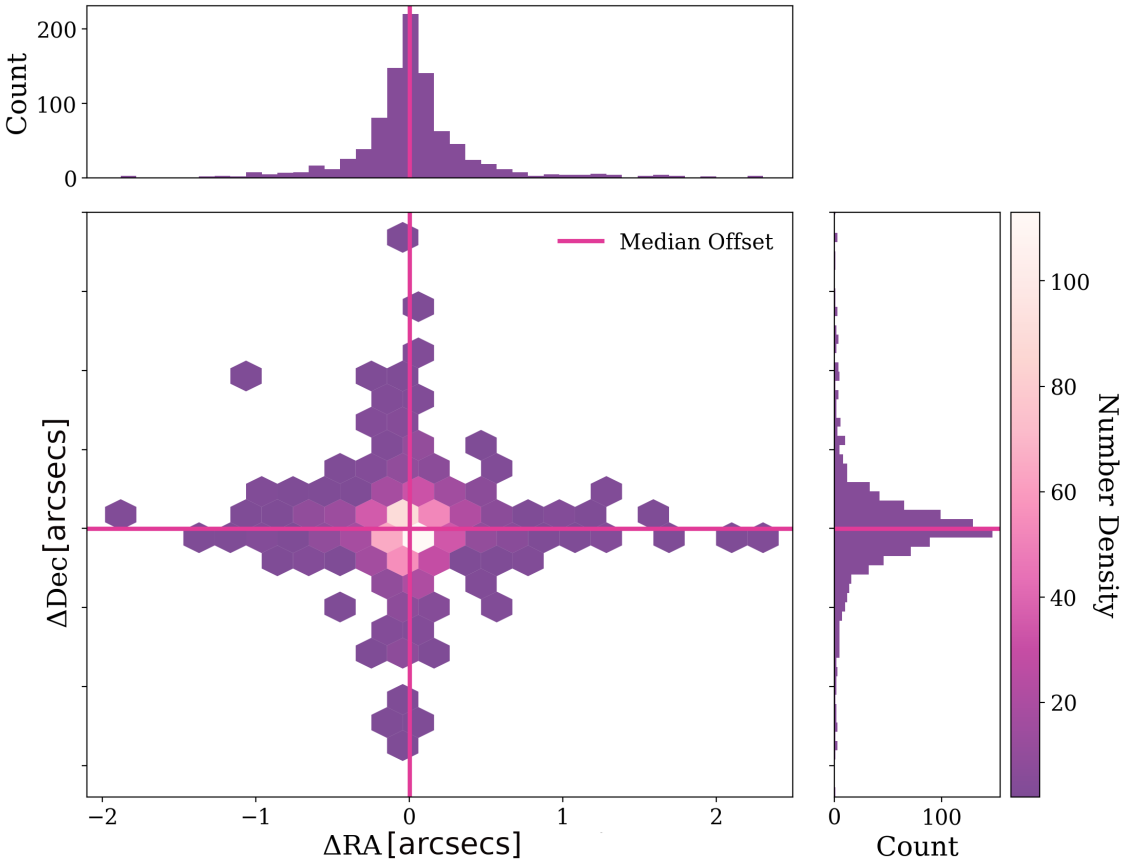

Figure 4.4: The relationship between ΔRA and ΔDec after applying the astrometry correction. I calculate the offset by subtracting the 0.3″ positions from the 6″ LoTSS positions. The sources shown are high-SNR, compact objects I select to measure the astrometric correction for each facets. Each hexbin contains at least two sources, with the colour scale tracing the number density. The pink lines indicate the median values of ΔRA and ΔDec, which cross near zero for both axes, as expected.

correction calculated for the 0.3″ image for each resolution as both the astrometry and flux scale offset is not dependent on the resolution as I create each resolution image using the same dataset.

To determine the flux scale correction I require, I use the total flux density measurements at 6″ and compare this to the measurement of flux density at 0.3″. For this correction I consider sources with $S_{\rm peak}/S_{\rm total} > 0.7$ and from these sources, I use a SNR cut off of 10 using the peak intensity measurement and the RMS (root mean squared) island noise from the 0.3″ image. This leaves 343 sources at 0.3″. I incorporate an initial universal flux scale correction of 1.111 to the high-resolution images. I investigate the scatter in the flux scale correction between facets to determine the uncertainties in this flux scale correction. I fit a Gaussian to the flux scale correction distribution and adopt the standard deviation of the fit, 24.8%, as the uncertainty in the flux scale correction. For Boötes I add a further flux scale to correct for flux measurement deviations between the LoTSS Deep 6″ image and a 6″ image produced with this data set and calibration methods. To do this, I locate sources in LoTSS with SNR greater than 20 with $S_{\rm peak}/S_{\rm total} > 0.9$, leaving 990 sources. Using the flux density measurements from LoTSS Deep and the new 6″ image, I find a flux scale correction of 0.92. Combining this with our previous flux scale correction, for the whole field I incorporate a flux scale of 1.02. In Figure 4.3, I show the final relationship between the corrected 0.3″ flux densities and the 6″ LoTSS flux densities. As expected, the median flux scale passes through the densest part of distribution.

To correct for the astrometric offset, I use the RA and DEC of the optical counterparts from Kondapally et al. (2021) to calculate the offsets between the LoTSS Deep 6″ catalogue and the 0.3″ resolution image. Our definition for compact sources is more lenient for the position offset as I correct per facet for this offset rather than a universal correction and therefore prioritise count statistics per facet. I reduce our criteria to $S_{\rm peak}/S_{\rm total} > 0.6$ followed by a SNR cut off of 7. This leaves 954 sources, with the largest number of compact sources in a single facet of 80 and a smallest of 3. I correct the astrometry per facet by taking the median RA and DEC offset in each facet. The RA correction ranges from 0.0982″ to 0.576″ with an overall median of 0.319″ and the DEC correction ranges from -0.425″ to 0.289″ with a median of 0.0367″. I show the final RA and Dec offsets between the 6″ and 0.3″ images in Figure 4.4. I see that the median offsets for both RA

and Dec are close to zero, demonstrating that the correction I apply is effective.

The astrometry correction in the images for Boötes is larger than that of the ELAIS-N1 field. The key reason for this is that the in-field calibrator source for ELAIS-N1 has a high frequency VLBI position based on Charlot et al. (2020). Therefore for this field the authors could achieve millisecond accuracy for the positioning of this source. For future fields that are to be reduced at sub-arcsecond scale, it is important to consider the astrometry early on and potentially select calibrators that have a highly accurate position available.

I note that facet 20 had relatively poor calibration in comparison to other facets within this image. Therefore, I apply a further flux scale correction to this facet using the same method as above. In Figure 4.2 I can see this has higher noise in comparison to the other facets.

Cataloguing

I produce the final catalogues, corrected for astrometry and flux scale, for each of the three resolution images using `pyBDSF` with a pixel detection threshold of 5σ and a detection island threshold of 3σ, an RMS box of (120,15), and for bright-source RMS box of (40,15) following de Jong et al. (2024). For the $0.3''$, $0.6''$, and $1.2''$ catalogues I detect 8391, 5851, and 2596 components respectively at 5σ.

In the published source catalogues, the components have been associated in several stages. If a single component at the relevant high-resolution image is isolated within the $6''$ beam of the LoTSS Deep Field image, I class it as a single component source. At $0.3''$, if multiple components are present within a separation $30''$ of each other, I perform visual inspection to check if components should be associated to a common source, by creating a $60'' \times 60''$ cutout. These cutouts also have information at other resolutions to allow simultaneous component association at each resolution. I present examples of montages of the cutouts for two components that are associated with the same single source at $0.3''$ and $0.6''$ in Figure 4.5 and Figure 4.6. At $1.2''$ this source only consists of a single component, so no component association was required. For instance, $6''$ alongside the $0.3''$ resolution images allow us to de-blend sources, which could be confused as multiple components for a single source rather than multiple sources. For a handful of cases, I require further information to determine whether components are blended sources rather than a single

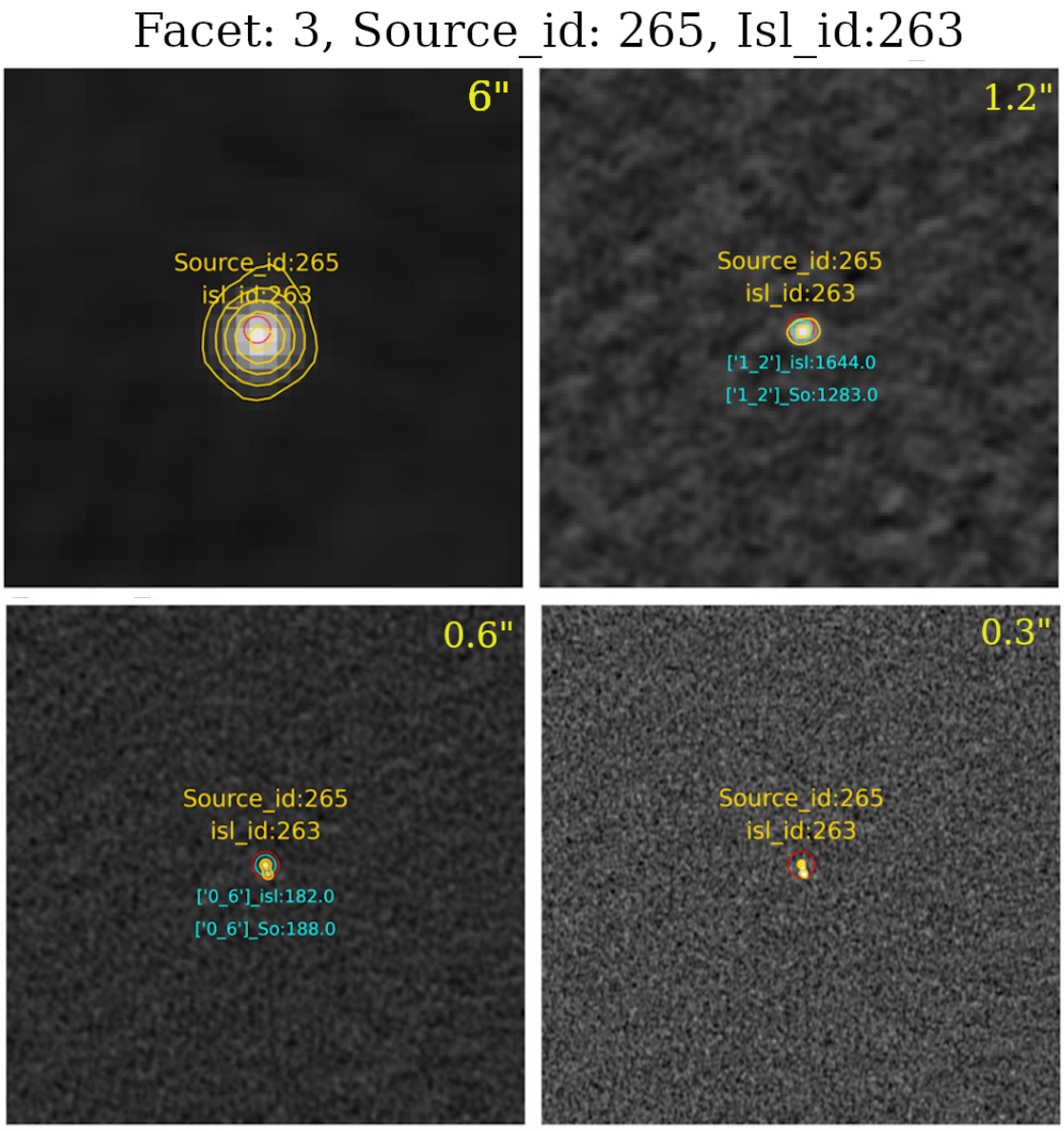

Figure 4.5: Example of a montage of 60″ × 60″ cutouts used to associate components into a common source. For this case, two components detected at 0.3″ and 0.6″ are associated together. *Top left:* 6″ resolution image (see Figure 4.6 for source details). *Top right:* 1.2″ cutout. *Bottom left:* 0.6″ resolution cutout. *Bottom right:* 0.3″ resolution cutout. For the second component, information is provided in Figure 4.6. Contours are shown at the 5σ level. The source ID and island (isl) ID common across all resolutions are assigned to the 0.3″ component. Additional component information (in turquoise and smaller font) is shown on the respective resolution image. The red circle is centred on the component position at 0.3″ in each cutout, and the turquoise circle is the component location for the relevant resolution image

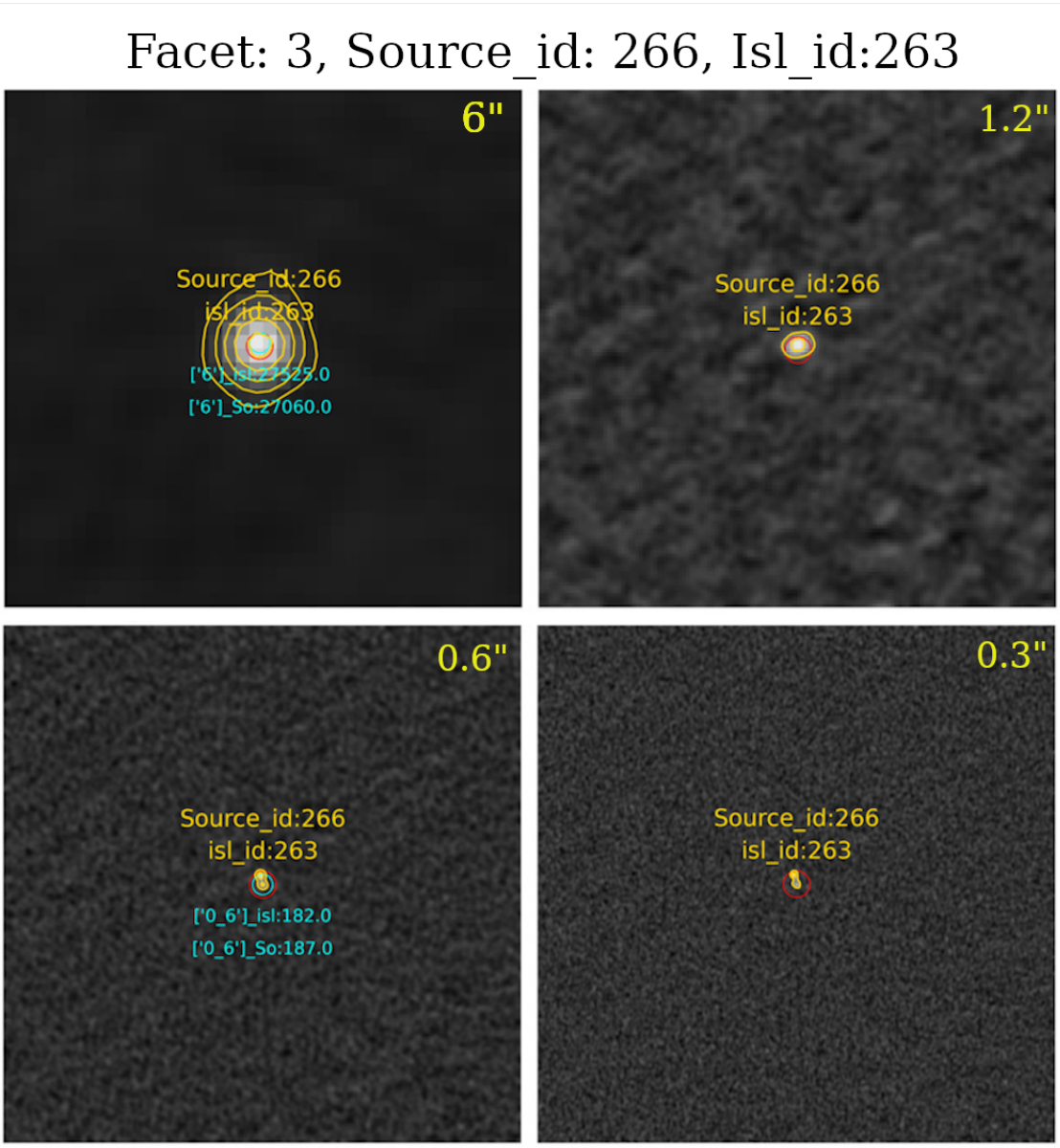

Figure 4.6: A montage of 60″ × 60″ cutouts of the second component associated with the same source shown in Figure 4.5. See the caption of Figure 4.5 for more details on n the cutouts.

source. In these cases I consult the NOAO Deep Wide Field Survey (NDWFS; Jannuzi & Dey, 1999) optical image of Boötes at I-band to either keep components separate or associate these components. Using a separation of 30″ misses giant radio galaxies within our images, therefore I also use the LOFAR Galaxy Zoo (LGZ) within Kondapally et al. (2021) to visually inspect sources with a LGZ size greater than 30″.

These methods result in a total of 585 components being merged into 223 sources at 0.3″. At 0.6″ 434 components are merged into 152 sources, and finally at 1.2″ 166 components are merged to 65 sources.

When merging sources, I sum the total flux density of all components and perform standard error propagation on their errors. I take the mean of the island RMS noise levels as a proxy for the local RMS noise of the associated source. I take the highest peak intensity value alongside the associated error. The RA and DEC for these sources is the flux density weighted position. Finally I calculate the Largest Angular Size (LAS) for these sources, by considering each component's major and minor axes, as well as their respective position angle. I set the major and minor axes and the position angle of these sources to zero in the catalogue. I obtain the uncertainties for the LAS by using the uncertainty extremities of the major and minor axis, as well as the position angle.

During the visual inspection of sources, several of the components within a certain separation appeared to be artifacts. I remove these from our final catalogues. For 0.3″ I remove 69 components, 45 at 0.6″ and 4 at 1.2″.

Many false detections are present within the initial `pyBDSF` catalogues. The 6″ image of Boötes from LoTSS is deeper than the images presented in this chapter and therefore can be used to help identify false detections. To remove these false detections, firstly I located sources which do not lie within 3″ of a LoTSS source, as sources within this radius would be associated to the LoTSS 6″ source. I only consider sources with a flux density below 500 µJy measured at the given high-resolution image because sources below this threshold are where I expect to start to see false detections. I then measure the median 5σ RMS noise within a 3″ radius region of the LoTSS position in the RMS map [11]. If the flux density in the high-resolution image of the source is greater than the 5σ median RMS at

[11]The RMS map is available at: `https://lofar-surveys.org/deepfields_public_bootes.html`

6″ then I class this as a false detection and remove this from our final catalogue. However, if the flux density is less than the 5σ median RMS then this is a possible real detection that was not detected at 6″. I remove 3524 false detections at 0.3″ with 151 potential new detections, at 0.6″ I remove 849 false detections and have 6 new detections, and at 1.2″ I remove 1 detections and have no new detections at this resolution.

Finally, I conduct one final round of visual inspection of the whole field to ensure the brightest sources have been correctly associated. In the 0.3″ image I associate four components into two sources and in the 1.2″ I associate three components into one source. This leaves us with the final catalogue at each resolution. The 0.3″ catalogue contains 4091 sources, 4675 at 0.6″, and 2488 at 1.2″. I note that the highest source count of the three resolution images released in this chapter is in the ∼0.6″ resolution image. This is because at the highest resolution, 0.3″, I are probing the smallest scale emission at this frequency, therefore as I decrease resolution I increase sensitivity to lower surface brightness emission and I are more likely to detect diffuse emission on larger scales, and therefore at 0.6″ I can detected sources which cannot be detected at 0.3″ as these would be too diffuse. I do not however see the highest source count at the ∼1.2″ image despite this being the lowest resolution as this image has the lowest sensitivity due to gaps in the *uv* coverage. In Section B.2, Figure B.1 I discuss how the ratio of the flux density at this resolution ($S_{\rm ILT}$) and the resolution at 6″ using LoTSS ($S_{\rm LoTSS}$) varies with SNR.

4.4 ILT Deep Fields Comparison

Now that I have access to three sub-arcsecond Deep Field images which I display all together in Figure 4.7, I will briefly discuss how the 0.3″ image of Boötes compares to the other 0.3″ images of Lockman Hole (Sweijen et al., 2022) and ELAIS-N1 (de Jong et al., 2024). The source count varies substantially between the three fields, with Lockman Hole having least (∼2500), then Boötes (∼4000), and ELAIS-N1 having the largest source count (∼9000). The increased source count in ELAIS-N1 can clearly be explained because this image combines four different 8-h observations to create an image with a 32-h integration time. This results in the image being significantly deeper than both the Lockman Hole image and the Boötes image, which use single 8-h observations. The increased depth

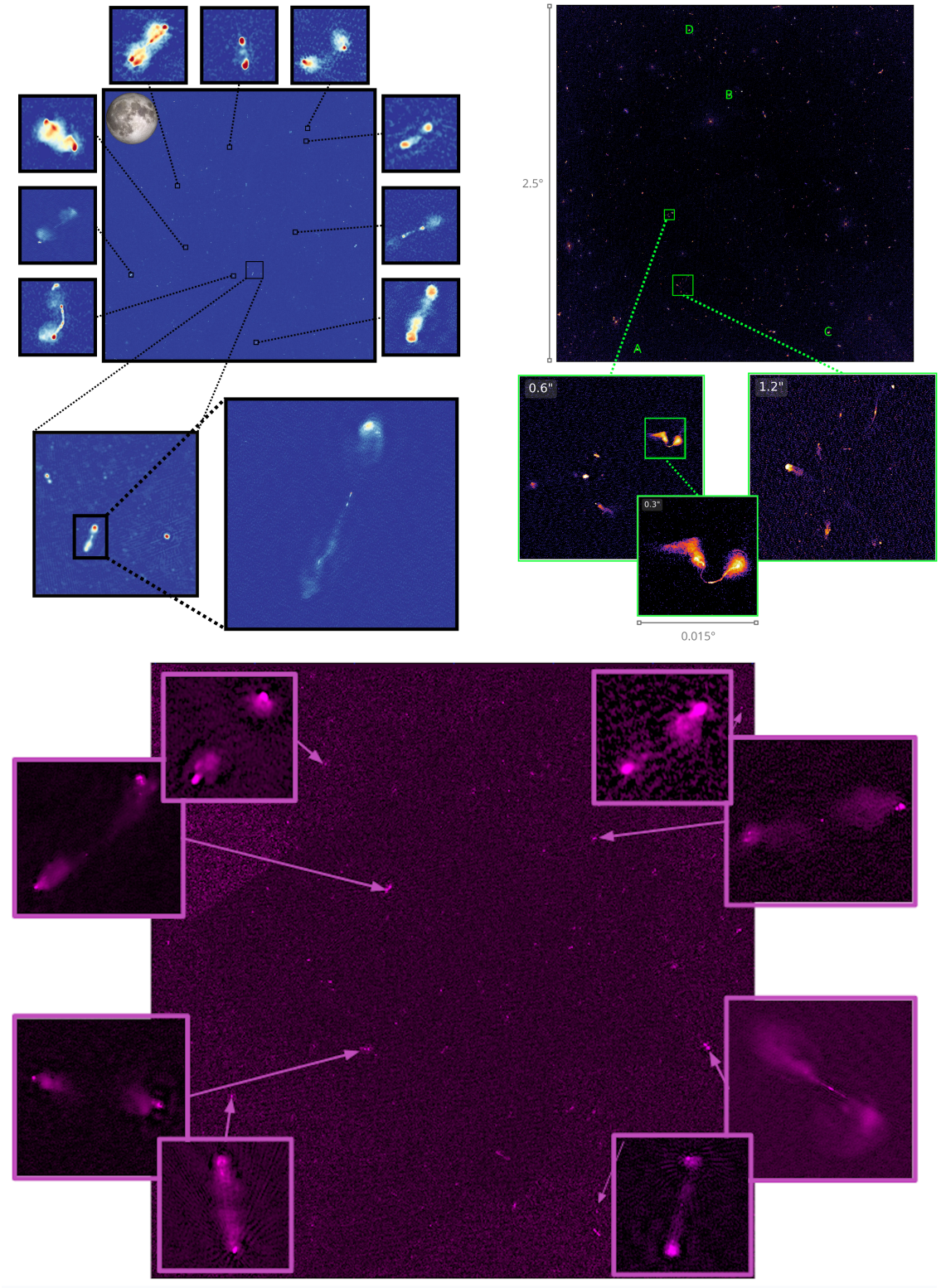

Figure 4.7: Here I show the three, wide-field sub-arcsecond resolution images of the LoTSS Deep Fields released in DR1. *Top left:* Lockman Hole (Sweijen et al., 2022). *Top right:* ELAIS-N1 (de Jong et al., 2024). *Bottom:* Boötes.

means that ELAIS-N1 probes sources with lower flux densities than Boötes and Lockman Hole. The source count rapidly increases towards fainter radio luminosity and this hence explains the higher source count in this image (Shimwell et al., 2025).

The variation between source counts from Lockman Hole and Boötes can be understood in two ways. Firstly, significant progress has been made in the calibration strategies that I use to create these ILT wide-field images (see de Jong et al., 2024, for more detail). However this is unlikely to be the only reason for the increased source count. In this chapter I use a different cataloguing strategy than the previous Deep Fields. For both Lockman Hole and ELAIS-N1 only sources that are also detected in the LoTSS Deep Field images which have an sub-arcsecond resolution counterpart associated are included in these field's catalogues to ensure no false detections are present in them. For Boötes I take a different approach by keeping all sources detected by pyBDSF (which is on the order of 9000) and remove false detections by consulting the LoTSS noise map to see whether the high-resolution flux density recorded could be a noise fluctuation (see Section 4.3.4 for more detail). This also ensures I do not remove high-resolution components from sources, which are unresolved at 6″ that have now become resolved at 0.3″. Therefore by not removing these sources I ensure all real detections of extended sources are within the catalogues.

I further note that the 0.3″, Boötes wide-field image has a higher noise level compared to the Lockman Hole image, despite both using a single 8-h observation. This is likely due to the low declination of the Boötes field because at low declinations calibration becomes more difficult.

4.5 Conclusions

In this chapter I present the first high-resolution images of the Boötes Deep Field at 144 MHz, at ∼0.3″, ∼0.6″, and ∼1.2″, each with a sensitivity of 37.0 μJy beam^{-1}, 48.2 μJy beam^{-1}, and 84.6 μJy beam^{-1} respectively, along with a source count of 4091, 4675, and 2488 respectively.

I have explored the main challenges in producing these wide-field, sub-arcsecond resolution images at 144 MHz including an in-depth discussion of the difficulties posed by

the ionosphere at low-frequencies. I have also outlined the data reduction techniques used to overcome these challenges. In particular, this includes the use of directional dependent calibrators alongside the main in-field calibrator, ensuring that the ionospheric conditions across the large FoV are accurately characterised.

I also describe the post-processing steps required to produce these radio images. This includes applying both a flux scale correction as well as an astrometric offset correction, ensuring that the flux density measurements and source positions presented alongside these images are consistent with known values in the literature. In addition I also outline the cataloguing strategy implemented for the Boötes field, including the procedure used for associating components with a common source.

CHAPTER 5

A Link Between Low-Frequency Kiloparsec Radio Morphology and AGN-driven Ionised Outflows

This chapter contains the scientific results from the manuscript submitted to Monthly Notices of the Royal Astronomical Society entitles "*Strap on your Boötes: A link between low-frequency kiloparsec radio morphology and AGN driven ionised outflows*". These results are only possible thanks to the wide-field, sub-arcsecond resolution images of the LoTSS Deep Fields DR1, such as the first Boötes wide-field, sub-arcsecond resolution image at 144 MHz which I present in Chapter 4. The text has been slightly adapted so that this is a stand-alone chapter.

5.1 Introduction

How feedback from Active Galactic Nuclei (AGN) operates is one of the major open questions in modern day astronomy. These accreting objects lie in the central regions of galaxies and are so powerful that they can alter the evolution of their host galaxy. This is clearly seen in both observations and simulations. Observations show that the mass of the Super Massive Black Hole (SMBH; Kormendy & Richstone, 1992, 1995; Magorrian et al., 1998) is correlated with the velocity dispersion of their galaxy (Gebhardt et al., 2000; Merritt & Ferrarese, 2001). Additionally, in cosmological simulations, AGN feedback is required to reproduce the observable Universe. For example, these AGN provide crucial heating processes in these models (Bower et al., 2006; Croton et al., 2006). This feedback mechanism can be understood using a variety of observational techniques (see, Harrison & Almeida, 2024, for a review). Although I can see the effects of AGN feedback occurring in our Universe, it still remains unclear how this feedback operates. One research area which can bring us closer to the answer is the study of AGN outflows.

AGN outflows, either molecular, atomic, or ionised, can propagate into the interstellar medium (ISM) on kiloparsec scales and insert energy into the surroundings, having a profound effect on the evolution of their host galaxies (e.g., Fiore et al., 2017; Harrison et al., 2018; Veilleux et al., 2020). The [O III] λ5007 Å forbidden emission line is a common tracer of ionised gas outflows. For forbidden emission lines to arise, low density environments are required where the time between particle collisions is long enough for excited ions to undergo spontaneous decay rather than being collisionally de-excited. Densities in laboratories on Earth are too high for these transitions to occur, so such lines are absent. In contrast, many astrophysical environments, such as the ionised gas around AGN or star-forming regions, have sufficiently low densities and high enough ionisation to allow forbidden lines to be visible in spectroscopic measurements. I can locate AGN outflows using [O III] by seeing if a second, broad, asymmetric, blueshifted, component is present when fitting this line alongside a narrow component. The outflows traced by [O III] have been firmly linked to radio emission and investigating the details of this connection is one way to understand AGN feedback (e.g., Rawlings et al., 1989; Mullaney et al., 2013; Nesvadba et al., 2017b; Zakamska et al., 2016; Albán et al., 2024). It is also notable that the narrow line region, where these forbidden lines originate, typically spans a few

kiloparsec in scale, which is on a comparable scale to the radio emission I observe from steep spectrum radio cores (see, Miley, 1980, for a review), further demonstrating the link between [O III] and radio emission.

Previous works have begun to investigate the link between radio morphologies and [O III] emission, however these have been limited by the resolution of large radio surveys. Molyneux et al. (2019) obtained a sample of 2922 spectroscopically confirmed AGN below a redshift of 0.2, selected to be jet dominated. The authors used this sample to study the relationship between 1.4 GHz radio morphologies with [O III] kinematics. For their morphological classifications the authors utilised the radio survey Faint Images of the Radio Sky at Twenty-centimeters (FIRST; Becker et al., 1995) at an angular resolution of $\sim 5''$. Using a combination of machine learning and size measurements to classify radio morphology they found that compact sources have the most extreme [O III] gas kinematics. Another notable work connecting [O III] to radio emission is Kukreti & Morganti (2024). The authors build on the work of Kukreti et al. (2023) using the Low Frequency Array Two-metre Sky Survey (LoTSS; Shimwell et al., 2017, 2019, 2022) alongside FIRST and the Very Large Array Sky Survey (VLASS; Lacy et al., 2020) to derive the spectral slopes for a sample of 5720 radio AGN and they study the [O III] line profiles using stacking analysis. They discover that peaked spectrum sources show more disturbed gas than non-peaked spectrum AGN, demonstrating that young jets have the strongest impact on [O III] kinematics. The authors extend this into a morphological study by defining compact radio emission where the FIRST deconvolved (DC) major axis size is $< 3''$ and extended radio emission where the DC major axis is $> 3''$. The authors find more distributed gas when a compact morphology is present compared to extended radio emission.

The studies above investigate radio emission at high frequencies with moderate angular resolution. In contrast, this chapter is part of a series studying the connection between the properties of the [O III] λ5007 Å emission line and radio emission in a novel regime combining low-frequency with high angular resolution down to $0.3''$allowing us to probe kpc-scale emission.

In chapter 3, I discovered that AGN detected in the LoTSS Deep Fields DR1 (Sabater et al., 2021; Tasse et al., 2021) have a higher [O III] outflow detection rate (67.2±3.4%), compared to AGN without a detection (44.6±2.7%). I also performed stacking and line

profile analysis of Sloan Digital Sky Survey (SDSS) spectra, finding that radio detected AGN exhibit a larger integrated flux density in the second component (which indicates the presence of an outflow), calculated using the peak and FWHM (Full Width Half Maximum), after normalising to the peak of the narrow component. This confirmed a clear link between low-frequency radio emission at 144 MHz and these ionised gas outflows as traced by [O III] λ5007.

Using the standard 6″ resolution that the Dutch stations of the International LOFAR Telescope (ILT) provide at 144 MHz, chapter 3 found that the majority of the radio detected AGN did not show a radio excess (Delvecchio et al., 2017; Best et al., 2023) and therefore the origin of radio emission from these AGN is not due to high-powered radio jets. I were unable to refine the origin of radio emission physically driving the increased outflow detected rate further because around 90% of the radio detected sample were unresolved. Other possibilities for the emission could be low-powered jets, shocks produced from winds, or star formation (Panessa et al., 2019). Therefore, the question still remains: Which physical mechanism is driving the link between [O III] outflows and low-frequency radio emission?

I now have access to three LoTSS Deep Fields at sub-arcsecond resolution; Lockman Hole (Sweijen et al., 2022, 8-h integration time, 25 μJy beam^{-1} central sensitivity, 2483 source detections), ELAIS-N1 (32-h, 14 μJy beam^{-1}, 9203 detections de Jong et al., 2024), and now Boötes (Chapter 4, 8-h, 37 μJy beam^{-1}, 4091 detections). Together these fields cover ∼19 deg^2 and for the sample of AGN from chapter 3 with $z < 0.83$, these sub-arcsecond resolution images allow us to probe low-frequency radio emission down to scales of ∼2 kpc, which now allows us probe down to sub-kiloparsec emission which is not possible at 6″. So, I can revisit the well-defined sample from chapter 3 which lies within the ILT's field of view (FoV) to obtain their sub-arcsecond radio morphologies. In this chapter, I use a combination of the low-frequency, sub-arcsecond morphology alongside brightness temperature measurements (Morabito et al., 2022a, 2025b) to identify the physical mechanism driving the low-frequency radio emission and its relation to the presence of [O III] outflows using our previous measurements from SDSS spectroscopy.

This chapter is organised in the following sections: Section 5.2 describes the sample selection and the data including a summary of the [O III] fitting procedure from chapter

3. I then move on to Section 5.3 which describes the morphological results. Section 5.4 introduces brightness temperature and summarises these results. A discussion then follows in Section 5.5 and I finish with the conclusions in Section 5.6. In this work I assume a WMAP9 cosmology (Hinshaw et al., 2013) with H_0 = 69.32 km s^{-1} Mpc^{-1}, Ω_m = 0.287, and Ω_Λ = 0.713.

5.2 Sample Selection and Definitions

Here, I briefly summarise the sample selection of the radio detected AGN from chapter 3. I take optical spectroscopic measurements from SDSS using two catalogues: the SDSS DR16 Quasar catalogue (Lyke et al., 2020) and a broad line AGN catalogue (Liu et al., 2019). I locate sources which lie within the three Deep Fields from LoTSS Deep DR1: Lockman Hole, ELAIS-N1, and Boötes. I then remove AGN with z > 0.83 to ensure [O III] is visible in the SDSS spectra and remove spectra with a signal to noise (SNR) ratio below 5. I remove a further 31 AGN after visual inspection revealed poor quality spectra, (e.g., missing [O III] spectral information), and I are left with a sample of 198 AGN. I crossmatch these sources to the LoTSS Deep Fields DR1 using the catalogue of Kondapally et al. (2021). I find that 115 AGN have a detection in LoTSS, which in chapter 3 I coin the "radio detected AGN". In this chapter I will only focus on the radio detected population as I are interested in linking the [O III] outflow detections to sub-arcsecond 144 MHz morphologies. To obtain these sub-arcsecond resolution images I use wide-field images produced using the ILT. The FoV for these images is smaller in comparison to the FoV of the Dutch stations due to the larger size of the international stations. Consequently, 50 radio detected AGN fall out of the international station FoV and the radio detected population decreases to 76. Therefore, for these 76 AGN I already have access to [O III] fitting results using SDSS, and do not need to conduct further spectroscopic decomposition. I present the 0.3″ morphologies at 144 MHz of these 76 AGN in this chapter in order to shed light on the origin of radio emission driving the connection between low-frequency radio emission and [O III] outflows.

5.2.1 [O III]

I take the [O III] spectroscopic fits of the 76 ILT detected AGN as described in chapter 3. To summarise the fitting procedure, I use the fitting module, `QUBESPEC` [1] (Scholtz et al., 2021), which incorporates the Markov Chain Monte Carlo approach (MCMC; Goodman & Weare, 2010). I fit various models to the spectra, for example one model will fit [O III] with a single Gaussian, and another will fit [O III] with two Gaussians. I also implement Fe-II templates in several of the models, for full details, see chapter 3. I firstly use the Bayesian Information Criterion (BIC) to select the model with the best fit to the data for each spectrum and confirm the selection via visual inspection.

In this chapter, I are interested in whether the AGN hosts an [O III] outflow or not. I use the same three diagnostics to determine if an outflow is present as chapter 3. If two Gaussians produce the best fit to the emission line, I class this as an [O III] fitted outflow. When a single component has the best fit and the width of [O III] at 80% of the flux (W_{80}) is over 800 km s^{-1}, I class this as an W_{80} outflow, and finally I class AGN as hosting a W_{80} likely outflow if one component is fitted and 600 km s^{-1} < W_{80} < 800 km s^{-1}. This leaves AGN which have one Gaussian fitted with W_{80} < 600 km s^{-1} to be defined as not hosting an outflow. I summarises these definitions below:

- Outflow Present
  - [O III] Fitted Outflow - Second, blueshifted Gaussian present
  - W_{80} Outflow - One Gaussian fitted with W_{80} > 800 km s^{-1}
  - W_{80} Likely Outflow - One Gaussian fitted with 600 km s^{-1} < W_{80} < 800 km s^{-1}
- No Outflow - One Gaussian fitted with W_{80} < 600 km s^{-1}

I acknowledge that due to the complexity of the kinematics of [O III], the classifications above could lead us to missing outflowing structure in this emission line, for example AGN

[1] Available at `https://github.com/honzascholtz/Qubespec`

within our "no outflow" category could also show signs of outflowing structure at smaller scales. For example, in Ward et al. (2024) the authors discuss that models demonstrate that physically slow outflows may not manifest themselves in optical spectroscopy. Therefore these weak outflow would be missed in our AGN within our "no outflow" population, meaning the outflows which I trace in this chapter and chapter 3 are notably strong outflows.

To ensure that any morphological differences which appear between the outflowing and non-outflowing populations are not driven by a luminosity bias, I match the two populations in $L_{6\mu m}$ and redshift, where $L_{6\mu m}$ is a tracer for AGN bolometric luminosity (Richards et al., 2006). I calculate this luminosity using the flux densities at 5.8µm and 8µm of the *Spitzer* Deep, Wide-Field Survey (SDWFS; Ashby et al., 2009) for AGN in Boötes, and *Spitzer* Wide-Area Infrared Extragalactic Survey (SWIRE; Lonsdale et al., 2003) fluxes for AGN in Lockman Hole or ELAIS-N1. I adopt the same tolerances used in chapter 3 of $\Delta\ z = 0.06$ and $\Delta \log L_{6\mu m} = 0.3$, as these successfully match our data as well as not substantially reducing our sample size. This reduces the overall AGN population from 76 AGN to 47, where I remove outliers in the $L_{6\mu m}$ and redshift distributions between the outflow and non-outflow populations, with 35 AGN hosting an outflow and 12 do not. I perform a 2D Kolmogorov-Smirnov (KS) test on these matched populations using the public code `ndtest`[2] and obtain a p-value of 0.192, confirming that the two populations are statistically indistinguishable. I present our matched $L_{6\mu m}$ and redshift population as coloured markers in Figure 5.1 and the unmatched AGN as grey markers, with AGN with outflows presented as stars, and AGN without an outflow as circles. The histograms represent the distribution in redshift (top) and $L_{6\mu m}$ (right), with the purple dashed histogram showing the outflowing population, and solid pink being the no outflow population. I show how many AGN are within each category and population in Table 5.1, including the morphological classes which I discuss in Section 5.3.

I present the relationship between L_{144MHz} and $L_{[OIII]}$ in Figure 5.2, with the $L_{6\mu m}$ and redshift matched population as coloured markers and circular markers as detected sources and downward triangles as the upper limit for the undetected sources. I calculate

[2]Written by Zhaozhou Li, `https://github.com/syrte/ndtest`

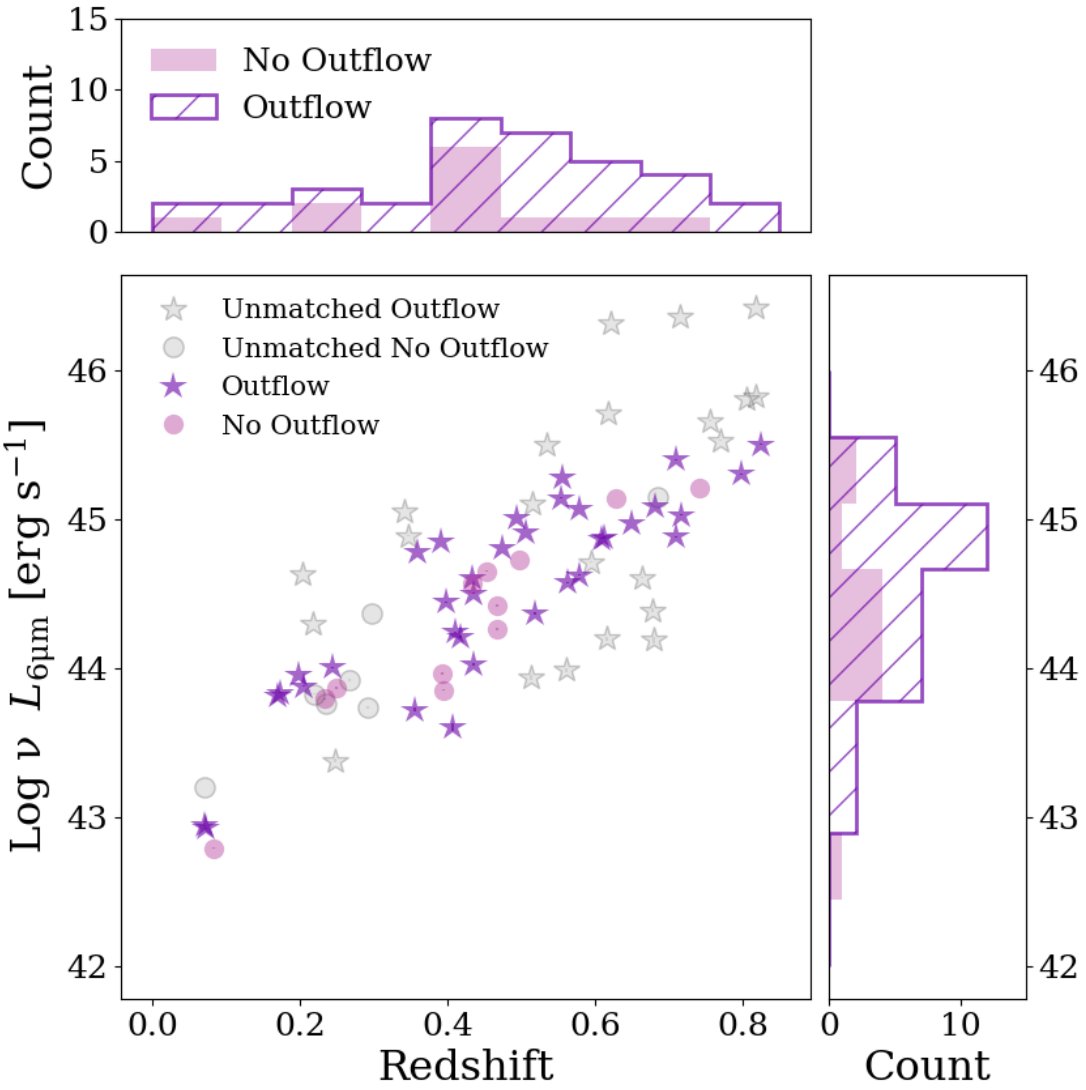

Figure 5.1: The $L_{6\mu m}$ and redshift relation of the AGN with and without an outflow. The coloured markers show the matched populations in $L_{6\mu m}$ and redshift, with an outflow (purple stars) and without an outflow (pink circles). The grey points represent the AGN which are removed as these are unmatched, with diamonds portraying the AGN with outflows, and circles for the AGN without an outflow. I show uncertainties but these are minimal. The top histogram conveys the redshift distribution and the right histogram is the distribution of $L_{6\mu m}$. The hashed purple histograms are the AGN with outflows and the pink solid histograms are the AGN which do not have an outflow.

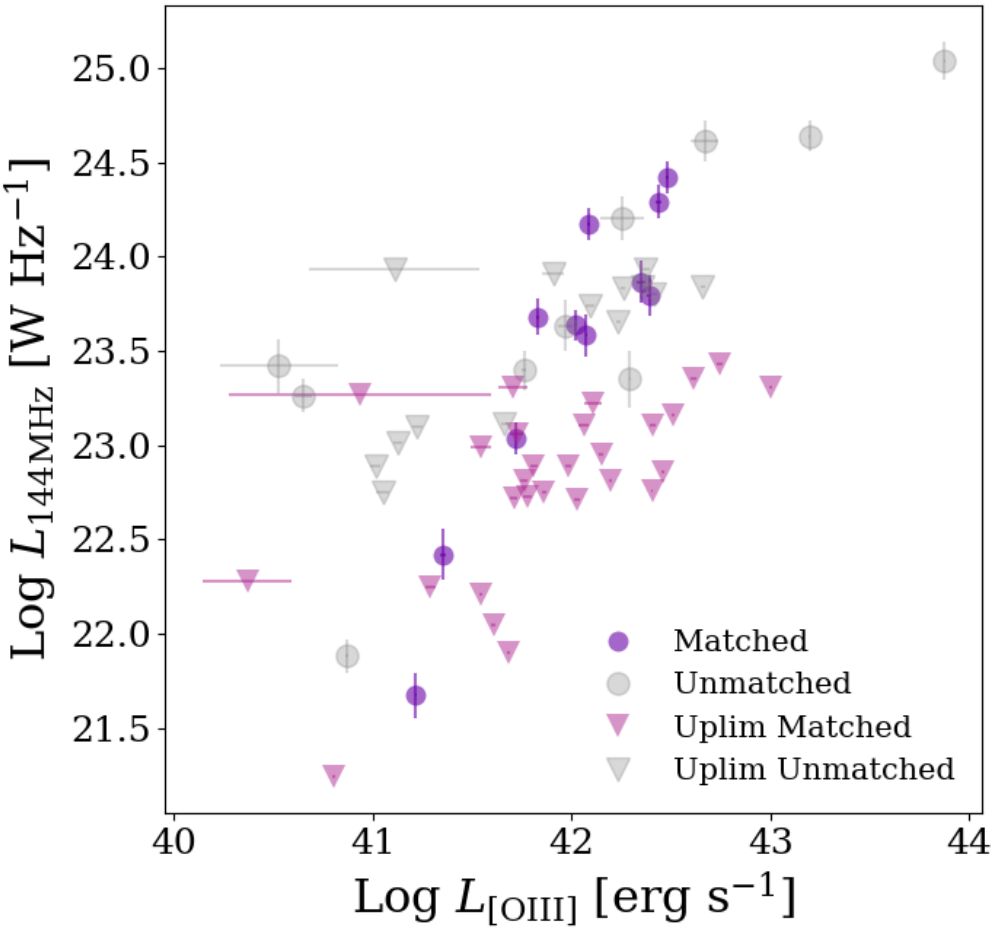

Figure 5.2: $L_{144\mathrm{MHz}}$ as a function of $L_{[\mathrm{OIII}]}$, the coloured markers are from the $L_{6\mu\mathrm{m}}$ and redshift matched population I use in this analysis, and the grey are unmatched. $L_{144\mathrm{MHz}}$ in this figure is calculated at 0.3″. Circles represent the detected AGN and downward triangles are the upper radio luminosity limits.

[O III] Outflow Type	Undetected	Compact	Extended	Total
[O III] Fitted Outflow	21 (13)	21 (12)	5 (4)	47 (29)
W_{80} Outflow	2 (1)	2 (1)	0 (0)	4 (2)
W_{80} Likely Outflow	4 (3)	2 (1)	0 (0)	6 (4)
All Outflows	27 (17)	25 (14)	5 (4)	57 (35)
No Outflow	14 (10)	5 (2)	0 (0)	19 (12)
Total	41 (27)	30 (16)	5 (4)	76 (47)

Table 5.1: Table summarising the number of AGN in each category of outflow and morphology type. The numbers in parentheses represent the $L_{6\mu\mathrm{m}}$ and z matched population.

the k-corrected $L_{144\mathrm{MHz}}$ for the detected AGN using the 0.3″ flux density, the spectral index, α (where $S_\nu \propto \nu^{-\alpha}$), assuming a typical synchrotron spectral index of $\alpha = 0.7$ (Klein et al., 2018), and the SDSS spectroscopic redshift. To calculate the associated uncertainties, I use the reported scatter in the flux scaling correction in each field, 25% for Boötes (see Section 4.3.4), 18% for Lockman Hole, and 15% for ELAIS-N1 and sum these uncertainties in quadrature with the flux density uncertainty from the source finding for each source. To calculate the upper limit of $L_{144\mathrm{MHz}}$ for the undetected sources at 0.3″, I take the relevant wide-field image and extract the 5σ noise level within a 3″ radius of the source's location and use this as the associated flux density. I do not report uncertainties for the upper limits, as they are not direct measurements but rather thresholds defined at a specific confidence level. I utilise the $L_{[\mathrm{OIII}]}$ presented in chapter 3 for these sources which are calculated by integrating the continuum-subtracted region between 4975 Å and 5030 Å using spectroscopic redshifts and the distance modulus, and then this is converted to a luminosity. The inverse square root of the inverse variance is taken to compute the associated uncertainties and then the sum of the uncertainties is taken in quadrature. I see that our $L_{6\mu\mathrm{m}}$ and redshift matched population follows a positive correlation between $L_{144\mathrm{MHz}}$ and $L_{[\mathrm{OIII}]}$, as expected.

5.3 Morphological Study

To study the link between the presence of [O III] outflows and the high-resolution morphologies I must first place each of the 76 AGN within our sample into a morphology category. The image I use for this is at the highest resolution: 0.3″. I define three categories: undetected, compact, and extended. AGN are classed as undetected if the source is not within the catalogues published alongside the relevant field's image. I note that for these AGN which are undetected at 0.3″ resolution, the radio emission detected in the 6″ resolution image must be below the surface brightness sensitivity in the higher resolution image.

I define compact AGN in two ways. Images can suffer from ionospheric smearing, meaning an unresolved source maybe mistaken for an extended source via visual inspection. In an ideally calibrated image the ratio between the integrated flux density, S_I, and peak

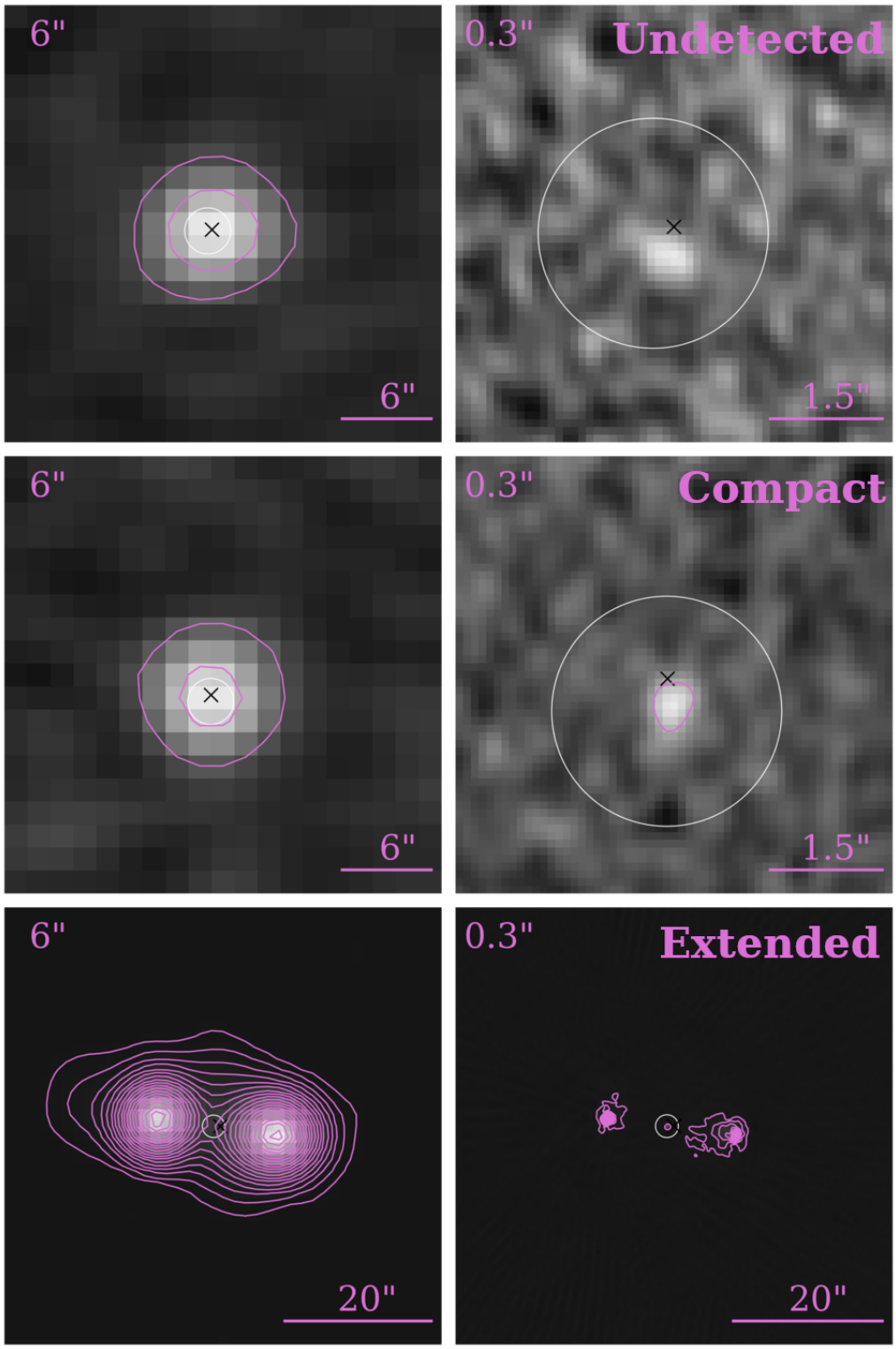

Figure 5.3: Demonstration of the morphology definitions in this work. *Left:* 6″ resolution, *right:* 0.3″ resolution. *Top:* Example of an "undetected" source, which does not have a 5σ detected at 0.3″ but is detected at 6″. *Middle:* A "compact" morphology. *Bottom:* "Extended" source. The black cross represents the LoTSS position, the white circle is the SDSS fibre and the contours are at a 5σ level.

flux density, S_P, for a unresolved source will be equal to one. However, in reality this is not the case, but the natural logarithm of (S_I/S_P) follows a Gaussian distribution (Franzen et al., 2015) and I can utilise this alongside its standard deviation to determine whether a source is resolved. I follow the procedure performed in Shimwell et al. (2019, 2022) to determine if a source is unresolved. I first locate the best candidates for real point sources by finding sources classified as S_code == "S" (pyBSDF has classified this source as a single compact component), and remove sources which are over three times (for Boötes and Lockman Hole) or four times (for ELAIS-N1) larger than the beam's major axis, as these sources could be resolved even if they are a single Gaussian component. For ELAIS-N1 I use four times the major axis of the beam as this provides a better sigmoid fit because ELAIS-N1 uses four observation nights meaning this image suffers from greater ionospheric smearing then the other fields. Also two of the four ELAIS-N1 pointings are averaged to 2 seconds instead of 1, hence contributing to time smearing. I perform a sigmoid curve fit and if a source is below this fit, then the source is unresolved, and hence I classify the source as compact. If a source is above this divide then this is a resolved source and I perform visual inspection on these to classify their morphology as these sources may still be compact. If a source shows spatially resolved structure, I define this AGN as extended, and if the source shows visually compact morphology I define these as compact. To summarise, I class the sources which are determined to be unresolved using Shimwell et al. (2019, 2022) as compact and perform visual inspection on all other sources. I present three sources, one of each morphological class in Figure 5.3, where the left hand panels show the sources morphology at 6″ and on the right is the respective 0.3 ″ morphology.

I present two example sources from the $L_{6\mu m}$ and redshift matched population which lies within the Boötes field in Figure 5.4. On the top I see the SDSS spectra for this AGN with the [O III] MCMC fit (from chapter 3) overlaid and from these fits I see that the AGN in Figure 5.4 hosts an [O III] outflow, specifically a [O III] fitted outflow as a second, broad, blueshifted Gaussian is present. In the bottom panel of these figures, I present four cutouts of these sources where I show purple 5σ contours. I start in the top left with the 6″ LoTSS cutout and proceeding clockwise with the 1.2″, 0.3″, and 0.6″ images. At all resolutions the source in Figure 5.4 is extended,.

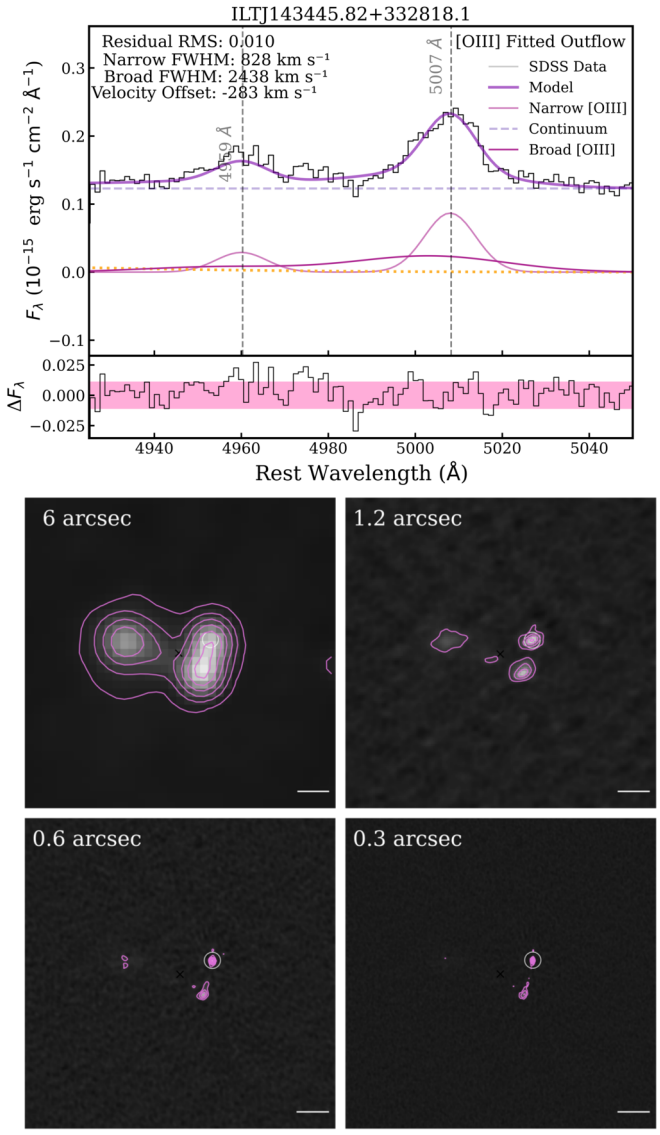

Figure 5.4: Montage showing the SDSS spectra and various morphologies of ILTJ143445.81+332818.1 (z = 0.197) which lie within the Boötes field. *Top:* SDSS spectra data (black) with the MCMC fitting results overlaid as a dark purple solid line. I display both the λ4959 Å and λ5007 Å [O III] emission lines. The pink Gaussians show the narrow component of [O III], the Gaussians in magenta are the broad component of [O III] which implies an outflow is occurring. The yellow dotted line shows the continuum. The lower panel of this subplot displays the residuals between the fitted model and SDSS data and the pink shaded region corresponds to the 1σ RMS region which I calculate over the full spectral range of the model. This AGN hosts an [O III] fitted outflow. *Bottom:* Cutouts of ILTJ143445.81+332818.1 at multiple resolutions. Starting top left and proceeding clockwise: 6″, 1.2″, 0.3″, and 0.6″ resolution. The background and the pink 5σ contours are from the respective resolution image. The scale bar in the bottom right corner demonstrates 6″ and the white circle near the centre of each cutout is the location of the SDSS fibre. At each resolution this source has been classified as extended, and I believe the radio core is located in the northern components due to its compact flux.

5.3.1 Morphological Results

To help us understand whether there is a link between ionised outflows and physical processes which produce low-frequency radio emission, I first investigate the relationship between outflow detection rates and the sub-arcsecond resolution morphology of the AGN within our sample. In Figure 5.5 I present the link between the various outflow detection rates and morphology via two different methods. The detection rate of AGN with outflows is shown with purple stars and the detection rate for the population without an outflow is shown with pink circles. To estimate uncertainties, I assume a binomial distribution, which is appropriate given the binary classification of sources as either outflowing or not. If the detection rate is equivalent to either 1 or 0, I do not show uncertainties. The grey dashed line separates the undetected AGN from the detected AGN. The results for Figure 5.5 are also shown quantitatively in Table 5.2.

On the top panel of Figure 5.5 I present the distribution of morphology class for sources with an outflow and those without an outflow, normalised by each outflow category i.e for the AGN with outflows, summing the detection rates across the various morphological classes is equivalent to unity. I see that among AGN without outflows, the majority of these AGN, 83.3± 10.8%, are undetected at sub-arcsecond resolution, compared to 48.6±8.4 of the outflowing population showing an undetected morphology. This is consistent with the results in chapter 3. Sources with a compact morphology are more likely to host an outflow than not and all AGN which show extended radio structure at 0.3″ host an [O III] outflow.

The bottom panel of Figure 5.5 shows the fraction of the population with/without outflows per morphology category. Therefore, the sum of with and without outflows within each morphology category is equivalent to unity. I see that in all morphological categories, there are more AGN which host an outflow than to those which do not. This panel also reiterates that all four AGN with an extended structure host an [O III] outflowing structure, and hence there are no AGN without an outflow which have an extended morphology. In fact, even if I consider AGN which are not within our AGN luminosity and redshift matched population, all five extended sources have an outflow. I also note that, for our extended population, not all of the radio flux density is confined within the SDSS fibre, and therefore I could be missing an outflow from the spectroscopy.

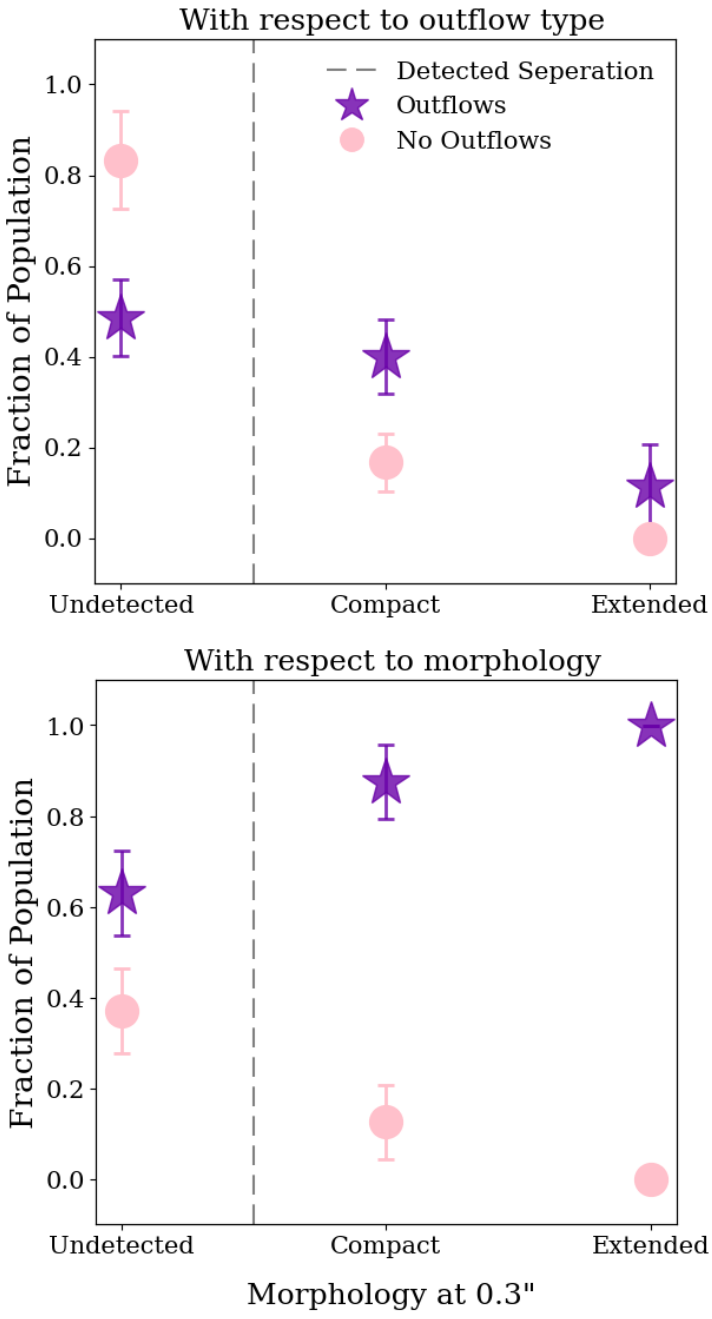

Figure 5.5: Fraction of population in relation to sub-arcsecond low-frequency radio morphologies, where a radio source is classified as either undetected, compact, or extended. *Top:* Distribution of morphology with respects to outflow population, i.e. for each outflow population, the fractions of different morphology categories add up unity. *Bottom:* Distribution of outflow population with respects to the morphology category, i.e. for each morphology class, the fractions of the outflow population adds to unity. The pink circle markers demonstrate the no outflow population and the purple stars represent the outflowing population. In cases where the fraction of the population is either zero or one, the uncertainty is omitted. The grey dashed line separates the undetected AGN from the detected AGN.

For example, see Figure 5.4, where the SDSS fibre only covers the the radio core of this extended source at 0.3″ resolution. However every extended AGN is hosting an outflow so I are not missing [O III] outflows connected to the extended radio emission, but I could be missing additional [O III] emission associated with the radio emission which does not lie within the SDSS fibre.

To summarise, for AGN without outflows, most are undetected at 0.3″, but are detected at 6″. This indicates that the radio emission is low surface brightness, which is consistent with star formation. In contrast, detected AGN (i.e. AGN showing compact or extended morphologies), are more likely to have outflows than not. This indicates that the radio emission could be due to AGN activity rather than star formation. I note that this result is based on small number statistics, and I require a large statistical sample to confirm this link.

Physical Size

To investigate the structure of our sources at sub-arcsecond resolution, in Figure 5.6 I examine the relationship between the luminosity at 144 MHz, their physical size, and the colour bar indicating redshift. For detected sources, I adopt the major axis as a proxy for physical size for sources within Lockman Hole and ELAIS-N1 as well as compact AGN within Boötes, but if a source is extended in Boötes I use the LAS (see Section 4.3.4). To estimate the lower limit angular sizes for the undetected sources, I extract the 5σ RMS noise from the 0.3″ image for the relevant field, and using the flux density at 6″, I calculate the major axis required for a source to be detected at 0.3″, assuming a circular morphology. For the associated asymmetric uncertainties, I use the upper and lower bounds of the flux density and then proceed to calculate the major axis. I convert these angular sizes to physical sizes using WMAP9 cosmology and spectroscopic redshift from SDSS. I note for the undetected sources, the $L_{144\mathrm{MHz}}$, and its uncertainties, are measured at 6″ (presented in chapter 3), whereas for the detected sources, I use 0.3″ measurements to calculate $L_{144\mathrm{MHz}}$. The use of radio maps with different angular resolutions in calculating $L_{144\mathrm{MHz}}$ may contribute to the apparent bimodality present between the detected and undetected sources.

In Figure 5.6, I depict compact sources with an outflow as crosses, compact sources

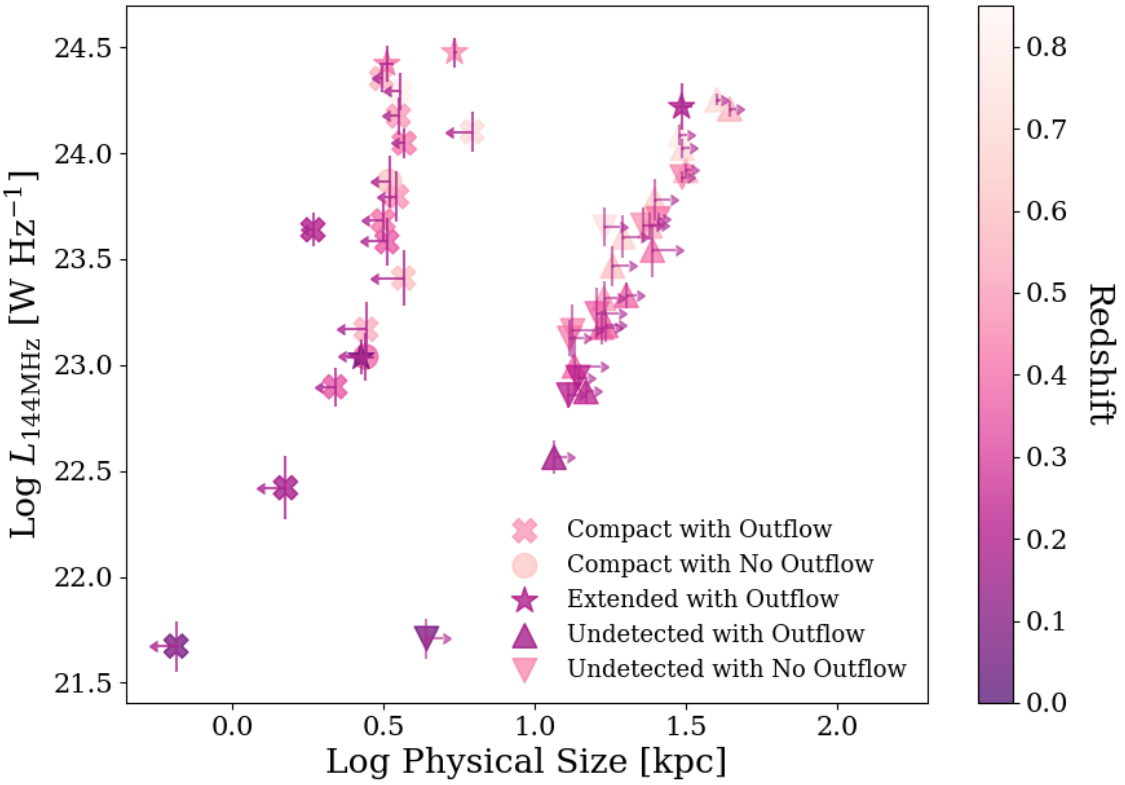

Figure 5.6: The relationship between the logarithm of the physical size, log $L_{144\mathrm{MHz}}$ and redshift (as traced by a colour bar). I show compact sources with an outflow as crosses, compact source without an outflow as circles, extended AGN with outflows as stars, undetected AGN with an outflow as upward-pointing triangles, and undetected AGN without an outflow as downward-pointing triangles. The sizes of compact sources are upper limits, while the sizes for undetected AGN are lower limits.

without an outflow as circles, extended sources with a outflow as stars, and the undetected sources as triangles, with upward triangles indicating undetected sources with an outflow, and downward triangles as undetected sources without an outflow. The sizes of compact objects are upper limits, as they remain unresolved at sub-arcsecond resolution. I observe a positive correlation between the physical size of sources and the luminosity at 144 MHz in all populations, along with a general increase in redshift with both variables. The largest source in our detected population is an extended source in the Boötes field, and here I use the LAS as proxy for its size. The undetected sources follow a tight trend with redshift and radio luminosity because their sizes depend on both variables. This population exhibits larger physical sizes than the detected sources, with values between 4 kpc and 39 kpc. This figure demonstrates that the more luminous a source is at 144 MHz, the more extended the source's radio emission is.

5.4 Brightness Temperature

LOFAR, with its sub-arcsecond resolution at low frequencies and high sensitivity, offers surface brightness sensitivity comparable to VLBI observations at higher frequencies. This is therefore an ideal instrument to identify radio emission from AGN (Morabito et al., 2022a, 2025a). Star formation is expected to have a maximum surface brightness (Condon, 1992) and anything above this must be produced by an AGN. This is often characterised by brightness temperature (T_b), which is not a physical temperature but it is a measure of the temperature that a black body would have in order to replicate the surface brightness of the source. Here I do not explicitly calculate brightness temperature for our sources, but rather the surface brightness.

Following Morabito et al. (2022a), I calculate the surface brightness using the total flux density and solid angle of the source, where the solid angle is,

$$\Omega = \frac{\pi\theta_1\theta_2}{4\ln 2}, \tag{5.4.1}$$

where θ_1 and θ_2 are the major and minor deconvolved axes. To determine the maximum surface brightness for star formation at 144 MHz, I use the same assumptions as Morabito

et al. (2022a) [3]. I find that 9 of our 16 compact sources are inconsistent with star formation, and are therefore due to an AGN (56.25%), with 7 (43.75%) sources falling below the threshold for AGN activity. I note that the brightness temperature measurements are lower limits as these measurements are conducted on compact sources with upper size limits, therefore the 7 compact sources not classified as AGN at the current resolution could still have low-luminosity AGN cores, so I cannot determine if these sources are consistent with star formation or AGN activity.

Figure 5.7 shows the relationship between Δ radio excess, which is the deviation of a source's radio emission from when a source would be classified as radio excess, and log star formation rates (SFR), where the SFR are from Best et al. (2023), calculated by taking a consensus value from four different Spectral Energy Distribution (SED) models. I only show detected sources at 0.3″ in this Figure and I note one detected source within Boötes is not shown due no consensus SFR being associated with this source. I flatten the radio excess and SFR-$L_{144\mathrm{MHz}}$ relation to demonstrate the Δ radio excess as a function of SFR. I do this with respect to the Boötes radio excess definition as this field has a slight redshift adjustment (see Best et al., 2023, for more details; here I use the maximum redshift of our sample, z=0.83, in this redshift dependent relation) in comparison to the other two fields. I scale sources within Lockman Hole (blue) and ELAIS-N1 (yellow) to match the radio excess definition in Boötes (pink). I note that the $L_{144\mathrm{MHz}}$ I use to obtain radio excess information is calculated using the 6″ flux density as presented in chapter 3 as the SFR-$L_{144\mathrm{MHz}}$ relation is derived using this resolution. Star markers show AGN with an outflow and circles show AGN without an outflow. Markers with a square around them are extended, and sources with a diamond are confirmed AGN from their T_b values.

Figure 5.7 shows us that 3 of the 4 extended sources are radio excess, demonstrating that the radio emission in these sources are AGN-driven. Combining this with the brightness temperature results, I see that the majority of sources detected at 0.3″ are AGN dominated. I also note that all sources classified as an AGN via brightness temperature host an outflow, thereby compact sources with no outflow do not have an AGN identification.

[3]Electron temperature of 10^4 K, a synchrotron spectral index of -0.8, and two key frequencies: the observed frequency of 144 MHz, as well as the assumed frequency of 3 GHz where synchrotron emission becomes optically thick.

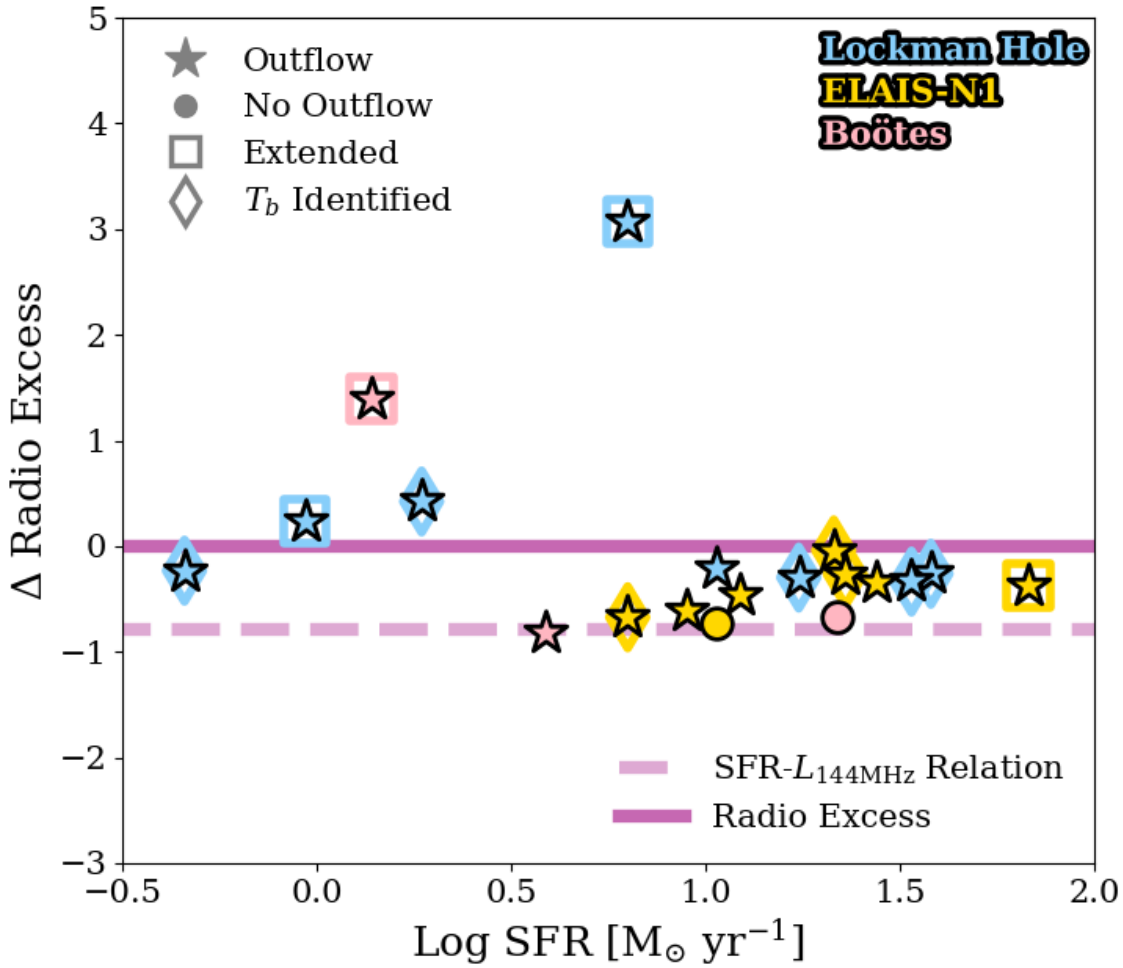

Figure 5.7: The relationship between Δ radio excess and log SFR. Only sources with a detection at 0.3″ contribute to this figure. The pink solid line is the radio excess divide which is centred at $y = 0$, with the SFR and $L_{144\mathrm{MHz}}$ relation as the dashed pink line. I define these relations using the Boötes field (pink), and hence I scale sources within Lockman Hole (blue) and ELAIS-N1 (yellow), which have a different radio excess definition, to match the Boötes definition. Star markers represent AGN with outflows and circular markers show AGN without outflows. Markers surrounded by a square have an extended morphology and sources with a diamond around them are confirmed AGN cores using brightness temperature measurements.

(a) With respects to outflow type

Morphology	Outflow	No Outflow
Undetected	48.6 ± 8.4	83.3 ± 10.8
Compact	40.0 ± 8.2	16.7 ± 6.3
Extended	11.4 ± 9.1	0 ± 0

(b) With respects to morphology

Population	Undetected	Compact	Extended
Outflow	63.0 ± 9.3	87.5 ± 8.3	100 ± 0
No Outflow	37.0 ± 9.3	12.5 ± 8.3	0 ± 0

Table 5.2: Tables summarising results shown in Figure 5.5 illustrating the connection between sub-arcsecond 144 MHz radio morphology and [O III] outflows. Table (a), with respects to outflow type. Table (b), with respects to morphology category. Values are percentages and I note that for Table (b), the uncertainties for the complementary categories are the same due to the binomial nature of the distribution.

5.5 Discussion

5.5.1 Origin of Radio Emission from Radio-Quiet AGN

Although the radio-loud and radio excess classes are defined in different ways, they both seek to identify where the radio emission is clearly dominated by AGN. The converse to these populations is considered to be 'radio-quiet' AGN and it is unclear what is the dominant form of radio emission in these sources (see Panessa et al., 2019).

Figure 5.7 shows the relationship between SFR and radio luminosity at 144 MHz. A similar figure is also shown in chapter 3, however in this chapter I add morphological information alongside brightness temperature identifications. I continue to see the majority of sources to be non-radio excess when a 0.3″ detection is present. Only four sources lie above the radio excess divide, and all the AGN showing radio excess host an outflow. This tells us that the radio mechanism produced by these radio AGN can not be produced by star formation alone and is likely to be produced by radio jets. Thus the origin of radio emission from 3 of the 4 extended sources is AGN-driven due to their radio excess nature. The other radio excess source is compact as well as being a radio AGN core, as confirmed using brightness temperature. As this is a radio AGN core, there will be a radio jet present (e.g., Blandford & Königl, 1979) which at this resolution with this frequency is unresolved. So I can now confirm that for the radio excess AGN, the radio emission is

produced by radio jets.

For AGN which are not radio excess, I could previously only rule out that the dominant radio emission mechanism was high powered jets. Looking at these sources, I see a mix of sub-arcsecond morphologies, containing AGN with compact morphologies, some being a confirmed radio AGN core and some not, and also a single extended AGN. I also note that all AGN which do not host an outflow are non-radio excess, show a compact morphology, and are not a detected radio AGN core. Therefore, the radio emission from AGN without outflows appears to be dominated by star formation.

It is also important to highlight that over half of the AGN which I detected at 6″ and which lie within the FoV of the ILT are undetected at 0.3″. As previously discussed in Section 5.5.2, this emission is on large scales and hence the responsible mechanism of this emission would be due to a large scale phenomenon which in this case would either be star formation or winds and therefore the radio emission is not due to jet and/or hotspots or AGN core emission.

Summing all this up, in this population of 42 non-radio excess AGN, i.e. radio-quiet AGN, there appears to be a combination of mechanisms driving the radio emission. Star formation or winds appears to drive 64% (27 out of 42) of these AGN, as the majority of sources are detected on large scales (6″), but not at small scales (0.3″). Small scale AGN driven emission is also driving a considerable amount of the radio emission as 19% (8 out of 42) show either an extended morphology, indicating small scale jets, or are a high T_b core.

5.5.2 Driving Radio Mechanism of [O III] outflows

I discuss how Figure 5.5 provides us with insight about the relationship between sub-arcsecond resolution morphology and the detection rates in the outflow and no outflow populations. I see that the majority of the population of AGN which do not host an outflow are undetected at 0.3″, but detected at 6″. A source is undetected at high-resolution when the radio emission has surface brightness which is too low to detect in a resolution element (beam). Therefore, the emission from these undetected AGN is produced on larger scales and hence consistent with star formation as demonstrated in Figure 5.6. For a source to be detected at sub-arcsecond resolution the emission must come from a much smaller

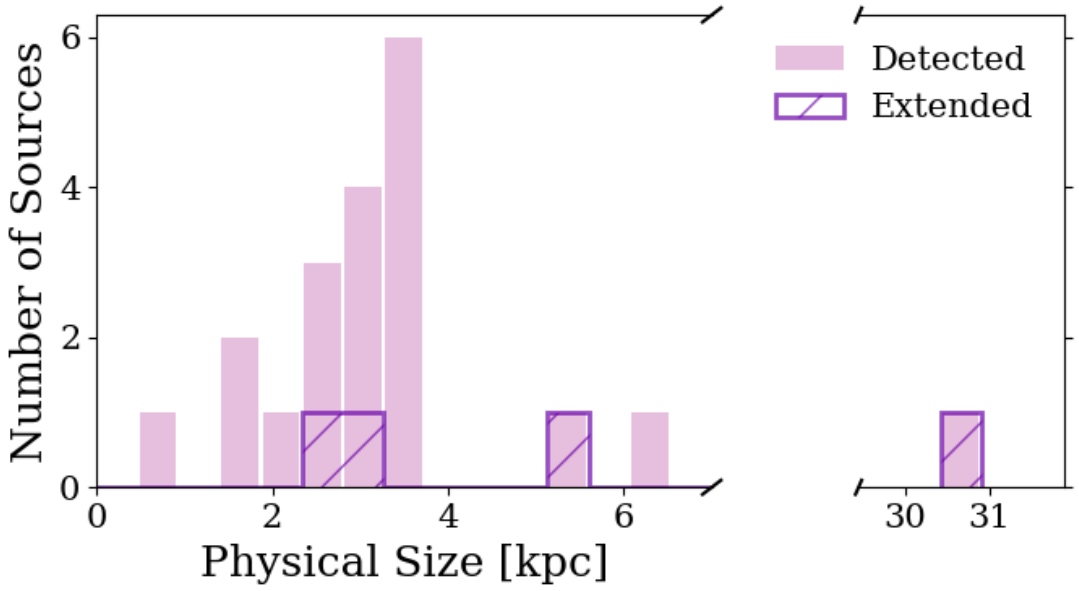

Figure 5.8: Histogram showing the distribution of the physical sizes in kpc of the detected sources at 0.3″. The pink solid histogram shows all detected AGN within the $L_{6\mu m}$ and z matched population. The purple dashed histogram shows the sizes of the extended AGN. The figure includes a break in the x-axis to account for a single outlying source with a physical size of approximately 30.5 kpc.

spatial scale. I show the physical size distribution of our detected sources in Figure 5.8 (see Section 5.3.1 for details about how I calculate these sizes). The physical sizes are all under 7 kpc, aside from one extended source which is >30 kpc. Hence, emission on the scale of 0.3″ is small-scale.

Around half of the AGN with outflows are also undetected at 0.3″, also indicating that this emission is driven by star formation. The remaining half of AGN with outflows are detected at 0.3″, with all extended AGN and all high T_b cores hosting an outflow. This implies that the radio emission is consistent with AGN activity.

The differences I see between these two populations is not driven by an AGN luminosity bias as I have matched in $L_{6\mu m}$ and z and I note that the radio luminosity at 0.3″ for the extended sources, is not significantly higher than the radio luminosity for the compact sources (<2σ).

I note that [O III] traces recent nuclear activity as it is produced from a region about 1 kpc in size, however the radio emission produced by large extended radio structure which can stretch 100s of kpcs occur on a much longer time scale of 10^8 years. Therefore

if the central engine has recently been shut down, the narrow line region, and hence [O III], may no longer be detected in the AGN, although the radio lobes will still be present. Therefore, for our detected sources, where I are mostly probing emission on scales <10 kpc, the timescales of nuclear activity traced by [O III] are likely comparable to those of the associated radio emission. In contrast, our undetected source, the emission is on larger scales, which is unlikely to be physically associated with the same timescales as the nuclear [O III] activity.

Putting all this together, I are seeing a physical link between small scale radio emission due to AGN, and ionised gas outflows, as traced by the [O III] emission line. The majority of sources which do not host an outflow are undetected at 0.3″ whereas the majority of sources with a compact morphology host an [O III] outflow. Furthermore all the sources with a compact morphology that are also a T_b core AGN host an [O III] outflow and all spatially resolved sources host an outflow. This supports the idea that small scale emission produced by the AGN core or radio jets and/or hotspots plays a key role in driving these outflows, while more diffuse, large scale emission from mechanisms such as star formation or winds is not a main driver. However it appears overall that for AGN with outflows there is around equal amounts of small and large scale emission contributing to the driving mechanism of these outflows as ~49±8.4% of AGN with outflows are undetected in the 0.3″ image.

In Appendix C.2 I investigate how [O III] kinematics vary between the detected AGN population and the undetected population. This is similar analysis to that performed in chapter 3, although the authors investigate the radio emission at 6″, whereas here I are probing emission at 0.3″. I see similar enhanced integrated flux of the broad area as well as enhanced W_{80} in the detected AGN compared to the undetected AGN. This suggests the enhancement I see is not driven by the radio emission which is resolved out between 6″ and 0.3″. Due to the limited sample size and lack of uncertainties I do not draw conclusions from Figures C.1 and C.2.

5.5.3 Comparing kpc-scale radio emission and [O III]

When investigating the origin of radio emission it is important to compare the results I see in this work to other work conducted at other frequencies and resolutions. Jarvis

et al. (2019) follows up 10 low redshift radio-quiet AGN which are originally selected in Mullaney et al. (2013) with images from the VLA and e-MERLIN. VLA images are between 0.3 and 1 arcseconds with a frequency range of 1.5-6 GHz and e-MERLIN images having a resolution around 0.25″ at 1.5 GHz for 9 targets and they discover that star formation only accounts for ∼10% of the radio emission with around 90% of these 9 targets showing extended radio structures on 1-25 kpc scales.

Njeri et al. (2025) presents similar work but at higher resolution with 42 e-MERLIN images at 6 GHz of low redshift quasars from the Quasar Feedback Survey. These images allow the authors to investigate sub-kiloparsec emission. Similarly to this study the authors use a combination of morphology and brightness temperature to classify their AGN. Combining these e-MERLIN and previous VLA images from Jarvis et al. (2021) they find that over 86% of these quasars are classified as radio AGN and therefore this emission is likely to be dominated by jet driven lobes and outflow driven shocks.

The results from Jarvis et al. (2019, 2021) and Njeri et al. (2025) appear to be contradictory to the results I present in this work, as I see that the majority of our matched AGN (27 out of 47) are undetected at 144 MHz and 0.3″ resolution and therefore the majority of the radio emission appears to be from star formation or winds. A key reason for the difference could be due to the low redshift nature of the samples presented in these as the AGN from these studies are below 0.2 redshift, whereas our sample spans to around 0.85. I note that the four extended sources within our sample are at low redshift. The high angular resolution images from the VLA and e-MERLIN in Jarvis et al. (2019, 2021) are at GHz frequencies whereas the high-resolution images for our sample are at MHz frequencies so I are probing a different regime of emission where the radio emission from the ILT is dominated by synchrotron emission. At GHz frequencies, there is an increased contribution from Bremsstrahlung emission. I also note that the selection of their targets is based on strong [O III] emission whereas our sample is optically selected and independent of [O III] properties until I split the population into sources with an outflow and those without. I see a clear correlation with [O III] outflows in our sample and resolved emission, therefore it may be the presence of powerful [O III] emissions that could be driving the kpc-scale and sub-kpc-scale resolved emission that is seen in Jarvis et al. (2019, 2021) and Njeri et al. (2025) . Finally, the Quasar Feedback Survey

targets AGN with AGN luminosity above 10^{45} erg s^{-1}, whereas all our AGN have an AGN luminosity below 10^{45} erg s^{-1}. The radio luminosities of sources in this survey is higher than ours. Taking a spectral index of -0.7 our sample probes emission down to $L_{1.4\mathrm{GHz}} \sim 10^{20}$ W Hz^{-1}. Therefore, these studies and ours lie in a different regime of both radio and AGN luminosity.

This high-resolution resolved study of the connection between [O III] and radio emission is consistent with previous unresolved analysis, which attribute the link to AGN activity (e.g., Molyneux et al., 2019; Kukreti et al., 2025). In addition, resolved Integral Field Unit (IFU) studies of individual sources, or small samples, have demonstrated that radio jets strongly interact with the ISM (e.g., Venturi et al., 2021; Girdhar et al., 2022; Speranza et al., 2024), in agreement with predictions from simulations (Meenakshi et al., 2022). IFU follow-up for the resolved, extended sources in our sample will therefore help us to disentangle the spatial interplay between ionised outflows and the ISM.

5.6 Conclusions

I present the morphological classification for the 76 optically selected AGN from chapter 3 which lie in the ILT FoV for three of the LoTSS Deep Fields: Lockman Hole, ELAIS-N1, and Boötes. I define three morphological categories: undetected AGN, where these sources are detected at 6″ but are undetected at 0.3″, compact AGN, which are unresolved at this resolution, and extended AGN, which show spatially resolved emission. I further separate our sample into two populations: AGN which host an [O III] outflow, and another where the AGN do not host an outflow. I then match these two populations in $L_{6\mu\mathrm{m}}$ and redshift to ensure that there is not an AGN luminosity bias between the two populations, leaving us with 35 AGN which host an outflow, and 12 which do not. Below I present the key findings in this work:

- If AGN are detected at both small, kpc-scales (0.3″) and large-scales (6″), 90±6.7% host an [O III] outflow. In contrast, 63±9.3% of sources detected on large-scales but undetected on small-scales host an outflow.
- Only 16.7±6.3% of sources without an outflow are detected on kpc-scales, however 51.4±12.2% of sources with an outflow are detected on kpc-scales.

- All four detected, extended sources host an outflow and 87.5±8.3% of sources with a compact morphology host an outflow.
- All 9 detected compact sources which are a high T_b radio core host an outflow.

The radio emission from the undetected AGN occurs on scales between 0.3″ and 6″ and is consistent with either the wide spread phenomena of star formation or winds. On the other hand, if a source is detected at 0.3″ and 6″, the emission is on small scales, and therefore the mechanism producing this emission is most likely AGN-driven. Putting everything together, if a source is detected at this resolution it is more likely to host an [O III] outflow than not, which indicates that the radio emission is likely due to AGN activity rather than star formation. Therefore, I are seeing that the connection between [O III] outflow and low-frequency radio emission is AGN-driven.

I also see that the majority of our detected sources are non-radio excess (i.e., radio-quiet AGN), and assuming the undetected sources are also non-radio excess, I find that the radio emission from these radio-quiet AGN is predominantly produced by large-scale star formation or winds, with around 19% (8 of 42 sources) showing AGN-driven radio emission.

I acknowledge that our sample size is limited, with 35 AGN with outflows and 12 without in our AGN luminosity and redshift matched population. The key limiting factor in the this study is the limited number of sources with SDSS spectroscopy within the ILT view of the LoTSS Deep Fields. WEAVE (William Hershel Telescope Enhanced Area Velocity Explorer) is a multi-fibre spectrograph mounted onto the WHT with a Multi-Object Spectroscopy (MOS) mode. Excitingly, there is a future three tiered survey planned: WEAVE-LOFAR (Smith et al., 2016). The Deep tier of this survey aims to target every radio source within the LoTSS Deep Fields which is above 100 μJy beam^{-1}, meaning an estimated 130,000 spectroscopic measurements will be taken. Even after limiting these measurements to sources within the ILT's FoV and incorporating an appropriate redshift cut off, I will have access to thousands of spectroscopic measurements as well as sub-arcsecond morphologies, which will revolutionise optical spectroscopic studies with radio counterparts. The first data release from the Dark Energy Spectroscopic Instrument (DESI; DESI Collaboration et al., 2025) will also increase the number of

spectroscopic measurements available within the LoTSS Deep Fields. The feasibility of fitting large samples with *QUBESPEC* arises from its flexibility to use either an MCMC or the significantly faster least-squares fitting method. This enables MCMC fitting for complex [O III] profiles while simpler cases can be efficiently handled with least-squares fitting.

With the increase of spectra within the Deep Fields from the WEAVE-LOFAR Deep tier and/or DESI, alongside the intermediate resolution images of Boötes and ELAIS-N1 (de Jong et al., 2024; Ye et al., 2024), I can expand our high-resolution studies to the slightly lower resolutions of $\sim$0.6″ and $\sim$1.2″. Using these images should allow us to further understand the relationship with [O III] outflows and more diffuse emission on intermediate scales as the long baselines at 0.3″ provide us information on compact levels, and short baselines at 6″ tell us about diffuse emission. Therefore these intermediate resolutions will tell us about the emission which becomes resolved out between the extremities of the baselines.

CHAPTER 6

Conclusions

In this thesis, I have outlined the research I have conducted over the course of four years of doctoral study at Durham University. I have utilised optical spectroscopic decomposition, allowing me to analysis warm ionised gas outflows to be analysed through the kinematics of the [O III] λ5007 Å emission line. I have also produced the first wide-field, sub-arcsecond resolution image of the Boötes Deep Field at 144 MHz using VLBI techniques, enabling thousands of sources to be studied on kpc-scales. By bringing together these two substantial pieces of data reduction, I have, for the first time, carried out a systematic study of both unresolved and resolved radio emission, utilising the same dataset of [O III] fitting results. For a sample of ~80 AGN, I have studied the connection between [O III] and low-frequency radio emission using sub-arcsecond resolution 144 MHz deep images to better understand the physical mechanisms driving both radio-quiet AGN, and the processes underlying the connection between warm ionised gas outflows and enhanced

radio emission.

I conclude this thesis by discussing potential avenues for future work to enhance my research, as well as the exciting new generation of radio telescopes to come. Before doing so, I first highlight key outcomes of this thesis below:

1 - Low-frequency radio emission enhances [O III] kinematics

In Chapter 3, I find that AGN with a radio detection at 144 MHz are more likely to host an [O III] outflow compared to AGN without a detection. This confirms a link between low-frequency radio emission and warm ionised outflows traced by [O III]. Furthermore, enhanced kinematics are observed in the radio detected AGN, which shows an increased integrated flux, calculated using the peak and FWHM of the outflowing component, compared to the radio non-detected AGN. I suggest that this is due to a greater amount of gas being present in outflows when there is a radio detection from LoTSS Deep DR1.

2 - Enabling statistical studies of AGN with wide-field sub-arcsecond 144 MHz VLBI imaging

I have produced three images of the Boötes Deep Field at 144 MHz with angular resolutions of $0.3''$, $0.6''$, and $1.2''$, each covering over 6 deg^2, which I present in Chapter 4. The highest resolution image ($0.3''$) achieves a central sensitivity of 37 μJy beam^{-1} and contains 4091 sources. This image allows kpc-scale radio emission from AGN within this Deep Field to be probed.

To produce images of this calibre, I had to overcome significant technical challenges. The primary difficulties are introduced by the ionosphere, which distorts radio signals as they propagate through this atmospheric layer. I addressed this by performing calibration through the use of 26 direction dependent calibrators, allowing me to characterise the ionospheric conditions across the wide-field.

3 - Star formation appears to be the dominant driver of low-frequency emission in radio-quiet AGN

In Chapter 3, I determine that the majority of the optically selected AGN sample with a radio detection in LoTSS Deep DR1 are non-radio excess, meaning that they are classified

as radio-quiet. Using only the 6″ resolution images, I rule out powerful radio jets as the dominant emission mechanism in these radio-quiet AGN, given their lack of radio excess.

Thanks to such images as the sub-arcsecond, wide-field, image of the Boötes Deep Field (Chapter 4), I further constrain the origin of radio emission from radio-quiet AGN in Chapter 5. We use a combination of morphological and brightness temperature measurements to determine that the dominant low-frequency radio mechanism in these radio-quiet AGN is star formation, as 64% are detected at 6″ but not at 0.3″. This indicates that these sources have low surface brightness and are produced by star forming processes. There is still a considerable amount of radio emission driven by AGN activity, with 19% of sources either extended at 0.3″ or exhibiting a high brightness temperature radio core.

4 - The connection between [O III] and low-frequency radio emission is AGN-driven

As discussed in Chapter 3, I find a significant link between the presence of [O III] outflows and low-frequency radio emission, and in Chapter 5, I investigate this further using resolved radio emission. I separate AGN with outflows from those without and then study their radio morphologies and brightness temperatures. For AGN without an outflow, 83±10.8% are undetected at 0.3″ but detected at 6″, indicating that their radio emission originates from large-scale star formation. For the detected population of AGN, all extended sources host an [O III] outflow, 87.5±8.3% of compact objects also host an [O III] outflow, and all compact sources with a high T_b AGN core host an outflow. This suggests that the enhanced [O III] properties are AGN-driven.

Due to the work presented in this thesis, we now have assess to an over 4,000 new sub-arcsecond resolution images of sources at 144 MHz, which allows the community to study the radio emission of these sources down to sub-kiloparsec scales. Thanks to these images alongside state-of-the-art spectral fitting of [O III], this work provides evidence that the higher outflow detection rate observed in radio detected AGN at 144 MHz, compared to their radio undetected counterparts, is AGN driven. Therefore, this thesis advances our understanding of the connection between low-frequency radio emission and ionised outflows.

6.1 Future Prospects

The work presented in this thesis represents just the tip of the iceberg in the research I aim to conduct. Below, I discuss future projects and surveys that will be beneficial in advancing my goal of understanding the connection between radio emission and ionised outflows.

WEAVE-LOFAR

With sub-arcsecond resolution images of the three LoTSS Deep Fields now complete, I have access to nearly 10,000 radio sources, each with a 0.3″ resolution detection. This provides an unprecedentedly large sample of high-resolution images for morphological studies. However, in the work presented in this thesis, the sample size is limited, with the primary constraint being the optical spectral coverage of the ILT LoTSS Deep Fields, with fewer than 100 AGN meeting the criteria in SDSS. Fortunately, a forthcoming three-tiered survey promises to bridge the gap between radio detections and optical spectroscopic measurements: WEAVE-LOFAR (Smith et al., 2016).

WEAVE (William Hershel Telescope Enhanced Area Velocity Explorer) is a new multi-fibre spectrograph installed on the William Hershel Telescope in La Palma, featuring a Multi-Object Spectroscopy (MOS) mode. The MOS mode allows around 1000 individual fibres to be positioned within the FoV, enabling spectroscopic observations of hundreds of sources simultaneously. Excitingly, WEAVE-LOFAR will target radio sources detected with the ILT and will deliver high-resolution spectroscopic measurements, providing astronomers with a prime opportunity for statistically robust spectroscopic studies of radio detected sources.

This survey will be conducted in three tiers, with the Deep tier being particularly beneficial to my research. This tier will target sources within the LoTSS Deep Fields that have a 6″ 150 MHz flux density above 100 μJy beam^{-1}, providing an estimated 130,000 spectral measurements across Boötes, Lockman Hole, and ELAIS-N1. The number of sources with both sub-arcsecond resolution images and spectroscopic data from WEAVE-LOFAR will be in the thousands, even after accounting for the smaller FoV of LOFAR-VLBI and the fact that many sources (~40%) will no longer be detectable at

the highest resolution.

With this large statistical sample, I will be able to fully analyse the connection between [O III] and radio emission. First, I will study how kinematics varies across different radio and bolometric luminosity bins to see where the enhancement in [O III] is most significant. For example, Mullaney et al. (2013) found that [O III] enhancements are most significant in radio-intermediate sources at high frequencies. I can also expand these studies across cosmic time by separating the sample into redshift bins.

Personally, I believe the most exciting prospect enabled by WEAVE-LOFAR is the ability to investigate [O III] outflows at intermediate spatial resolutions. For example, both ELAIS-N1 and Boötes have 0.6″ and 1.2″ resolution images available, but in this thesis I did not utilise them, as including them would further constrain the already limited sample size. With more spectra at my disposal, I will be able to investigate the outflow detection rate and the kinematics of the [O III] emission line across multiple spatial scales, thereby providing a deeper understanding of the origin of radio emission in these AGN.

Furthermore, if increasing the sample size can enhance my research, I can utilise another tier of WEAVE-LOFAR: Wide tier. This will target sources from LoTSS with a flux density above 10 mJy beam^{-1}. Currently, the wide survey of the ILT, LoTSS, is limited to 6″, however a new survey is reprocessing many LoTSS detections to include the international stations in the data reduction process, thereby achieving 0.3″ resolution for these sources. This is the LoTSS-HR (LOFAR Two Meter Sky Survey high-resolution) project, which also targets sources within LoTSS with a flux density of 10 mJy beam^{-1}. Therefore, for an estimated 150 sources per pointing, we will have access to 0.3″ resolution images alongside high quality spectra measured from the Wide tier of the WEAVE-LOFAR survey. I hope this highlights the exciting era we are entering for both spectroscopic surveys and high-resolution radio imaging.

DESI

While spectroscopic measurements with WEAVE-LOFAR remains a future prospect, DESI has recently released its first spectroscopic dataset (DESI Collaboration et al., 2025). DESI aims to provide spectra for over 1.5 million quasars, resulting in this instrument being a powerful tool for quasar science. The first data release already offers

substantial coverage of the Boötes and ELAIS-N1 fields, which are covered by the wide-field, sub arcsecond images created using the ILT. Consequently, I now have access to both spectroscopic measurements and sub-arcsecond resolution imagining across these fields. In fact, I have already obtained spectral fitting results for approximately 650 quasars with $z < 0.96$, allowing me to study [O III] outflows. This represents a significant increase over my precious SDSS-based sample, which contained only 76 quasars. With this expanded sample, I will perform statistically robust analysis of the connection between unresolved and resolved AGN morphologies and their warm ionised gas properties, as traced by [O III].

Multi-phase outflows

The study of multi-phase outflows is essential for understanding the impact of outflows on AGN feedback. In this work, I have focused on the single warm ionising phase of outflows, however, in future work it will be important to obtain observations that allow the study of multiple phases. I will identify a small population of AGN for which I have performed [O III] fitting, showing strong [O III] outflows along with extended sub-arcsecond 144 MHz radio structures, and propose for ALMA time to observe the spatially resolved molecular gas. The combination of spatially resolved kinematics of molecular gas and the kinematics of ionised gas, alongside the sub-arcsecond, 144 MHz, jet morphology, will allow me to probe jet-ISM interactions in a regime never explored before.

Another potential avenue to further our understanding of multi-phase outflows is to connect the warm ionised outflows with the hot ionising gas phase, such as UFOs or WAs. The detection of UFOs requires deep X-ray observations, therefore, for the same population mentioned above, I will propose for deep X-ray observations to investigate whether these strongly ionised outflows also host an UFO or a WA. Current studies indicate that approximately 60% of local AGN have an associated WA, so it is likely that we will obtain several detections, and potentially more if there is a connection between the presence of an [O III] outflow and UFOs or WAs.

Looking (much) further ahead, the Athena mission will conduct wide-field surveys with sufficient depth to detect UFOs, which will revolutionise the study of the hottest phase of outflows (Xu et al., 2024). This will allow samples of UFOs to be obtained alongside radio

morphologies from I-LoTSS (see below) with spectroscopic measurements performed by WEAVE-LOFAR, enabling us to study the interaction between the hot and warm ionising phases of outflows and their connection to kpc-scale radio emission.

Further [O III] analysis

This thesis has focused on linking the kinematics of the [O III] emission line to low-frequency radio emission. I aim to expand this work by investigating the energetics of [O III] alongside its kinematics. For instance, I can study how the mass outflow rates of the observed [O III] outflows vary with radio luminosity. Furthermore, I plan to extend the [O III] study by obtaining spatially resolved spectroscopy for a population of AGN with strong [O III] outflows and extended 144 MHz radio morphology at 0.3″. This will allow me to investigate the interaction between the radio jet and the ISM by tracing [O III] across the host galaxy. With the Large Integral-Field Unit (LIFU) mode of WEAVE now operational, I will propose for WEAVE-LIFU time to study the spatially resolved [O III] kinematics for these objects in order to trace ionised outflows.

LOFAR 2.0

As previously mentioned, due to the current solar maximum, LOFAR has been temporarily shut down to enable an upgrade to LOFAR 2.0. With this upgrade, several new large observing programs will commence, three of which will particularly benefit my research.

Firstly, the LOFAR 2.0 Ultra Deep Observation (LUDO; PIs Morabito and Best) will obtain a 3000 hour observation of the Euclid Deep Field North (EDFN), free from confusion noise limitations. This will achieve a noise level of 2 μJy beam^{-1} at 150 MHz, with resolution of ∼0.3″. I am a member of the radio data reduction team and will play a key role in producing the final high-resolution image of this field. LUDO will cover an area of 3.7 deg^2, and, due to the depth of the observation, we estimate detecting around 280,000 sources from this field alone.

At these low flux densities, many of the sources will be high redshift star-forming galaxies, allowing us to study star formation at the epoch of reionisation. More specifically, my AGN focused research will benefit from the detection of sub-arcsecond high redshift jets, which will help us understand radio emission mechanisms in the early universe. At

lower redshift, where existing spectroscopic measurements are available for [O III], I will be able to probe unpresidentially low luminosities, enabling a detailed investigation of how [O III] kinematics varies across a wider range of flux densities.

Secondly, the International LOFAR Two-metre Sky Survey (ILoTSS; PIs Shimwell and O'Sullivan) will be the first wide-area, high-resolution (0.3″) radio survey, achieving a sensitivity ∼30 μJy beam^{-1}. This survey will not only complete the 10% remaining sky area needed to finish LoTSS, but it will also include the international stations in the data reduction process, enabling radio emission to be probed at kpc-scales.

ILoTSS will facilitate extensive studies across the AGN population, probing both low luminosities and resolved radio structures. It will also revolutionise gravitational lens studies, with an expected 5000 radio-loud lenses to be discovered. As a member of this survey team, I will combine ILoTSS with the Wide tier of WEAVE-LOFAR which will provide spectra for radio bright AGN, to increase my sample statistics across the northern sky. This will allow me to place robust statistical constraints on the connection between [O III] kinematics and radio emission.

Finally, as previously mentioned, the LOFAR 2.0 upgrade will particularly benefit the LBA, which operates at a lower central frequency of 58 MHz compared to the HBA (144 MHz). One of the most anticipated large programs of LOFAR 2.0 utilises the LBA, and is the LBA LOFAR Community Sky Survey (LLoCuSS; PIs van Weeren, de Gaperin, Vedantham). This survey will allow me to probe the connection between AGN outflows and even lower frequencies.

Since LLoCuSS will also provide LBA data for the LoTSS Deep Fields, which are included in the coverage, I will be able to study multiple frequencies by combining the LBA, HBA, and Apertif (Kutkin et al., 2023, 1.4 GHz) images across the three LoTSS Deep DR1 fields, allowing me to analyse the spectral indices and estimate source ages of a population of AGN with both [O III] spectral information and high-resolution radio morphologies.

SKAO

The future of radio astronomy is not only bright in the northern hemisphere due to LOFAR 2.0, but the southern sky will also be revealed in a new light thanks to the

Square Kilometre Array Observatory (SKAO; Dewdney et al., 2009). The SKAO will consist of two telescopes; SKA-Mid, and SKA-Low. As my research focuses primarily on low-frequency radio astronomy, I will concentrate on SKA-Low.

SKA-Low is currently under construction in Western Australia and will be composed of over 130,000 dipoles arranged across 512 separate stations. Building a telescope of this calibre requires global collaboration, and currently 16 SKAO partner countries are contributing to its construction. Personally, I am most enthusiastic about SKA-Low because it will unlock the southern radio sky at low frequencies with relatively high resolution. This is especially important because the southern hemisphere hosts most of the world-class optical and NIR facilities, enabling radio observations to be incorporated into multi-wavelength studies.

This new generation of telescopes also brings a substantial challenge: data processing and storage. The SKAO will truly test our technical capabilities, as the combined instruments are expected to archive over 700 pb of data every year. In this new era of "big data", radio astronomers will need to adapt to new ways of accessing their observations. The SKAO plans to provide the community with finalised data products produced by SKAO built pipelines, after which the raw visibility data is then deleted. While this approach will benefit astronomers who do not have extensive radio data processing experience by providing science-ready images, it will pose a significant challenge for the SKAO in meeting the high quality standards expected by the radio community.

With the inclusion of international stations, the ILT currently has an advantage over SKA-Low thanks to its VLBI capabilities. However, a future project could shift the balance for high-resolution observations in the southern hemisphere. The Low-frequency Australian Megametre-Baseline Demonstrator Array (LAMBDA) aims to built additional SKA-Low style stations across Australia, enabling VLBI with SKA-Low. Once these stations are successfully integrated with each other, further afield low-frequency radio telescopes could also be incorporated into the network, providing extremely long baselines and enabling high-resolution observations. The next stage of my career will involve joining the LAMBDA team at CSIRO, where I will build on the expertise gained during my PhD with LOFAR-VLBI and apply this knowledge to this new state-of-the-art interferometer.

I'm thrilled to step into this new era of radio astronomy with my involvement in both

LOFAR 2.0 and LAMBDA. The discoveries from these next-generation facilities will be truly transformative for the radio and AGN communities. Radio astronomy is undergoing a massive transformation, and I can't wait to be a part of it. I hope you strapped on your Boötes tight enough for this long journey through the past four years of my research. There will be plenty more to come! Thank you for reading.

APPENDIX A

Appendix A

A.1 Additional Material for Chapter 3

A.2 Additional cumulative distribution functions

Here we present additional CDFs to support the discussion in Section 3.4.2 to further demonstrate how the [O III] line profiles differ in the radio detected AGN compared to the radio non-detected AGN. The top panels of Figure A.1 and Figure A.2 show the results for the CDFs of W_{80} for AGN with [O III] fitted outflows (Top panel of Figure A.1) and AGN with only a single component fitted to [O III] (Top panel of Figure A.2). The lower panels show the CDFs for the FWHM of the narrow component, with the bottom panel of Figure A.1 containing AGN with an [O III] fitted outflow and the bottom panel in Figure A.2 containing AGN with no broad component, so only a narrow component is fitted.

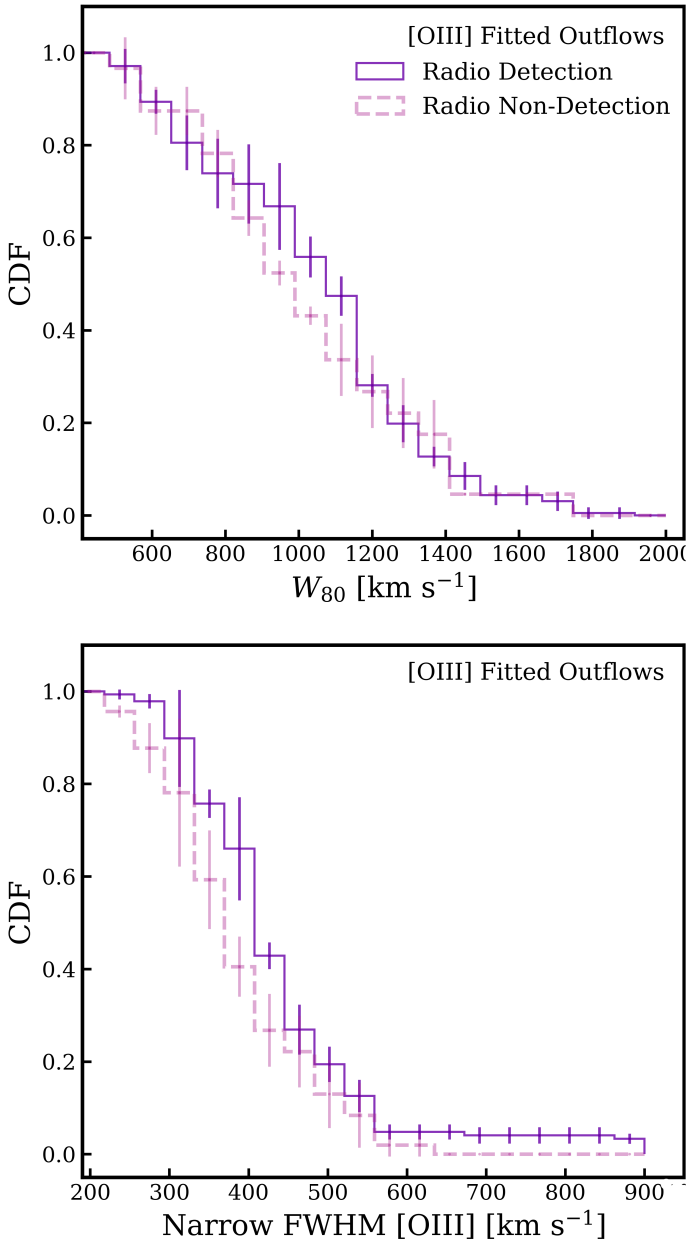

Figure A.1: Further average cumulative distribution functions of [O III] properties. The solid purple step function shows the distribution for the radio detected AGN and the dashed pink line shows the information from the radio non-detected sources. *Top:* CDFs of W_{80} [O III] showing the results only AGN which are fitted with a second component. *Bottom:* CDFs of the FWHM of the narrow component of [O III] with only AGN which are fitted with a second component. The uncertainties presented are as a result of bootstrapping.

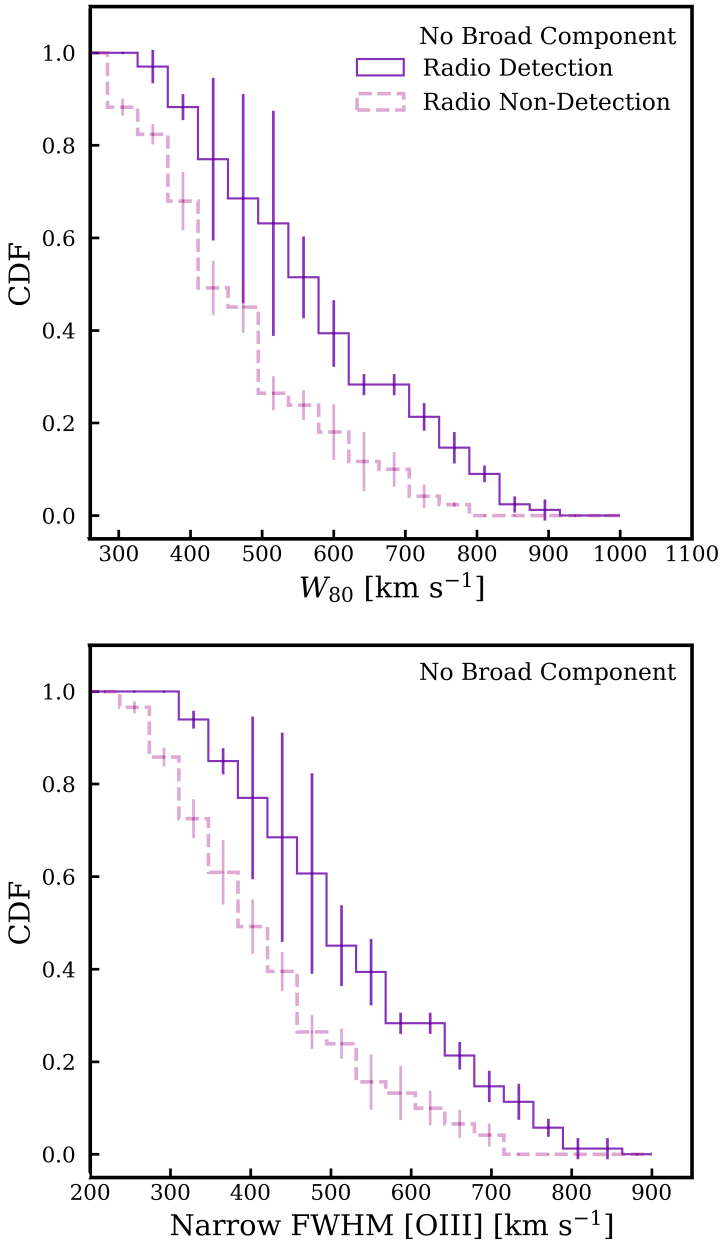

Figure A.2: Further average cumulative distribution functions of [O III] properties. The solid purple step function shows the distribution for the radio detected AGN and the dashed pink line shows the information from the radio non-detected sources. *Top:* CDFs of W_{80} [O III], all AGN which are fitted with a single Gaussian. *Bottom:* CDFs of the FWHM of the narrow component of [O III] with only AGN which are fitted with a second component. The uncertainties presented are as a result of bootstrapping.

APPENDIX B

Appendix B

B.1 Additional Material for Chapter 4

B.2 Image Properties

Figure B.1 shows us how the ratio of flux density at 0.3″ ($S_{\rm ILT}$) and flux density at 6″ ($S_{\rm LoTSS}$) varies with SNR which we measure from the 0.3″ image by taking the ratio of peak intensity and flux densities as measured by pyBDSF. The sources contributing to this figure are detected within 1″ of their LoTSS position. As expected, we see the majority of sources lie at low SNR and have a logarithmic ratio of ($S_{\rm ILT}$) and ($S_{\rm LoTSS}$) slightly below zero, as we expect some emission to be resolved out when we increase the length of our baselines. We do see some sources which lie above zero, and this appears to occur at a lower SNR ratio. This happens as at lower SNR it becomes increasingly difficult for

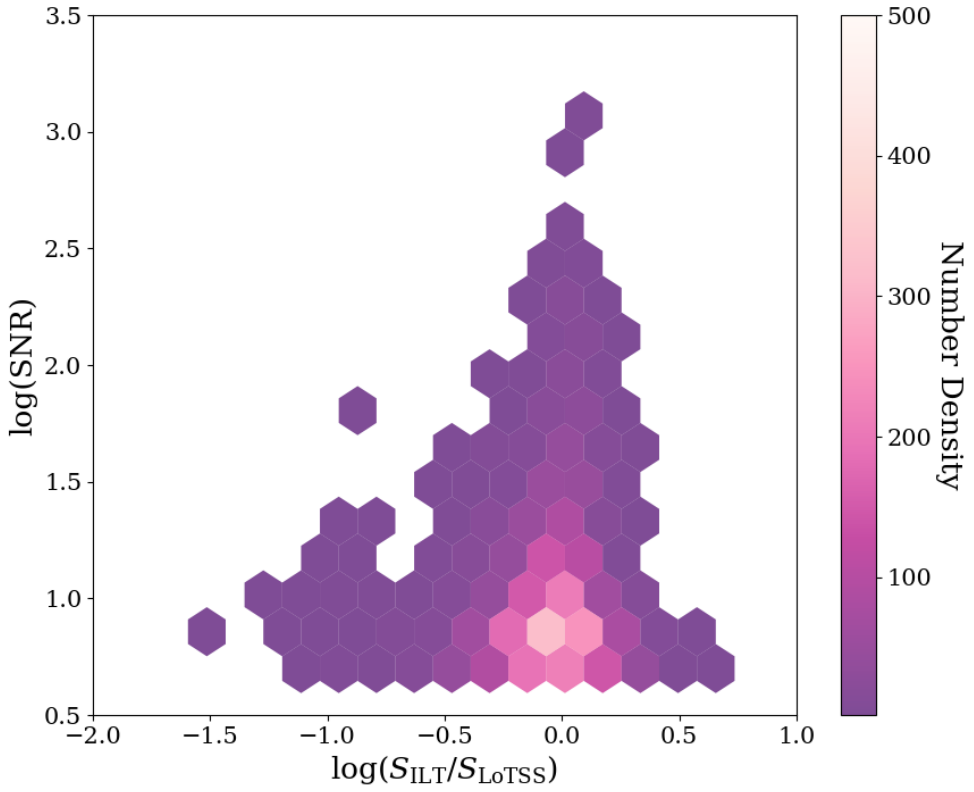

Figure B.1: The SNR of the ∼0.3″ resolution image as a function of the ratio between the flux density at 0.3″ ($S_{\rm ILT}$) and flux density at 6″ ($S_{\rm LoTSS}$), where we trace the number density with the colour bar. For a hexagon to be plotted, at least 2 sources must lie within the bin.

pyBDSF to measure flux density and hence the fluxes maybe overestimated, because not all the flux detected is associated with the source, and is likely to be a noise contribution.

APPENDIX C

Appendix C

C.1 Additional Material for Chapter 5

C.2 [O III] kinematics

To further investigate the relationship between [O III] and high-resolution radio morphologies, we investigate how [O III] kinematics (derived from Escott et al., 2025) vary depending on whether a source is detected or undetected at 0.3″ using cumulative distribution functions (CDFs). Here, we are not investigating the variation between AGN with outflows and AGN with no outflows, and therefore we do not use the $L_{6\mu m}$ and redshift matched population. We check that the 2D KS test for $L_{6\mu m}$ and redshift between the detected and undetected populations outputs a p value above 0.05, and therefore these two populations can be compared without matching being necessary. We note that we do not

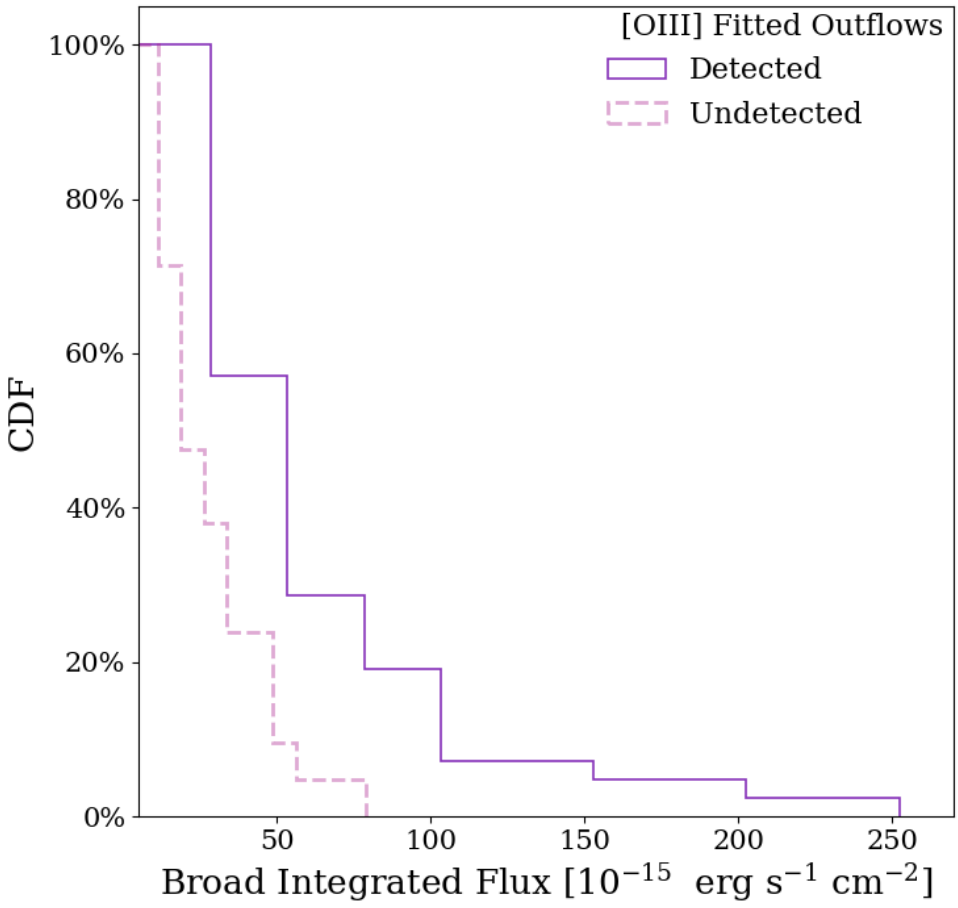

Figure C.1: Cumulative Distribution Function AGN with an [O III] fitted outflow comparing the integrated flux of the broad component fitted to [O III] of detected and undetected AGN at 0.3″. The solid purple histograms show the results for the detected AGN and the dashed pink histogram portrays the undetected AGN.

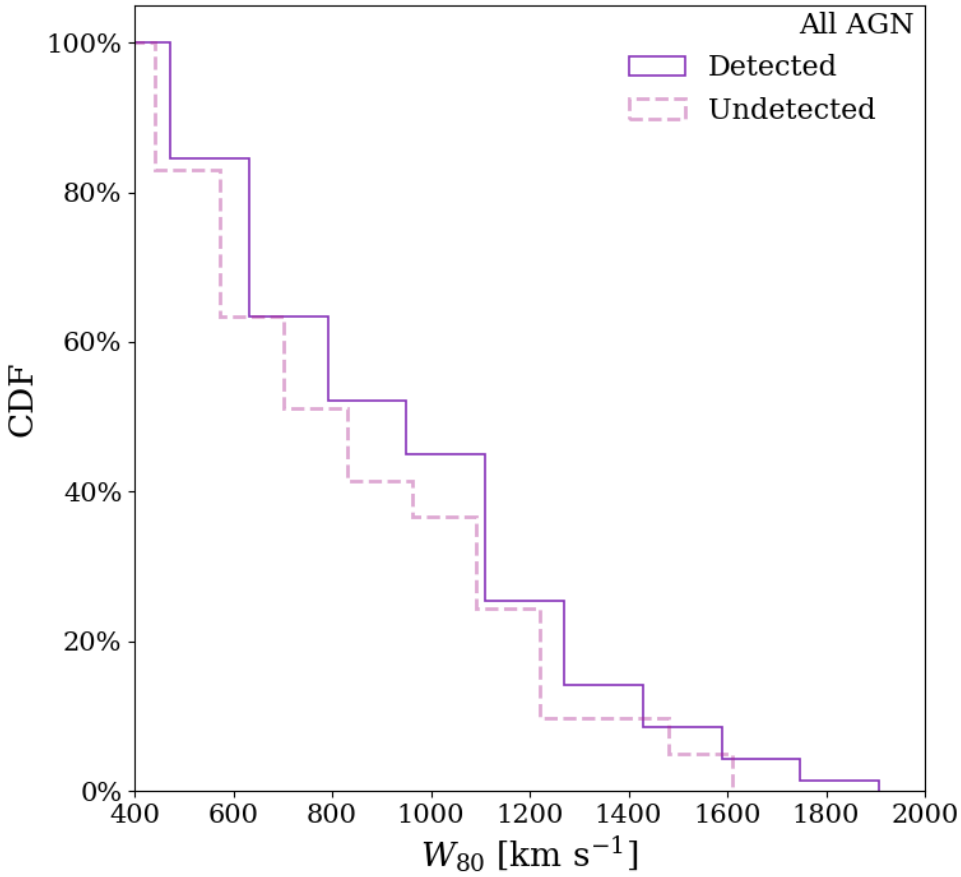

Figure C.2: Cumulative Distribution Function all AGN, regardless of outflow type comparing the W_{80} of detected and undetected AGN at 0.3″. The solid purple histograms show the results for the detected AGN and the dashed pink histogram portrays the undetected AGN.

draw any significant conclusions from these CDFs due to our limited sample size as the detected population has 35 AGN and the undetected have 41 AGN.

Figure C.1 and Figure C.2 illustrates the relationship between two kinematics properties of [O III] and how they vary depending on if they are detected at sub-arcsecond resolution or not. Detected AGN are depicted with purple solid lines, and we show undetected AGN with dashed pink lines. Figure C.1 shows the results for the integrated flux of the broad component of [O III] which we define as the area of the component which we calculate using the peak and FWHM of the broad Gaussian component. Only AGN which are within the [O III] fitted outflow category are included as we require a broad component to be present. We see a higher integrated flux of the broad component when the AGN are detected compared to AGN which are undetected at 0.3″.

Figure C.2 compares how the W_{80} varies between the two populations. Again, here we see that compact AGN have a larger W_{80} (which is a non-parametric proxy) compared to the undetected AGN, however this is at a lesser extent in comparison to the increase we see in the integrated flux of the broad component.

Both these CDFs show similar results to the kinematic analysis in Escott et al. (2025) where the authors compare these kinematics between AGN detected at 6″ and AGN not detected at 6″, whereas in this work, we are comparing AGN which are all detected at 6″, but the detected AGN are still detected at 0.3″ and the undetected population are not detected at 0.3″. As we still see the enhanced kinematics of [O III] in the detected population at 0.3″, this suggests that the relation is not driven by the emission which is resolved out in-between 6″ and 0.3″. Due to our limited sample size and lack of uncertainties, we require larger samples in further work to probe the concreteness of this result.

Bibliography

AAS 2018, This Month in Astronomical History | American Astronomical Society, https://aas.org/posts/news/2018/07/month-astronomical-history-1 1.2.1

Aihara H., et al., 2018, Publications of the Astronomical Society of Japan, 70, S8 3.2.1

Albán M., Wylezalek D., Comerford J. M., Greene J. E., Riffel R. A., 2024, Astronomy & Astrophysics, 691, A124 5.1

Alexander D. M., Hickox R. C., 2012, New Astronomy Reviews, 56, 93 3.1

Andonie C., et al., 2022, Monthly Notices of the Royal Astronomical Society, 517, 2577 3.2.4

Antonucci R., 1993, Annual Review of Astronomy and Astrophysics, 31, 473 3.1

Arnaudova M. I., et al., 2024, Exploring the radio-loudness of SDSS quasars with spectral stacking, http://arxiv.org/abs/2401.08774 3.3.3

Ashby M. L. N., et al., 2009, The Astrophysical Journal, 701, 428 1.3, 3.2.1, 5.2.1

Audibert A., et al., 2023, Astronomy & Astrophysics, 671, L12 1.1.3

Ayubinia A., Woo J.-H., Rakshit S., Son D., 2023, The Astrophysical Journal, 954, 27 1.1.4, 3.1

Baloković M., Smolčić V., Ivezić , Zamorani G., Schinnerer E., Kelly B. C., 2012, The Astrophysical Journal, 759, 30 1.1.2

Baug T., et al., 2021, Monthly Notices of the Royal Astronomical Society, 507, 4316 1.1.3

Becker R. H., White R. L., Helfand D. J., 1995, The Astrophysical Journal, 450, 559 5.1

Beckmann R. S., et al., 2017, Monthly Notices of the Royal Astronomical Society, 472, 949 1.1.1

Bell E. F., McIntosh D. H., Katz N., Weinberg M. D., 2003, The Astrophysical Journal Supplement Series, 149, 289 1.1.1

Benton C. E., et al., 2024, The Astrophysical Journal Letters, 974, L28 1.1

Bertin E., Mellier Y., Radovich M., Missonnier G., Didelon P., Morin B., 2002. p. 228, https://ui.adsabs.harvard.edu/abs/2002ASPC..281..228B 4.3.4

Best P. N., et al., 2023, Monthly Notices of the Royal Astronomical Society, 523, 1729 1.1.2, 1.1.2, 3.2.1, 3.4.4, 4.2.1, 5.1, 5.4

Binney J., Tremaine S., 2011, Galactic Dynamics: Second Edition. Princeton University Press 1.1

Birzan L., Rafferty D. A., McNamara B. R., Wise M. W., Nulsen P. E. J., 2004, The Astrophysical Journal, 607, 800 3.1

Blandford R. D., Königl A., 1979, The Astrophysical Journal, 232, 34 5.5.1

Blanton M. R., et al., 2017, The Astronomical Journal, 154, 28 1.1.3

Bondi M., et al., 2024, Astronomy & Astrophysics, 683, A179 2.1.5, 4.1

Bonzini M., et al., 2015, Monthly Notices of the Royal Astronomical Society, 453, 1079 1.1.2, 3.1

Boroson T. A., Green R. F., 1992, The Astrophysical Journal Supplement Series, 80, 109 3.3.1

Bowen I. S., 1927, Publications of the Astronomical Society of the Pacific, 39, 295 1.1.3

Bower R. G., Benson A. J., Malbon R., Helly J. C., Frenk C. S., Baugh C. M., Cole S., Lacey C. G., 2006, Monthly Notices of the Royal Astronomical Society, 370, 645 1.1.1, 3.1, 5.1

Brown M. J. I., Dey A., Jannuzi B. T., Brand K., Benson A. J., Brodwin M., Croton D. J., Eisenhardt P. R., 2007, The Astrophysical Journal, 654, 858 3.2.1

Brown M. J. I., et al., 2008, The Astrophysical Journal, 682, 937 3.2.1

Calistro Rivera G., et al., 2021, Astronomy and Astrophysics, 649, A102 3.4.5

Calistro Rivera G., et al., 2023, Ubiquitous radio emission in quasars: predominant AGN origin and a connection to jets, dust and winds, doi:10.48550/arXiv.2312.10177, https://ui.adsabs.harvard.edu/abs/2023arXiv231210177C 3.1, 3.4.5

Carnall A. C., 2017, SpectRes: A Fast Spectral Resampling Tool in Python, http://arxiv.org/abs/1705.05165 3.3.3

Carniani S., et al., 2015, Astronomy & Astrophysics, 580, A102 3.3.2

Charlot P., et al., 2020, Astronomy & Astrophysics, 644, A159 4.3.4

Chartas G., et al., 2021, The Astrophysical Journal, 920, 24 1.1.3

Cicone C., Brusa M., Ramos Almeida C., Cresci G., Husemann B., Mainieri V., 2018, Nature Astronomy, 2, 176 1.1.3

Cirasuolo M., Celotti A., Magliocchetti M., Danese L., 2003, Monthly Notices of the Royal Astronomical Society, 346, 447 1.1.2

Clavel J., Schartel N., Tomas L., 2006, Astronomy & Astrophysics, 446, 439 1.1.3

Condon J. J., 1992, Annual Review of Astronomy and Astrophysics, 30, 575 5.4

Cooley J. W., Tukey J. W., 1965, Mathematics of Computation, 19 2.1.2

Croton D. J., et al., 2006, Monthly Notices of the Royal Astronomical Society, 367, 864 1.1.1, 3.1, 5.1

DESI Collaboration D., et al., 2025, Data Release 1 of the Dark Energy Spectroscopic Instrument, doi:10.48550/arXiv.2503.14745, http://arxiv.org/abs/2503.14745 1.1.3, 1.1.3, 5.6, 6.1

Daddi E., et al., 2007, The Astrophysical Journal, 670, 156 1.1

Dawson K. S., et al., 2016, The Astronomical Journal, 151, 44 1.1.3

De Vries W. H., Morganti R., Röttgering H. J. A., Vermeulen R., Van Breugel W., Rengelink R., Jarvis M. J., 2002, The Astronomical Journal, 123, 1784 1.3

Dekel A., Silk J., 1986, The Astrophysical Journal, 303, 39 1.1.1

Delvecchio I., et al., 2017, Astronomy & Astrophysics, 602, A3 1.1.2, 1.1.2, 3.1, 5.1

Dewdney P. E., Hall P. J., Schilizzi R. T., Lazio T. J. L. W., 2009, IEEE Proceedings, 97, 1482 6.1

Dickinson M., Papovich C., Ferguson H. C., Budavári T., 2003, The Astrophysical Journal, 587, 25 1.1

Dimitrijević M. S., Popović L. \., Kovačević J., Dačić M., Ilić D., 2007, Monthly Notices of the Royal Astronomical Society, 374, 1181 3.3.1

Duncan K. J., et al., 2021, Astronomy & Astrophysics, 648, A4 3.4.4

Edge D. O., Shakeshaft J. R., McAdam W. B., Baldwin J. E., Archer S., 1959, Memoirs of the Royal Astronomical Society, 68, 37 1.1.2, 2.1.1

Escott E. L., et al., 2025, Monthly Notices of the Royal Astronomical Society, 536, 1166 3, C.2

Fabian A. C., 2012, Annual Review of Astronomy and Astrophysics, 50, 455 3.1

Fawcett V. A., et al., 2023, Monthly Notices of the Royal Astronomical Society, 525, 5575 3.2.4

Feldmann R., Hopkins P. F., Quataert E., Faucher-Giguère C.-A., Kereš D., 2016, Monthly Notices of the Royal Astronomical Society, 458, L14 1.1

Fiore F., et al., 2017, Astronomy & Astrophysics, 601, A143 1.1.3, 5.1

Fitzpatrick E. L., 1999, Publications of the Astronomical Society of the Pacific, 111, 63 3.3.3

Fluetsch A., et al., 2021, Monthly Notices of the Royal Astronomical Society, 505, 5753 1.1.3

Foreman-Mackey D., Hogg D. W., Lang D., Goodman J., 2013, Publications of the Astronomical Society of the Pacific, 125, 306 3.3.1

Franzen T. M. O., et al., 2015, Monthly Notices of the Royal Astronomical Society, 453, 4020 5.3

Frey S., Paragi Z., An T., Gabányi K. E., 2012, Monthly Notices of the Royal Astronomical Society, 425, 1185 3.2.3

Förster Schreiber N. M., Wuyts S., 2020, Annual Review of Astronomy and Astrophysics, 58, 661 1.1

García-Bernete I., et al., 2021, Astronomy & Astrophysics, 645, A21 1.1.3

Gebhardt K., et al., 2000, The Astrophysical Journal, 539, L13 1.1.1, 3.1, 5.1

Geréb K., Maccagni F. M., Morganti R., Oosterloo T. A., 2015, Astronomy & Astrophysics, 575, A44 1.1.3

Gibson R. R., Brandt W. N., 2012, The Astrophysical Journal, 746, 54 1.1.3

Girdhar A., et al., 2022, Monthly Notices of the Royal Astronomical Society, 512, 1608 1.1.4, 3.1, 5.5.3

Gitti M., Brighenti F., McNamara B. R., 2012, Advances in Astronomy, 2012, e950641 3.1

Gofford J., Reeves J. N., McLaughlin D. E., Braito V., Turner T. J., Tombesi F., Cappi M., 2015, Monthly Notices of the Royal Astronomical Society, 451, 4169 1.1.3

Gonzalez A. H., et al., 2010, in American Astronomical Society Meeting Abstracts #216. p. 415.13 1.3, 3.2.1

González V., Labbé I., Bouwens R. J., Illingworth G., Franx M., Kriek M., Brammer G. B., 2010, The Astrophysical Journal, 713, 115 1.1

Goodman J., Weare J., 2010, Communications in Applied Mathematics and Computational Science, 5, 65 3.3.1, 5.2.1

Google 2011, Books of the world, stand up and be counted! All 129,864,880 of you., http://booksearch.blogspot.com/2010/08/books-of-world-stand-up-and-be-counted.html 1.1

Greene J. E., Ho L. C., 2005, The Astrophysical Journal, 627, 721 1.1.3, 3.1

Greenwell C., Gandhi P., Stern D., Boorman P., Toba Y., Lansbury G., Mainieri V., Desira C., 2021, Monthly Notices of the Royal Astronomical Society: Letters, 503, L80 3.2.3

Gupta M., Sikora M., Rusinek K., 2020, Monthly Notices of the Royal Astronomical Society, 492, 315 1.1.2

Gültekin K., et al., 2009, The Astrophysical Journal, 698, 198 1.1.1

Gürkan G., et al., 2019, Astronomy & Astrophysics, 622, A11 1.1.2

Haarlem M. P. v., et al., 2013, Astronomy & Astrophysics, 556, A2 3.1

Hamaker J. P., Bregman J. D., Sault R. J., 1996, Astronomy and Astrophysics Supplement, v.117, p.137-147, 117, 137 2.1.1

Harrison C., 2014, Doctoral, Durham University, http://etheses.dur.ac.uk/10744/ 1.1.2, 1.3

Harrison C. M., Almeida C. R., 2024, Observational Tests of Active Galactic Nuclei Feedback: An Overview of Approaches and Interpretation, doi:10.48550/arXiv.2404.08050, http://arxiv.org/abs/2404.08050 1.1.3, 5.1

Harrison C. M., Alexander D. M., Mullaney J. R., Swinbank A. M., 2014, Monthly Notices of the Royal Astronomical Society, 441, 3306 1.1.3, 1.1.3, 3.3.2, 3.4.3

Harrison C. M., Thomson A. P., Alexander D. M., Bauer F. E., Edge A. C., Hogan M. T., Mullaney J. R., Swinbank A. M., 2015, The Astrophysical Journal, 800, 45 1.1.3, 1.1.4

Harrison C. M., Costa T., Tadhunter C. N., Flütsch A., Kakkad D., Perna M., Vietri G., 2018, Nature Astronomy, 2, 198 1.1.3, 5.1

Hazard C., Mackey M. B., Shimmins A. J., 1963, Nature, 197, 1037 1.1.2

Hinshaw G., et al., 2013, The Astrophysical Journal Supplement Series, 208, 19 3.1, 4.1, 5.1

Holden L. R., Tadhunter C., Audibert A., Oosterloo T., Ramos Almeida C., Morganti R., Pereira-Santaella M., Lamperti I., 2024, Monthly Notices of the Royal Astronomical Society, 530, 446 1.1.3

Huggins W., Miller W. A., 1864, Philosophical Transactions of the Royal Society of London, 154, 437 1.1.3

Hughes D. H., et al., 1998, Nature, 394, 241 1.1

Husemann B., et al., 2019, Astronomy and Astrophysics, 627, A53 1.1.3

Högbom J. A., 1974, Astronomy and Astrophysics Supplement Series, 15, 417 2.1.2

Intema H. T., Tol S. v. d., Cotton W. D., Cohen A. S., Bemmel I. M. v., Röttgering H. J. A., 2009, Astronomy & Astrophysics, 501, 1185 4.3.1

Intema H. T., Weeren R. J. v., Röttgering H. J. A., Lal D. V., 2011, Astronomy & Astrophysics, 535, A38 4.3.1

Intema H. T., Jagannathan P., Mooley K. P., Frail D. A., 2017, Astronomy & Astrophysics, Volume 598, id.A78, 598, A78 4.3.2

Jackson N., et al., 2016, Astronomy & Astrophysics, 595, A86 4.3.2

Jackson N., et al., 2022, Astronomy & Astrophysics, 658, A2 4.3.2

Jannuzi B. T., Dey A., 1999, The NOAO Deep Wide-Field Survey, https://ui.adsabs.harvard.edu/abs/1999ASPC..193..258J 1.3, 3.2.1, 4.3.4

Jansky K. G., 1933, Nature, 132, 66 1.2.1

Jarvis M. E., et al., 2019, Monthly Notices of the Royal Astronomical Society, 485, 2710 1.1.4, 1.2.3, 3.1, 3.5.1, 5.5.3

Jarvis M. E., et al., 2021, Monthly Notices of the Royal Astronomical Society, 503, 1780 1.1.2, 1.2.3, 3.5.1, 5.5.3

Jong J. M. G. H. J. d., et al., 2025, Scalable and robust wide-field facet calibration with LOFAR's longest baselines, doi:10.48550/arXiv.2508.12115, http://arxiv.org/abs/2508.12115 4.3.2

Kaiser N., et al., 2010, in Stepp L. M., Gilmozzi R., Hall H. J., eds, Society of Photo-Optical Instrumentation Engineers (SPIE) Conference Series Vol. 7733, Ground-based and Airborne Telescopes III. p. 77330E, doi:10.1117/12.859188 3.2.1

Kakkad D., et al., 2020, Astronomy & Astrophysics, 642, A147 3.3.1, 3.3.2

Karouzos M., Woo J.-H., Bae H.-J., 2016, The Astrophysical Journal, 819, 148 1.1.3

Keller P. M., Thyagarajan N., Kumar A., Kanekar N., Bernardi G., 2024, Monthly Notices of the Royal Astronomical Society, 528, 5692 1.1.2

Kellermann K. I., Sramek R., Schmidt M., Shaffer D. B., Green R., 1989, The Astronomical Journal, 98, 1195 1.1.2, 1.4, 3.1

Kellermann K. I., Sramek R. A., Schmidt M., Green R. F., Shaffer D. B., 1994, The Astronomical Journal, 108, 1163 1.1.2

Kenter A., et al., 2005, The Astrophysical Journal Supplement Series, 161, 9 1.3

Klein U., Lisenfeld U., Verley S., 2018, Astronomy & Astrophysics, 611, A55 3.2.3, 5.2.1

Klindt L., Alexander D. M., Rosario D. J., Lusso E., Fotopoulou S., 2019, Monthly Notices of the Royal Astronomical Society, 488, 3109 1.1.2, 1.1.4, 3.4.5

Kollmeier J. A., et al., 2017, SDSS-V: Pioneering Panoptic Spectroscopy, doi:10.48550/arXiv.1711.03234, http://arxiv.org/abs/1711.03234 1.1.3

Kondapally R., et al., 2021, Astronomy & Astrophysics, 648, A3 1.3, 3.2.1, 3.2.3, 3.2.3, 3.2.4, 4.2.1, 4.3.4, 4.3.4, 5.2

Kormendy J., Richstone D., 1992, The Astrophysical Journal, 393, 559 1.1, 3.1, 5.1

Kormendy J., Richstone D., 1995, Annual Review of Astronomy and Astrophysics, 33, 581 1.1, 3.1, 5.1

Kukreti P., Morganti R., 2024, Connecting the radio AGN life cycle to feedback: Ionised gas is more disturbed in young radio AGN, http://arxiv.org/abs/2407.06265 1.2.3, 5.1

Kukreti P., Morganti R., Tadhunter C., Santoro F., 2023, Astronomy & Astrophysics, 674, A198 1.1.4, 3.1, 5.1

Kukreti P., Wylezalek D., Albán M., Dall'Agnol de Oliveira B., 2025, Astronomy and Astrophysics, 698, A99 5.5.3

Kutkin A. M., et al., 2023, Astronomy & Astrophysics, 676, A37 1.3, 6.1

Lacy M., et al., 2020, Publications of the Astronomical Society of the Pacific, 132, 035001 1.2.3, 3.5.1, 5.1

Lansbury G. B., Jarvis M. E., Harrison C. M., Alexander D. M., Moro A. D., Edge A. C., Mullaney J. R., Thomson A., 2018, The Astrophysical Journal Letters, 856, L1 1.1.3

Lanzuisi G., et al., 2014, The Astrophysical Journal, 781, 105 1.1.3

Lawrence A., et al., 2007, Monthly Notices of the Royal Astronomical Society, 379, 1599 3.2.1

Lehnert M. D., Tasse C., Nesvadba N. P. H., Best P. N., Driel W. v., 2011, Astronomy & Astrophysics, 532, L3 1.1.3

Leslie S. K., et al., 2020, The Astrophysical Journal, 899, 58 1.1

Liao M., Wang J., Ren W., Zhou M., 2024, Outflow-related radio emission in radio-quiet quasars, https://arxiv.org/abs/2401.05212v1 1.2.3, 3.5.1

Liu G., Zakamska N. L., Greene J. E., Nesvadba N. P. H., Liu X., 2013, Monthly Notices of the Royal Astronomical Society, 436, 2576 3.4.3

Liu H.-Y., Liu W.-J., Dong X.-B., Zhou H., Wang T., Lu H., Yuan W., 2019, The Astrophysical Journal Supplement Series, 243, 21 3.2.2, 3.2.3, 5.2

Liu Y., et al., 2021, The Astrophysical Journal, 908, 124 1.1.2

Lonsdale C. J., et al., 2003, SWIRE: The SIRTF Wide-Area Infrared Extragalactic Survey 3.2.1, 3.2.4, 5.2.1

Lyke B. W., et al., 2020, The Astrophysical Journal Supplement Series, 250, 8 1.1.3, 3.2.2, 3.2.3, 5.2

Macfarlane C., et al., 2021, Monthly Notices of the Royal Astronomical Society, 506, 5888 1.1.2, 1.5, 3.1

Madau P., Dickinson M., 2014, Annual Review of Astronomy and Astrophysics, 52, 415 1.1

Magnelli B., et al., 2024, Astronomy & Astrophysics, 688, A55 1.1

Magorrian J., et al., 1998, The Astronomical Journal, 115, 2285 1.1, 1.1.1, 3.1, 5.1

Majewski S. R., et al., 2017, The Astronomical Journal, 154, 94 1.1.3

Marconi A., Hunt L. K., 2003, The Astrophysical Journal, 589, L21 1.1.1

Martin D. C., et al., 2005, The Astrophysical Journal, 619, L1 3.2.1

Masini A., et al., 2020, The Astrophysical Journal Supplement Series, 251, 2 1.3

Mauduit J. C., et al., 2012, Publications of the Astronomical Society of the Pacific, 124, 714 3.2.1

McNamara B. R., Nulsen P. E. J., 2012, New Journal of Physics, 14, 055023 3.1

Meenakshi M., et al., 2022, Monthly Notices of the Royal Astronomical Society, 516, 766 5.5.3

Merritt D., Ferrarese L., 2001, The Astrophysical Journal, 547, 140 1.1.1, 3.1, 5.1

Miley G., 1980, Annual Review of Astronomy and Astrophysics, 18, 165 5.1

Moldón J., et al., 2015, Astronomy & Astrophysics, 574, A73 4.3.2

Molyneux S. J., Harrison C. M., Jarvis M. E., 2019, Astronomy & Astrophysics, 631, A132 1.1.3, 1.2.3, 5.1, 5.5.3

Morabito L. K., Dai X., Leighly K. M., Sivakoff G. R., Shankar F., 2014, The Astrophysical Journal, 786, 58 1.1.3

Morabito L. K., et al., 2020, Astronomy and Astrophysics, 640, C4 1.1.3

Morabito L. K., et al., 2022a, Identifying active galactic nuclei via brightness temperature with sub-arcsecond International LOFAR Telescope observations, doi:10.48550/arXiv.2207.13096, http://arxiv.org/abs/2207.13096 1.1.2, 5.1, 5.4, 5.4

Morabito L. K., et al., 2022b, Astronomy & Astrophysics, 658, A1 2.1.5, 2.3, 2.1.5, 3.6, 4.3.1

Morabito L. K., et al., 2025a, Astrophysics and Space Science, 370, 19 2.1.5, 4.1, 5.4

Morabito L. K., et al., 2025b, Monthly Notices of the Royal Astronomical Society: Letters, 536, L32 1.1.2, 5.1

Morganti R., Tadhunter C. N., Oosterloo T. A., 2005, Astronomy & Astrophysics, 444, L9 1.1.3

Morrissey P., et al., 2007, The Astrophysical Journal Supplement Series, 173, 682 3.2.1

Mullaney J. R., Alexander D. M., Fine S., Goulding A. D., Harrison C. M., Hickox R. C., 2013, Monthly Notices of the Royal Astronomical Society, 433, 622 1.1.3, 1.1.4, 1.2.3, 3.1, 3.4.5, 3.5.1, 5.1, 5.5.3, 6.1

Murray S. S., et al., 2005, The Astrophysical Journal Supplement Series, 161, 1 1.3

Mutch S. J., Croton D. J., Poole G. B., 2013, Monthly Notices of the Royal Astronomical Society, 435, 2445 1.1.1, 1.1

NASA 2023, Galaxies - NASA Science, https://science.nasa.gov/universe/galaxies/ 1.1

Nesvadba N. P. H., De Breuck C., Lehnert M. D., Best P. N., Collet C., 2017a, Astronomy and Astrophysics, 599, A123 3.1

Nesvadba N. P. H., Drouart G., Breuck C. D., Best P., Seymour N., Vernet J., 2017b, Astronomy & Astrophysics, 600, A121 1.1.4, 5.1

Nims J., Quataert E., Faucher-Giguère C.-A., 2015, Monthly Notices of the Royal Astronomical Society, 447, 3612 1.1.2, 1.1.3, 3.5.1

Njeri A., et al., 2025, The Quasar Feedback Survey: zooming into the origin of radio emission with e-MERLIN, doi:10.1093/mnras/staf020, http://arxiv.org/abs/2501.03433 1.1.2, 1.2.3, 5.5.3

Offringa A. R., 2010, Astrophysics Source Code Library, p. ascl:1010.017 4.3.2

Offringa A. R., et al., 2014, Monthly Notices of the Royal Astronomical Society, 444, 606 4.3.2

Padovani P., 2016, The Astronomy and Astrophysics Review, 24, 13 1.1.2, 1.1.2

Padovani P., Miller N., Kellermann K. I., Mainieri V., Rosati P., Tozzi P., 2011, The Astrophysical Journal, 740, 20 3.1

Padovani P., et al., 2017, The Astronomy and Astrophysics Review, 25, 2 1.1.2, 1.1.2

Panessa F., Baldi R. D., Laor A., Padovani P., Behar E., McHardy I., 2019, Nature Astronomy, 3, 387 1.1.2, 1.7, 3.1, 5.1, 5.5.1

Park D., Barth A. J., Ho L. C., Laor A., 2022, The Astrophysical Journal Supplement Series, 258, 38 3.3.1

Petley J. W., et al., 2022, Monthly Notices of the Royal Astronomical Society, 515, 5159 1.1.2, 1.1.3, 3.1

Petley J. W., et al., 2024, Monthly Notices of the Royal Astronomical Society, 529, 1995 1.1.3

Rawlings S., Saunders R., Eales S. A., Mackay C. D., 1989, Monthly Notices of the Royal Astronomical Society, 240, 701 1.1.4, 3.1, 3.4.3, 5.1

Reber G., 1944, The Astrophysical Journal, 100, 279 1.2.1

Richards G. T., et al., 2006, The Astrophysical Journal Supplement Series, 166, 470 3.2.4, 5.2.1

Rodríguez Zaurín J., Tadhunter C. N., Rose M., Holt J., 2013, Monthly Notices of the Royal Astronomical Society, 432, 138 3.4.3

Rosario D. J., Fawcett V. A., Klindt L., Alexander D. M., Morabito L. K., Fotopoulou S., Lusso E., Calistro Rivera G., 2020, Monthly Notices of the Royal Astronomical Society, 494, 3061 3.2.4

Rubeis E. D., et al., 2025, Revealing the intricacies of radio galaxies and filaments in the merging galaxy cluster Abell 2255. I. Insights from deep LOFAR-VLBI sub-arcsecond resolution images, doi:10.48550/arXiv.2505.13595, http://arxiv.org/abs/2505.13595 4.1

Ruiz N. H., Middelberg E., Norris R. P., Maini A., 2016, Astronomy & Astrophysics, 589, L2 1.1.2

Rupke D. S. N., Veilleux S., 2011, The Astrophysical Journal, 729, L27 1.1.3

Ryle M., Hewish A., 1960, Monthly Notices of the Royal Astronomical Society, 120, 220 2.1

Sabater J., et al., 2021, Astronomy & Astrophysics, 648, A2 1.3, 3.1, 3.2.1, 4.1, 5.1

Santini P., et al., 2009, Astronomy & Astrophysics, 504, 751 1.1

Scaife A. M. M., Heald G. H., 2012, Monthly Notices of the Royal Astronomical Society: Letters, 423, L30 4.3.2

Schawinski K., Thomas D., Sarzi M., Maraston C., Kaviraj S., Joo S.-J., Yi S. K., Silk J., 2007, Monthly Notices of the Royal Astronomical Society, 382, 1415 1.1.1

Schinnerer E., et al., 2004, The Astronomical Journal, 128, 1974 1.3, 3.1

Schinnerer E., et al., 2007, The Astrophysical Journal Supplement Series, 172, 46 1.3, 3.1

Schlegel D. J., Finkbeiner D. P., Davis M., 1998, The Astrophysical Journal, 500, 525 3.3.3

Scholtz J., et al., 2020, Monthly Notices of the Royal Astronomical Society, 492, 3194 3.3.1

Scholtz J., et al., 2021, Monthly Notices of the Royal Astronomical Society, 505, 5469 3.3.1, 5.2.1

Scoles S., 2019, The Virgo Supercluster: Our 100,000 closest galaxies | Astronomy.com, https://www.astronomy.com/science/the-virgo-supercluster-our-100000-closest-galaxies/ 1.1

Shimwell T. W., et al., 2017, Astronomy & Astrophysics, 598, A104 1.1.2, 2.1.5, 3.1, 4.1, 5.1

Shimwell T. W., et al., 2019, Astronomy & Astrophysics, 622, A1 1.1.2, 2.1.5, 2.1.5, 3.1, 4.1, 5.1, 5.3

Shimwell T. W., et al., 2022, Astronomy & Astrophysics, 659, A1 1.1.2, 2.1.5, 3.1, 4.1, 5.1, 5.3

Shimwell T. W., et al., 2025, Astronomy & Astrophysics, 695, A80 1.3, 4.1, 4.4

Smethurst R., Simmons B., Lintott C., Shanahan J., 2019, Monthly Notices of the Royal Astronomical Society, 489, 4016 1.1.3

Smirnov O. M., 2011, Astronomy & Astrophysics, 527, A106 2.1.1

Smith D. J. B., et al., 2016, The WEAVE-LOFAR Survey, doi:10.48550/arXiv.1611.02706, http://arxiv.org/abs/1611.02706 5.6, 6.1

Speranza G., et al., 2023, Multi-phase characterization of AGN winds in 5 local type-2 quasars, http://arxiv.org/abs/2311.10132 3.1

Speranza G., et al., 2024, Astronomy and Astrophysics, 681, A63 5.5.3

Springel V., et al., 2005, Nature, 435, 629 1.1.1

Sun A.-L., Greene J. E., Zakamska N. L., Nesvadba N. P. H., 2014, The Astrophysical Journal, 790, 160 1.1.3

Sweijen F., et al., 2022, Nature Astronomy, 6, 350 2.4, 2.1.5, 3.1, 3.2.1, 3.6, 4.1, 4.2.1, 4.3.1, 4.3.2, 4.4, 4.7, 5.1

Tadhunter C., Tsvetanov Z., 1989, Nature, 341, 422 3.1

Tadhunter C., Morganti R., Rose M., Oonk J. B. R., Oosterloo T., 2014, Nature, 511, 440 1.1.3

Tasse C., et al., 2021, Astronomy & Astrophysics, 648, A1 1.3, 3.1, 3.2.1, 3.13, 4.1, 5.1

Terrell J., 1986, The Astrophysical Journal, 300, 669 1.1.1

Timmerman R., et al., 2022, Astronomy & Astrophysics, 658, A5 1.1.2, 3.1

Tombesi F., Cappi M., Reeves J. N., Palumbo G. G. C., Yaqoob T., Braito V., Dadina M., 2010, Astronomy & Astrophysics, 521, A57 1.1.3

Tombesi F., Cappi M., Reeves J. N., Nemmen R. S., Braito V., Gaspari M., Reynolds C. S., 2013, Monthly Notices of the Royal Astronomical Society, 430, 1102 1.1.3

Tsuzuki Y., Kawara K., Yoshii Y., Oyabu S., Tanabe T., Matsuoka Y., 2006, The Astrophysical Journal, 650, 57 3.3.1

Urry C. M., Padovani P., 1995, Publications of the Astronomical Society of the Pacific, 107, 803 1.1.2, 3.1

Veilleux S., Maiolino R., Bolatto A. D., Aalto S., 2020, Astronomy and Astrophysics Review, 28, 2 5.1

Venturi G., et al., 2021, Astronomy and Astrophysics, 648, A17 5.5.3

Venturi G., et al., 2023, Astronomy & Astrophysics, 678, A127 1.1.3

Villar-Martín M., Binette L., Fosbury R. A. E., 1999, Astronomy and Astrophysics, 346, 7 3.1

Véron-Cetty M.-P., Joly M., Véron P., 2004, Astronomy & Astrophysics, 417, 515 3.3.1

Ward S. R., Costa T., Harrison C. M., Mainieri V., 2024, AGN-driven outflows in clumpy media: multiphase structure and scaling relations, doi:10.48550/arXiv.2407.17593, http://arxiv.org/abs/2407.17593 5.2.1

Webster B., Croston J. H., Harwood J. J., Baldi R. D., Hardcastle M. J., Mingo B., Röttgering H. J. A., 2021, Monthly Notices of the Royal Astronomical Society, 508, 5972 3.1

Weeren R. J. v., et al., 2016, The Astrophysical Journal Supplement Series, 223, 2 4.3.3

Werner M. W., et al., 2004, The Astrophysical Journal Supplement Series, 154, 1 3.2.1

Whitaker K. E., et al., 2014, The Astrophysical Journal, 795, 104 1.1

White S. V., Jarvis M. J., Häußler B., Maddox N., 2015, Monthly Notices of the Royal Astronomical Society, 448, 2665 1.1.2, 3.1

Williams W. L., et al., 2021, Astronomy & Astrophysics, 655, A40 1.3

Woo J.-H., Bae H.-J., Son D., Karouzos M., 2016, The Astrophysical Journal, 817, 108 1.1.4, 3.1

Wright W. H., 1918, Publications of Lick Observatory, 13, 191 1.1.3

Wylezalek D., Flores A. M., Zakamska N. L., Greene J. E., Riffel R. A., 2020, Monthly Notices of the Royal Astronomical Society, 492, 4680 1.1.3

Xia H., Yuan F., Li Z., Zhu B., 2025, Radio signatures of AGN-wind-driven shocks in elliptical galaxies: From simulations to observations, doi:10.48550/arXiv.2507.19716, https://ui.adsabs.harvard.edu/abs/2025arXiv250719716X 1.1.2

Xu C., Livio M., Baum S., 1999, The Astronomical Journal, 118, 1169 1.1.2

Xu Y., et al., 2024, Astronomy & Astrophysics, 687, A179 6.1

Ye H., et al., 2024, Astronomy & Astrophysics, 691, A347 4.3.2, 5.6

Yepes G., Kates R., Khokhlov A., Klypin A., 1997, Monthly Notices of the Royal Astronomical Society, 284, 235 1.1.1

York D. G., et al., 2000, The Astronomical Journal, 120, 1579 1.1.3

Yue B.-H., et al., 2024, Monthly Notices of the Royal Astronomical Society, 529, 3939 1.1.2, 3.1

Yue B. H., et al., 2025, Monthly Notices of the Royal Astronomical Society, 537, 858 1.1.2

Zakamska N. L., Greene J. E., 2014, Monthly Notices of the Royal Astronomical Society, 442, 784 1.1.2, 1.1.2, 1.2.3, 3.1, 3.5.1

Zakamska N. L., et al., 2016, Monthly Notices of the Royal Astronomical Society, 459, 3144 1.1.4, 3.1, 3.5.1, 5.1

Zhou H., Wang T., Zhang X., Dong X., Li C., 2004, The Astrophysical Journal, 604, L33 3.2.3

de Gasperin F., et al., 2019, Astronomy & Astrophysics, 622, A5 4.3.1

de Jong J. M. G. H. J., et al., 2024, Into the depths: Unveiling ELAIS-N1 with LOFAR's deepest sub-arcsecond wide-field images, http://arxiv.org/abs/2407.13247 2.4, 2.1.5, 3.1, 3.2.1, 3.6, 4.1, 4.2.1, 4.3.1, 4.3.4, 4.4, 4.7, 5.1, 5.6

van Diepen G., Dijkema T. J., Offringa A., 2018, Astrophysics Source Code Library, p. ascl:1804.003 4.3.2

van Weeren R. J., et al., 2021, Astronomy and Astrophysics, 651, A115 4.3.2